

© Copyright 1998

Jeffrey S. George

Experimental Study of the Atmospheric ν_μ/ν_e Ratio in the
Multi-GeV Energy Range

by

Jeffrey S. George

A dissertation submitted in partial fulfillment
of the requirements for the degree of

Doctor of Philosophy

University of Washington

1998

Approved by _____

(Chairperson of Supervisory Committee)

Program Authorized

to Offer Degree _____

Date _____

In presenting this dissertation in partial fulfillment of the requirements for the Doctoral degree at the University of Washington, I agree that the Library shall make its copies freely available for inspection. I further agree that extensive copying of this dissertation is allowable only for scholarly purposes, consistent with "fair use" as prescribed in the U.S. Copyright Law. Requests for copying or reproduction of this dissertation may be referred to University Microfilms, 1490 Eisenhower Place, P.O. Box 975, Ann Arbor, MI 48106, to whom the author has granted "the right to reproduce and sell (a) copies of the manuscript in microform and/or (b) printed copies of the manuscript made from microform."

Signature_____

Date_____

University of Washington

Abstract

Experimental Study of the Atmospheric ν_μ/ν_e Ratio in the Multi-GeV Energy Range

by Jeffrey S. George

Chairperson of Supervisory Committee

Research Professor R. Jeffrey Wilkes

Department of Physics

The atmospheric neutrino flux ratio ν_μ/ν_e and its zenith angle dependence have been measured in the multi-GeV energy range using an exposure of 33.0 kiloton-years of the Super-Kamiokande detector. By comparing the data to a detailed Monte Carlo simulation, the ratio $(\mu/e)_{DATA}/(\mu/e)_{MC} = 0.65 \pm 0.05(\text{stat.}) \pm 0.07(\text{syst.})$. In addition, a strong distortion in the shape of the event zenith angle distribution was observed. The ratio of the number of upward to downward μ -like events was found to be $0.61 \pm 0.05(\text{stat.}) \pm 0.02(\text{syst.})$ with an expected value of $0.98 \pm 0.03(\text{stat.}) \pm 0.02(\text{syst.})$. The same ratio for e-like events was consistent with unity. These data provide strong evidence for $\nu_\mu \leftrightarrow \nu_X$ neutrino flavor oscillations with Δm^2 between 3×10^{-2} and 3×10^{-4} eV² and $\sin^2(2\theta) = 1$. These results are fully consistent with Super-Kamiokande results obtained at sub-GeV energies and also consistent with previous measurements.

TABLE OF CONTENTS

List of Figures	vi
List of Tables	x
Chapter 1: Introduction: Neutrinos and Physics	1
1.1 Introduction	1
1.2 Neutrino History	11
1.3 Neutrinos in the Standard Model	19
1.4 Beyond the Standard Model	21
1.5 Experimental Motivations for Non-Zero ν Mass	27
Chapter 2: Cosmic Rays and Atmospheric Neutrinos	33
2.1 Cosmic Ray Primary Fluxes	33
2.2 Cosmic Ray Secondaries	35
2.3 Meson Decay	35
2.4 Production Height	37
Chapter 3: Other Experiments	38
3.1 The Kamiokande Experiment	40
3.2 The IMB Experiment	42
3.3 The MACRO Experiment	44
3.4 The Fréjus Experiment	46
3.5 The Soudan 2 Experiment	47

3.6	The NUSEX Experiment	48
3.7	The Baksan Experiment	49
Chapter 4:	The Super-Kamiokande Experiment	51
4.1	Neutrino Interactions in Water-Cherenkov Detectors	51
4.2	Cherenkov Radiation	55
4.3	Cherenkov Ring Imaging	58
4.4	Detector Description	59
Chapter 5:	Inner Detector Data Acquisition	64
5.1	Front End Electronics	64
5.2	Data Buffering Electronics	68
5.3	Online Workstations	68
5.4	Trigger Electronics	69
Chapter 6:	Outer Detector Data Acquisition Electronics	72
6.1	Overview	72
6.2	Quadrant Hut Electronics	73
6.3	Central Hut Electronics	81
Chapter 7:	Outer Detector Data Acquisition Software	93
7.1	Anti-Counter Collector Program	93
7.2	Anti-Sorter Program	99
7.3	Anti-Sender Program	102
Chapter 8:	Data Flow: Online to Offline	104
8.1	Run Control	104
8.2	Event Builder	105
8.3	Super Low Energy Event Processing	105

8.4	The Reformat Process	106
8.5	The TQREAL and FLOW Processes	107
Chapter 9:	Detector Performance	108
9.1	Water Clarity	108
9.2	Photo-multiplier Tubes	108
9.3	Trigger Rates and Number of Events	111
Chapter 10:	Calibrations	115
10.1	Laser Timing Calibration	115
10.2	Linac	117
10.3	Nickel Source	118
10.4	Cosmic Ray Muons	118
10.5	Michel Electrons	119
10.6	π^0 Rest Mass	120
10.7	Xenon Lamp	121
Chapter 11:	Simulation	122
11.1	Atmospheric Neutrino Flux	123
11.2	Neutrino Interactions	126
11.3	Particle Tracking	128
11.4	Monte Carlo Event Summary	129
11.5	Outer Detector Monte Carlo Tuning	129
Chapter 12:	Event Selection	141
12.1	Initial Sample	141
12.2	Fully Contained Neutrino Data Reduction	145
12.3	Partially Contained Event Reduction	149

Chapter 13: Data Summary	157
13.1 Flavor Double Ratio	157
13.2 Vertex Distributions	158
13.3 Event Properties	162
13.4 Zenith Angle Distributions	164
13.5 Systematic Errors	170
Chapter 14: Analysis	184
14.1 Vacuum Oscillations	184
14.2 Neutrino Flight Path	187
14.3 How Oscillations Affect the Zenith Angle Distribution	189
14.4 Chi-square Oscillation Analysis	190
Chapter 15: Other Explanations for Results	207
15.1 Backgrounds	207
15.2 Sources of Neutrinos	209
15.3 Detector Asymmetries	210
15.4 Physics Effects	212
15.5 Summary	213
Chapter 16: Conclusions	214
16.1 Summary of Results	214
16.2 Comparison with Other Analyses	215
16.3 The Future	216
Bibliography	218
Appendix A: Calculating Live-time	230
A.1 Event by Event Corrections	230

A.2 Sub-run Corrections	234
A.3 Net Live-time	239

LIST OF FIGURES

1.1	QED photon emission and Fermi's analogous β -decay model	14
2.1	Observed fluxes of cosmic ray protons, helium nuclei, and CNOs from the compilation of Webber and Lezniak ¹ . Solid lines are a parameterization [1] for solar mid, dashed lines for solar min., and dotted lines for solar max.	34
3.1	Relative depths of atmospheric neutrino experiments	39
3.2	MACRO detector	44
3.3	MACRO detector supermodule detail	45
4.1	Angular deviation of outgoing lepton in simulated CC interactions . .	55
4.2	Particle with $v < c/n$	56
4.3	Particle with $v > c/n$	56
4.4	Cherenkov ring from charged particle track in water	59
4.5	Super-Kamiokande detector construction	60
4.6	Super-Kamiokande support structure (ICRR, University of Tokyo) . .	62
6.1	Overview of outer detector DAQ electronics	73
6.2	OD DAQ quadrant electronics	74
6.3	OD DAQ central hut VME crate modules	82
9.1	Attenuation length over time	109
9.2	ID tube death	110

9.3	Outer detector tube death	111
9.4	Dark rate for inner detector photo-multiplier tubes	112
9.5	Live-time since detector commissioning	113
9.6	Integrated number of events since detector commissioning	113
9.7	Trigger rate since detector commissioning	114
10.1	Reconstructed π^0 Mass	120
11.1	Neutrino flux ratio versus E_ν (GeV), from [2].	124
11.2	Contour map of rigidity cutoff for the ν arrival directions at Kamioka. Azimuth angles of 0° , 90° , 180° , and 270° show directions of south, east, north, and west respectively [2]	126
11.3	Atmospheric ν fluxes multiplied by E_ν^2 for the Kamioka site at solar mid from [2]. The dotted line is a high energy calculation without the rigidity cutoff.	127
11.4	Time distributions	139
11.5	Good hit distributions for data	140
11.6	Good hit distributions for Monte Carlo and 5kHz dark noise	140
13.1	Z vs. R^2 (FC)	159
13.2	Z vs. R^2 (PC)	159
13.3	Z Distribution (FC)	160
13.4	Z Distribution (PC)	160
13.5	Z Distribution (FC e-like)	161
13.6	Z Distribution (FC mu-like)	161
13.7	R^2 Distribution (FC)	162
13.8	R^2 Distribution (PC)	162
13.9	Radial Distribution (FC)	163

13.10Radial Distribution (PC)	163
13.11Radial Distribution (FC e-like)	164
13.12Radial Distribution (FC mu-like)	164
13.13Radial Distribution (PC ingoing)	165
13.14Radial Distribution (PC outgoing)	165
13.15Number of rings (FC)	166
13.16Number of rings (FC e-like)	167
13.17Number of rings (FC mu-like)	167
13.18Visible energy (FC)	168
13.19Visible energy (PC)	168
13.20PID Likelihood for Multi-GeV 1-ring events (FC)	169
13.21Electron-like momentum, 1-ring, multi-GeV (FC)	170
13.22Muon-like momentum, 1-ring, multi-GeV (FC)	170
13.23Zenith angle distribution, 1-ring e-like, multi-GeV (FC)	171
13.24Zenith angle distribution, 1-ring μ -like, multi-GeV (FC)	171
13.25Zenith angle distribution, (PC)	172
13.26Zenith angle distribution, μ -like, multi-GeV (FC+PC)	172
13.27Compare μ data to MC, multi-GeV (FC+PC)	173
13.28(μ/e) Ratio vs. zenith angle, 1-ring, multi-GeV (FC)	174
13.29R versus zenith angle, multi-GeV (FC)	175
13.30R versus zenith angle, multi-GeV (FC+PC)	175
13.31R versus momentum, multi-GeV (FC+PC)	176
13.32R versus wall distance, multi-GeV (FC+PC)	176
13.33Comparison of calibration sources with Monte Carlo.	180
14.1 Neutrino Path Length Calculation	188
14.2 Neutrino flight path length vs. $\cos(\theta_z)$	188

14.3 Oscillation probability as a function of zenith angle for $\sin^2(2\theta)=1$ and $\Delta m^2=10^{-2}$	197
14.4 Oscillation probability as a function of zenith angle for $\sin^2(2\theta)=1$ and $\Delta m^2=10^{-2}$. The same distribution with 20% angular smearing is superimposed.	198
14.5 $\Delta\chi^2 = 2.7$ contours	199
14.6 $\Delta\chi^2/\text{d.o.f}$ for $\sin^2(2\theta)=1$	200
14.7 R vs Δm^2	201
14.8 $\Delta\chi^2 = 2.7$ contours	202
14.9 $\Delta\chi^2/\text{d.o.f}$	203
14.10 $\Delta\chi^2 = 7.78$ contours	204
14.11 $\Delta\chi^2/\text{d.o.f}$	205
14.12 Comparison of data and Monte Carlo at best fit parameters	206
15.1 Azimuthal arrival directions for simulated events at Super-Kamiokande	212
A.1 Muon rate distribution	236
A.2 Mismatched events vs. run	238
A.3 PC bad subruns cut by hand	240

LIST OF TABLES

1.1	Current density terms	15
1.2	Atmospheric neutrino results	30
1.3	Direct neutrino mass limits	31
2.1	Branching ratios for π , K	36
4.1	Fraction of simulated events from various interaction modes	53
11.1	Fully contained multi-GeV MC sample summary	130
11.2	Partially contained multi-GeV MC sample summary	130
11.3	Common parameters used to tune the OD Monte Carlo Simulation	131
11.4	Reflectance of Tyvek as a function of wavelength	135
12.1	Initial sample criteria	142
12.2	2 nd PC reduction criteria	150
12.3	3 rd PC reduction criteria	152
12.4	4 th PC reduction criteria	155
13.1	Event summary. MC expectations are scaled to 33.0 kton-yrs.	157
13.2	Up/down asymmetry	168
13.3	Summary of systematic error	177
13.4	Effect of $E^{-\gamma}$ uncertainty	178
13.5	Difference between eye-scan and automatic ring counting.	178
13.6	Effects of the energy scale uncertainty	180

13.7	Systematics due to cross-section parameters	182
13.8	Effect of OD cluster cuts on FC/PC separation	182
A.1	Event by event corrections to live-time	231
A.2	Reasons to cut a sub-run	234

ACKNOWLEDGMENTS

I would like to first thank my advisor, Dr. R. Jeffrey Wilkes. He understood what it meant to have a family in graduate school and continually reminded me to remember the important things. I deeply appreciated his constant support of me as a student and a scientist. Dr. Kenneth Young pushed me to think harder and gave valuable scientific direction as an unofficial second advisor. Drs. Wick Haxton, George Wallerstein, and Toby Burnett rounded out my graduate committee with valuable perspective.

The other members of the UW Particle Astrophysics Group have also benefited me greatly. Dr. Larry Wai was a mentor to me. I appreciated his leadership in joining the on-site atmospheric neutrino analysis group. I learned everything I know about electronics from Hans Berns. He is an extraordinarily skilled engineer whose contributions to the DUMAND and Super-Kamiokande experiments go far beyond what most people realize. Dr. Jere Lord could be counted on for an enthusiastic word at any time of the day or night. Linda Vilett managed the administrative nightmares with grace and courage. Fellow graduate students Andrew Stachyra and Ross Doyle helped carry the load of building and running a new experiment. Eric Zager and Erik Olsen shared many a computing adventure.

I should like to thank the members of the DUMAND collaboration, especially John Learned and the University of Hawaii group. DUMAND was a great experiment and I will always be proud to have been a part of it. The

failure of the final ATV cruise to repair the junction box was one of the most devastating days of my life. Thanks to Hans Berns, Jeff Bolesta, and Kristal Mauritz for sharing the misery and finding ways for us to move on.

The Super-Kamiokande experiment is a joint effort of many groups. I joined the experiment a little too late to pay my way hanging photo-multiplier tubes and I always appreciated those who did. John Flanagan deserves special mention as one of those people who “made it happen”.

I would like to express particular thanks to the leadership of the Super-Kamiokande experiment, in particular Y. Totsuka, Y. Suzuki, M. Nakahata, and T. Kajita from ICRR (U. Tokyo), and H. Sobel and J. Stone for the US institutions. Their hard work and leadership made the detector a reality.

I have to thank T. Kajita in particular. As a leader in the atmospheric neutrino analysis he welcomed me into the group and went to great efforts to make it possible for me to participate from across the Pacific Ocean. He became a surrogate advisor to me and I greatly appreciated his counsel. The on-site atmospheric analysis group went to a lot of trouble to welcome this English speaker. In particular, Y. Hayato, M. Shiozawa, K. Okumura, and K. Ishihara provided me with immeasurable help during construction of the outer detector data acquisition. Y. Fukuda’s friendly singing to his computer will never be forgotten. These people also gave me a lot of assistance when I turned to the atmospheric neutrino analysis. Thank you for your friendship.

Looking farther back, I would like to thank my professors at Seattle Pacific University who went to a lot of trouble to ensure that I had the finest undergraduate physics education they could possibly provide. I hope I can return the favor to my own students one day. Dr. Roger Anderson hired me for a summer for a project I never really finished (but still have the notes for!). Dr.

James Crichton was a role model for me.

Thanks to Dr. Norval Fortson and Dr. Steve Lamoreaux of the University of Washington for allowing me to spend nine months in their atomic physics laboratory. Some part of me will always regret the lack of funding that sent me into neutrino astrophysics.

I am particularly grateful to Jeff Wilkes, Ken Young, Hank Sobel, and Jordan Goodman for their strong letters of recommendation. I wish I could have accepted all of the jobs you found for me. Your support was really appreciated.

My parents deserve great thanks for their support over many years. Mom, we've come a long way from when we were learning algebra together! Both of them listened even when I made no sense and reminded me that He who created all this wonderful stuff is also a part of my life.

Lastly I want to express my great appreciation for my wife, Gaye. She put up with eight years of student living in the hope that "sometime soon" I would be done and have a real job. That time stretched far beyond what she ever thought possible and the "real job" isn't yet what she deserves. Thank you for your patience, your endless work raising our children, your love, and your support. Natasha and Spencer, you make my heart glad.

The experiment was made possible with the cooperation and assistance of the Kamioka Mining and Smelting Company and the Japanese Ministry of Education, Science, Sports, and Culture (Monbusho). This work was supported by the United States Department of Energy (DOE) under grant numbers DE-FG01-96ER40956, DE-FG02-96ER40956, and DE-FG03-96ER40956.

DEDICATION

For Mark Roberts,
missionary, teacher, inventor, and friend.

You told a young boy in the Peruvian Andes that God is a physicist.

I never forgot.

Chapter 1

INTRODUCTION: NEUTRINOS AND PHYSICS

1.1 *Introduction*

Since its postulation in 1933, the neutrino has played a central role in the understanding of particle physics. Its properties probe the very small; high energy particle physics, to the very large; cosmology and the structure of the universe. Rarely does a single particle have the opportunity to influence thought in such a wide range of our understanding of the universe.

The neutrino has become a fundamental part of physics. Its unique position as the only neutral fundamental particle both completes the standard model and challenges it. Its interaction properties make it an ideal probe for otherwise unobservable reaches of the universe. The sheer numbers of neutrinos in the universe make them a critical issue for the large scale gravitational evolution of the cosmos. Exactly what neutrinos are and precisely how they behave may provide the key to questions in many very diverse fields. Three types are currently known, each one paired with its corresponding charged lepton, the electron, muon, or tau particle. As far as is known they are stable against decay.

Neutrino Properties

Neutrinos have zero electric charge. No electric or magnetic dipole moments have yet been measured. Astrophysically this is important because they travel in straight lines from the point of origin without bending by galactic magnetic fields. It also means

that they cannot be detected directly by their electric or magnetic properties.

Neutrinos interact only through the weak interaction. In the standard V-A theory of weak interactions, the weak force only couples to negative helicity (left-handed) neutrinos and positive helicity (right-handed) anti-neutrinos. The extremely small (possibly zero) mass means neutrinos always move at essentially the speed of light. This tends to polarize all particles with spin to left-handed states.

No evidence for the existence of right-handed neutrinos has ever been found. Whether this is because such particles do not exist or simply because of the small mass or the lack of coupling to the weak force remains an open question. Searches for right-handed neutrinos or right-handed weak interactions provide stringent tests of the standard model and its possible extensions.

The neutrino interaction cross-section is extremely small. On the good side, this allows neutrinos to escape from stellar interiors and pass through dense galactic structures, bringing us information directly from regions that could not be observed in any other way. They easily pass through the earth, making our planet into a large filter for everything else. The tiny cross-section makes life very difficult for the experimenters, though. Huge volumes or high luminosity are required to see any neutrino interactions in a reasonable time. Neutrino physics has been the story of ever-larger detection volumes and ever-higher accelerator beam luminosities.

Neutrinos are present all around us from many sources. Experiments have gone on in many energy regimes to study neutrino properties. At the lowest energies, radioactive decay measurements put direct limits on the possible electron neutrino mass. Atomic power reactors emit neutrinos which can be detected nearby through layers of shielding. The first detection of neutrinos was done in a reactor experiment. A rather larger nuclear reactor is our sun. Solar neutrinos have been an exciting field of study since they are a direct probe of the nuclear processes occurring in the otherwise totally inaccessible core of the sun. Observation of fewer than the expected number of neutrinos comprises the “solar neutrino problem” with exciting implications for

either solar models or particle physics.

At somewhat higher energies, the neutrino flux on earth is dominated by those produced by cosmic rays striking earth's atmosphere. Early experiments measured a ratio of muon to electron type neutrinos that was inconsistent with expectations. Since cosmic rays are nearly isotropic one would expect to see the same effect in all directions but one experiment observed a dependence of the ratio on the direction of observation. These observations became known as the "atmospheric neutrino anomaly".

Neutrinos in Super-Kamiokande

The Super-Kamiokande detector is the latest entry in the atmospheric and solar neutrino detection arena. Vastly larger than any of its predecessors, this experiment has surpassed all previous data in both quantity and quality. The large size also allow measurements at higher energies than ever before possible.

The majority of neutrino events detected are events whose interaction products are fully contained within the detector. These offer the highest statistics and best energy measurements but tend to be at energies where the neutrino products do not well respect the direction of the incident neutrino. As a result the benefit of large numbers of events is partly balanced by a large uncertainty in the neutrino flight path.

At multi-GeV energies ($E_{vis} > 1.33$ GeV) a significant fraction of muons produced in the interaction escape from the inner detector. These "partially contained" events have much lower statistics than the "sub-GeV" samples and only a minimum energy estimate can be made. However, the multi-GeV neutrinos contain a much lower uncertainty in arrival direction and reflect a much higher distribution in energy. This gives them an analyzing power far surpassing what might be expected from statistics alone.

This thesis describes a new measurement of the ν_μ/ν_e ratio in atmospheric neutri-

nos using the recently constructed Super-Kamiokande neutrino detector at multi-GeV energies. High energy fully contained muon and electron events are extracted from the standard data reduction streams and a completely separate data reduction path created specifically for partially contained muons. Measurements in this energy range serve as an important check on the lower energy results. Effects of neutrino flavor oscillations should increase with energy and be even more visible in high energy data than in lower regimes.

Neutrinos and Me

My participation in the Super-Kamiokande experiment began in the summer of 1995, just in the construction phase of the outer detector. The preparation for this job, however, actually began three years earlier when I joined the DUMAND (Deep Underwater Muon and Neutrino Detector) experiment [3]. It was there that I learned about water Cherenkov detection, neutrino physics, and data acquisition, all skills that I could later bring to Super-Kamiokande .

The DUMAND experiment was designed to study TeV and higher energy neutrinos from extra-galactic sources using deep ocean water as a Cherenkov medium. I worked primarily with the Junction Box Environmental Module designed to control the array sonar systems that would determine the photo-multiplier tube positions [4]. I designed the power distribution system and mechanical chassis for this module and assembled the subsystems into a complete sonar system with continuous monitoring of the ocean environment. I wrote the underwater operating software that gave control over a number of oceanographic instruments and sonar channels. My experience in digital electronics culminated in the redesign of a four channel signal processing board capable of timing sonar signal transit times and recording raw hydrophone signals from the ocean environment.

My original thesis topic was an attempt to connect my data acquisition experience to high energy neutrino astrophysics. I planned to use the signal processing board I

had redesigned to search for acoustic signals from high energy neutrino interactions [5]. The ability to do this could vastly increase the effective volume of the detector. The cancellation of the DUMAND experiment ended this hope and after presenting a paper on acoustic neutrino detection at the 24th International Cosmic Ray Conference in Rome [6], I joined the rest of University of Washington particle astrophysics group in working on Super-Kamiokande .

The University of Washington was a relative late-comer to the Super-Kamiokande experiment, and I was the last of the group to make an official switch from the DUMAND experiment. Other members of the group, especially Dr. Ken Young and fellow graduate student Andrew Stachyra, had been exploring various options for the outer detector data acquisition system for some time [7]. I came in just at the time when construction funds were finally beginning to appear and hardware could be purchased. It was time to fill in the data acquisition system flow chart boxes with real electronics.

My experience with system integration and low level control software made it natural for me to assume responsibility for the outer detector data acquisition system. My primary job was to write an interface to allow a SUN workstation to access electronics modules in the VME crate that would buffer the entire data stream. This interface eventually became the control program ("collector") for the entire front end data acquisition system [8]. I also wrote the initial version of the program to take data blocks gathered from the four quadrants of the detector and repack them into event blocks ready to merge with inner detector data ("sorter"). Larry Wai, a postdoctoral researcher, joined the group soon after and eventually took responsibility for the sorter program.

I worked closely with Hans Berns, a University of Washington electronics engineer, to define the requirements for custom electronics boards which he designed for latching auxiliary event information such as the detector event number, and a relative time stamp. I devised a scheme to latch the UTC time obtained from a GPS satellite

receiver to provide absolute event timing [9, 10]. We added a variety of digital control signals to improve the "collector" program's ability to monitor and control all aspects of the front end data acquisition hardware.

One of my duties at this time was to integrate work done by the University of Maryland group into the framework of the control software that I was writing. Drs. Mei-li Chen and Jordan Goodman had written programs to drive the FSCC crate controller modules for the FASTBUS electronics crates in the quadrant electronics huts. The FSCCs buffer digitized photo-multiplier data into dual-port memories through the DC-2 VME auxiliary bus controller, for which they also provided a control program. I worked with them to learn how to control their code from my VME-workstation interface. We added new features to help the "collector" program better monitor the status of the FASTBUS crates and to automatically recover from occasional glitches. We also managed to diagnose several data acquisition problems using these programs.

Construction became frantic as the April 1996 detector commissioning deadline drew near. I went to Japan to help complete the installation of the outer detector electronics and cabling. This was the first time that we had access to more than one quadrant worth of data acquisition modules. It was also the first time that my control software had to be integrated into the main detector run control. I made these changes while at the same time diagnosing hardware and software faults with the help of Larry Wai and expert guidance of Hans Berns. In some cases we rebuilt the custom electronics cards on the spot. The outer detector became functional just before the April 1 deadline and I was privileged to be part of the commissioning ceremony with a fully operational experiment.

Data acquisition problems continued to plague the outer detector, as might be expected from any brand new system. I spent much of the next year at the detector improving the control program and diagnosing data acquisition problems that would periodically stop data taking or cause problems when restarting. I helped to identify several major problem areas which were addressed by Hans Berns in an upgrade

of the custom electronics. Larry Wai and I corrected innumerable small errors in both the "collector" and "sorter" programs. Within a few months after the detector commissioning, the data acquisition system was stable. I worked then to improve the monitoring of the detector status and to solve a few nagging problems which were not a serious threat to the integrity of the data stream.

With the detector running smoothly, I had time to begin analysis work. The Super-Kamiokande collaboration initially created two independent atmospheric neutrino analysis teams which happened to split largely along national lines. Larry Wai and I made the pioneering step of asking to join the "on-site" analysis team in order to get immediate access to data and to tap the experience of the Kamiokande members. Dr. Ken Young followed us shortly afterwards. In addition to general analysis duties we were given the responsibility for developing a reduction algorithm for "partially contained" neutrino events, those whose interaction products escape the detector. Larry developed fast clustering algorithms and worked to remove stopping and corner clipping muons from the raw data. I developed a cut based on outer detector activity near the projected entrance point. Real neutrino events should have not have light at the entrance to the detector. This turned out to be a powerful way to separate entering contamination from exiting neutrino events.

As part of the development of the partially contained reduction stream I spent some time working to improve the tuning of the outer detector Monte Carlo simulation. This was important because estimates of the efficiency of the reduction algorithms depended on this simulation. I adjusted the values of previous tuning parameters and added new ones to allow the reflectivity of the outer detector liner to be set separately for the top, bottom, and wall sections of the detector. I was able to bring the simulated hit and charge distributions for a sample of events to within about 10% of the real data distributions for all regions of the detector. This was enough to produce reasonable estimates of the partially contained reduction performance.

I managed the processing of the partially contained neutrino data reduction for

the first 414 live-days of exposure. This involved running each data file through all the reduction stages and creating a final sample of events. I managed the groups of human scanners that were initially a part of the reduction process and were later reduced to quality control. For much of the sample I served as “final” scanner, arbitrating previous scan results. The reduction process entails a lot of bookkeeping also, to be sure that the entire sample is processed and that the detector exposure is correctly calculated. My re-calculation of the partially contained live-time corrected significant errors in previous results presented by other members. Ross Doyle assisted with the bookkeeping after the first 414 days and Dr. Kate Scholberg brought the final sample up to 535 days of exposure with new reduction monitoring tools.

The partially contained events comprise my contribution to the atmospheric neutrino analysis. These sample the highest energies of neutrinos which interact in the detector volume. I prepared a summary of these events for various collaboration meetings and showed that they exhibit a strong zenith angle dependence. The “on-site” and “off-site” independent analysis groups have now merged after demonstrating consistency between their respective results for fully contained neutrino events. My data currently remain the only set of partially contained events available from Super-Kamiokande .

I combined the partially contained event sample with the multi-GeV fully contained events provided by other members of the analysis group to make a complete multi-GeV neutrino data set. This dissertation presents an analysis of that data in the context of $\nu_{\mu} \leftrightarrow \nu_{\tau}$ neutrino flavor oscillations. The results are consistent with other analyses performed with lower energy data and provide good confirmation for evidence supporting the existence of a neutrino mass.

Outline of the dissertation

The rest of the introductory chapter will provide a background to the history and relevance of neutrino physics. A theoretical basis for the role of neutrinos in the stan-

dard model and the framework for neutrino masses is provided. Current experimental limits on neutrino masses are also reviewed.

Chapter 2 describes the cosmic rays interactions that produce atmospheric neutrinos. The physics of these interactions form the basis for the expected neutrino flavor ratios. The exciting aspect of current neutrino results is a deviation from these expectations. Chapter 3 discusses previous experimental measurements of atmospheric neutrinos.

The structure of the new Super-Kamiokande experiment is described in Chapter 4. The principle of operation of a water Cherenkov detector is described, including neutrino interactions in water and the detector's response to those interactions. Following chapters will describe the Super-Kamiokande detector operation in greater detail.

Building such a large experiment is very much a collaborative effort. Construction of the inner detector and associated data acquisition electronics was primarily a responsibility of the Japanese collaborators. However, the actual event data are recorded by the inner detector. A description is included in Chapter 5. The outer detector is a much simpler, but vitally important component supplied by the US institutions. The University of Washington group led the work of designing and constructing the outer detector data acquisition system, an effort in which I was heavily engaged. Electronics for the outer detector system are described in Chapter 6.

The “collector” program, for which I was completely responsible, handles the control and readout of the entire outer detector electronics system. I also contributed to the online event sorting and repackaging routines, all of which are described in Chapter 7. Chapter 8 discusses the means by which the raw data are handled before finally being delivered to analysis groups.

The detector performance and calibrations are discussed in Chapters 9 and 10. These are vitally important monitors of the operation of the detector. Regular energy and timing calibrations ensure that the experiment stays healthy and form the basis

of our knowledge of the accuracy of our energy estimates.

Chapter 11 describes the atmospheric neutrino detector simulation. This simulation (along with an independent calculation) forms the basis of the collaboration's claim that the measured data do not agree with expectations. My work in tuning the outer detector simulation to more closely match reality is also described.

Chapter 12 finally describes the process by which atmospheric neutrino events are selected from the hundreds of thousands of raw triggers recorded every day. Two separate reduction streams are presented. The fully contained event selection is the high energy extension of the same analysis used to produce atmospheric results in the sub-GeV energy range. A second data reduction stream was built to find partially contained neutrino interactions. The author and Larry Wai, then a post-doctoral researcher in the University of Washington group had complete responsibility for the partially contained event reduction. The creation of the data reduction algorithms was shared roughly equally and I was responsible for processing the raw data. A summary of the data from both analysis streams in the multi-GeV energy range is presented in Chapter 13.

Chapter 14 presents the author's analysis of the neutrino data based on an assumption of $\nu_\mu \rightarrow \nu_\tau$ flavor oscillations. Allowed regions of oscillation parameter space are calculated.

Chapter 15 summarizes what other effects could cause the observed results. Various backgrounds and detector systematic effects are discussed. Studies of these backgrounds have shown that it is very unlikely that they could be responsible for what is measured.

The Super-Kamiokande data are opening up an exciting new window on neutrino physics. Data from the sub-GeV event sample have already provided very strong evidence for the existence of a neutrino mass. The present study of higher energy events confirms that data and its interpretation in terms of neutrino flavor oscillations. It is hoped that this work, along with the efforts of the entire Super-Kamiokande

collaboration, will contribute to our continuing understanding of the neutrino and its properties.

1.2 Neutrino History

1.2.1 Probing the nucleus: 1896-1930

The story of the neutrino really begins in 1896 with the discovery of radioactivity [11]. At the suggestion of Poincarè, Henri Becquerel was investigating the properties of various uranium salts. To his amazement, tightly wrapped photographic plates nearby were found to have been exposed. Pierre and Marie Curie continued investigations into the phenomenon of radioactivity, chemically separating isotopes which caused the effect. In 1898 they succeeded in isolating polonium and radium. By 1899, Rutherford had shown that there were several different types of radiation which had different deflections in a magnetic field. He called dubbed the types alpha, beta, and gamma. J.J. Thompson had discovered the electron as “cathode rays” in 1897. By 1902 the Curie’s had shown that beta radiation consisted of these electrons. The 1903 Nobel prize in physics would be shared by Becquerel and the Curie’s for their work in radioactivity.

Excited work by many people led to the conclusion by 1904 that all three types of radiation emitted from the nucleus. Alpha radiation had been shown to be a ${}^4\text{He}$ nucleus; gamma radiation a very energetic photon; and beta radiation an electron. The view at this time and through the 1920’s was that nature consisted of only two fundamental particles; the electron and proton. The nucleus was considered to be a combination of the two.

Beta radiation quickly presented a problem. Since the electron was the only observed particle emitted, it should have had a well-defined, fixed energy corresponding to a two body decay. The kinetic energy was shared only between the recoiling nucleus and the electron. Moreover, the kinetic energy available, or Q value, is simply the

mass loss of the nucleus. All of the initial nuclei started with the same mass so the Q value should be identical. Alpha and gamma radiation showed narrow spectral peaks, clearly showing excitation of discrete nuclear states. Beta radiation was drastically different.

It was clear by 1914 from studies by Lise Meitner, Otto Hahn, Wilson and von Baeyer, James Chadwick and others, that the electron energy spectrum was in fact continuous. Conservation of energy appeared to fail. In addition, there was a problem in accounting for the spin-statistics of ^{14}N and ^6Li which did not appear to obey the exclusion principle for spin-1/2 objects.

1.2.2 Postulating the neutrino: 1930-1934

On December 4, 1930, Wolfgang Pauli made a “desperate remedy” to save the idea of conservation of energy as well as the statistics problem. In a letter to Meitner and Hans Geiger who were attending a conference at Tübingen [12] [13], he proposed that an undetected third particle is emitted which shares the energy with the electron. This “neutron” had to be neutral, have a mass comparable to or less than the electron mass, carry spin-1/2 statistics and have a high penetrating power. He expressed little hope that his solution could work since particles with the properties he imagined should have been detected already. “However,” he wrote, “only those who gamble can win” and urged the attenders to consider his idea. Supported by Meitner and Geiger, the idea was discussed favorably. Pauli did not attend the conference personally, declaring himself “indispensable” at a ball to be held in Zurich at the same time.

In 1932, James Chadwick discovered a neutral particle inside the nucleus and took the name “neutron” to match the proton. The charge and statistics fit Pauli’s idea, but the mass was comparable to the proton mass. This large mass was much too high to explain the beta-decay spectrum.

By 1933, the impasse began to break. Pauli finally became bold enough to publish something of his idea as a footnote to Heisenberg’s report at the Seventh Solvay

Conference in Brussels. The concept was already well known to most physicists. It appears, though unclear, that Pauli still thought of the electron and the neutrino as constituents of the nucleus. F. Perrin, who attended the conference, showed soon after that a massless neutrino could be *created* at the time of emission. He also attempted to extract an upper mass limit from experimental β -decay spectra and concluded that the mass was effectively zero [14].

Enrico Fermi also had attended the conference in Brussels. Shortly afterward, he published his theory of beta-decay which assumed that a neutrino always accompanies the decay electron and that both are created at the moment of emission [15]. This took care of the problems of explaining numerous spin-1/2 particles coexisting as nuclear constituents. He coined the term “neutrino” at this time, Italian for “little neutral one”.

Fermi’s model was fashioned in close analogy to Dirac’s relativistic quantum theory for electromagnetism. QED described the radiation of a photon by an electron as a three pronged vertex carrying coupling strength $-e$. Following the presentation by Commins [16], the effective Lagrangian density takes the form:

$$\mathcal{L}_{EM}(\mathbf{x}, t) = -ej_\alpha(\mathbf{x}, t)A^\alpha(\mathbf{x}, t) \quad (1.1)$$

where j_α is the electromagnetic current density and A^α is the four-vector potential for the electromagnetic field. The current density is written

$$j_\alpha(\mathbf{x}, t) = \overline{\Psi}_e(\mathbf{x}, t)\gamma_\alpha\Psi_e(\mathbf{x}, t) \quad (1.2)$$

Here Ψ_e represents the electron field. In Fermi’s prescription for beta decay, the electron and anti-neutrino together play the role of the emitted photon, see Figure 1.2.2. Terms in the interaction are replaced in a straightforward way by analogy with QED.

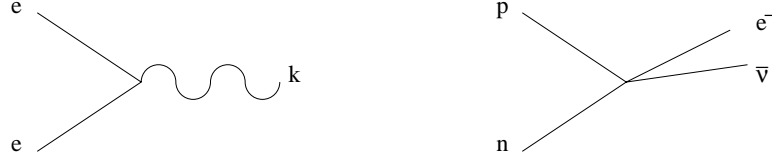


Figure 1.1: QED photon emission and Fermi's analogous β -decay model

$$j_\alpha \rightarrow \overline{\Psi}_p \gamma_\alpha \Psi_n \quad (1.3)$$

$$A^\alpha \rightarrow \overline{\Psi}_e \gamma^\alpha \Psi_\nu \quad (1.4)$$

$$-e \rightarrow \frac{G}{\sqrt{2}} \quad (1.5)$$

The new coupling constant G at this point was a free parameter that remained to be determined by experiment. Fermi's beta decay Lagrangian became:

$$\mathcal{L}_\beta = \frac{G}{\sqrt{2}} \overline{\Psi}_p \gamma_\alpha \Psi_n \cdot \overline{\Psi}_e \gamma^\alpha \Psi_\nu + \text{h.c.} \quad (1.6)$$

The hermitian conjugate term accounts for positron emission and e^- capture. Fermi's theory broke down at high energies, but gave a very good explanation of the beta decay electron spectrum. It became the prototype for modern field theories.

It was shortly afterward pointed out by Gamow and Teller [17] that this is not the only form of the interaction which could be written. Fermi chose the vector form in analogy to QED. Actually, five different types of matrices can be sandwiched into the weak current term, classified by their transformation properties. These are listed in Table 1.1. Gamow and Teller showed that the S and V type occur only for transitions with angular momentum $\Delta J = 0$ while A or T are required for $\Delta J = \pm 1$. After the discovery of parity violation intense work showed that the weak interaction has a vector axial-vector form which violates parity maximally. At low energies the only substantive modification to the Fermi model is to replace γ_α by $\gamma_\alpha(1 - \gamma_5)$.

Table 1.1: Current density terms

$\mathbf{1}$	scalar	S
γ_μ	vector	V
$\sigma_{\mu\lambda}$	tensor	T
$\gamma_\mu\gamma_5$	axial-vector	A
γ_5	pseudo-scalar	P

Also in 1933, Anderson discovered the positron and at the end of the year Frederic Joliot-Curie demonstrated beta-plus radioactivity with emission of a positron instead of an electron. These begin to provide crucial evidence for P.A.M. Dirac’s relativistic quantum theory and Fermi’s weak interaction model.

Circumstantial evidence was mounting but the quest itself was still a difficult one. By 1934 it was becoming clear that the neutrino cross-section must be extremely small, less than 10^{-44} cm^2 [18]. This fact would thwart the hopes of would be neutrino hunters for the next twenty two years. The discovery of the neutrino would require a huge source of neutrinos, a huge detector, or both.

1.2.3 Confirmation and Consequences: 1934-1983

The largest man made sources of neutrinos were on the way. In 1942 at the University of Chicago, Enrico Fermi successfully operated the world’s first atomic pile. The chain reaction released neutrons and neutrinos. The success of the test launched the Manhattan Project, centered at Los Alamos, New Mexico, culminating in the explosion of the first atomic bomb in 1945. Frederick Reines was working on the project. With the bomb program largely behind him, he was searching for an “important but impossible problem”. He proposed putting a detector near an atomic blast to take advantage of the vast quantities of neutrinos expected. A rough calculation led him to believe the experiment was possible with a one cubic meter sized detector. Reines

broached the idea to Fermi in 1951 in a timid chat. Fermi agreed the bomb was a good source of neutrinos, but also could not see how to build the detector [19]. Feeling that if Fermi didn't know how to do it, it couldn't be done, Reines put the idea aside for some months.

In 1952 a chance conversation with Clyde Cowan while grounded at the Kansas City airport changed all that. The two began talking about interesting physics problems to work on and quickly found themselves partnering to study neutrinos. The initial plan was still to use the bomb as a source of neutrinos and was actually approved by the Los Alamos Laboratory management.

The Reines/Cowan experiment relied on detecting the photons from interaction products of anti-neutrinos in the reaction $\bar{\nu} + p \rightarrow e^+ + n$. 400 liters of an aqueous cadmium chloride solution provided a target. The positron annihilates with an atomic electron to make two simultaneous gamma ray photons. The neutron is captured by the cadmium nucleus with more photon emission at a characteristic time of 15 microseconds later.

As an example of how ideas are formed, Reines and Cowan gave a talk at Los Alamos in which they described their proposed detector. They discussed the coincidence between the positron and neutron pulses as a label for the reaction without even thinking that the same signal could be used to reduce background. Asked in the seminar if a fission reactor might not be as suitable a source as the bomb, the pair argued persuasively against the idea. That very night, both realized how the coincidence could be used, thereby making the reactor a much more attractive option. Plans were changed the next day and the Hanford experiment was born [20].

In an amazingly short time by today's standards, the plan was put into action. The experiment was proposed in February 1953 [21], constructed at Hanford, Washington by the spring, and results were published by the summer [22]. A strong hint of a signal was observed, but not enough to claim unambiguous detection. In 1956 the experiment was upgraded and moved to the brand new Savannah River plant in

South Carolina. This plant, in addition to having more flux than the Hanford reactor, also had a room that could house the detector 12 meters underground. The added level of shielding from background cosmic rays made the difference and this time the neutrino signal was clear. Thirty six years after its proposal by Pauli, the existence of the neutrino was experimentally confirmed [23]. This landmark experiment would lead many years later to a long-awaited Nobel prize in Physics for Reines in 1995.

Now that the neutrino had been experimentally verified, new ideas and projects flowed quickly. A discussion between T. D. Lee and Mel Schwartz in a Columbia University cafeteria in 1959 led the latter to realize that an intense beam of neutrinos was possible from pion decay. Lee and C.N. Yang tackled the theoretical calculations while Schwartz went to Leon Lederman, Jack Steinberger, and Jean Marc Gaillard to design the experiment. They found a detector to suit their needs in a spark chamber built by Jim Cronin at Princeton. Cronin went on to share the 1980 Nobel Prize with Val Fitch for symmetry violations in K^0 decays.

Construction proceeded over the next several years at Brookhaven while Lee and Yang became more and more convinced that if $\mu^- \rightarrow e^- + \gamma$ was not observed then there must exist two types of neutrinos [24].

In 1962 the question was finally settled. Out of the millions of neutrinos produced by the Brookhaven accelerator, 40 interacted in the detector. 34 of those produced a muon, a clear signal. Only six produced electrons, consistent with background. There was no significant electron component and the issue was settled. There were two distinct types of neutrinos [25]. Schwartz, Lederman, and Steinberger would share the 1988 Nobel prize for discovery of the muon neutrino and their work with neutrino beams.

1.2.4 A unified approach: 1983-present

The next twenty years were fruitful ones for particle physics. The quark model developed and many new particles were discovered. The neutrino was hardly forgotten.

Much of the new data on nuclear structure and quark content came from studies of the weak interaction for which neutrinos are the prototype.

Parallels between the quarks and leptons were hard to ignore. In 1970, Glashow, Illiopoulos, and Maiani proposed the existence of a second quark family [26]. Similarities between quark and lepton families were more and more suggestive.

A unified field theory for the weak interactions proposed by Weinberg and Glashow [27] and Salam [28] had been gaining ground. Some of the predictions of the theory were the existence of three intermediate vector bosons mediating the weak interaction. Two of these were charged and reactions that could involve them were well known. The third, however, was neutral. No known reaction went by way of a weak neutral current. The existence of such reactions would provide a decisive test of the new theory. In 1973, after a furious race, neutral current reactions were discovered at CERN's Gargamelle bubble chamber [29]. Fermilab confirmed the result later the same year [30].

In 1977, Leon Lederman with the Stanford team discovered the b quark, part of a new third quark family [31]. About the same time Martin Perl discovered the tau lepton, pointing to a third lepton family [32]. The tau neutrino is expected to also exist, but as of now (early 1998) it has not been detected experimentally.

The 1980's brought the pieces of the story together into the picture we see today. The gauge theory based on $SU(3)_{color} \times SU(2)_{flavor} \times U(1)_{EM}$ by Weinberg, Glashow, and Salam was generating excitement. For the first time a gauge theory appeared to completely unify the weak and electromagnetic forces at only the cost of a few extra gauge bosons whose masses, by invoking the Higgs mechanism, could be predicted. Discovery of the predicted weak neutral currents was already a triumph of the theory. All that remained was direct detection of the actual gauge particles.

Discovery of the W in 1983 and later the Z at CERN at almost precisely the predicted masses brought a Nobel Prize to Carlo Rubbia and great acclaim to the new theory. In little more time the new "electroweak" theory became the basis for what

is now considered the Standard Model. At the same time it became the prototype for all subsequent efforts at unification of forces.

A side bonus of the discovery of the Z^0 is that its decays limit the number of light neutrino flavors. Since $Z^0 \rightarrow q\bar{q}, l\bar{l}$ one can measure the partial decay width into “invisible”, presumably neutrino, channels. The limit applies to so called sterile neutrinos as well as the known active ones as long as the mass is less than half the rest mass of the Z^0 . By this time in 1998, millions of Z decays have been recorded and the measurement of the number of channels is now 2.991 ± 0.016 [33].

In the current version of the Standard Model, neutrinos occupy a prominent place as the only leptons interacting solely via the weak interaction. With their lack of electric charge they are a unique probe into reactions that would be inapproachable with any other particle.

1.3 Neutrinos in the Standard Model

The weak interaction has been modified somewhat from Fermi’s four fermion point-like interaction. Analogous to QED’s exchange of photons, the weak interaction is mediated by the exchange of massive vector bosons, W^\pm and Z^0 , accounting for the short range of the force. Following discovery of CP violation in the kaon system [34] the interaction was given a vector-axial vector (V-A) form which violates parity maximally. The weak Lagrangian takes the form of

$$\bar{\Psi}\gamma_\mu(1 - \gamma_5)\Psi \tag{1.7}$$

and the $(1 - \gamma_5)$ serves as a projection operator for the left handed chirality states in Ψ .

The presence of the left handed projection in the weak Lagrangian means that right-handed neutrinos do not enter into the theory at all. This mirrors the state of the experimental reality in which a right handed neutrino has never been observed.

On the other hand, it means that the theory has no opinion about the existence of such particles.

The left handed leptons enter into the theory as SU(2) doublets, coupling the electron with its neutrino, the muon with its neutrino, and the tau with its as yet undiscovered neutrino. The right handed electron, muon, and tau enter as SU(2) singlets without an associated neutrino.

$$\begin{array}{ccc}
 \left(\begin{array}{c} e \\ \nu_e \end{array} \right)_{LH} & \left(\begin{array}{c} \mu \\ \nu_\mu \end{array} \right)_{LH} & \left(\begin{array}{c} \tau \\ \nu_\tau \end{array} \right)_{LH} \\
 e_{RH} & \mu_{RH} & \tau_{RH}
 \end{array} \tag{1.8}$$

Lepton number conservation by flavor is assumed by the Standard Model because of nuclear beta decay studies and the absence of reactions like $\mu \rightarrow e\gamma$. It has become a near article of faith for most physicists. This faith may be misplaced. Lepton flavor number conservation is not demanded by a fundamental symmetry in the same way that, for example, electron charge conservation is. Many grand unified theories and extensions to the standard model naturally allow violation of lepton number.

The assumption of lepton number conservation along with the lack of right handed neutrinos leads to a massless neutrino. Typical Dirac mass terms analogous to the charged leptons are excluded because there are no right handed fields in the theory. The Majorana terms which could generate a mass explicitly violate lepton number conservation and furthermore make the theory non-renormalizable. These terms are discussed in more detail in section 1.4.2.

1.4 Beyond the Standard Model

1.4.1 Neutrino Masses

One of the most immediate extensions one might make to the standard model is the addition of a neutrino mass term. There are several reasons why this is a very natural thing to do. Neutrinos in the standard model lack a mass analogous to that of the charged leptons because there are no right-handed neutrino fields. The other possible type of mass term (Majorana) is excluded because of an *a priori* assumption of lepton number conservation. Furthermore, the neutrino belongs to a lepton multiplet which contains a massive charged lepton. Most grand unified theories place the leptons and quarks together in the same multiplet. A massless neutrino in a multiplet where all the other members are massive would be exceptional indeed.

The motivations for investigating non-zero neutrino masses are also compelling. Fermion masses are not well understood in the standard model anyway. Better understanding of neutrino masses may help our understanding of the rest. Most grand unified theories and standard model extensions include massive neutrinos. Experiments probing neutrino masses also probe the predictions of these theories. If the universe contains hot dark matter, massive neutrinos could be an important part of that and have a significant role in cosmology. Further, the experimentally observed solar and atmospheric neutrino anomalies are suggestive of neutrino flavor oscillations. Many indications tell us that neutrino masses are not only a natural extension to present theories, but that nature may well have chosen to use them.

We are led, then, to some very deep questions which center around the properties of the neutrino. Do neutrinos have mass? If not, why don't they? If yes, why is the mass so small? Is the neutrino equivalent to the anti-neutrino? How many species of neutrinos are there?

The first question is obviously a key one. If neutrinos are massive, it implies that there could be a leptonic mixing matrix analogous to the Cabibbo-Kobayashi-

Maskaya (CKM) quark mixing matrix. This could lead to neutrino flavor oscillations. Massive neutrinos could constitute a significant fraction of the mass of the universe. If neutrinos do not have mass, one has to ask why that should be so. A precisely massless neutrino should require some fundamental reason that is not at all obvious at this point.

The first question begs the second. If neutrinos are indeed massive, why is the mass so small? Limits on the electron neutrino mass have fallen from Pauli's guess of a mass comparable to that of the electron to under 5 eV. The neutrino mass scale is a factor of 10^5 lower than the corresponding charged leptons and a definite mass has still not been measured. Why should the scales be so different?

Another profound question is whether the neutrino is a two-component or a four-component object. In the general case where both Dirac and Majorana masses exist the natural basis is a two-component Majorana one. In the limit where the Majorana masses disappear, as is the case with the charged leptons, the mass eigenstates become pairwise degenerate and can be patched together to form a Dirac four-component particle. A Dirac four-component neutrino has a nice analogy with the other leptons but makes the small mass of the neutrino difficult to explain. A Majorana two component neutrino provides a “natural” way of explaining the small masses by the introduction of a higher mass scale and the seesaw mechanism. This approach also requires use of a Higgs triplet and causes explicit lepton number violation.

Finally, we might ask how many neutrino species exist. One might imagine continuing to add generations *ad infinitum*. LEP data on the Z^0 line shape now limit the number of light ($< \frac{1}{2}M_{Z^0}$) active neutrino species to 2.991 ± 0.016 [33]. Big bang nucleosynthesis limits the number of sterile species. Sterile species could be SU(2) singlets and thus ignored by the weak interaction.

Big bang nucleosynthesis provides a limit on the number of neutrino species in the following way. In nucleosynthesis models, a gas of baryons is followed as the universe cools. The input physics is well determined. The weak interaction drops

out of equilibrium around a temperature of 1 MeV. At this point, the neutron to proton ratio is determined entirely by the thermodynamic equilibrium. It is assumed that at the time of nucleosynthesis, photons, electrons, and several neutrino species are present along with the nucleons. The number of species of neutrinos affects the equilibrium and hence the abundance of the light elements. Observation of light element abundances can restrict the allowed number of species. Data on ${}^4\text{He}$ strictly limit N_ν to 4 or less, with 4 being only marginally allowed [35]. Here “light” means up to around 10 MeV.

Supernova 1987A also provided a somewhat looser limit on the number of species of neutrinos. In the collapse of a neutron star, the binding energy is radiated as neutrinos. About 10% of the energy comes away in the initial neutronization burst while the rest comes out in thermal pairs from $e^+e^- \rightarrow \nu\bar{\nu}$ for all species of neutrinos with masses less than around 10 MeV. Assuming some form of equipartition of energy among species, the number of ν_e or $\bar{\nu}_e$ events detected depends on the number of neutrino species. Data from Kamiokande and IMB limit N_ν to 6.7 or less [35].

1.4.2 Theory of Neutrino Mass

There are a limited number of ways that one can add a neutrino mass term to the standard model. The following discussion is based on that of Haxton and Stephenson [36]. Neutrinos may have the same Dirac mass terms as the charged leptons, but in addition, because of their neutral charge, they may include Majorana terms which are forbidden for other particles.

As mentioned above, the Dirac four component particle is a special instance of the more general case of two Majorana fields. In the limit where the Majorana masses vanish, as is required for any particle but the neutrino, the two mass eigenstates become pairwise degenerate and can be patched together into a single four component particle. Given this, a natural way to understand the Majorana terms is to begin with the Dirac mass term and generalize it to the case of n particles with distinct left and

right fields, each with their own couplings. The Dirac mass term for n fields is:

$$\mathcal{L}_m^D = -\frac{m_D^{ij}}{2} \overline{\psi}_i \psi_j + \text{h.c.} \quad (1.9)$$

If we introduce left and right handed fields defined according to $\psi_L = \frac{1}{2}(1 - \gamma_5)\psi$ and $\psi_R = \frac{1}{2}(1 + \gamma_5)\psi$, the term can be rewritten as

$$\mathcal{L}_m^D = -\frac{m_D^{ij}}{2} [\overline{\psi}_{iL} \psi_{jR} + \overline{\psi}_{iR} \psi_{jL}] + \text{h.c.} \quad (1.10)$$

Now allow the left and right fields to be distinct and to have distinct couplings.

$$\mathcal{L}_m^D \rightarrow -\frac{m_D^{ij}}{2} \overline{\psi}_{iL} \psi'_{jR} - \frac{\tilde{m}_D^{ij}}{2} \overline{\psi}'_{iR} \psi_{jL} + \text{h.c.} \quad (1.11)$$

$$= -\overline{\psi}_L M_D^\dagger \psi'_R - \overline{\psi}'_R M_D \psi_L \quad (1.12)$$

where $\overline{\psi}_L M_D \psi'_R = M_D^{ij} \overline{\psi}_{iL} \psi_{jR}$ is a matrix product over the n fields and $2M_D^{ij} = \tilde{m}_D^{ij} + (m_D^{ij})^*$.

Take further that

$$\overline{(\psi_L)^c} (\psi'_R)^c = \overline{\psi'_R} \psi_L \quad (1.13)$$

$$\overline{(\psi'_R)^c} (\psi_L)^c = \overline{\psi_L} \psi'_R \quad (1.14)$$

so the Lagrangian density finally becomes

$$\mathcal{L}_m^D = -\frac{1}{2} \left[\overline{\psi}_L M_D^\dagger \psi'_R + \overline{\psi}'_R M_D \psi_L + \overline{(\psi'_R)^c} M_D^* (\psi_L)^c + \overline{(\psi_L)^c} M_D^T (\psi'_R)^c \right] \quad (1.15)$$

In matrix form,

$$\mathcal{L}_m^D = -\frac{1}{2} \left[\overline{(\psi_L)^c}, \overline{\psi'_R}, \overline{\psi_L}, \overline{(\psi'_R)^c} \right] \begin{bmatrix} 0 & 0 & 0 & M_D^T \\ 0 & 0 & M_D & 0 \\ 0 & M_D^\dagger & 0 & 0 \\ M_D^* & 0 & 0 & 0 \end{bmatrix} \begin{bmatrix} (\psi_L)^c \\ \psi'_R \\ \psi_L \\ (\psi'_R)^c \end{bmatrix} \quad (1.16)$$

This is the most general Dirac mass term. However, it is not the most general possible mass term for neutrinos. It is possible to add Majorana terms of the form

$$\mathcal{L}_m^M = -\frac{1}{2} \left[\overline{(\psi_L)^c} M_L \psi_L + \overline{(\psi'_R)^c} M_R \psi'_R \right] + \text{h.c.} \quad (1.17)$$

These terms are not invariant under the gauge transformation $\psi \rightarrow e^{i\alpha}\psi$ and do not conserve lepton flavor number. They explicitly transform a particle into its anti-particle. An equivalent interpretation is that it creates or annihilates two neutrinos, an important prescription for neutrino-less double beta decay. Such terms would also violate the conservation of electric charge for charged particles, hence only Dirac terms are allowed in that case. The neutrino is unique in allowing the possibility of including the extra Majorana terms.

One can take M_L and M_R to be symmetric and write the general mass term for the neutrino as the sum of the Dirac and Majorana contributions $\mathcal{L}_m = \mathcal{L}_m^D + \mathcal{L}_m^M$. Again in matrix form,

$$\mathcal{L}_m = -\frac{1}{2} \left[\overline{(\psi_L)^c}, \overline{\psi'_R}, \overline{\psi_L}, \overline{(\psi'_R)^c} \right] \begin{bmatrix} 0 & 0 & M_L & M_D^T \\ 0 & 0 & M_D & M_R^\dagger \\ M_L^\dagger & M_D^\dagger & 0 & 0 \\ M_D^* & M_R & 0 & 0 \end{bmatrix} \begin{bmatrix} (\psi_L)^c \\ \psi'_R \\ \psi_L \\ (\psi'_R)^c \end{bmatrix} \quad (1.18)$$

The middle array is a $4n \times 4n$ matrix. It is sufficient to work with the upper corner as all the information is contained there. In general the “mass matrix” (here only

the upper quarter is actually used) is complex and symmetric, but if CP is conserved then M will be real. The mass eigenvalues can be found by diagonalizing M .

$$M = \begin{pmatrix} M_L & M_D^T \\ M_D & M_R^\dagger \end{pmatrix} \quad (1.19)$$

A particularly interesting limit happens when the right hand mass coupling M_R is dominant. This occurs naturally in left-right symmetric models. In these models, the neutrino Dirac mass term comes from the same spontaneous symmetry breaking that generates the quark and lepton masses. One expects then that the neutrino Dirac mass M_D should be on the scale of the quark or charged lepton masses.

For the Majorana masses in these models, the left handed coupling M_L is related to neutral current neutrino scattering parameters which have been measured. These results indicate that M_L would be very small. M_R is related to the scale of spontaneous symmetry breaking and is very large, much larger than the quark or charged lepton masses.

To summarize, in the right hand dominant model we can take $M_L = 0$, $M_D \sim M_q$ or M_l , and $M_R \gg M_D$. This limit provides for the famous “seesaw” mechanism which gives a natural explanation for the lightness of the neutrinos.

Diagonalizing the mass matrix

$$\begin{pmatrix} 0 & M_D \\ M_D & M_R \end{pmatrix} \quad (1.20)$$

in this limit yields two mass eigenvalues:

$$\begin{aligned} m_1 &\sim M_D^2/M_R \\ m_2 &\sim M_R \end{aligned} \quad (1.21)$$

There is one very light and one very heavy neutrino arising naturally. Precisely what the scales should be is another question, but it is clear that this mechanism easily explains the lightness of the neutrino as a result of an effective interaction at a higher scale.

The Dirac mass scale m_D is typically taken to be on the order of the corresponding charged lepton mass. Some grand unified theories suggest it should be related to the lower mass quark in each family. The Majorana scale, M_R , can be almost anything from a few TeV to the Planck mass (10^{19} GeV). An intermediate choice between $10^{12} - 10^{16}$ GeV gives neutrino masses in around the right range for solar and atmospheric neutrino oscillations and is also relevant to hot dark matter calculations.

$$m_1 \sim \frac{(.5MeV)^2}{10^{15}} \sim 2eV \quad (1.22)$$

This estimate of the lower mass eigenvalue is easily consistent with experimental limits on the mass of the electron neutrino. It is assumed here that the electron neutrino mass comes “mostly” from m_1 and that the mass eigenvalues for the three flavors have roughly the same hierarchy as the charged lepton masses.

1.5 Experimental Motivations for Non-Zero ν Mass

The lack of a fundamental symmetry preventing neutrinos from having a non-zero mass is hardly proof that God in fact gave it one. In spite of the philosophically compelling implications of a neutrino mass, all of it is wishful thinking without experimental support. Fortunately, there are experimental anomalies that might well indicate that the neutrino has a definite mass. All use some form of neutrino flavor oscillations to explain the discrepancy between theory and experiment.

1.5.1 *The Solar Neutrino Problem*

The “solar neutrino problem” came out of an experiment started by R. Davis in 1966 to measure the solar neutrino flux. For about twenty years this was the only neutrino detector observing the sun. It produced the surprising result that around one third as many neutrinos were observed as were expected from standard solar model calculations [37].

The Davis experiment consisted of a tank of 615 tons of perchloroethylene (C_2Cl_4). The liquid happens to be manufactured in pure form with large quantities as a fabric cleaning fluid. The tank is located 4850 feet underground in the Homestake Gold Mine near Lead, South Dakota. Neutrino capture on the ^{37}Cl atoms produces ^{37}Ar and an electron with a threshold energy of 0.8 MeV. The argon, roughly 15 atoms, is extracted every few months in an incredible feat of chemical separation.

The solar neutrino problem was initially the simple fact that only half as many neutrinos as expected were actually observed. Later experiments confirmed this with a variety of methods. Kamiokande and IMB were water-Cherenkov experiments, GALLEX [38] and SAGE [39] use a chemical method similar to Homestake, but with pure gallium metal. Because the different methods and detectors have different energy thresholds, they test different parts of the solar neutrino spectrum. Fitting their results yielded the second part of the solar neutrino problem, that the ^7Be are highly suppressed relative to the ^8B neutrinos even though the latter is a branch of the ^7Be decay chain. Attempts to reproduce this behavior by changing the solar models have largely been unsatisfactory, even when introducing highly non-standard models. The failure of these attempts is not a conclusive victory for solar model aficionados, see for example Haxton and Cummings [40], but it is enough to push current thinking toward a particle physics solution.

Nearly all particle physics solutions require a massive neutrino. If the neutrino has a magnetic moment it could interact with the magnetic fields at the surface of the sun.

This could flip a normal left-handed electron neutrino into a right handed neutrino. The weak interaction does not involve right handed particles so it would be effectively sterile and not detected. A magnetic moment on the order of $10^{-10}\mu_B$ or so would be required to flip a neutrino in typical fields at the solar surface. This is barely within current experimental limits [41], but it is far higher than conventional electroweak models. Credence for this idea came largely from an apparent anti-correlation of rate with the solar sunspot cycle. Data taken during the most recent solar cycle do not support such a correlation [42].

The other particle physics solution is that massive electron neutrinos oscillate into other flavors which are not detected. The water Cherenkov detectors could detect muon neutrinos, but only at much higher energies. For example, a 15 MeV ν_e that turns into a ν_μ is far below the threshold for producing a muon. A variation on this scenario is the MSW effect which allows for greatly enhanced oscillations in the presence of matter.

1.5.2 Atmospheric Neutrino Anomaly

Solar neutrinos are not the only indicator of neutrino oscillations. Atmospheric neutrinos exhibit a similar discrepancy. Atmospheric neutrinos are decay products of π and K mesons created in interactions of primary cosmic rays in the atmosphere. The dominant decay is

$$\pi^\pm \rightarrow \mu^\pm + \nu_\mu(\overline{\nu}_\mu) \quad (1.23)$$

$$\mu^\pm \rightarrow e^\pm + \overline{\nu}_e(\nu_e) + \nu_\mu(\overline{\nu}_\mu) \quad (1.24)$$

From this one expects the ratio of $(\overline{\nu}_\mu + \nu_\mu)/(\overline{\nu}_e + \nu_e)$ to be around two. Instead, it is found to be close to one. This apparent deficit of muon neutrinos has been called the atmospheric anomaly. Typically, the ratio from the data is divided by the expected ratio from detailed simulations as shown in Equation 1.25. This is done to

cancel uncertainties in the cross-sections and absolute fluxes.

$$R \equiv \frac{(\mu/e)_{DATA}}{(\mu/e)_{MC}} \quad (1.25)$$

Not all experiments measured this deficit, especially in smaller data samples, but by now the anomaly is fairly well established. Table 1.2 summarizes the world results on atmospheric neutrinos.

Table 1.2: Atmospheric neutrino results

Kamiokande	$R=0.60\pm0.07(\text{stat.})\pm0.05(\text{syst.})$	4.92 kton·yr
IMB	$R=0.54\pm0.05(\text{stat.})\pm0.07(\text{syst.})$	7.7 kton·yr
Soudan 2	$R=0.61\pm0.14(\text{stat.})\pm0.07(\text{syst.})$	1.52 kton·yr
Frejus	$R=0.99\pm0.13(\text{stat.})\pm0.08(\text{syst.})$	2.0 kton·yr
Baksan	$R=0.95\pm0.22(\text{stat.})$	
NUSEX	$R=1.0\pm0.3(\text{stat.})$	0.74 kton·yr

The suggestion of a neutrino oscillation explanation became very compelling in 1994 when Kamiokande reported a dependence of R on the zenith angle [43]. Zenith angle translates directly into neutrino path length.

Comparison of the mixing parameters from solar and atmospheric neutrinos make it clear that they do not come from the same solution. Both could be explained by some form of oscillation if $\nu_e \rightarrow \nu_\mu, \nu_X$ at solar energies and $\nu_\mu \rightarrow \nu_\tau, \nu_X$ at atmospheric neutrino energies. Reactor data from CHOOZ [44] nearly rule out the parameter space for $\nu_\mu \rightarrow \nu_e$ explanations of the atmospheric neutrinos.

1.5.3 Short Baseline – LSND

A third glimpse of possible neutrino oscillations comes from a short baseline experiment known as the Liquid Scintillator Neutrino Detector (LSND) at the Los Alamos Meson Physics Facility (LAMPF). The experiment is illuminated with muon neutrinos

from π^+ in-flight decays. The appearance of ν_e is detected through $\nu_e + p \rightarrow e + n$ in 167 tons of liquid scintillator viewed by photo-multiplier tubes. Cosmic rays produce a large background, especially in regions of the detector which are not well shielded. The results are at best low-statistics with large backgrounds.

The first positive results were published in 1995 [45]. The analysis was not convincing and a dissenting interpretation was published simultaneously in the same volume [46]. Since that time the experiment has continued to run and the signal has grown while remaining relatively consistent with the first hints [47].

1.5.4 Direct Experimental Mass Limits

No experiment has yet directly measured a neutrino mass. Upper limits have been established by various kinematic methods. Table 1.3 lists the current mass limits for the three species of neutrino. The experiments are difficult and the limits get correspondingly worse as the mass of the associated lepton goes up and its lifetime goes down.

Table 1.3: Direct neutrino mass limits

Flavor	Limit	Method
M_{ν_e}	$< 5.1eV$	3H β -decay
M_{ν_μ}	$< 160keV$	$\pi \rightarrow \mu + \nu_\mu$
M_{ν_τ}	$< 24MeV$	$\tau \rightarrow \nu_\tau + 5\pi(\pi^0)$

The best limits for the electron neutrino mass come from 3H beta decay experiments. The spectrum of the ejected electrons in the region near the energy endpoint should be qualitatively different if the neutrino has mass. Tritium is chosen as it has the lowest Q value, imparting only 18.6 keV in total kinetic energy to the electron and neutrino. This enhances the number of decays in the endpoint region and lowers the required energy resolution of the electron spectrometer used to measure the

electron energy. Further, the initial and final nuclear states are easier to calculate than in heavier nuclei. The Los Alamos group used a gaseous ^3H source that avoided many remaining difficulties with calculating the nuclear matrix elements. Their result became mainly statistics limited. The one disturbing trend among all of the tritium experiments was that they pointed to a negative value for m_ν^2 . This suggested a common systematic error in the technique which was not taken into account. Present indications are that this error has been found and the experiments will give a positive upper limit.

The best limits on the muon neutrino mass come from careful studies of stopped pion decays: $\pi^+ \rightarrow \mu^+ \nu_\mu$ [48]. Measurement of the momentum of the muon and knowledge of the rest masses of the muon and pion provide limits on the possible neutrino mass. Advances in the magnetic spectrometers used to measure the muon momentum have improved this result greatly.

The limit on the tau neutrino mass is even more difficult. The current upper limit is set by the ALEPH collaboration at CERN's Large Electron Positron (LEP) collider [49]. The limit is set by fitting the invariant mass and energy in 27 $\tau \rightarrow 5\pi^\pm(\pi^0)\nu_\tau$ decays. The two dimensional likelihood fit provides a substantial gain in sensitivity over previous limits set by ARGUS ($\tau \rightarrow 5\pi^\pm\nu_\tau$) and CLEO II [50] ($\tau \rightarrow 5\pi^\pm\nu_\tau$, $\tau \rightarrow 3\pi^\pm 2\pi^0\nu_\tau$) using only the invariant mass.

Clearly neutrinos are deep in the middle of fundamental questions about the standard model and extensions to it. In presenting new data from Super-Kamiokande it is hoped that this thesis can add a little bit to the answers.

Chapter 2

COSMIC RAYS AND ATMOSPHERIC NEUTRINOS

2.1 Cosmic Ray Primary Fluxes

Cosmic rays are high energy particles filling the interstellar void. They are made up largely of protons (90 % by number), alpha particles (9%) and heavier elements, but nuclei from all known elements as well as photons and electrons are also present. Given the gyro-magnetic radius of these charged particles in the galactic magnetic fields, it appears they are contained in the galaxy but are not local to our solar system. The very highest energy particles may be extra-galactic. When cosmic rays collide with Earth's atmosphere they produce interactions nearly isotropically in the upper regions. These can lead to showers and hadronic cascades detected many different ways at ground level.

There are various techniques for detecting cosmic ray interactions. Gamma ray telescopes observe the gamma rays produced by decays of the neutral mesons in the shower. These typically reach a maximum in the middle atmosphere. Air Cherenkov telescopes detect Cherenkov radiation from the charged mesons and electrons in the high upper atmosphere. Ground air shower arrays detect the pions and K 's that reach the ground in scintillator or Cherenkov detector arrays. Some of these experiments include underground muon detectors to measure the muon component after the light mesons have been filtered out by a layer of earth. Much deeper, underground neutrino detectors study the neutrino component by either observing the neutrino reactions themselves or upward coming muons induced by neutrinos passing through the earth.

The true origin of the cosmic rays remains largely a mystery. Events have been

observed with primary energies over 10^{20} eV. The acceleration mechanisms to get protons to these energies are widely debated.

Most of the components of cosmic rays are well described with a power law spectrum of $E^{-2.71 \pm 0.05}$ [51]. Figure 2.1 shows a compilation of cosmic ray spectra due to Webber and Lezniak [52] for hydrogen, helium, and CNO nuclei. The power law behavior and dominance of the proton flux is clearly evident.

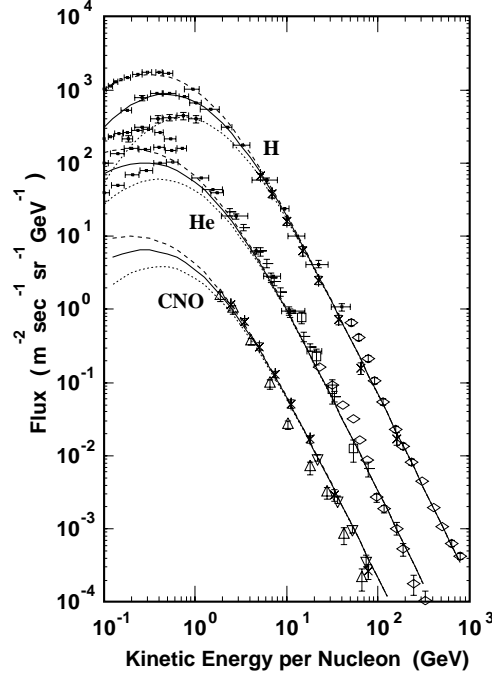


Figure 2.1: Observed fluxes of cosmic ray protons, helium nuclei, and CNOs from the compilation of Webber and Lezniak¹. Solid lines are a parameterization [1] for solar mid, dashed lines for solar min., and dotted lines for solar max.

The level of solar activity changes the expected cosmic ray spectrum. Solar flares pump large quantities of low energy protons into earth's atmosphere. Figure 2.1 shows predictions for various points in the solar cycle. The effect persists up to a few GeV per nucleon for the primary particles. Neutrinos from these particles will only carry a fraction of that energy, so this is not a concern for the current analysis.

2.2 Cosmic Ray Secondaries

Cosmic rays hitting the atmosphere produce a wide array of hadronic and electromagnetic debris. The impact of a highly relativistic proton or higher mass on the oxygen and nitrogen nuclei in the top of the atmosphere results in nuclear fragmentation and the release of huge amounts of energy into hadronic showers. The lightest mesons, π 's and K 's, are produced in copious numbers.

Charged mesons undergo bremsstrahlung and ionization losses, shaking off highly energetic photons which convert to electron pairs. This gives an electromagnetic component to the shower. The K 's and π 's undergo similar decays ending in electrons and neutrinos. The neutral pion component goes to gamma rays which initiate electromagnetic showers. Neutral kaons contain a mixture of K_L^0 and K_S^0 which can produce $\pi^+\pi^-$ pairs.

Of the hadronic interaction products leading to atmospheric neutrinos, pions are by far the most dominant. In one atmospheric neutrino flux simulation [1], the K/π ratio is taken as 7% at 10 GeV, 11% at 100 GeV, and 14% at 1 TeV for proton-nucleus collisions in the lab frame. Accelerator studies of charged particle multiplicities in proton-proton collisions bear this out, finding a K/π ratio of roughly 10% in the relevant energy regions [53].

Charmed particles such as D and \overline{D} can also produce neutrinos. Their contribution to the total flux, however, is extremely small at energies detectable in Super-Kamiokande. Charmed particle neutrino production becomes significant to atmospheric neutrinos only above 100 TeV.

2.3 Meson Decay

Atmospheric neutrinos are actually produced in the decays of the cosmic ray secondaries. Branching ratios for these decays are given in Equation 2.1 [54].

Virtually all charged pions wind up as an electron and neutrinos after muon decay.

Table 2.1: Branching ratios for π , K

π^\pm	$\rightarrow \mu^\pm \nu_\mu (\bar{\nu}_\mu)$	(100 %)	
μ^\pm	$\rightarrow e^\pm \nu_e (\bar{\nu}_e) \bar{\nu}_\mu (\nu_\mu)$	(100 %)	
K^\pm	$\rightarrow \mu^\pm \nu_\mu (\bar{\nu}_\mu)$	(63.5 %)	
	$\rightarrow \pi^\pm \pi^0$	(21.2 %)	
	$\rightarrow \pi^\pm \pi^+ \pi^-$	(5.6 %)	
	$\rightarrow \pi^0 \mu^\pm \nu_\mu (\bar{\nu}_\mu)$	(3.2 %)	$(K_{3\mu\nu})$
	$\rightarrow \pi^0 e^\pm \nu_e (\bar{\nu}_e)$	(4.8 %)	$(K_{3e\nu})$
	$\rightarrow \pi^\pm \pi^0 \pi^0$	(1.73 %)	
(2.1)			
K_S^0	$\rightarrow \pi^+ \pi^-$	(68.6 %)	
K_L^0	$\rightarrow \pi^+ \pi^- \pi^0$	(12.37 %)	
	$\rightarrow \pi^\pm \mu^\mp \nu_\mu (\bar{\nu}_\mu)$	(27 %)	$(K_{3\mu\nu})$
	$\rightarrow \pi^\pm e^\mp \nu_e (\bar{\nu}_e)$	(38.6 %)	$(K_{3e\nu})$

Over half of the kaons decay through this same channel, most of the rest go to charged pions first. Only 4.8% of all charged K decays (the $K_{3e\nu}$ mode) result in a final lepton configuration other than the familiar $e\nu_e\mu\bar{\nu}_\mu$ pattern. The neutral kaons are a mixture of K_L^0 and K_S^0 . Again, only the $K_{3e\nu}$ mode breaks the dominant trend. These decays represent only a very small fraction of the total flux of neutrinos from the cosmic ray interactions.

From these branching ratios one expects that the flux ratio $(\nu_\mu + \bar{\nu}_\mu)/(\nu_e + \bar{\nu}_e)$ should be very close to 2. The presence of the “anomalous” K decays should have very little effect as the overall ratio is dominated by the pions. In practice there are a few corrections to these expectations which are included in detailed simulations. The effects of non-decaying muons, polarization, and the geomagnetic field are described in Chapter 11.

2.4 Production Height

Cosmic rays that produce atmospheric neutrinos interact at a characteristic height in the atmosphere. The specific production altitude has some dependence on the angle of incidence of the neutrino, particles with a lower slant angle will encounter more atmosphere while still at relatively high altitudes. This is usually described in terms of the zenith angle of the particle direction at the experiment location. Gaisser and Stanev have made a calculation of production altitude as a function of zenith angle which was used in this analysis to determine the length of the neutrino flight path. [55].

Chapter 3

OTHER EXPERIMENTS

Super-Kamiokande is by no means the first experiment to study the atmospheric neutrino anomaly. Serious hints that neutrino flavor oscillations might be possible came first in the pioneering solar neutrino experiment of Ray Davis in the Homestake gold mine near Lead, South Dakota. Subsequent solar experiments were the water Cherenkov detectors IMB and Kamiokande as well as the gallium radiochemical experiments GALLEX and SAGE. These experiments observed fewer neutrinos from the sun than expected from the standard solar models of nuclear burning.

Several of these experiments were also sensitive to atmospheric neutrinos. Data from Kamiokande showed a deficit in the ratio of muon to electron type neutrinos originating from atmospheric primaries. This was later confirmed in low energy data by the IMB collaboration, but IMB did not see the effect at higher energies. The iron calorimeter experiments, Fréjus, NUSEX and Soudan 2, originally built for nucleon decay, did not see this effect at all. The Soudan group later added data that did begin to support the deficit.

For a long time there was some concern that the effect was simply due to either particle identification problems in Kamiokande, or some badly understood feature of the water Cherenkov type detectors. To address these questions, the Kamiokande group duplicated their detector (in smaller scale) at the KEK accelerator facility to study the particle identification question. Tests with controlled beams confirmed that the identification algorithms were in fact very accurate and robust.

The MACRO experiment came online and in 1995 reported an up-going muon result that is consistent with Kamiokande (though large uncertainties made it also

consistent with no oscillation at all). This helps to address the question of the detection medium. The depth of the experiment did not seem to bear on the observation of the deficit. Figure 3 shows the relative depths of the main experiments in meters of water equivalent shielding.

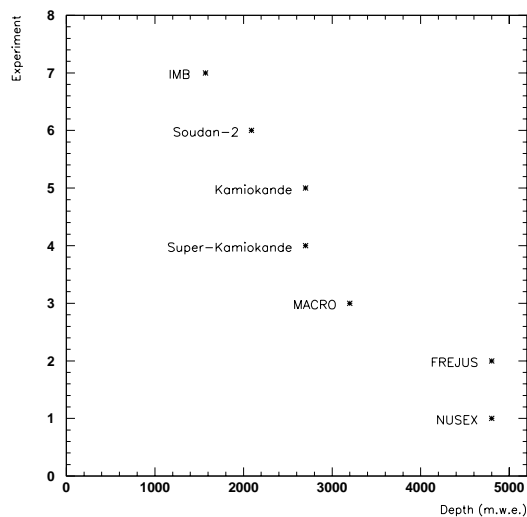


Figure 3.1: Relative depths of atmospheric neutrino experiments

The Soudan experiment is an iron calorimeter detector that began taking data in 1989 in Minnesota. The initial results were consistent with no effect. More recent data from a longer exposure are still not decisive, but the central value of the flavor ratio now lands very close to the Kamiokande and IMB results. This is especially important because of the different detection technique. It is now very unlikely that the atmospheric neutrino anomaly is an artifact of water Cherenkov detectors.

3.1 *The Kamiokande Experiment*

The Kamiokande experiment is the immediate predecessor to the Super-Kamiokande detector. Located just one quarter of a mile down the tunnel in the same Kamioka mine in central Japan, it contains 3000 tons of pure water. The tank is cylindrical, 15.5 meters in diameter and 16 meters in height [56]. Over 1000 photo-multiplier tubes view the detector volume, giving a photo-cathode coverage of nearly 20%. The detector uses 20" photo-multiplier tubes developed by the Hamamatsu Photonics Corporation for the experiment[57]. Construction of the primary detector began in 1982 as a nucleon decay experiment [58]. Data became available in July 1983 and the first proton decay candidate was recorded two months later. None of the candidates has survived closer scrutiny.

Soon after construction, studies of stopping cosmic ray muons and low energy background showed that there was a window in which ^8B solar neutrinos might be observable if sufficient care in rejecting background could be taken. Several physicists from the United States, including A. Mann, E.W. Beier, R. Van Berg (U.Penn), B.Cortez (Caltech), and D.H.White (Brookhaven) expressed interest in joining the project. They helped to design new discriminators and timing electronics suitable for solar neutrino searches. In July 1984 the detector was upgraded. A 1.5 meter water shield was added on all sides, viewed by 123 of the same photo-multiplier tubes. After delays due to an inability to seal the rock outer surface of the anti region, a high pressure pump was installed to simply keep the area full of water. Construction of Kamiokande-II was completed in March, 1985. A water purification system was also installed at this point to remove ^{222}Rn from the natural mine water. The Pennsylvania electronics were completed in November, 1985 and allowed charge and timing measurements with far higher resolution, greatly improving the vertex reconstruction.

The solar neutrino peak became visible during this phase. Constant improvements

to the detector led to the reduction in the radon background, eventually pushing the analysis threshold down to 7 MeV [59] [60].

Fortune smiled on the group on February 25, 1987 when supernova 1987A exploded in the Large Magellanic Cloud. The detector recorded 11 events within 13 seconds, some of them pointing back to the LMC. The detection was fortuitous. The group had intended to shut down the experiment while a steel roof was constructed over the detector. The construction company had met with difficulty in arranging workers and had delayed the job. The IMB collaboration in the United States also observed neutrinos from SN 1987A. This was the birth of extra-solar neutrino astronomy [61].

Kamiokande also made important measurements of the atmospheric neutrino flux. This flux was a background to the solar neutrino measurements, but became an important measurement on its own. The group first confirmed the existence of the so-called “atmospheric neutrino anomaly” [62] [63] and later found a strong zenith angle dependence [43]. This provided strong hints that neutrino oscillation might be occurring and gave great motivation to continue work toward the completion of the Super-Kamiokande detector [64].

In April, 1990, the detector was shut down again for improvements. 110 dead photo-multiplier tubes were replaced with a newer design being prototyped for the proposed Super-Kamiokande detector. Aluminized reflectors were installed around each photo-cathode to increase the photo-cathode coverage to 25%. The data acquisition electronics were also replaced with prototype Super-Kamiokande electronics. In November 1990 the detector resumed data taking as “Kamiokande-III”. The final solar neutrino results [42] came from this configuration and covered the end of the solar cycle. No anti-correlation with sunspot activity had been seen.

Kamiokande is still running in a largely automatic mode as a supernova watch detector. All other physics activities have now shifted to the newer Super-Kamiokande. Kamiokande-III’s life is expected to end at the end of 1998 when it is to be removed from its cavity. The world’s largest (1000 tons) liquid scintillation detector will be

installed in its place by a group from Japan’s Tohoku University. The KAMLAND detector, as it is known, hopes to detect low energy anti-neutrinos from nuclear reactors. It is also very sensitive for relic neutrino searches and studies of double beta decay.

3.2 The IMB Experiment

The “Irvine-Michigan-Brookhaven” (IMB) neutrino detector began taking data in September 1982. It, like Kamiokande, was a direct response to the prediction of the minimal SU(5) grand unified theory that the proton lifetime should be on the order of 10^{29} years [65]. The detector was located in the Fairport salt mine operated by Morton International, formerly Morton Thiokol, about 65 kilometers east of Cleveland, Ohio. The experiment sat at 1570 meters water equivalent depth and consisted of a nearly cubical tank 22.5 meters by 17 meters by 18 meters tall, holding 8 kilotons of pure water.

The original IMB-1 detector was designed specifically for the $p \rightarrow e^+ \pi^0$ mode, only about 1% photo-cathode coverage was required [66]. 2048 13 centimeter hemispherical EMI photo-multiplier tubes were used. Data was taken between October 1982 and May 1984 in this configuration. These results, among others, refuted minimal SU(5), but the new supersymmetry was beginning to favor modes like $p \rightarrow \mu^+ K^0$ and $p \rightarrow \nu K^+$. More massive secondaries mean less radiated (and visible) energy in the tank. In order to enhance the light collection efficiency, the number of photo-multiplier tubes was to be doubled by adding 2048 new 20 centimeter tubes, and coupling each to a large wavelength shifting plate.

IMB-2 was a short-lived mode between September 1984 and June 1985. The light collection upgrade was to have been done at this time, but a high number of photo-multiplier tube failures in a “flashing” mode made the detector insensitive to the interesting physics. Wavelength shifter plates had been added to the 13 centimeter

tubes, but no new tubes were installed. After June 1985, operation became impossible due to the failure rate.

IMB-3 began operation in May 1986. It was not the upgrade that had been hoped for, but was greatly improved over the original IMB-1 detector. The new 20 centimeter tubes replaced the old 13 cm tubes and the wavelength shifter plates were modified to fit the new tubes. New photo-multiplier tube bases were constructed to lower the stress on the tube pins, correcting the failure problems. This mode ran through March 1991. A water leak which could not be repaired without draining the tank ended this phase and eventually, the experiment. The story of IMB does not end there, however. In 1995 the photo-multiplier tubes were fitted with new bases and shipped to Japan where they now serve as the an active veto counter for the Super-Kamiokande experiment.

IMB had its share of physics. The group confirmed the solar neutrino deficit found by Ray Davis [37], and supported by Kamiokande [60]. In 1987 it observed neutrinos from SN1987A [67]. The difficulties with operation shortened the live-time exposure, but its larger fiducial mass made up for this in setting new limits on proton decay lifetimes [68].

IMB made observations of the atmospheric neutrino flux as well. The ratio of muon to electron neutrinos compared to expectation $R = (\mu/e)_{DATA}/(\mu/e)_{MC}$ was measured to be $0.71 \pm 0.04 \pm 0.08$ [69]. This is consistent with the Kamiokande and Soudan 2 measurements of an atmospheric neutrino anomaly. More recently, additional data was analyzed with special attention to the events with energies above 1 GeV for a 2.1 kton-yr exposure [70]. This study measured R to be $1.1 \pm 0.12(\text{stat.}) \pm 0.11(\text{syst.})$. The zenith angle distribution is consistent with being flat, unlike the Kamiokande result with higher exposure [43].

3.3 The MACRO Experiment

The MACRO (Monopole, Astrophysics, and Cosmic Ray Observatory) experiment is a massive underground detector located in Hall B of the Laboratori Nazionali del Gran Sasso (LNGS) near L’Aquila, Italy. The laboratory houses several large experiments and is part of the Istituto Nazionale Fisica Nucleare (INFN). The experiment was built with the intention of searching for magnetic monopoles, but it is also sensitive to cosmic ray muons and neutrinos from cosmic rays and supernova explosions. The Gran Sasso infrastructure is particularly useful because of the presence of surface array detectors on top of the mountain (GRACE and EAS-TOP) which can be placed in coincidence with MACRO.

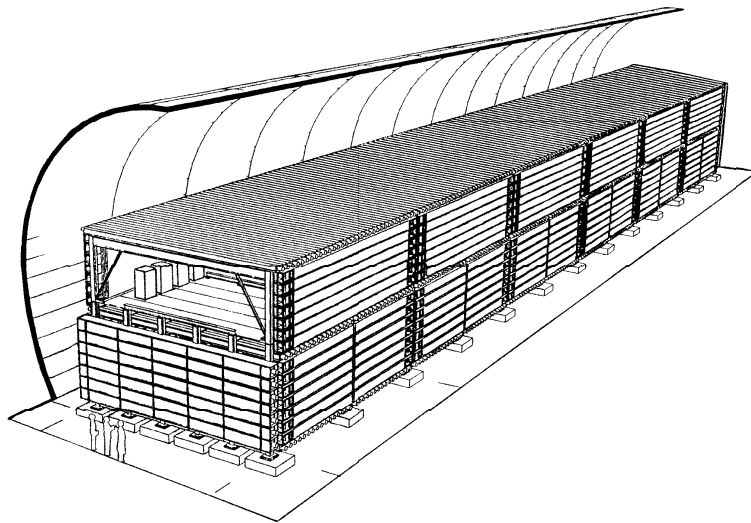


Figure 3.2: MACRO detector

The MACRO detector uses three different detection systems[71]. The full detector consists of six “supermodules” 3.2. Each supermodule is about 12m square by 9 meters high and consists of ten streamer tube planes sandwiching layers of crushed rock absorber on the inside. All outside faces are covered with scintillator tanks

similarly sandwiched between streamer tube planes. The scintillator tanks are viewed from both ends by photo-multiplier tubes. A horizontal plane of CR39 track-etch material is placed at the center of the stack. One side and one end of the full detector are also covered with CR39. Figure 3.3 illustrates the layout of one supermodule.

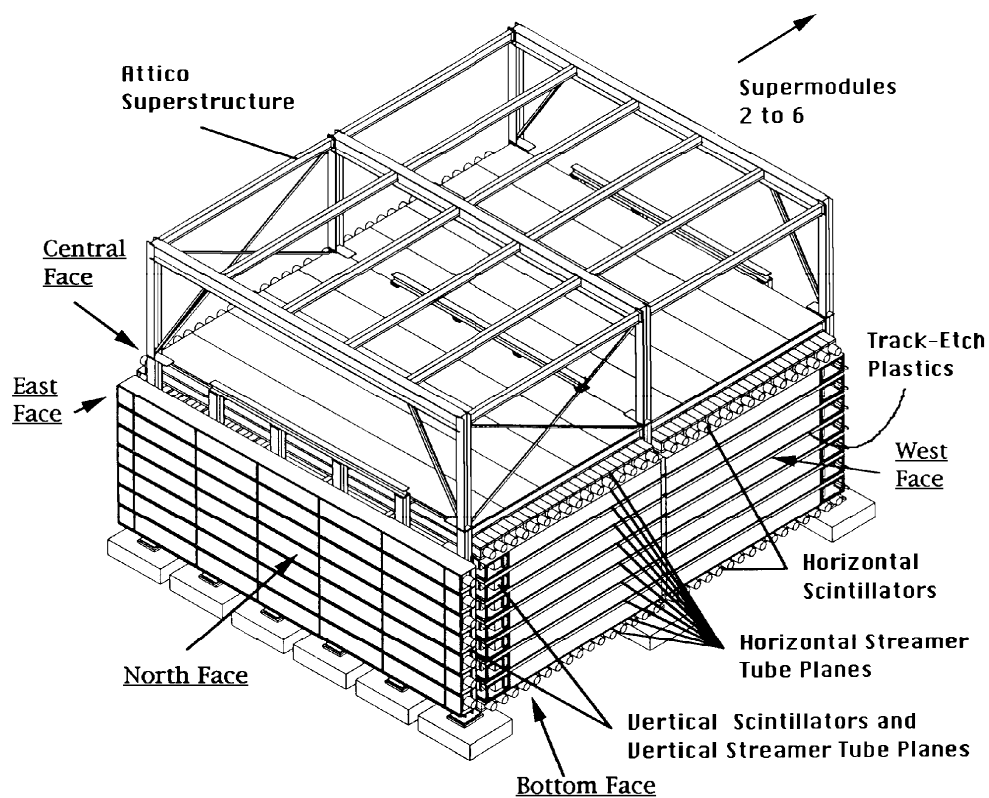


Figure 3.3: MACRO detector supermodule detail

The MACRO detector is sensitive to atmospheric neutrinos by studying up-going muons in the detector. These muons should have come from neutrino interactions in the rock below the detector. There is a known background from down-going muons which scatter at large angle and “bounce” back up into the detector. This background

has been simulated and is now well understood.

An analysis of the up-going muons was published in [72]. The ratio of the number of muons seen to that expected was 0.73 ± 0.09 (stat) ± 0.06 (sys) ± 0.12 (theor.) using the Bartol (1993) flux. The zenith angle distribution is consistent with the Monte Carlo simulation. The result was that the data to that point was consistent with both the previous Kamiokande suggested oscillation parameters and with no oscillations at all.

3.4 The Fréjus Experiment

Another contributor to data on the atmospheric neutrino anomaly is the Fréjus experiment. The experiment sits in the L.S.M. (Laboratoire Souterrain de Modane) or Fréjus Underground Laboratory. The laboratory is in a highway tunnel under the French-Italian border linking Modane to Bardonnechia in the Alps. The high mountains provide a rock overburden of 4800 meters water equivalent (m.w.e.). Detector construction began in 1983 by a French and German collaboration. Data taking began in February 1984 with 240 tons of detector mass, the full 900 ton detector was completed in June 1985. The experiment is nominally a proton decay detector, but atmospheric neutrinos form a background worthy of study.

The detector consists of a 900 ton sandwich of iron plates and plastic flash chambers [73]. The iron plates are 3 mm thick, the chambers are 5 mm thick. The detector is triggered by planes of Geiger tubes every few layers of plates and flash chambers. When a trigger is formed by adding the Geiger tube outputs, a high voltage is applied to aluminized sheets on either side of the flash chambers. If an ionizing particle has passed through the gas mixture in the chamber, the sudden high voltage will cause a discharge in the chamber which can be read out by pickup strips across the top of each cell. The Fréjus detector contains almost one million channels of flash chamber signals to process.

The collaboration has published results on the detection of atmospheric neutrinos [74] and interpreted them in terms of a neutrino flavor oscillation hypothesis [75]. With an exposure of 1.56 kton-yr, they find no disagreement between the measured ν_μ/ν_e flavor ratio and the expected one. The zenith angle distribution of atmospheric neutrino events is flat. Fréjus hence rules out neutrino oscillations (albeit with low significance) in the parameter region allowed by Kamiokande and IMB.

3.5 The Soudan 2 Experiment

The Soudan 2 experiment is an iron tracking calorimeter located 710 meters (2090 m.w.e.) underneath Soudan Underground Mine State Park in Minnesota. The main detector consists of sheets of corrugated steel stacked to form a honeycomb [76]. Plastic drift tubes with a gas mixture are run through the spaces of the honeycomb and placed in a longitudinal electric field. Charged particles passing through the detector ionize the gas in the tubes. The ionization drifts to the end of the tube where it is read out by sense wires. This technique allows the position of the particle track along the drift tube to be measured using time projection. The experiment also contains an active shield of aluminum proportional tubes to help to veto incoming cosmic ray muons or other background.

The Soudan collaboration has also investigated the atmospheric neutrino anomaly [77]. Data was taken from April 1989 to December 1993 while the detector was under construction, starting with 275 tons of detector mass and ending with the full 963 tons. The total exposure is calculated to be 1.52 kton-yr. It is coincidental that the detector mass and exposure for this sample is roughly the same as that used for the Fréjus results. The differences in detector technique, geometry, and the active shield make the two experiments quite different from each other.

The result of the Soudan measurement was not decisive on its own, but addressed several questions with the other detectors. After 1.52 kton-yrs of expo-

sure, the collaboration measured the flavor double ratio $R = (\mu/e)_{DATA}/(\mu/e)_{MC}$ to be $0.72 \pm 0.19 \pm 0.06$. While on its own the measurement does not deviate significantly from one, the central value is reasonably close to that measured by the water Cherenkov detectors with smaller reported errors.

The Soudan measurement is important for two more reasons. First, it provides corroborative evidence that the atmospheric neutrino anomaly exists using completely different experimental techniques. The fact that the main proponents of the muon deficit were water Cherenkov experiments while the dissenter (Fréjus) was an iron calorimeter raised concerns about the experimental techniques. Secondly, Soudan was able to measure the track to shower ratio (showering versus non-showering) for neutron produced events. One proposed explanation of the Kamiokande result held that neutron contamination with an anomalous track to shower ratio might be to blame (see [78] for further details). The Soudan results do not support this hypothesis.

The Soudan detector continues to take data at this time while being prepared for participation in a new long baseline experiment, Fermilab E875, or MINOS (Main Injector Neutrino Oscillation Search). In this project now under construction, a neutrino beam from Fermilab will be aimed at the Soudan detector in a muon disappearance experiment designed to study neutrino oscillations starting with a known beam composition. A possible twist to this experiment is being considered in which photographic emulsion would be used to detect τ appearance.

3.6 The NUSEX Experiment

NUSEX (NUcleon Stability EXperiment) is a proton decay detector located in a highway tunnel under Mont Blanc in the French Alps. The mountains provide 4800 m.w.e. of shielding. The detector is an iron calorimeter consisting of a 3.5 meter cube made of layered iron slabs and plastic streamer tubes. Orthogonal rows of pickup strips determine the track coordinate in the plane of the streamer tubes. The total

mass is 150 tons, 130 of which is used as a fiducial mass for contained event data [79].

The NUSEX group has studied atmospheric neutrinos [80]. The small size of the detector means that the data taken between June 1982 to June 1988 amount to only 0.74 kton-yr of exposure. The detector is similar in concept and granularity to the Fréjus detector, but the geometry is different. The NUSEX iron planes are horizontal, in Fréjus vertical. Triggering is also handled differently.

The NUSEX detector was calibrated in a test beam at CERN. This test showed that the experiment is able to distinguish flavors with good efficiency and is able to detect charged leptons well.

The reported atmospheric neutrino sample consists of only 50 events. 32 of these are muon-like, 18 electron-like. The flavor can be determined with fairly good efficiency by looking at the hit distributions in the planes. These numbers are all in good agreement with Monte Carlo studies and the flavor double ratio $R = (\mu/e)_{DATA}/(\mu/e)_{MC}$ is quoted as $R=0.96\pm0.30$. The data therefore do not support a muon deficit or evidence for neutrino oscillations. Measurements of upward going muons give similar results [81].

3.7 The Baksan Experiment

The Baksan Underground Scintillation Telescope is located in an underground laboratory underneath Anderchi Mountain in the Baksan Valley of the North Caucasus in Russia. It is operated by the Institute for Nuclear Research and was built before 1979.

The detector consists of a roughly cubic array [16x16x11m] of 3132 liquid scintillator cells [82]. Charged particles passing the array cause the scintillator to fluoresce, in turn creating a signal in a 15 cm photo-multiplier tube viewing each cell.

The Baksan group reported results on data taken over a period of more than ten years for both up-going muons and neutrinos [83]. A search for neutrino point sources

and analysis of neutrino oscillation parameters was also done [84]. Using up-going muon data, the group finds a ratio of N_{exp}/N_{MC} for muons to be 0.93 ± 0.15 .

Chapter 4

THE SUPER-KAMIOKANDE EXPERIMENT

The Super-Kamiokande neutrino detector is a new astrophysical neutrino detector located on the western coast of the main Japanese island of Honshu not far from the coastal city of Toyama. It is similar in construction to its predecessor Kamiokande-III experiment, but a factor of ten larger in scale. The two detectors are located roughly one quarter of a mile apart in the Kamioka mine owned and operated by the Kamioka Mining and Smelting Company. The mine contains lead and zinc ore, but had been largely unused due to the market conditions and costs of extraction. Mining operations recently resumed in March 1998. The mine entrances are at the base of Mt. Ikeno and feature a 2 km horizontal access tunnel to the detector cavity. The overburden consists of over 1000 meters of rock, about 2800 m.w.e. (meters of water equivalent).

Super-Kamiokande is a water-Cherenkov detector. Before detailing the construction of the experiment it will be helpful to briefly discuss some general principles of operation for these types of detectors. Many of the design considerations for Super-Kamiokande depend critically on various aspects of the Cherenkov effect and neutrino interactions in pure water.

4.1 Neutrino Interactions in Water-Cherenkov Detectors

There is no known experimental technique by which the neutrino can be directly observed. Its neutral charge eliminates all detection methods which rely on electric or magnetic field effects. The only way to observe a neutrino is to look for a neutrino

interaction and show that the parent was invisible.

Neutrinos interact in the tank via the weak interaction in one of only a few general modes. These include neutrino electron scattering and neutrino-nucleon interactions. The interaction can proceed in either a charged current mode, producing a final state charged lepton, or a neutral current mode in which the neutrino still exists in the final state.

The simplest interaction is neutrino scattering off the atomic electrons. This mode is dominant at lower energies where other processes are not accessible.

All three flavors of neutrinos can produce a recoil electron via the neutral current interaction by exchanging a Z^0 . This reaction is flavor-blind and each species has essentially the same cross-section of about $0.1 \times 10^{-43} (E_\nu/10 \text{ MeV})$. Muon and electron neutrinos are produced in abundance from the cosmic rays but tau neutrinos are not expected to appear from any source. Tau neutrinos could be produced from muon neutrinos through oscillation effects but since the neutral current reaction does not distinguish between the flavors of the incident neutrinos, the total number of recoil electrons from this process would remain unchanged.

In addition the electron neutrino can also interact with atomic electrons via the charged current mode by exchanging a W boson. The charged current ν -e cross-section is somewhat higher than the neutral current cross-section due to the presence of a second tree-level scattering diagram. The total ν -e cross-section is $9 \times 10^{-44} (E_\nu/10 \text{ MeV}) \text{ cm}^2$, or about 10^{-41} cm^2 at 1 GeV [56].

The nucleon is the major target in the Super-Kamiokande detector. Neutrino-nucleon scattering can be either “quasi-elastic” producing only a single charged lepton and an excited nuclear state, or “inelastic” where quarks are popped out of the nucleon and extra particles appear in the final state.

The ν -N quasi-elastic cross-section is quite analogous to the ν -e elastic scattering and can be calculated the same way. The results are essentially the same but the ν -N cross-sections are higher by roughly m_p/m_e , the ratio of the proton mass to

the electron mass. This can be seen by the simple replacement of the electron with a nucleon in the diagrams for ν -e scattering. This means that at 1 GeV and above where the data for this analysis are taken, neutrino-nucleon scattering completely dominates over ν -e interactions. Scattering from electrons can be completely disregarded for this analysis.

Neutrino-nucleon elastic scattering is not a perfect analogy to ν -e scattering because the targets now have structure. Nuclear form factors have to be taken into account as measured from neutrino accelerator experiments.

As the energy of the neutrino increases, inelastic processes such as excitation of baryon resonances and pion (or multi-pion) production become more relevant. Analytic calculations of the total cross-section are difficult due to the large number of final states. Careful simulations of the neutrino interactions can be done. These are used as input to the detector simulations to predict what the detector will see.

From these Monte Carlo simulations one finds that in the multi-GeV energy range the charged-current (CC) quasi-elastic and inelastic processes occur at about equal rates, and far dominate the neutral current (NC) reactions for energies above 1 GeV. Table 4.1 gives a breakdown of the fraction of simulated events from each mode in the energy range relevant to this analysis.

Table 4.1: Fraction of simulated events from various interaction modes

$\nu_e, \overline{\nu}_e$ CC	QE	17%
	non-QE	21%
$\nu_\mu, \overline{\nu}_\mu$ CC	QE	30%
	non-QE	28%
NC		4%
Total		100.00%

For the partially contained events (see Section 4.3) which sample a higher distribution in energy, the fraction of inelastic interactions rises to over 80% with less than

1% contribution from the flavor blind neutral current mode.

It is clear that the great majority of neutrino interactions in the detector at these high energies are of the charged current type. These produce a charged lepton, possibly along with other particles, which can be used to identify the flavor of the incoming neutrino. This is an important conclusion. If the neutrino interaction cross-section were dominated by the neutral current mode then use of Super-Kamiokande to investigate the ν_μ/ν_e ratio in atmospheric neutrinos would be impossible.

There is one further key point in regard to neutrino interactions. The success of a water Cherenkov detector depends not only on its ability to identify the flavor of incoming neutrinos, but also to reconstruct their direction. However, what is detected is not the neutrino but rather the charged lepton that comes out of the interaction. The extent to which the lepton respects the direction of the neutrino determines how well the source of the neutrino can be determined.

In neutrino-electron scattering at anything over a few MeV the recoil electron direction in the lab frame is highly peaked in the direction of the neutrino. This happens because the center of momentum frame is essentially that of the incoming neutrino. Unfortunately, this does not hold true when the target becomes much more massive as for neutrino-nucleon scattering. Neutrino direction is not as well preserved in the interaction, but it does improve with energy. Figure 4.1 shows the angular deviation between the incoming neutrino and outgoing lepton as a function of energy from the Monte Carlo simulation. It is clear that below 1 GeV, reconstruction of the direction is difficult if not impossible. Higher energies mean better direction reconstruction. This point is the key reason for using the high energy data to study the atmospheric neutrinos.

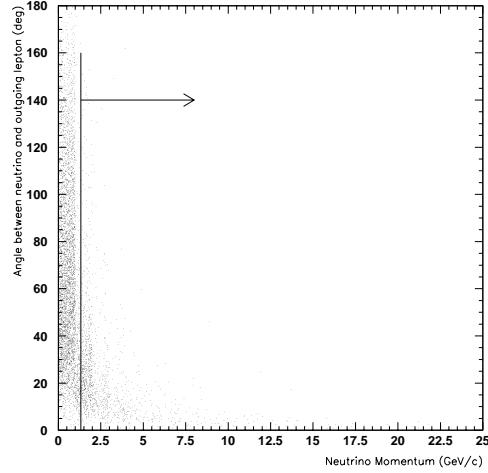


Figure 4.1: Angular deviation of outgoing lepton in simulated CC interactions

4.2 Cherenkov Radiation

When a charged particle passes through a dielectric material at a velocity higher than the speed of light in that material, a “shock wave” of light is produced in the material. The expanding cone of light is known as Cherenkov radiation after its discoverer who observed the effect in 1934. Super-Kamiokande uses an enormous tank of pure water as both target and detection medium. Water has the nice properties of being both cheap and transparent, allowing the radiated photons to pass through the detector to the wall where they are collected by sensitive photo-multiplier tubes.

The electric field of a moving particle can be thought of as expanding in spherical wavelets about the point of emission on the particle’s track. Figure 4.2 shows the familiar wavefronts for a particle with velocity v less than c/n , the velocity of light in a medium with index of refraction n . The motion of the particle causes the wavefronts to be closer together in the direction of motion and farther apart in the opposing direction. This is the well known Doppler shift effect in the arrival frequency of the

wavefronts.

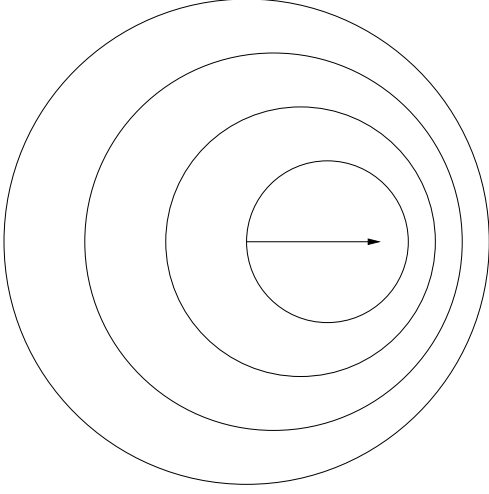


Figure 4.2: Particle with $v < c/n$

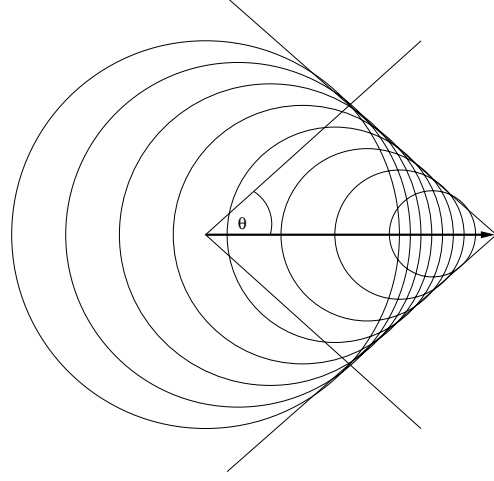


Figure 4.3: Particle with $v > c/n$

If the velocity of the particle exceeds the velocity of light in the medium (i.e. the expansion velocity of the wavefronts), then the picture is qualitatively different. The wavefronts pile up to form a coherent “shock front” analogous to the acoustic pressure waves in a sonic boom or the bow wake left by a fast speedboat [85]. Figure 4.3 illustrates how this happens.

From the figure it is clear that in the time it takes for the particle to travel a distance $v \cdot t$, the spherical wavefront has traveled a distance $\frac{c}{n} \cdot t$. All of the different wavelets are now adding coherently to form a shock front expanding with an angle

$$\cos(\theta_c) = \frac{ct}{nvt} = \frac{c}{nv} = \frac{1}{\beta n} \quad (4.1)$$

with respect to the charged particle’s direction of travel.

To summarize, the passage of the charged particle generates a coherent response by the medium. This coherent radiation is observed as an outwardly expanding cone of radiated photons with cone angle $\theta_c = \frac{1}{\beta n}$ and centered on the particle track.

In pure water, the index of refraction is $n = 1.33$ so for extremely relativistic particles ($\beta \sim 1$) the Cherenkov photons are radiated with a characteristic angle of about 42° . Since the opening angle does depend on the velocity of the particle, this can be used as additional information for particle identification algorithms. Once the particle is identified, the opening angle then becomes an extra handle for fitting the energy of the charged particle.

A more detailed analysis is required to extract the frequency dependence and number density of the radiated photons [85]. The total energy content radiated per unit track length for a particle with charge z is:

$$\frac{dE}{dx} = \frac{4\pi^2 z^2 e^2}{c^2} \int \left(1 - \frac{1}{\beta^2 n^2}\right) \nu d\nu \quad (4.2)$$

It is important to remember that the radiation is a response by the medium and so is constant for all positions along the particle track to the extent that β remains close to 1.

The total energy deposited into a given frequency interval $E_{rad}(\nu)$ is proportional to the integrand. That energy is divided among a number of photons with energy $E_{phot}(\nu) = h\nu$. This means that the number of photons radiated at a given energy is proportional to $d\nu$, or more transparently, to $d\lambda/\lambda^2$. Dominant numbers of photons appear at short wavelengths, limited by the dispersion characteristics of the medium. These are described by the frequency dependence of $n(\nu)$. In water, blue-green light is the dominant component.

The index of refraction in water is roughly constant in the small visible band between 400 and 700 nanometers. In this range, a singly charged particle with $\beta \sim 1$ will produce about 400 eV/cm or 200 photons/cm. This is very small compared to the total energy loss due to ionization of the particle of about 2 MeV/cm.

As an aside, it is interesting to note that this effect is the same as that responsible for the famous blue glow around submerged fuel cells in the core of a nuclear reactor.

In that case it is caused by large numbers of alpha particles being kicked out of the radioactive uranium and plutonium materials that generate the Cherenkov radiation with enough photons to be easily seen with the naked eye. Super-Kamiokande detects the passage of single particles and relies on sensitive light detection techniques to observe the same phenomenon.

4.3 Cherenkov Ring Imaging

A ring imaging Cherenkov detector relies on the cone shape of the emitted light pattern to reconstruct the direction and energy of the charged particles. This information is used to infer the properties of the incident neutrino.

The wavefront of the light emitted from a given point on a particle's track forms a cone around the track. For fully contained events, those which start and stop inside the volume of the detector, the intersection of the cone with the detector walls is a hollow ring. Figure 4.3 illustrates the light cone lighting up photo-multiplier tubes with intensity depending on the number of photons reaching the tube. The width of the ring is directly proportional to the length of the charged particle track. The shape of the ring can be used to reconstruct the relative orientation of the cone with respect to the cylindrical walls. The overall size of the outer edge of the ring determines the position of the interaction vertex.

The photo-multiplier tubes lining the walls measure the relative arrival times and the numbers of photons which strike them. A track which passes near a wall will produce photons which strike the nearby wall more quickly than photons which must cross the detector before being collected. The number of photons per unit track length is constant, but attenuation and scattering in the water reduce the number measured far away from the production point. Cone fits to reconstruct the direction of the particles can use both these pieces of information to get very precise reconstructions.

A second class of events is also used in this analysis. These are the so-called

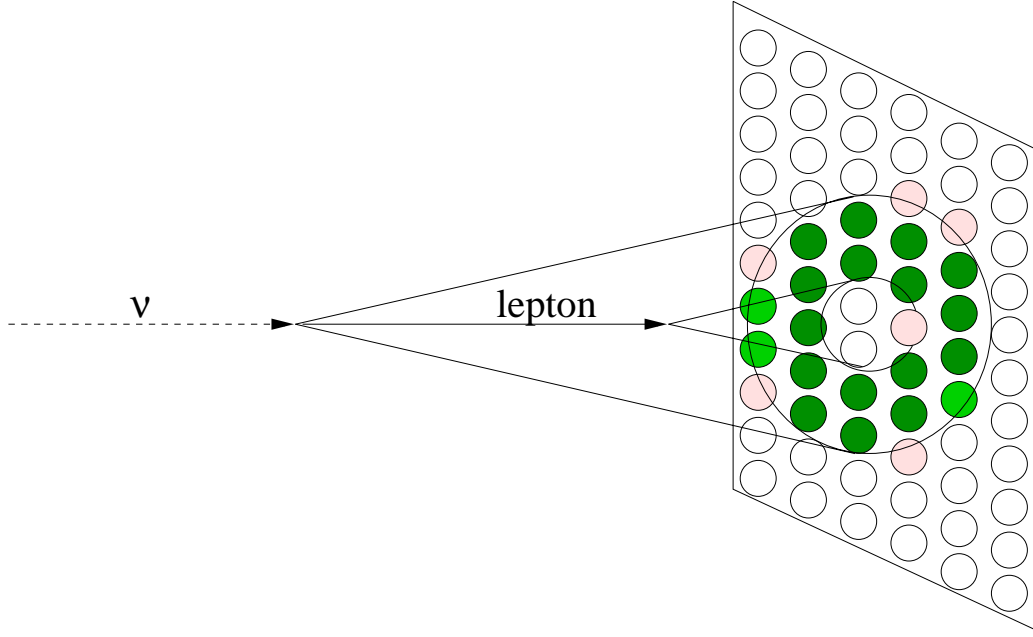


Figure 4.4: Cherenkov ring from charged particle track in water

“partially contained” events. This type has an interaction vertex inside the fiducial volume of the detector but the charged particle escapes, exiting the inner volume through one of the inner walls. In this case the Cherenkov ring is filled in to form a disk as the particle continues to generate photons all the way up to the wall. Typically a high amount of charge is left in the tubes near the exit point. The total number of photons per track length is not changing, but as the particle nears the wall the area in a differential ring section decreases, concentrating the same number of photons in a smaller number of photo-multiplier tubes.

4.4 *Detector Description*

The detector consists of a cylindrical stainless steel tank 39 meters in diameter by 42 meters in height (see Figure 4.5). The tank is self-supporting with concrete backfilled against the rough-hewn walls to counteract the water pressure when the tank is filled.

The capacity of the tank exceeds 50,000 tons of ultra-pure water. The tank is built into a cavity 2 kilometers horizontally inside Mt. Ikeno.

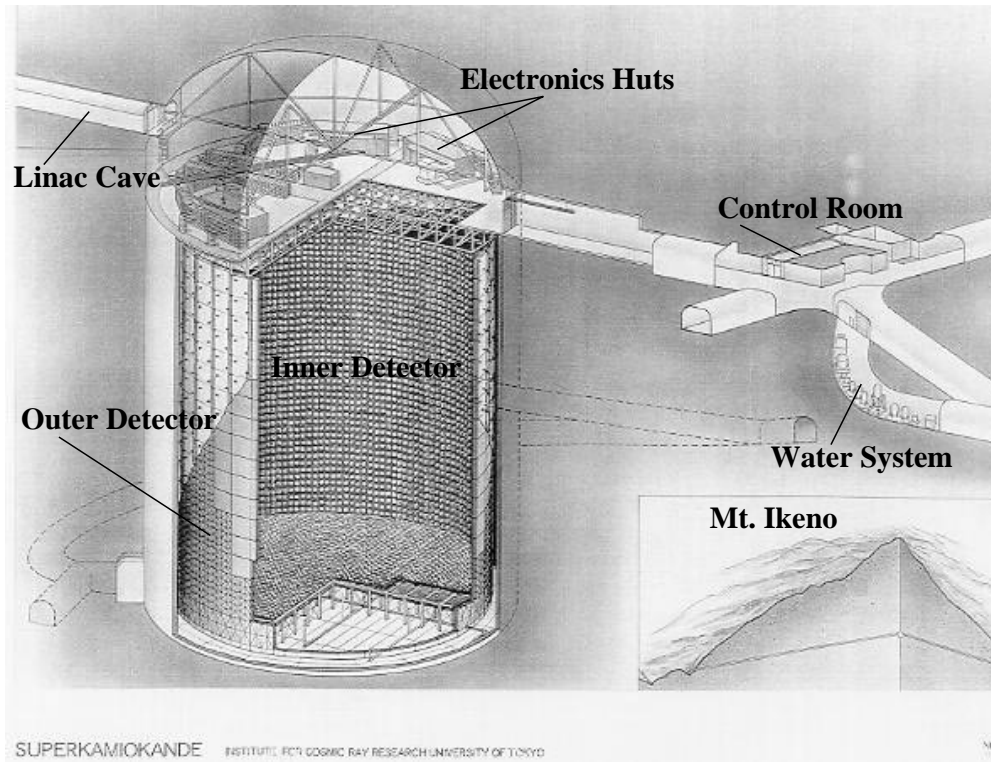


Figure 4.5: Super-Kamiokande detector construction

A cylindrical photo-multiplier tube support structure nearly as large as the tank itself (see Figure 4.6) divides the tank into two distinct volumes. The inner volume contains 32 kilo-tons of pure water and is viewed by 11,146 50 cm photo-multiplier tubes. The tubes are set nearly touching each other and provide a 40% photo-cathode coverage for the walls. Two meters of water remain on all sides outside the support structure. This outer volume serves as an active veto counter against incoming particles. It is instrumented with 1885 20 cm photo-multiplier tubes recycled from the IMB experiment. The two detector volumes are optically isolated from each other by a lightproof black sheet on the photo-multiplier tube support structure. The 55 cen-

timeter thick support structure comprises a 3rd distinct volume, a dead space in which light can in principle not be collected. Because the inner detector photo-multiplier tubes are not covered in back, some light is still detected from this region.

To protect against low energy background from radon decay products in the air, the roof of the cavity and the access tunnels were sealed with a spray-on coating. Double doors in the access tunnels restrict airflow from the mine into the detector cavern. An overpressure of “radon-free” air is piped in from the outside to further hold back contaminated mine air. The outside air contains relatively little radon when taken from an area away from the mine entrances.

The average geomagnetic field is about 450 milli-gauss and is nearly horizontal at the detector site. This presents a problem for the very sensitive photo-multiplier tubes which prefer a much lower ambient field. The strength and uniform direction of the geomagnetic field could systematically bias the photo-electron trajectories and timing in the photo-multiplier tubes. To counteract this, 26 sets of Helmholtz coils are arranged around the outside of the tank. With these in operation the average field in the detector is reduced to 50 milli-gauss.

The inner volume of the Super-Kamiokande experiment is close to the ultimate practical limit in large volume water Cherenkov detectors. The inner tank is a cylinder 33.8 meters in diameter by 36.2 meters in height. The long diagonal length of about 70 meters is approaching the typical values of water attenuation length and scattering parameters. Absorption lengths in pure water tend to be on the order of 40-80 meters. Without adding instrumentation at the center of the volume in some way it is not really practical to simply scale the size any larger, even if one could afford to dig the hole to build such a tank in.

The inner volume contains 32,000 metric tons of water inside the photo-multiplier tube plane. About 22.5 ktons is inside the fiducial volume, defined somewhat arbitrarily as the volume inside of a cylinder drawn 2.00 meters from the the inner detector wall. This definition provides a further passive shield against entering events

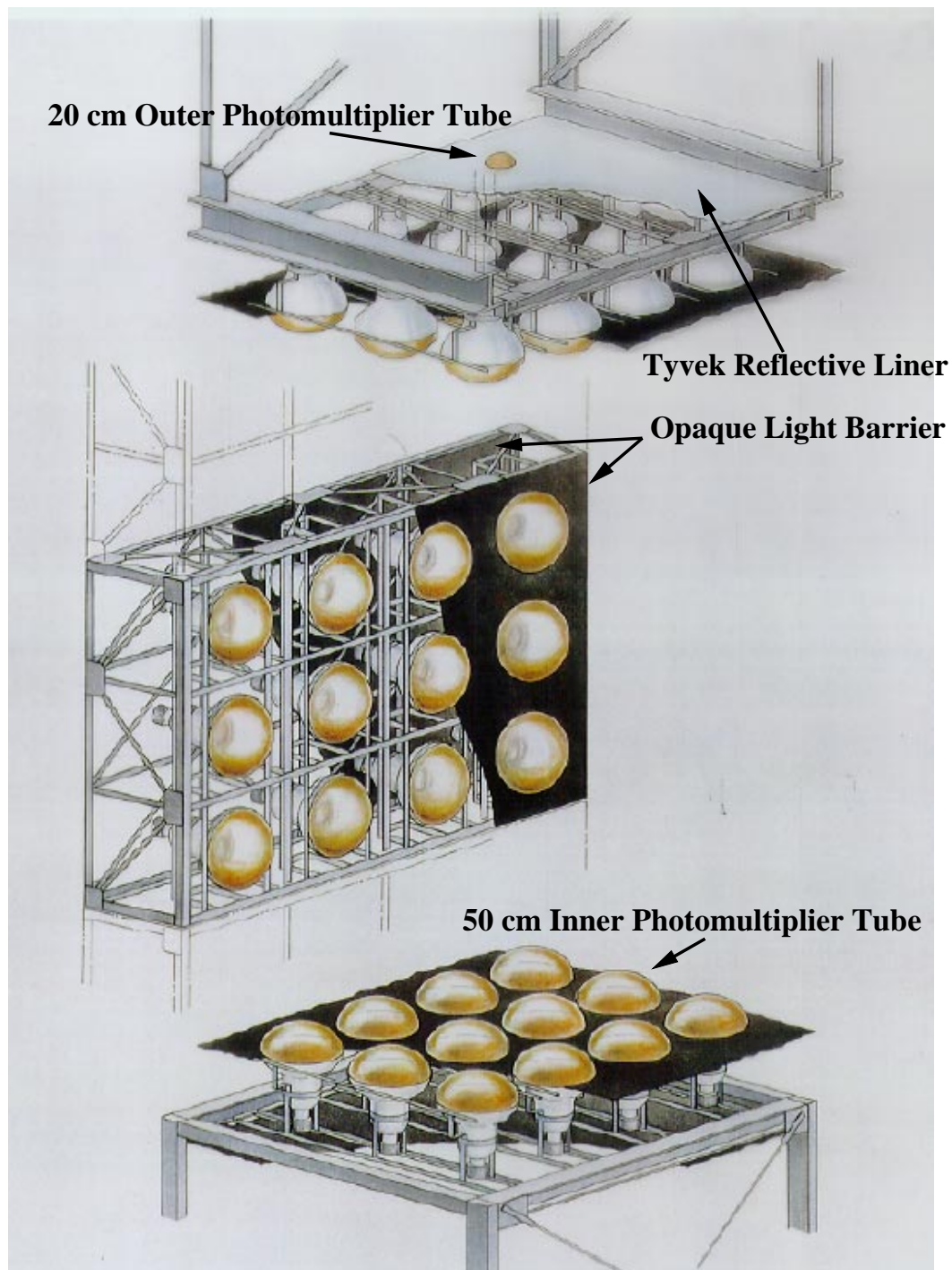


Figure 4.6: Super-Kamiokande support structure (ICRR, University of Tokyo)

and restricts event reconstruction to a region of minimum fitter bias.

The outer volume is lined with a reflective material known as Tyvek manufactured by DuPont. This is the same material often seen used as house wrap in new home construction. Express mailing envelopes are also made of the same substance. The purpose of the liner is to maximize light collection efficiency. The smaller size and number of photo-multiplier tubes in the outer detector make each one especially important. Failure of a tube has the potential to open a gap in the coverage of the veto counter. The reflective surface helps to spread light to many tubes and reduce the significance of individual tubes.

Chapter 5

INNER DETECTOR DATA ACQUISITION

The inner detector data acquisition system is necessarily very complicated. The immense number of channels and fast timing requirements as well as the large physical size of the detector dictates a data acquisition system that is modular, well-buffered, and fast.

The size of the detector presents the first challenge to the design of the data acquisition system. The more cables that are bundled, the larger the opportunity for electrical cross-talk. Photo-multiplier signals degrade over long cable distances. Mechanical considerations alone have a major impact. Digitizing and other recording equipment for nearly twelve thousand channels requires a huge amount of physical space. Simply getting that many cables out of the tank with relatively equal cable lengths is a challenge.

The solution for Super-Kamiokande was to divide the detector into four quadrants. Data are collected separately in one of four quadrant electronics “huts” on top of the tank. Trigger and event timing information is distributed to all quadrants from a fifth “central” hut.

5.1 Front End Electronics

Data acquisition begins at the photo-multiplier tubes. Cables molded to the tube bases provide high voltage and return the input signal. Charge and timing information are held for each channel and if the signals are above an internal threshold, the information is digitized and stored. All of this must be fast, to avoid dead-time, and

local, at the cable ends in the quadrant huts.

5.1.1 ID Photo-multiplier Tubes

Super-Kamiokande uses 50 cm Hamamatsu R3600 photo-multiplier tubes that were specially constructed for the experiment [86]. These tubes were designed with very large photo-cathode area and fast time response. The basic design was used in the earlier Kamiokande experiment and improved for Super-Kamiokande. Typically they are run at a gain of 10^7 with 2000 volts of applied high voltage. Quantum efficiency is 22 percent with a typical transit time jitter of 2.5 nanoseconds. Dark noise rates at this gain setting are about 3 kHz per tube.

5.1.2 ID Front End Electronics Overview

Initial acquisition of the photo-multiplier tube signals is done using the TKO (Tristan-KEK-Online) system developed by the University of Tokyo and Toshiba for use in previous experiments. This system combines in one electronics crate twenty Analog Timing Modules (ATMs) to digitize the tube signals, a Go/NoGo (GONG) trigger module, and a Super-Controller Header bus interface module. The result is a complete front end data acquisition package for 240 photo-multiplier channels. Twelve such crates are built into each quadrant hut [87].

5.1.3 ID ATM Modules

Each ATM module has twelve input channels for photo-multiplier tube signals. Each channel has a pair of switching time-to-analog converters and charge-to-analog converters to measure the time and size of the input pulses. The ability to switch between “A” and “B” buffers on a single channel assures nearly dead-time-free operation of the front end. It also allows recording of both muon and electron signals from muon decays in separate triggers with high efficiency.

Each input channel in the ATM has an amplifier with a gain of 100 and a discriminator. Signals crossing the discriminator level (set by the run control panel) cause a standard 15 mV, 200 nanosecond hit pulse and a 400 nanosecond gate pulse to be generated. The 12 hit pulses from each module are summed and made available on the front panel HITSUM output. This is used by the TRG module to generate detector triggers. The gate signal is used to provide a standard time window for the charge integration.

The time-to-analog converters work by integrating a constant current from the arrival of the first hits on the channel until receipt of a global trigger from the TRG module (see section 5.4). This gives a relative time measurement with 0.3 nanosecond resolution. The full range of the time-to-analog converters is 1.2 microseconds, far more than necessary by any causal effect related to a single event in the detector.

The charge-to-analog converters measure the total charge in the photo-multiplier tube signal. They do this by integrating the signal input during the standard gate pulse generated by the initial ATM channel discriminator. Charge resolution is 0.2 pC (0.1 photo-electron) with 550 pC full range.

Both the charge and timing information are stored in capacitors until arrival of the global trigger. At that point each channel in the module is digitized sequentially, first the “A” buffers, then the “B” buffers. The 12 bit data are stored with the lower 8 bits of the the global event number supplied by the GONG module in a 1 Kword FIFO memory. The FIFO can be read out asynchronously with data taking so readout introduces no dead time.

The sequential readout of the ATM channels causes an electronics effect which must be corrected for. Because the “B” channels are always read out second if the “A” channels contain data, the signals are held for a longer time. Leakage currents from the storage capacitors systematically reduce the measured charge in the B channels. In addition, the presence of large numbers of hits in the A channels was found to draw down the ATM supply voltages, affecting the reference levels used for digitization.

Both effects are more pronounced when the A channel records a high charge event and the B channel takes a second event immediately afterwards, as in muon decay. In this case, the electron energy is systematically reduced, distorting the Michel electron spectrum and throwing off the energy calibration that should be possible based on these events. The effect was explicitly demonstrated and a correction calculated by using special “decay-electron” data runs. In these runs the ATM was adjusted so the A channel would trigger on a stopping cosmic ray muon but not record hits, leaving the B channel free to catch the decay electron without bias from hits in the A channel.

5.1.4 GONG

The Go/NoGo (GONG) trigger distribution module resides in each TKO crate along with the ATMs. It latches the lower 16 bits of the detector event number. This full number is read out along with the ATM data for use in repacking the hits into event blocks. The lowest 8 bits of the event number are converted to TTL levels and distributed to the ATM modules by a small ribbon cable. The board also serves as a convenient point for level conversion of the trigger signals and fan out to the ATM modules. The GONG module also has the ability to generate pulses with programmable delays to calibrate the ATMs.

5.1.5 SCH

The Super-Controller Header (SCH) module also resides in each TKO crate. It serves to control the crate and handle the data readout of the ATMs. On command, data are transferred from the ATM module buffers along with the 16-bit event numbers from the GONG module to a Super Memory Partner (SMP) module located in one of two VME crates per quadrant hut. The SCH modules controls the TKO crate bus under instructions from the SMP.

5.2 Data Buffering Electronics

The 1 Kword buffer in each ATM module is capable of storing several events worth of data. In practice, a “LIME” limiter module is used as a prescaler to initiate readout of the TKO crates once every 16 events. This module ensures that the TRG module does not fire faster than the ATMs are able to be read out. Readout and control of the TKO system is handled by the SMP modules.

5.2.1 SMP Modules

The Super Memory Partner (SMP) modules reside in 6U VME crates in the quadrant huts. Each TKO system crate is connected to its own SMP module, 6 in each of 2 crates per hut. Upon receipt of a prescaled trigger signal from the LIME trigger limiter module, the SMP initiates a sparse data scan of the modules in the TKO crate, beginning with the GONG module.

The SMP modules contain two 1 Mbyte memory buffers. Data from the TKO crate are stored in one of the buffers until either a programmed data size has been read or a specified number of scans have been made. This allows the online software to quickly adjust to a sudden jump in trigger rate. One might expect such a spike in the rate to happen if a nearby supernova were detected. More typically spikes are seen from flashing photo-multiplier tubes. In any case, one does not want the detector to be shut down from this condition. When either of these conditions are met the SMP switches to the opposite buffer. Data in the original buffer are then available for read by the online workstation. Switching of the buffer generates an interrupt signal to the online workstation.

5.3 Online Workstations

Each of the 2 VME crates in each quadrant hut is connected to a SPARClassic S4/CI workstation (recently upgraded to Sun UltraSPARC workstations). The connection

is made via a Bit3 Computer Corporation model 467-1 Sbus to VME adaptor[88], just as with the outer detector. This adaptor allows the workstation to map the VME crate into an Sbus slot and treat the crate as an extension of its own bus. Interrupt lines are also provided for. Block transfer is supported, allowing for fast, efficient transfer of data from the SMPs into shared RAM memory space.

Readout of the 6 SMP modules assigned to the workstation occurs on receipt of the interrupt signal generated when the SMP switches buffers. Completion of the read frees the SMP buffer for use by the SMP during the next switch.

5.4 *Trigger Electronics*

The trigger electronics determine when the detector is to be read out. Mostly residing in the central hut, their function is to determine if an event has happened, and if so, distribute trigger signals to the front end workstations and at the same time record the event time and trigger type information.

Each ATM channel supplies a HITSUM output. These are added together to produce trigger logic signals. The size of these signals is proportional to the number of hit photo-multiplier tubes (15 mV/hit) within a 200 nanosecond time window. If the summed signal exceeds one of several thresholds a global trigger is generated and time and trigger ID information are stored in several FIFO modules in the TRG VME crate in the central hut.

There are four main self-generated triggers in Super-Kamiokande as well as several external trigger types. Depending on the size of the summed HITSUM pulse, it might pass any of three discriminator levels. These levels are labeled Super Low Energy (SLE), Low Energy (LE), and High Energy (HE). In practice these thresholds are not so different, that is, the HE threshold is not much higher than the low energy threshold. Additionally, an Outer Detector (OD) trigger is possible, triggering the detector without any corresponding inner activity. Typically events produce some

combination of these triggers. High energy events will also have an LE trigger bit set, for example.

The HE trigger is used mainly to quickly identify cosmic ray muons, atmospheric neutrino, and proton decay candidates. It requires a coincidence of 31 hits within 200 nanoseconds. LE triggers select events in the solar neutrino analysis range beginning at about 5.7 MeV. Attempts to push the solar neutrino analysis threshold to 5 MeV or lower requires a much lower trigger threshold to get good efficiency at the analysis threshold. Unfortunately, as the trigger threshold is reduced the radon background drastically increases the event rate. A computer and network upgrade in early 1998 has improved the performance of the online data handling. Until then, a prescaling arrangement was used in which only a small fraction of the very low energy events (corresponding to a short time window) were saved for analysis. This allowed the low energy analysis groups to see unbiased data at a very low trigger threshold (4.6 MeV), albeit with much reduced exposure compared to the higher energies. This is the reason for the existence of a separate SLE trigger rather than simply lowering the LE threshold.

The fourth type of trigger is an outer detector (OD) trigger. This type is determined by a coincidence of 19 hits within 200 nanoseconds in the outer detector. The trigger is formed by adding the HITSUM output of the QTC modules in the central hut. If an outer detector trigger is formed, the trigger signal is presented to the TRG module input. The TRG waits for 100 nanoseconds to see if the inner detector will also trigger. If not, a global detector trigger is generated anyway based on the the outer detector trigger alone.

In addition to the four self-generated triggers, various external triggers are possible. Clock triggers provide a prescaled unbiased sample of everything to check detector performance. LINAC or FISSION triggers are used to identify time periods when events should be expected from certain calibration runs.

All of the trigger types involved in a particular event are stored in one of the TRG

FIFO modules as an 8 bit trigger ID word. This word stays with the event data for use in analysis streams for event classification.

Global timing for events is provided by a 48 bit counter driven by a 50 MHz clock. This corresponds to 20 nanoseconds accuracy for the least significant bit (LSB). The 48 bit counter is reset to 0 at the start of each run and at 50 MHz could run for over 65 days before rolling over. Runs in Super-Kamiokande are stopped every 24 hours for convenience in handling the data so there is no danger of over-running the clock and having ambiguous times. Absolute timing comes from the UTC timestamp supplied by the anti-counter electronics.

Chapter 6

OUTER DETECTOR DATA ACQUISITION ELECTRONICS

The outer detector data acquisition electronics were provided by the American institutions. Because of budget constraints it was impossible to instrument the outer detector in the same manner as the inner. In any case the requirements for the outer detector do not demand the same level of photo-multiplier coverage and timing resolution. It became clear during the design phase that the outer detector only needed to tag incoming events, it did not need to reconstruct them with great accuracy. With this in mind the collaboration designed for maximum light collection ability. This served to enhance the performance of the outer detector as a veto counter and minimize the danger of “holes” opening up around failed photo-multiplier tubes.

6.1 Overview

The large size of the tank and the many channels involved made it quite useful to modularize the outer detector data acquisition electronics. Figure 6.1 shows the general layout of the hardware. Signals collected in the outer detector photo-multiplier tubes are digitized in each of each of four quadrant electronics huts. Local hitsum signals are created for use as an outer detector trigger. When a detector trigger from any source occurs, data are passed out of the quadrant huts to the central hut for further processing.

In the central hut, data from each of the four quadrant huts are buffered and then matched together. Local time stamps from a 50 MHz clock counter are added to

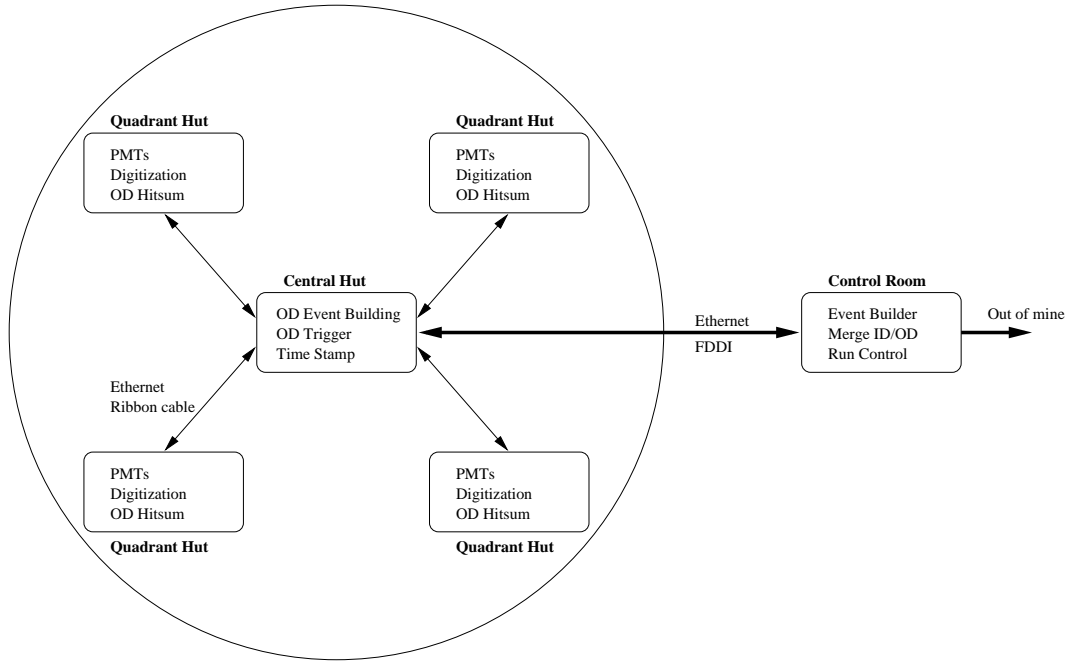


Figure 6.1: Overview of outer detector DAQ electronics

each event, as well as a global UTC time. The detector event number is also folded in. Finally the completed outer detector events are passed off to the event builder program running in the control room which matches up inner and outer detector information to form a completed full detector event.

6.2 Quadrant Hut Electronics

The front end digitizing happens in each of four quadrant electronics huts. The photomultiplier cables are fed into these huts. From here the signals are picked off, digitized and stored. Local hit-sum pulses are formed and sent to the central hut to form an outer detector trigger signal. Figure 6.2 illustrates the data flow in the quadrant huts.

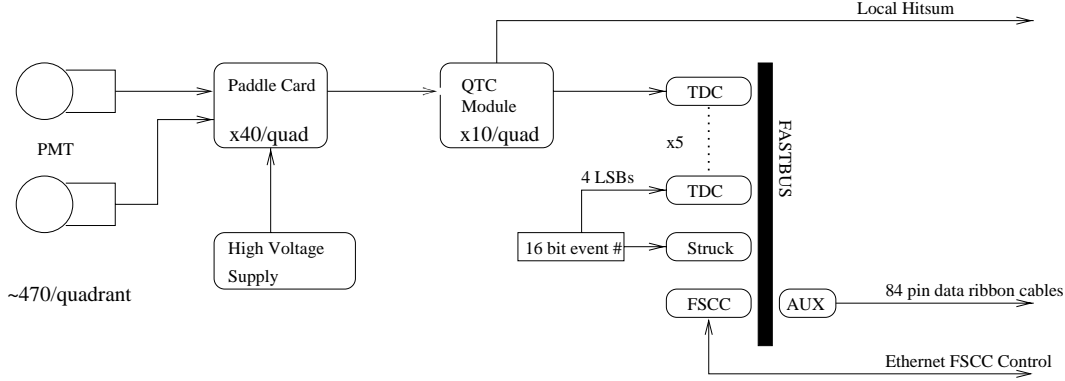


Figure 6.2: OD DAQ quadrant electronics

6.2.1 Outer Detector Photo-multiplier Tubes

The outer detector uses 20 centimeter diameter Hamamatsu R1408 photo-multiplier tubes augmented by wavelength shifter plates [68]. The tubes and wave-shifter plates were recovered from the Irvine-Michigan-Brookhaven (IMB) neutrino detector after a major water leak prevented further operation in March 1991.

The photo-multiplier tubes are hemispherical in shape. New watertight (and opaque) housings were built to protect the PMT bases for the Super-Kamiokande experiment. A total of 1885 are used in the outer detector, mounted 2 per supermodule. (Each supermodule is a structural block containing 12 inner detector photo-multiplier tubes in a 3 x 4 arrangement). The tubes themselves have a timing resolution of about 11 nanoseconds for single photoelectrons. This cannot begin to compete with the roughly 2 nanosecond resolution of the inner tubes, but is quite adequate for the purpose of tagging entering events.

The wavelength shifter plates are square acrylic panels, 60 cm on each side and 1.3 cm thick, doped with 50 mg/l of bis-MSB. The point of this is that the additive absorbs light in the blue-green where the water transmits the most light and re-radiates in the ultraviolet where the photo-multiplier tubes are most sensitive. Timing resolution is necessarily degraded, but the light collection efficiency improves dramatically. The

PMT is mounted into a machined hole at the center of the plate so the optical coupling is a simple physical contact near the sides of the tube glass. Aluminized mylar tape on the plate edges helps reflect photons back toward the photo-multiplier tube.

The use of the wavelength shifter plates degrades the timing resolution to more than 15 nanoseconds (FWHM), but the overall photon collection efficiency increases by 60%[68]. Since the design of the outer detector is optimized for use as a calorimeter rather than a particle tracker the extra photons are important and the lower timing resolution is of little importance.

The photo-multiplier signals are AC coupled and placed on top of the high voltage line. This avoids the need for a separate set of cables to carry the signals from the tube base.

6.2.2 Outer Detector High Voltage System

The photo-multiplier tubes are operated nominally at 1800V. High voltage is distributed by a set of four LeCroy 1454 High Voltage Mainframes, one in each of the four quadrant huts. These mainframes each control 48 channels of high voltage. Each channel is connected to a paddle card which fans out the voltage to 12 tubes. The mainframes are connected to an ARCNET network with a node in a VME crate in the central hut. This allows the high voltage to be set and monitored under control of the slow control computer “sukslc”.

A monitoring program maintains tables of the nominal settings for each channel and monitors the voltage and current for each channel. Bad tubes are often found this way, and shift workers can be alerted to the problem. An alert system is necessary because a single tripped channel affects 12 adjacent photo-multiplier tubes. This leaves the potential for a large hole opening up in the veto counter so the health of the outer tubes and high voltage supplies are watched closely.

6.2.3 *Paddle Cards*

The paddle cards fan out high voltage from one of the mainframe channels into 12 photo-multiplier tube outputs. The cards also pick off the photo-multiplier tube signals through a high voltage capacitor and feed them to a coaxial ribbon cable leading to the discriminators. Each of the 12 outputs has a jumper allowing the channel to be disconnected.

6.2.4 *QTC Modules*

Once the photo-multiplier tube signals have been picked off from the paddle cards, cables take them into the custom charge-to-time conversion modules designed and constructed by the Boston University group. The purpose of these modules is to measure the hit time and charge of the photo-multiplier pulse and convert it to a form which can be easily read and stored by the time-to-digital converters (TDCs). The output of the QTC modules is a logic pulse (ECL level) whose leading edge is the hit arrival time and whose width represents the “time over threshold”. Time over threshold is proportional to the natural logarithm of the charge.

The QTC modules also provide a hitsum output from each module. The output is the sum of a 200 nanosecond, 20 mV pulse generated for each hit in the module. In other words, it is proportional to the number of tubes hit in a 200 nanosecond coincidence window. These outputs are summed in each quadrant hut. The four quadrant sums are added together in the central hut. If the global hitsum crosses the OD triggering threshold corresponding to a coincidence of 19 tubes, a signal is presented to the detector triggering module as an OD trigger. If the inner detector does not trigger on its own within 100 nanoseconds, the outer detector hitsum pulse will go ahead and trigger the detector. In any case the OD trigger flag is latched in the trigger type data word in each event.

6.2.5 *Time-to-Digital Converters*

Super-Kamiokande uses twenty LeCroy 1877 Time-to-Digital Converters to record signals from the QTC modules. Five of these modules sit in a FASTBUS crate in each of the four quadrant huts. Each module can take up to 96 ECL level inputs.

The 1877 TDC modules are operated in “Common Stop” mode. Each module serves as a pipeline buffer that can be up to 32 microseconds long. When a stop signal is received by the module, it goes into “buffering mode” in which the location of up to 16 of the most recent edges in the pipeline is digitized and stored in memory buffers. Each photo-multiplier tube hit requires 2 edges to latch the width of the pulse. Eight memory buffers are available for storing data from different stops before the module becomes busy and stops acquisition. Readout of a buffer releases it to store new information.

The least count accuracy of the TDC modules is 0.5 nanoseconds. The buffering (digitization) time is a function of the number of edges in the pipeline. The LeCroy specification [89] states the conversion time is $750 \text{ ns} + 50 \text{ ns/edge}$ with a 1.6 microsecond minimum. This quantity was also measured from the Super-Kamiokande data and found to be $1339 \text{ nanoseconds} + 49.91 \text{ nanoseconds/edge}$ [90].

The window length is programmable and can be shifted around by delaying the stop signal relative to the detector trigger. In the early part of detector operations the window was set at the full 32 microseconds, centered around the trigger time. In September 1996 (starting at run 2800), this was cut to 16 microseconds with the trigger coming 10 microseconds into the window. This was done to reduce the amount of data coming from the outer detector and to help the buffer saturation problem.

There was a problem with the 1877 TDC’s in early detector operation. This has to do with the fact that the 1877 can record at most 16 edges in its pipeline. Later hits push earlier ones out of the pipeline so only the last 16 edges are recorded. This means that when the TDC digitization window is set very wide, many pulses can

arrive after the trigger. In the event of afterpulsing after an energetic muon, for example, a photo-multiplier tube might receive ten to twenty additional hits after the initial triggered event. Since the TDC can only store the most recent edges, hits from the original trigger are lost, creating “holes” in an otherwise clearly recorded event. This problem is solved by shortening the TDC window size after the initial trigger to less than the minimum trigger time for 8 events.

6.2.6 *Struck Latch*

To help keep track of which hits in the TDC pipeline go with which events, another module is provide to latch the detector event number along with the TDC data. The STR137-ECL Multi-Event Input Latch is manufactured by the Struck Corporation [91]. The hope, and the promise of the Struck Corporation, was that the latch could be read out in an identical fashion with the LeCroy 1877 TDC modules so that each TDC buffer could be associated with its own unique detector event number. In reality, several things made this more difficult.

Contrary to expectations, the Struck module latches only once for each stop signal received. In contrast, the TDC pipeline can latch up to 8 events in each window ending with the stop signal. This means that the Struck only latches one detector event number per window, not per event.

A second problem is that only the lowest 16 bits of the 32 bit detector event number are provided outside the central hut trigger module itself. This means that while the trigger module records the full 32 bit event number as a tag for the inner detector data, only the lower 16 are accessible by any other module. At normal detector trigger rates this event number rolls over many times a day and the upper bits must be tracked in software.

In order to resolve ambiguity concerning the event numbers when there are multiple events in the TDC window, the lowest 4 bits of the detector event numbers are fed into spare TDC channels. These four bits are recorded in the TDC’s for every event.

This uniquely tags events within each TDC buffer. The Struck latch provides the full 16 bit event number for one event in each TDC buffer at the common stop. This allows every event to be uniquely identified and matched with hits in other modules for the same event. The TDC pipeline records edges only so the lower bits had to be chopped by logic AND'ing them with the trigger signal (see section 6.3.7. The trigger (TRG) signal itself was also fed into a spare TDC channel. This allows precise timing of the trigger (including offsets to each quadrant hut), and also uniquely identifies the event number of the hits in each TDC buffer.

6.2.7 Fastbus Interface Board

There is one additional board in the FASTBUS electronics crate. This is a custom built module by Hans Berns which interfaces the signals from the central hut VME crate with the modules in the FASTBUS crate. There are several functions.

Due to the long distance between the quadrant huts and the central hut, control and calibration signals are converted to differential ECL levels on twisted pair cables. These signals must be converted back to appropriate levels for use in the FASTBUS crate.

In addition, this board delivers the stop signals (BIP and STROBE) to the FASTBUS modules. It also handles the “chopping” of the event number to allow the event number data to be recorded as edges by spare TDC channels.

6.2.8 FSCC FASTBUS Crate Controller

The LeCroy TDC modules and the Struck latch module in each quadrant hut sit in a FASTBUS electronics crate. All modules in this crate are controlled and read out by a FASTBUS Smart Crate Controller (FSCC) [92] designed at Fermilab and manufactured by BiRa for use in high energy physics detector data acquisition. The FSCC is built around a Motorola 68020 processor and has serial and thin-wire ethernet

connections to allow it to boot an operating system and run code from an external workstation.

On receipt of an external stop signal (suitably delayed from the trigger pulse to set the TDC window appropriately), the FSCC reads out all modules on the FASTBUS backplane and buffers the data in a FIFO memory. A leading word count is added, then the entire block is pushed out a 32-bit port onto the FASTBUS auxiliary connector. An FSCC-DARTAC auxiliary “personality card” [92] translates the 32-bit parallel TTL data into RS-485 with line drivers to get the data over the 30 meter ribbon cables to the central hut. This connection actually consists of two ribbon cables, a 50 pin cable for the lower 16 bits of differential data and control signals, and a second 34 pin cable for the upper 16 bits of differential data.

An annoying problem related to the FSCC word count persists to this day. The FSCC was designed in an era of single-buffer FASTBUS modules and was never modified to deal with the large data sizes provided by today’s multi-buffer TDCs. As a result, if the amount of data to be read is larger than the FSCC’s data FIFO, the leading word count is incorrect and some data can be lost. Fortunately, an accurate byte count is made by the central hut electronics of the received data and a comparison of the transmitted and received counts can detect this possible corruption of data. Shortening the TDC window to 16 microseconds in September 1996 helped this problem greatly and it now occurs very seldom. Fermilab claims to be working on a solution, but because they have little direct participation in Super-Kamiokande there is little motivation for them to work on the problem. A solution is not yet forthcoming.

The FSCC code is written under the VxWorks realtime operating system made by Wind River Systems. It is largely written by Mei-Li Chen and the group at University of Maryland. Object code is compiled by them or another group member having access to a VxWorks site license. These licenses are extremely expensive and hence severely limit participation by other collaboration members in the FSCC coding

effort. The code is then transferred to specific directories on the outer detector online workstation “sukant”. The FSCCs boot their operating system and program code via FTP from sukant on power-up or when they receive a “reset” signal on their front panel inputs.

The ethernet connection to sukant provides an additional means of communication which has only begun to be exploited. Maintaining a socket connection with the FSCC allows the online workstation to query the FSCC for its status, trigger rate, last event processed, and other information. The main difficulties for this have to do with getting the connections established at the beginning of a run with limited network awareness on the part of the FSCC.

6.3 Central Hut Electronics

The data taken in the quadrant huts are fed into the central electronics hut for further processing. The decision was made early on to feed the outer detector data to the main host event builder in a fully packaged way, rather than sending data from the 4 huts individually. We also want to add timestamps and other auxiliary information to the events for diagnostic purposes.

All outer detector data are finally merged in the central hut OD-DAQ VME electronics crate. Various modules buffer the data until it can be read out and sorted by the outer detector online workstation “sukant”. Figure 6.3 shows the layout of the central hut VME crate.

6.3.1 Buffering of quadrant PMT information

At each detector trigger, any photo-multiplier tube data stored in the quadrant hut TDC modules is read out by the quadrant FASTBUS FSCC controller and piped into an RS-485 ribbon cable through the FSCC auxiliary port. The other end of these ribbon cables is a two module combination called the (DM115/DC2) attached to the

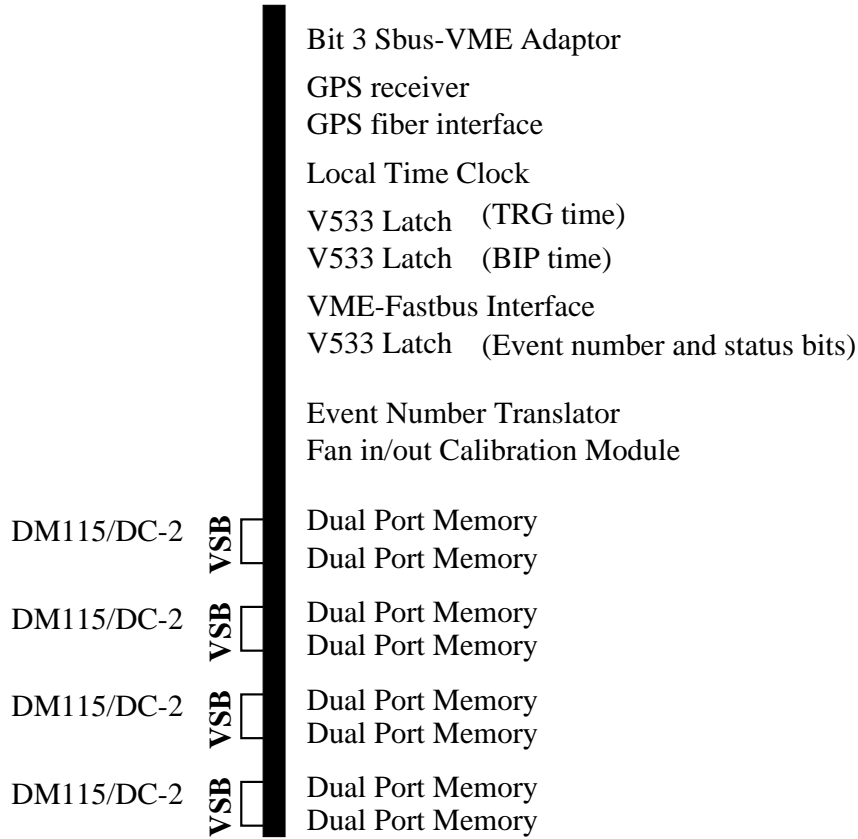


Figure 6.3: OD DAQ central hut VME crate modules

auxiliary (VSB) bus side of the VME crate backplane. This unit translates and buffers the incoming RS-485 data and stores it into dual-port memories for processing by the online data acquisition software.

DM-115/DC-2 Modules

The DM-115 RS-485 Input Module [93] is manufactured by Access Dynamics. It serves as an asynchronous data acquisition module. It can receive 32 bit differential RS-485 data at rates up to 40 megabytes per second. It also supports incoming control signals such as END-OF-RECORD, DATA-STROBE, DATA-SIZE, etc. It provides outgoing signals to the data source to wait if the buffer is full. This ensures reliable

communication over the long ribbon cable between the FSCC in the quadrant hut, and the VME electronics in the central hut.

The DC-2 VSB Input Controller [94] is also manufactured by Access Dynamics to work in conjunction with the DM-115 Input Module. The two units are actually mounted together into a single module. The DC-2 is a bus controller in its own right and contains a Motorola 68340 microprocessor which can be programmed through a pair of EPROM chips or through a pair of standard RS-232 serial ports. The DC-2 module has the ability to address the VME crate's auxiliary (VSB) bus from the rear of the backplane, thereby taking up no additional slots in the front of the VME crate. One DM-115/DC2 module is provided for each of the four quadrants.

The DC-2 accepts data from the plug-in input board (DM-115) and buffers it in an 8Kx32 bit FIFO buffer. As defined by the DC-2 program, these data are then written into one of a pair of dual port memories for each quadrant in the VME crate.

Upon receipt of a full event from the FSCC through the DM-115 input module, the DC-2 program adds a two word header to the event consisting first of the number of words actually read by the DM-115 for the event including the added header words, and a status word unused by the Super-Kamiokande data acquisition code. This allows the integrity of the data transfer to the central hut to be verified by comparing this count word with the FSCC count word. The DC-2 count (in bytes) should correspond to exactly 2 4-byte words more than the FSCC count since it includes the new additional header words. This has proved important in view of the FSCC data fifo overflow problem. It is also extremely useful to have a count of the entire amount of data corresponding to the event so that the data can be later read out as a block for each event.

The DC-2 program is burned into a set of EPROMs and is also provided by the University of Maryland group. It handles the transfer of data from the DM-115 input module to the dual port memories. It allows for external control by the online outer detector data acquisition workstation. A portion of the lowest memory of each dual

port memory module is set aside as a “mailbox”. DC-2 status, heartbeat, and current addresses are updated here by the DC-2, and various addresses are also monitored for new commands from outside. By writing specific command words into this memory region, the online workstation is able to command the DC-2 program without a direct serial connection to each module.

The DC-2 module is physically connected to a VSB bus module. The VME backplane, according to standard, has auxiliary bus connections for each slot available on the rear of the backplane, but these connections are made separately for each slot. The auxiliary “bus” is a misnomer, connections between slots must be made externally via a VSB bus module. This module is a simple passive device that busses two (or more) slots together with another device to be mounted in the rear of the backplane. Proper termination is provided for reliable bus operation. The use of this module means that only slots connected by a bus module can see each other on the VSB auxiliary bus. More precisely, we use four separate auxiliary VSB buses, one for each quadrant, each connecting one DM-115/DC-2 module with two VSB-VME dual port memories.

One of the most common commands issued to the DC-2 program is the “ping-pong” command. In order to avoid dead-time due to full dual port memory modules or long readout times, two dual port memory modules are used for each quadrant. After a specified number of events, typically 256, the DC-2 is commanded to finish writing the current event, and with the start of the next event, to fill the second dual port memory. This leaves the first free to be read out on the VME side at the convenience of the online data collection program “collector”. Several handshaking flags are set on both sides to be certain that the switch is handled smoothly and that both ends are ready.

6.3.2 VME Crate

The VME electronics crate in use in the OD-DAQ central hut electronics is a standard 6U, 21 slot VME backplane and chassis manufactured by Dawn VME, Inc. This crate, and a spare which serves as a test stand crate also in the central hut, have been modified by the addition of support rails in the rear of the chassis for the DC2/DM115 cards, and by the addition of an auxiliary power supply also in the rear of the chassis. This additional supply provides -5.2V to slots 7 (VME-FASTBUS Interface), 9 (Event Number Translator), and 12 (Fan In/Out and Calibration Module). This voltage is used by these boards to power the ECL and NIM level circuits for signal transfer between boards and the quadrant huts.

The boards in the VME crate serve to buffer the data and to latch additional information which can be added to the data stream. Dual-port memory modules buffer TDC data from each quadrant. Two FIFO latch modules store a local counter for relative timing between events and measurement of the TDC dead-time. A third module latches the detector event number and various status bits to assist in matching up event data from the four quadrants. A GPS (Global Positioning Satellite) interface allows storage of absolute universal time. In addition, several custom boards were designed and built by University of Washington engineer Hans Berns. These simplify the communications and data transfer between modules and between the central and quadrant huts. Another provides high resolution timing for the outer detector events.

6.3.3 Bit3

The crate controller for the VME crate also serves as a link to the online workstation. We use the Bit3 Computer Corporation's Model 467-1 SBus-VME Adaptor [88]. This device consists of two boards, one located in the VME crate and one in the Sun SPARCStation 20 online workstation "sukant". The 6U VME card serves as the crate controller and bus master. A special cable connects this module to the SBus

interface card. This allows the SUN to map the VME address space to its own SBus memory address space and in this way directly address cards in the VME crate. The adaptor includes a provision to provide up to four VME crate interrupts to the SBus as Sbus interrupts as well.

There are a few tradeoffs with this system. The cable connecting the interface cards is only 16 bits wide, so data transfer speeds are somewhat limited. It is enough for our requirements, though. Secondly, the adaptor can address cards in only one address mode (A16,A24,A32) at a time. Up to 6 logical devices may be defined (pending memory considerations) so that the addressing mode for each space can be predefined [95]. Software locking must then be used consistently to ensure that multiple processes do not attempt to access the adaptor in different address modes (i.e., different VME cards) at the same time. These details were dealt with and overcome, but present a challenge to the programmer attempting to service multiple cards in close to real time conditions.

6.3.4 Dual Port Memory Modules

The data stream from each quadrant ends in a pair of Micro Memory Inc. MM6390/32 dual port memory modules. These modules contain a 32 megabyte memory block which can be addressed by either the VSB bus or the VME bus, hence the term “dual port memory”. Data are written into the memory by the DC-2 module on the VSB bus and extracted by the online workstation via the VME bus. The modules are addressable in either the VME A24 or A32 addressing modes. This presents a conflict with the A24 read CAEN V533 FIFO latches so the A24 mode was disabled in the dual port memory modules.¹

The lowest 256 words of each DPM module are reserved for the “mailbox”. This is a region of memory reserved for use as communication and status registers to allow

¹Disabling of the A24 mode is easily done with jumper E7 on each dual port memory card.

commands and responses to be sent back and forth from the online workstation to the DC-2 without maintaining multiple serial connections to each one.

6.3.5 V533 FIFO Latches

The anti-counter VME crate uses 3 CAEN V533 FIFO Latch Modules. These are used to latch the 32 bit 50MHz Local Time Clock, the 16 bit Event Number, and various flags and status bits.

Each CAEN V533 module [96] contains a 32 bit differential TTL pipeline clocked by the external 50MHz signal from the Local Time Clock. At an external trigger signal, data words can be removed from the circular buffer and stored in a separate fifo without stopping the acquisition of data into the pipeline. Occasional problems with the data fifo overflowing before it could be read out were corrected by replacing the original 256 word FIFO chips with 4096 word versions. With the minimum of 3 latched data words per trigger, we can now store data from over 1300 triggers without danger.

Two of the FIFO modules are used to latch the 32 bit Local Time Clock counter. One triggers on the global detector trigger to latch this high resolution time-stamp for each event. The second triggers on a globally OR'd version of the end-of-buffering pulse from the TDC modules. The purpose is to determine when the last TDC finishes digitizing and is ready to take data again. With a little sorting in the data, this can serve as a measure of the TDC dead-time of the outer detector. In practice this has been very difficult to make reliable and analysis imposed dead-time cuts make the measurement unnecessary.

The third V533 module is used to latch the 16 bit detector event number. This is used to as a reference to match the auxiliary data with the TDC data from each quadrant for each event. The upper 16 bits of this module are used for various status bits. These include the FSCC busy signals showing whether a FASTBUS crate was available during any given trigger.

6.3.6 *GPS Interface*

For several reasons, it is important to be able to tag events with the absolute time that they occurred. This is necessary to point neutrino tracks in the detector back to their sources in the sky, such as for muon astronomy and finding the neutrino peak from the sun. The absolute time is also needed for coordination with other laboratories and telescopes in the event of a supernova occurrence, or for long baseline neutrino oscillation experiments. For astronomy the precision demands are not high. The angular resolution is large enough that very precise timing is unnecessary. Supernova time structure scales, however, are on the order of milliseconds. Pending long baseline experiments will need microsecond or better timing to gate the accelerator beam.

The Super-Kamiokande experiment uses a TrueTime Model XL-DC-602 Global Positioning Satellite (GPS) receiver to provide the absolute time [97]. The system begins with a satellite antenna mounted on a 5 foot pole on the roof of the radon hut located near the mouth of the Atotsu car tunnel entrance. The antenna is connected via a grounded lightning arrestor to the XL-DC receiver unit mounted inside the hut. This receiver was set to position mode for some time before the experiment began. After several days of sampling, very high statistics were acquired and the position was very well known. Given this known position, the universal time can now be determined accurately using only a single satellite.

The XL-DC receiver module outputs a time code on a fiber optic cable which runs approximately 2km down the Atotsu mine tunnel and terminates in the central hut anti-counter VME crate. There it connects to a simple VME board which receives the laser signal on the fiber optic input connector and converts it to RS-485 in an industry standard DC-shifted IRIG-B format. The converted signal is passed through a connector on the back side of the VME backplane to a TrueTime VME-SG Timing Card [98].

The VME-SG Timing Card contains its own clock which is conditioned by the

input signal from the XL-DC receiver. The time code on the fiber optic cable is transferred at 100 bits per second (1 kHz resolution) but with a precise starting point (<200 nanoseconds) for each IRIG-B “frame”. By itself it is not capable of providing the high accuracy inherent in the GPS system. Instead, the card uses a phase locked loop to lock onto the input signal and uses this to correct the internal clock. The use of phase locking allows the clock to remain relatively stable even during short periods of a noisy or missing input signal. The status of the phase error is reported with the data during readout so the online control software can warn the shift worker about any failure of the UTC input signal.

The Timing Card in the Super-Kamiokande configuration is triggered by the rising edge of bit 29 of the Local Time Clock which is fed into the VME-SG’s External Event input. This freezes the UTC time at precise intervals 21.475 seconds apart. A VME interrupt is generated and carried to the Sun workstation as an SBus interrupt by the Bit 3 adaptor. This informs the online data acquisition software program “collector” that UTC information is available to be read out when convenient.

The UTC time collected in this way is in principle accurate to 1 microsecond (modulo delays in the receivers and fiber optic line that have not yet been measured). The limiting factor is the width of the clock pulses in the VME card. When the triggering pulse from the Local Time Clock arrives, the “current” UTC value is frozen. On the other hand, the leading edge of the VME-SG 1 pps signal output is accurate to 100 nanoseconds. If this were used to latch the Local Time clock (with 20 nanosecond resolution) instead of the other way around, the UTC could in principle be latched to its full 100 nanosecond resolution. A circuit to do this was included in the University of Washington custom VME boards and could be used when needed. The pending long baseline experiments will require this accuracy or better to gate the beam spills.

6.3.7 *Event Number Translator*

The Event Number Translator board deals with the problem that many modules which latch the detector event number require signals at different levels. It receives the 16 bit detector event number from the main event count driver module, traditionally part of the inner detector electronics. The board provides level translation to RS-485 for latching by one of the V533 FIFO modules. The global trigger signal is converted to NIM and RS-485 levels and fanned out to the quadrant huts. Test trigger logic is included to feed trigger pulses through the OD-DAQ system to help diagnose problems.

6.3.8 *Fan In/Out and Calibration Module*

The Fan In/Out and Calibration Module (FCM) provides fan out of trigger and TDC test/calibration signals to the Fastbus Interface Modules located in the quadrant huts FASTBUS crates. These signals proceed over the “CAL” group of cables to each hut. The FCM also takes a fan in of manual test trigger pulses activated by pushbuttons on the Fastbus interface modules in the quadrant huts. The logic-OR'd result is then provided to the the Event Number Translator for further distribution.

The FCM also has a VME-programmable 16-bit test pattern. This is useful for verifying the addressing capability of the Bit 3 controller when diagnosing errors. It also provides a convenient general purpose set of digital outputs controllable by the online workstation. In addition, there are 3 auxiliary output also programmable over the VME bus. These can be set to either NIM or TTL output with an on-board jumper setting.

6.3.9 *VME-Fastbus Interface*

The VME-FASTBUS Interface board is the main trigger interface between the VME electronics and the Fastbus electronics in the outer huts. It provides the common

stop trigger for the TDCs, the common clock (stop trigger) for the Struck latches, a remote FSCC reset signal, and returns the Busy-In-Progress (BIP) signals from the TDCs.

The common stop trigger is made by digitally delaying the global trigger signal. Dip switches allow programming the delay in 20 nanosecond steps from 0 to 19.5 microseconds. The clock for the digital delay is taken from the 50 MHz Local Time Clock board.

The TDC common stop and struck latch stop trigger are vetoed if any TDC is busy (BIP is logic high), while the digital delay is busy (during the TDC digitization window), if the online workstation sets a VME veto command, or if there is an optional manual veto signal provided on the front panel.

The TDC BIP signals are also level converted to RS-485 and provided to one of the V533 inputs for recording at each trigger. On request by the online workstation, a remote FSCC reset pulse can be generated for any hut. This is used to recover from occasional problems with the FSCCs. Typically, all four quadrants are reset at the same time to maintain synchronization of data across the detector.

The VFI board also serves as a driver for the very useful LED display box. This small box with several labeled LEDs provides information to shift workers about OD triggers, TDC busy status, and the trigger vetos. It has been so useful in monitoring the status of the outer detector that the central hut monitoring camera has been largely dedicated to a close-up view of this box. Live video of its LEDs flashing is available in the experiment control room and the main experiment offices in the town of Mozumi.

6.3.10 Local Time Clock

The final custom board in the OD-DAQ VME crate is the Local Time Clock board. This board provides a 50 MHz reference clock for the V533 FIFO modules as well as the VFI board for use in the TDC Common stop digital delay. It incorporates a

32 bit clock counter that provides a local time stamp for outer detector events to 20 nanosecond resolution.

For reasons which are now lost to the mists of time, we chose a 32 bit counter for the local time stamp. This decision was probably made because the V533 modules which latch the counter are 32 bits wide. The inner detector electronics uses a similar timestamp with a 48 bit counter. The longer counter eliminates the possibility of counter roll-over. Future upgrades to this board may wish to use a longer counter as dealing with the 80 second rollover of the 32 bit counter proved to be a largely unnecessary inconvenience.

Chapter 7

OUTER DETECTOR DATA ACQUISITION SOFTWARE

7.1 *Anti-Counter Collector Program*

7.1.1 Collector Introduction

The “front end” of the anti-counter data acquisition software consists of a program called “anticollector”. The anticollector (or simply “collector”) program has the task of reading out all the data which are stored in various modules in the central hut VME crate by the front end electronics. Photo-multiplier tube data are stored in dual port memory modules, the UTC time is stored in registers on the VME-SG GPS receiver board, and the local time clock, the event number, and various other status bits are latched into 3 CAEN V533 fifo modules.

All of these data must be read out of the VME crate in a timely fashion and packed together to be handed off to the next program in the chain. The tasks of the collector are to get the data out of the VME crate as quickly as possible, then to get rid of that batch of data so it is free to read some more.

7.1.2 VME Bus Addressing

The VME bus has some special features that make addressing VME modules slightly different than other buses. Under the VME specification [99], the 16, 24, and 32 bit address spaces are actually independent to avoid having smaller addresses repeat themselves up through the address space of modules which use longer addresses. The address space is selected by use of an address modifier code which is placed on 7 additional address lines on the VME bus. Accessing a VME address is a two-step

process, first the correct address modifier code is written to the bus, then the address may be accessed.

The data transfer may also be configured. This is usually done by a hardware jumper setting on the VME module. The data width may be configured to 8, 16, or 32 bit words. A burst mode is also allowed under the VME specification.

7.1.3 Collector Program Flow

In order to readout all the data from the front end electronics modules in a timely manner, the collector program must follow a strict procedure. The main parts of the program are initialization, run control, V533 reading loop, DPM reading, NOVA memory management, and data quality monitoring.

7.1.4 Collector Startup Initialization

The first step in the initialization of collector is to setup the logical devices to be used for accessing the VME crate using the Bit3 adaptor. Each type of module in the VME crate must be accessed using different address and data width parameters. In order to simply access to the VME modules and to avoid conflicts, the Bit3 adaptor supports the creation of up to 6 “logical devices”, each with its own unique address configuration [95]. This allows a user to maintain open device descriptors to each type of module without having to completely reconfigure the adaptor each time a different module is being accessed.

Following the Bit 3 Adaptor initialization, the network shared memory is set up. This first initializes the message server that handles messages sent from the collector to the main host computer. Then a region of shared memory is allocated and structured according to definitions known to all networked online workstations.

The VME-SG GPS board is also initialized at this point. The board must be instructed to look at the DC-shifted IRIG-B input signal. Putting this initialization here allows the board to phase-lock to the input signal before the run is actually

activated. This avoids the problem of having the first several hundred events of a run having false GPS time while the unit attempts to lock to the reference signal.

7.1.5 Network Run Control

The detector operation is controlled by a set of flags in the network shared memory areas that are shared by all of the detector online workstations. There are 3 main stages of detector operation that are controlled by these flags. The beginning of each run starts with the INIT stage. This stage checks that the online processes on each workstation are in fact alive and running, and does the preliminary initialization of front end hardware. When all processes are alive and ready, they each respond to the main host by setting an INIT_OK flag in their respective shared memory regions, and signalling the main host to note the change in status.

The SETUP stage is for initializing front end hardware. At the end of the SETUP stage the entire detector must be completely ready to take data. For the anti-counter, this involves reinitializing the DC2 modules which write into the Dual Port Memories, opening run log files, and initializing the VME modules. The FSCC modules have already been rebooted. The V533 modules must be programmed to the correct pipeline length and transfer size. The GPS module must be programmed to use the DC-shifted IRIG-B pulse and an interrupt generated on the workstation when it is triggered.

It turns out to be important that the DC2 modules are initialized after the FSCCs are completely rebooted. This is because when the DC2s are initialized first, the FSCC reboot can cause a fake “event” to be latched into the DPMs. This appears as a corruption of the data in the first NOVA buffer to be sorted.

Only after all workstation report SETUP_OK via their shared memory flags will the main host computer allow the shift worker to start the actual run. When he or she presses the start button, an ACTIVATE flag is flashed to all workstations. The trigger host begins delivering triggers and all workstations are expected to begin

gathering data and feeding them to the main host event builder.

Two other shared memory flags are commonly used for run control. The STOP flag instructs each process to end normal data taking and revert to the INIT state in preparation for the start of a new run. The ABORT flag is a special cue that causes each online process to die abruptly.

7.1.6 The NOVA Buffer System

The NOVA system is a method of managing blocks of shared memory in an organized and efficient way [100]. The system was originally developed under the OS-9 operating system for use in balloon flight experiments. The main feature of the system used in the Super-Kamiokande experiment is its ability to pass control of varying sized blocks of shared memory between different processes and to reuse the blocks of memory in an efficient manner. Different processes may be assigned varying levels of priority to determine in which order they have access to the memory segments, or if they in fact get access to all of the buffers at all.

Processes connect to the NOVA daemon using the `nova_open()` call. This registers the process with a priority. The `nova_get()` and `nova_put()` calls are used to request access to a shared memory block and then to release control of it when the process is finished. The first time a block is requested, a large default size is allocated. When the first process is finished, it may snip the buffer to the actual length used. Subsequent processes receive only the smaller block. Processes may always shorten the length of the buffer they put out, but can never expand the buffer size once it has been snipped. The unused memory after a snip is returned to the shared memory pool to be reused in the next available buffer.

The choice of default size for the allocated blocks must be made carefully. In the OD software, it was found that the collector was unable to read out the front end electronics for periods on the order of tens of seconds because it had to wait excessively long for too large a default block of memory.

Processes are assigned priorities, buffers are given significance. The priority determines the order in which a buffer is delivered to various processes. The significance determines whether a buffer is delivered to all processes. If the priority plus the significance is greater than a given threshold, the buffer is always delivered to the process. If not, the buffer may skip the process.

7.1.7 The FIFO Reading Loop

The FIFO reading loop is the heart of the collector program. It actually consists of two nested loops, creatively called “inner” and “outer”. The outer loop continues until the number of events read exceeds 256. Data are actually read in inner loop, which exits only when there is no more to be read from the FIFO Multievent Buffers. This structure causes the fifo data to be read in bursts. Events pile up in the fifos, then the inner loop reads continuously until they are empty. This allows the collector to spend less cpu time polling the status of the fifos, and ensures that when it switches to other tasks, such as reading out the dual port memory modules, the fifo buffers are completely empty and available for storing new events.

While the number of events has not yet exceeded 256, collector uses periods during which the fifo buffers are empty to either read the GPS time if a new timestamp has been signaled, or to simply sleep, allowing other running programs to share the cpu.

FIFO 1 and 2 store the time stamp from the 50 MHz Local Time Clock counter and the event number and status bits for each trigger. They are triggered together by the TRG trigger signal from the inner detector electronics. FIFO 1 is polled for data availability and if there are data are available in the Multievent buffers, collector enters the “inner loop” and reads 3 words from each module. This corresponds to the minimum number of 32-bit words copied from the pipeline into the Multievent buffer at each trigger. All 3 modules are programmed to use this minimum number. The middle word is the one that will eventually be put into the data stream, determined by programming the fifo pipeline length.

Once all events are read from FIFOs 1 and 2, then FIFO 3 is checked for data. FIFO 3 is triggered separately by a signal that marks the end of the veto for TDC buffering (BIP). It is effectively a measure of the dead-time of the outer detector and latches a time stamp from the Local Time Clock. The fact that FIFO 3 is read out after FIFOs 1 and 2 means that events are no longer guaranteed to be sequential. It is possible that we could read out several global triggers from fifos 1 and 2, followed by several BIP trigger events from fifo 3. The time stamps are simply loaded into the current header for later sorting.

The “inner loop” exits when no further global trigger data are available in fifos 1 and 2. This prevents multiple triggers from being split across NOVA buffers. Also, the number of events must be greater than 256 and the last read LTCBIP must be later than any previous LTCTRG. This assures that the last event has its dead-time properly accounted for.

7.1.8 Finishing the NOVA buffer

After at least 256 events have been latched into the fifo modules, collector shifts tasks to completing the data in the NOVA buffer and then disposing of it. First, the array containing the header information for each event is copied to the NOVA buffer memory. Then, data from the dual port memory modules are copied into the NOVA buffer.

Reading out the dual port memory modules involves telling the DC2s to finish writing the current event and to switch to the second DPM of the pair for each quadrant.

The data are simply copied out of the modules into the NOVA buffer in block copy mode. Collector never sees anything related to the individual events in these data.

A quick check is then made for a flag file. If the file exists, collector will do another reboot of the FSCCs and reinitialize the DC2s. This is the so-called “manual” or

“pushbutton” reboot that allows the shift worker to cause a reboot on demand using a single command from the main host.

Various diagnostics are printed out about the buffer. Several more checks are made of the header data at this point. GPS times are tested to see if they are in range and other parts of the header are checked for sanity.

When all this is complete, the NOVA buffer is “put” out to the sorter and a new buffer is retrieved so the entire process can start all over again.

7.2 *Anti-Sorter Program*

The second program in the online outer detector software trio is the antisorter. The main purpose of this program is to serve as an event builder for outer detector events and prepare complete events for transfer to the main detector host workstation [101]. Data are received by the sorter program through the NOVA memory buffers after they are filled by the collector program. The sorter must take the blocks of data from each hut and match pieces of individual events from one quadrant with those from another quadrant. The data are repackaged as a complete event with data from all four quadrants along with the header and auxiliary timing information for that event. The sorter’s main components are a matching algorithm and numerous error checking routines to detect problems in the data and to avoid improperly matched quadrant data. The skeleton program was originally laid out by J. George, and was made fully functional by L. Wai. It is now under the care of H. G. Berns who added a lot of good status logging to diagnose possible detector problems.

Sorter has a similar run control structure to the collector program. On startup it sets up a network shared memory segment to monitor flags from the main workstation host. It also connects to the local NOVA memory manager daemon so that it will have access to the data buffers coming from collector. On receipt of the INIT flag from the main host run control, internal arrays are initialized. When the ACTIVATE

flag is set, sorter initializes the internal event counters and waits for data to become available from the collector.

When a NOVA buffer is available from collector, the data must be unpacked before repacking it in the desired output format. The first step is to copy the event headers into a local array where they can be easily called for. As each event header is copied to the structured array, the event numbers recorded in the central hut FIFO module for each event are expanded to 32 bits. Recall that only the lower 16 bits are actually latched in the VME crate FIFO. The upper 16 bits are added by hand by monitoring the event numbers to keep track of how many times the 16 bit word has rolled over.

The problem of event number rollover created a situation which is humorous to look back on, but created a great deal of strife at the time. At the commissioning of the detector on April 1, 1996 a small ceremony was held to celebrate the start of the experiment. The outer detector functioned perfectly through this ceremony until the last distinguished guest left the mine. At that moment the detector data acquisition system crashed and had to be restarted every two hours for several weeks until the problem was solved. It turned out that the event rates were such that the 16 bit event number was rolling over two hours into each run. The rollover was not properly handled by the OD software and hence no outer detector data could be fully matched with inner data after that point even though the data were being recorded.

With the event headers stored, the next step is to break out the TDC data from each quadrant hut. These data are stored in blocks from each quadrant with data from the 5 TDC modules in each crate coming sequentially for each event. Each block of TDC data for each event contains the word lengths written by the FSCC and DC2 modules so these can be checked to monitor the integrity of the data stream. If data are corrupted and the lengths do not check correctly the sorter is able to scan through the data block to find the next uncorrupted event. Only a few events are lost in this way and data taking can continue without crashing the data stream. As each event's data are copied out to the corresponding internal array for that quadrant, the event

numbers latched in the Struck Latch (corrected by TDC bits) are also expanded to 32 bits in the same way as for the FIFO data. The TDC data are repacked into the internal arrays, dropping the crate header words. The entire process is repeated using a new internal array for each quadrant.

With all of the data now copied into internal arrays, the NOVA buffer can be reused in a new format. The sorter program proceeds down the array of event headers and attempts to match up TDC data from each quadrant array that corresponds to the same event number. When found, the event header and its corresponding photo-multiplier tube data are repacked together into the now empty NOVA buffer. Various filters are applied to the TDC hits with the result stored to specific bits in the upper part of the hit channel word. No data are discarded at this point but the result can be used downstream to quickly accept or reject hits with certain criteria, such as nearness to the trigger time or clustering parameters.

Any event headers, or TDC event blocks from any quadrant, which could not be matched in one NOVA buffer are saved in temporary arrays for the next NOVA buffer. Since the DC2 modules do not receive the signal to switch pages simultaneously, it is possible for data from one quadrant to appear in a different buffer than the equivalent data from a different quadrant. Unmatched blocks nearly always find their partners and can enter the data stream when the next batch of events is processed.

With all of the matched data in place, a final outer detector data acquisition check happens. Various algorithms are used to check for dead or excessively active photo-multiplier tubes, mismatched data, and other possible problems.

Finally, the now repacked NOVA memory buffer is returned to the control of the NOVA daemon for transfer to the sender process. If the data quality checks turned up more than the allowed number of mismatched events, a signal is sent to the FSCC modules to reset themselves to get back into synchronization. Statistics regarding the number of matched events, unmatched events, and other data are updated and the sorter returns to waiting for another NOVA buffer of raw data from the collector

program.

If the NOVA buffer received from collector contains only four bytes, having no data at all, this is interpreted as a signal that a run is ending. The sorter does not monitor the network shared memory segment for this flag directly as we wanted it to process any remaining data available in collector before re-initializing. When this signal is received, the sorter updates the final event number and run statistics, writes out these figures to a performance file, and returns to the INIT state in preparation for a new ACTIVATE signal from the main host run control. A new run is ready to start.

7.3 *Anti-Sender Program*

The third program in the online outer detector suite is the “antisender”, or simply, “sender”. This program manages the transfer of event blocks to the main host computer for integration with the inner detector data. The sender program was first constructed by A. Stachyra, based heavily on the corresponding program written by Y. Hayato for the inner detector workstations. This program, as with the other online software, is now under the care of H. G. Berns who has added good logging to help diagnose problems.

Sender uses the same run control structure as the other online programs. On startup it sets up a network shared memory segment to monitor flags from the main workstation host. It also connects to the local NOVA memory manager daemon so that it will have access to the data buffers coming from the collector. On receipt of the INIT flag from the main host, internal variables are initialized. When the ACTIVATE flag is set, the sender initializes the internal event counters and waits for data to become available from the sorter.

The sender does not do any repackaging of the data. Rather, its main function is to monitor the data request flags in the network shared memory region for updated

requests from the main host event builder. When the event builder requests a range of events (specified by their event numbers), the sender responds by putting as many of these as are available in an output NOVA buffer and making this region of memory accessible via the network by the main host. The main host can copy these events directly from memory and informs the sender when the operation is complete by means of the flags in the network shared memory tables.

This kind of transfer is naturally more complicated in practice. The sender is the last program in the NOVA buffer chain and is responsible for returning the finished NOVA buffers to the memory pool for reassignment by the NOVA manager daemon. If some events are not passed to the event builder for some reason, the sender must take care that the buffers are still recycled. Often the range of event numbers requested by the main host event builder will span several NOVA buffers of data from the sender. In this case the sender must be able to keep track of what has been delivered and what is still pending. When a run is ended, sender attempts to deliver any data still in the pipeline.

Chapter 8

DATA FLOW: ONLINE TO OFFLINE

8.1 *Run Control*

The overall operation of the detector is managed from a single point on the main host computer. The shift worker can sit in front of this display and start or stop runs with a single interface. All of the data acquisition programs on all of the online workstations are started automatically by the run control scripts and controlled through network shared memory.

Each data acquisition program that will communicate with the main hosts establishes a pointer to a shared region of memory that will be reserved as a table of flags. The region contains tables for all of the online workstations and the main host so each program has access to all of the control flags for all other data acquisition programs. Communication is done by setting a flag in the network shared memory region and sending a request via socket to the main host to update and refresh that section of memory on all workstations. Responses from the main host are found by simply checking the appropriate memory locations when the data are required. The use of network shared memory run control is described further in Section 7.1.5.

A graphical interface is provided for the convenience of the shift worker. The X Windows display program presents a control panel with buttons for initializing and starting the data acquisition system. Only buttons for the next step are made available to guide inexperienced workers through the correct startup procedure. Additional windows provide information on current events being processed by each workstation, the status of each data acquisition program on each workstation, and warning mes-

sages in the event of a problem. Other menus allow configuration of the detector trigger, setting of the ATM and trigger thresholds, and run type setting. A form interface allows workers to log in for their shift and make comments about the operation of the detector for a given run.

8.2 Event Builder

Data taken by the 8 online workstations (sukon1-8), the trigger workstation (sukon9), the anti workstation (sukant), and the slow control workstation (sukslc) are merged together in the main host. These data are all fed into the event builder program.

The purpose of the event builder is to match up event sections from all parts of the detector, add in latched trigger information and package the events for storage. Data from each workstation are repacked so that all the header pedestal, trigger, and slow control information is together followed by the photo-multiplier tube data in a logical order. The event number is used to match up each data section.

Events packed by the event builder are stored together in subrun groups. A subrun is defined as the amount of data that can be stored in a data file of about 100 Mbytes. Before the SLE trigger this corresponded to about 10 minutes of data. These files are stored on a local disk drive connected to the main host (sukonh). Enough storage capacity is available to buffer data for approximately 15 hours in the mine. This allows operation to continue in case of temporary failure of the network connection out of the mine.

8.3 Super Low Energy Event Processing

Starting in April 1997, a new “super low energy” trigger was introduced to allow the solar neutrino threshold to be pushed down to 5 MeV. Lowering of the trigger threshold means an exponential increase in trigger rate due to radon and other low energy background. At that time the online computing power was insufficient to

process so much data. The solution was to include a very fast point fitter in the online stream to reject events very near the walls.

SLE triggers are flagged with a particular bit in the trigger word. In the event builder, a table is made of all event numbers and a mask prepared for the super low energy events. A very fast point fitter is applied to the SLE events in each subrun and the mask updated for those events which fit away from the walls. Only these are passed along to the reformat program with the usual (higher threshold) low energy, high energy, and outer detector triggers. The procedure was arranged in a very nice way so that if anything went wrong with the fitter, SLE data would be simply dropped and the normal operation of the detector would continue normally.

8.4 *The Reformat Process*

The reformat process checks the status and content of each event. Trigger information is extracted for use in fast filtering by the analysis groups. Inner time and charge data are extracted and compressed. Anti time and charge data are copied. Inner pedestal data are extracted and used to update the current pedestal tables. It has not yet been subtracted from the charge data. Other run, slow control, camac ADC, information is also extracted and used to update monitoring tables. The reformat process can process one subrun file in about 4.5 minutes, roughly twice as fast as they are produced.

Reformatted events leaving the main host are sent via a fiber optic network out of the mine and down a nearby highway about 10km to the experiment's computing facilities in the town of Mozumi. Permanent tape storage and the collaboration's main computing power is located here. Comfortable offices, a library, and conference facilities are also provided for good working conditions without the difficulties of access and working inside the mine.

8.5 *The TQREAL and FLOW Processes*

The path for reformatted data splits at this point. The subrun files are fed into new files of about 150 MBytes each corresponding to a particular run. These are placed on a large storage disk where a background process moves them to magnetic tape storage.

In addition, the reformatted data go directly to the TQREAL process for recalibration. In the TQREAL process, the pedestal tables updated by the reformat process are used to subtract out the pedestal bases from the photo-multiplier tube signals. Pulse arrival times are corrected for known delays based on the laser calibration studies. Data are also repacked into ZEBRA banks at this point and is in the final data format which will be used by the analysis groups.

The output of the TQREAL process is the flow process. This consists of a large ring buffer in memory which holds events. Basic trigger information, numbers of hits, total charge, etc. is made available in a small table with each event. A large number of reduction processes may connect to this ring buffer and look at this table to make their event selection. If an event is desired, the data for the event are copied to an offline FDDI network and made available to the reduction process. Major reduction processes which connect to the flow process include the low energy neutrino, up-going muon, atmospheric neutrino and proton decay, and supernova analysis groups. A special process filters data to the US tape machines for making DSTs to be mailed to the United States.

Chapter 9

DETECTOR PERFORMANCE

The performance of the Super-Kamiokande detector depends on several factors. The operational live time limits the number of events that can be collected. The water transparency limits how much light can be collected, its stability affects the gain corrections. Tube failures affect the ability of the inner detector to gather light, in the outer detector it can mean low efficiency gaps in the veto counter.

9.1 *Water Clarity*

The attenuation length of the light increased dramatically during the period after filling the tank. As the water was recirculated through the filtering systems it became more and more clean. By June 1996 it had settled and has remained relatively stable. Some variations have happened due to injection of new water to replace water lost through small leaks in the tank. Cleaning of the fine filters also improves the clarity. Xenon lamp calibrations are taken every few weeks to track the gain changes. Laser attenuation length measurements are taken on an even more frequent basis to make sure the analysis programs can reconstruct the energy accurately. Figure 9.1 shows the change in the attenuation length over time.

9.2 *Photo-multiplier Tubes*

The number of bad channels has increased over time. Photo-multiplier tubes fail occasionally for several reasons. Some tubes fail mechanically when stress on a joint allows water to flood the tube or short electrical connections. Some tubes have a

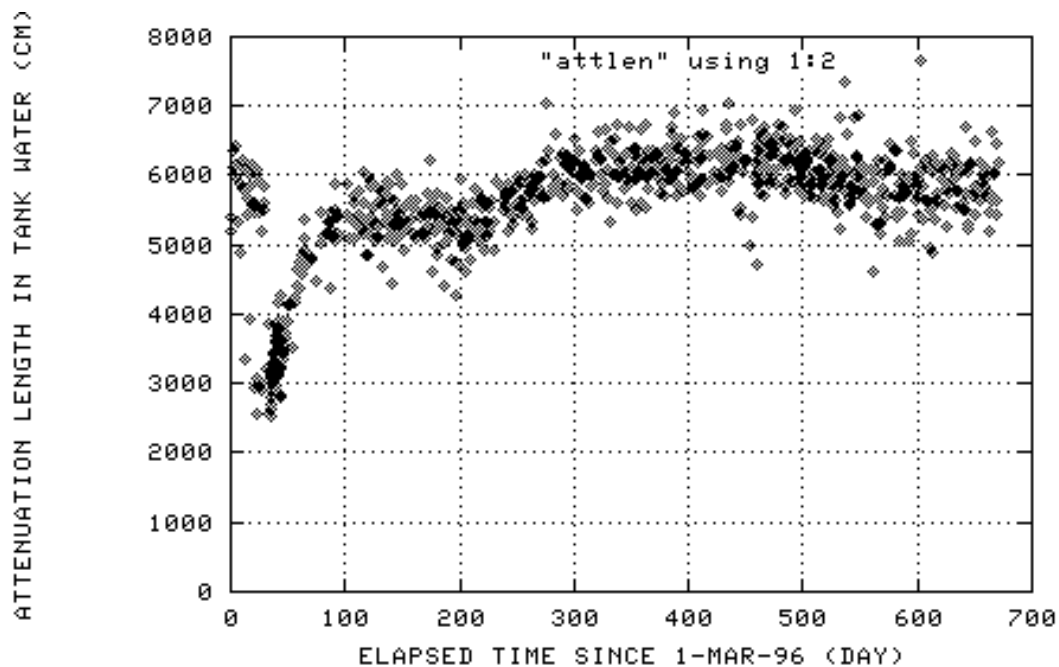


Figure 9.1: Attenuation length over time

failure in the dynode structure that causes internal discharge, the so-called “flashing” tubes. Tube death rates for inner and outer photo-multiplier tubes are roughly the same in terms of numbers. This is more serious for the outer detector which has far fewer tubes to begin with. Figures 9.2 and 9.3 illustrate the tube failures over time. Tube failures are distributed fairly evenly over the tank, with a few more toward the bottom in the outer detector tubes. The outer detector tubes are older, having been salvaged from the IMB experiment. A large fraction of the inner dead tubes are ones which were moved to KEK to be used in the beam test experiment.

The failure of the outer detector tube death to level off is a cause for concern. At this point dead channels are widely scattered and no areas are significantly at risk for allowing entering particles to get through unnoticed. This will change as tubes continue to die. The rate of death at this time is one tube about every 8 days. The reason for the deaths is not clearly understood. If some mechanical stress is to blame,

it is hoped that the problem can be detected and identified during the upcoming maintenance period. In the summer of 1999, the tank will be drained and access will be allowed to replace and repair the photo-multiplier tubes.

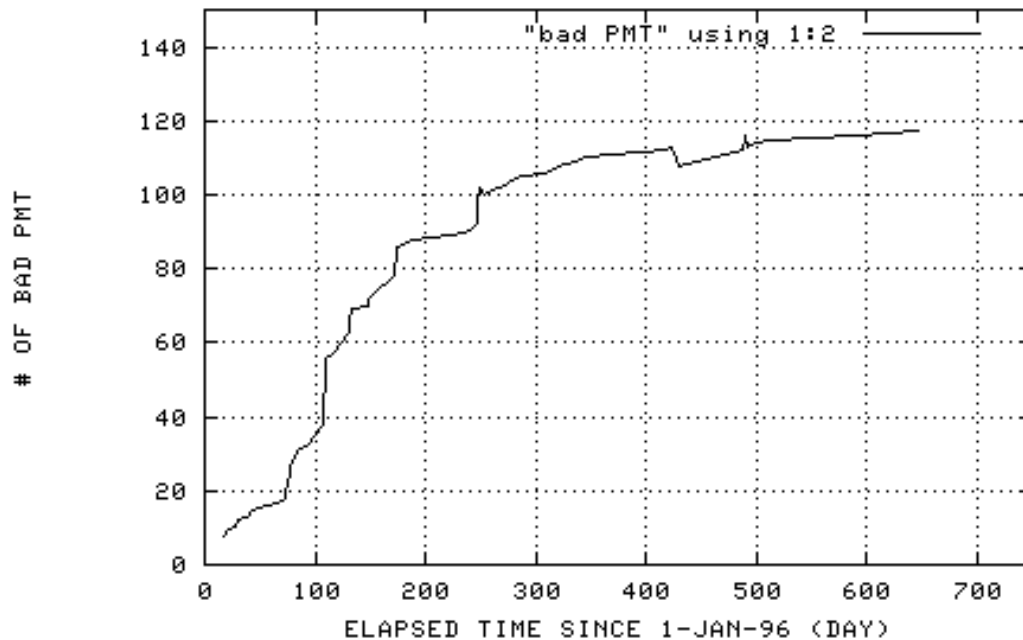


Figure 9.2: ID tube death

The dark rate of the tubes affects the trigger rates and can be a sign of detector problems. A high rate might indicate a flashing tube or other. Normal dark rates for these tubes are 3 kHz for the inner tubes and 5 kHz for the outer ones. This is quite good as photo-multiplier tubes go and is one of the excellent qualities of both sets of tubes. Figure 9.4 shows the stability of the average inner detector photo-multiplier tube dark rate over time.

Live-time is an important issue. The number of neutrinos collected depends directly on the time spent taking data. Super-Kamiokande has achieved an amazing 89% overall up-time, with over 95% in recent months. One of the biggest causes of detector down-time is actually calibration studies, not equipment failures. Figure 9.5

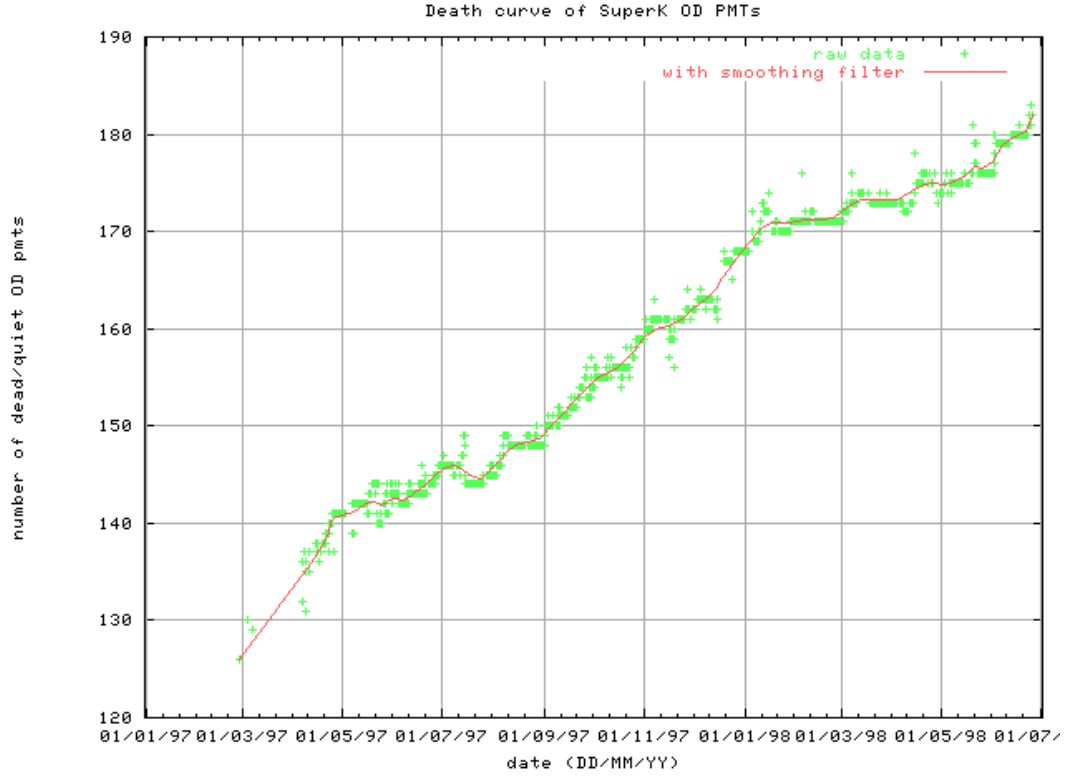


Figure 9.3: Outer detector tube death

shows the integrated live-time since the start of detector operations.

9.3 Trigger Rates and Number of Events

Closely related is the number of events. Figure 9.6 gives the integrated number of recorded events over time. Note the increase in number of events recorded when the super low energy trigger was installed.

The trigger rate is another important factor to watch. Higher trigger rates indicate flashing or noisy photo-multiplier tubes, lower rates might indicate that the water is getting less clear. Figure 9.7 shows the change in trigger rates over time.

High energy triggers have remained relatively stable. The main source of these

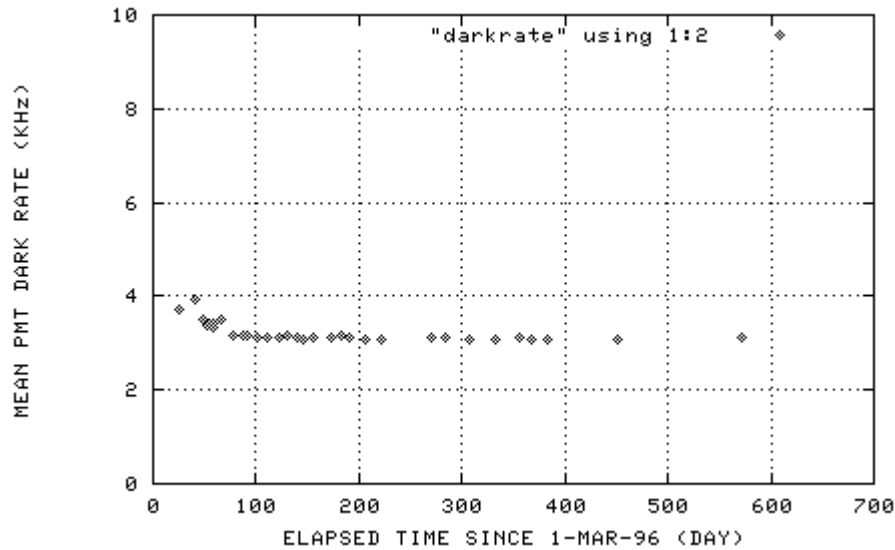


Figure 9.4: Dark rate for inner detector photo-multiplier tubes

events is cosmic ray muons which are relatively constant in time. The detection efficiency is also quite good for almost all of these events. The low energy trigger rate, however, has a much closer association with the water clarity. Purer water means it is more likely that light from a very weak event will reach the walls and trigger the detector.

For both triggers, a few isolated runs show very high trigger rates. These indicate a detector problem such as a flashing photo-multiplier tube or oscillating discriminator channel. Often the trigger rate is one of the first clues to this type of problem.

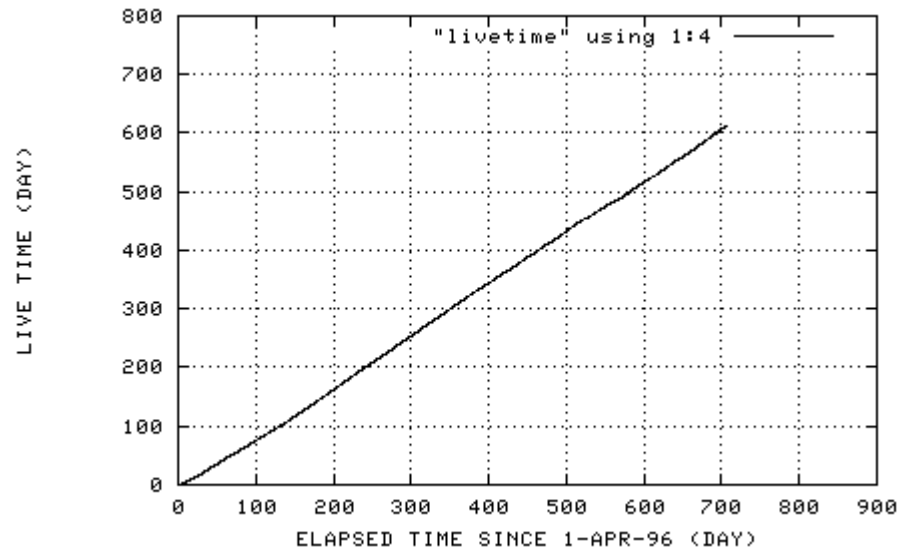


Figure 9.5: Live-time since detector commissioning

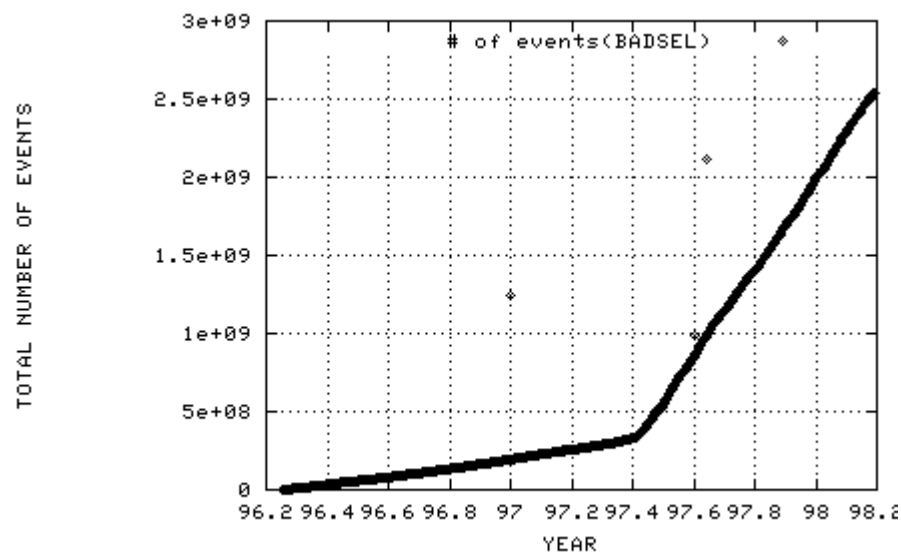


Figure 9.6: Integrated number of events since detector commissioning

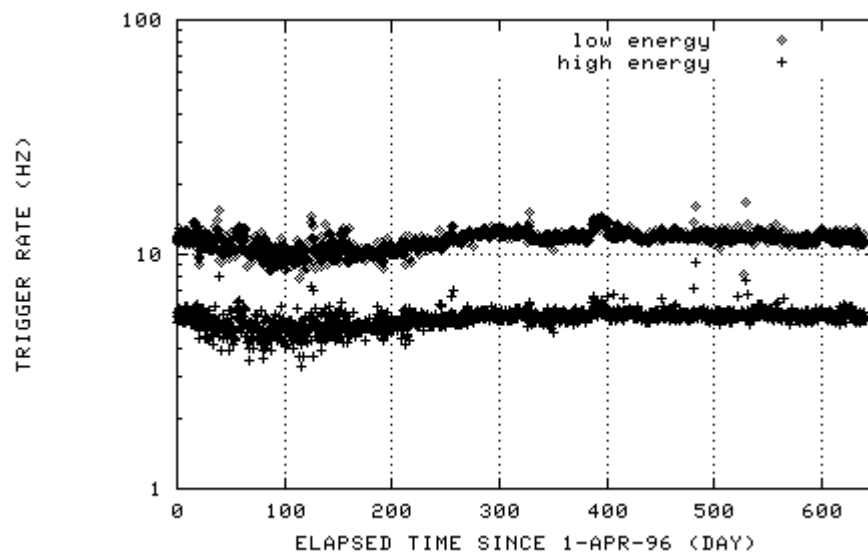


Figure 9.7: Trigger rate since detector commissioning

Chapter 10

CALIBRATIONS

The high rate of neutrino interactions in the Super-Kamiokande detector would do researchers little good if the energy deposited could not be well measured. Fits would not be accurate if the relative timing were not well understood. Both the solar neutrino problem and the atmospheric neutrino anomaly could be written off to a shift in energy scale in this case. It is important to determine the energy scale and relative timing as precisely as possible. To this end, the Super-Kamiokande collaboration has used a variety of methods to ensure that the energy measured by the detector is both precise and accurate. These methods span a wide range of applicability in energy and serve to fully determine the energy response of the detector in ranges covering both the solar and atmospheric neutrino spectra.

10.1 Laser Timing Calibration

The relative timing of the photo-multiplier tube signals is critical to our ability to reconstruct events. The actual digitization time of signals from each channel varies according to the cable length and relative delays in the QTC (charge to time converter, see section 6.2.4) modules. The pulse height can affect when the leading edge crosses the discriminator threshold. Since event reconstruction depends on knowledge of the relative photon arrival times, relative acquisition delays must be measured precisely and corrected for.

Calibrating the timing is done by firing laser light into the detector, calculating the light travel time to each photo-multiplier tube, and measuring the time the tube pulse

is digitized. In this way the time delay for the photo-multiplier tube to digitization chain can be extracted [102].

The laser is a tunable dye laser (Laser Science VSL-V337ND-S pulsed nitrogen laser pumping a Laser Science DLMS-220 dye module). The dye chosen was an Exalite 384 dye, which at 384 nm nearly matches the peak Cherenkov light in water. The laser pulse is monitored by a photo-multiplier tube. A filter wheel adjusts the intensity of the light which is then fed into optical fibers for transmission to the tank. The laser is fired by a trigger signal which also triggers the detector.

In the inner detector, a single diffuser is sufficient to illuminate all the tubes. The fiber with diffuser is lowered into the tank at the start of calibration runs and can be inserted into any of the calibration ports in the top of the tank. This allows a wide variety in the desired distribution of light in the inner tank. The outer tank photo-multiplier tubes cannot be seen from a single light source. For the outer detector, a network of 52 optical fibers is permanently installed to illuminate the tubes. These fibers can be selected at will using an optical switch.

The end of the fiber which rests in the tank must have some sort of diffuser so the light gets out into the tank. By simply dabbing a mixture of TiO_2 powder and optical cement onto the ends of the fibers, the collimated laser light was made nearly isotropic with the added benefit that the ends of the fibers were sealed against moisture. This low tech solution worked well.

The inner detector calibration light has a much higher isotropy requirement. The simple TiO_2 mixture was not isotropic enough. A small sphere (known as the “laser ball”) was filled with a mixture of silica spheres suspended in water, sold under the name of “Ludox” by DuPont. A double mirror assembly was used inside the ball to improve isotropy even in the backward direction.

10.2 *Linac*

Super-Kamiokande was constructed with its own linear accelerator built in-situ. It resides in a short tunnel just above and next to the main tank cavern. A beam pipe extends into the main cavern and can be inserted into the tank at various locations and depths through access ports constructed for the purpose.

The electron linac is a Mitsubishi ML-15MIII medical linac formerly used in a hospital at Miyazaki Medical University [103]. It has been modified by the removal of the original bending magnets used to direct the beam around the hospital operating room. The electron gun was also changed to produce less than one electron per bunch at the exit window of the beam pipe.

The operating principle of the linac is simple. The electron gun consists of a fine hairpin tungsten filament from which electrons are boiled off due to an applied current less than $200\ \mu A$. These electrons are injected into the accelerating tube fed by microwaves produced by a klystron. The microwaves are bunched at up to 66 Hz. The intensity of the output beam is controlled by the current applied to the electron gun and the energy is determined by the frequency and input power of the microwave source. Adjusting these parameters allows the linac to produce electrons from 5 to 16 MeV.

After the linac, the beam is bent 15 degrees down into a beam pipe built through the rock floor to reduce beam induced background. The pipe exits the rock into the main cavern dome just above the tank lid and is taken horizontally to a 90 degree bending magnet that sends the beam straight down into the tank at whatever location is desired. A plastic scintillator just above the end of the vertical beam pipe triggers the detector when a calibration electron is injected into the tank.

The beam energy is measured with a Germanium detector. This detector has itself been calibrated using various radioactive gamma ray sources, and with electrons at the air-core beta spectrometer at KEK (Tanashi branch).

Calibration data in the Super-Kamiokande detector were processed with the solar neutrino analysis reduction path. The result is that in the energy range of 5 to 16 MeV, the detector absolute energy scale is known to $\pm 5\%$. The response of the detector is reproduced by the Monte Carlo simulation within 2%.

10.3 Nickel Source

An additional calibration source for the low end of the energy spectrum is a radioactive source. A compound Cf-Ni source was made to produce gamma rays at 7 and 9 MeV. The source consists of a small sphere of Californium in a water filled bucket. The Cf source is a source of neutrons from spontaneous decays. The neutrons thermalize in the water surrounding the source and are captured by coils of nickel wire at the outside walls of the bucket. These captures release gamma rays at several energies, the dominant ones being 9.0 MeV from ^{58}Ni and 7.8 MeV from ^{60}Ni . The gamma rays convert to electrons via Compton scattering or pair production in the tank. One of the difficulties with a nickel calibration is that the calibration depends on a simulation of the gamma ray interactions. Also, since the source is quite extended the interaction vertices for the gamma conversion must be fit. This introduces some additional uncertainty. The nickel source is now used to check the stability of the energy calibration over time and to provide a bridge to the energy scale of the Kamiokande experimental data.

10.4 Cosmic Ray Muons

The highest energy calibration is done using a natural source, cosmic ray muons. The idea is that since most of the muons tend to be minimum ionizing particles, then if the track length is known, one can calculate the amount of energy that should be deposited in the tank as Cherenkov radiation. This can be simulated and compared to the amount of light actually collected. The study does depend on the simulation

of the detector, but for similar types of events the comparison gives us a statement of our knowledge of the measured energy. This is a straightforward systematic effect. It can be used to further tune the simulation and the fitting routines in order to minimize systematic effects.

Of course, not all cosmic ray muons are minimum ionizing, and not all have the same track length. Strict cuts are applied to get a clean sample for calibration. Only muons passing vertically downward near the center of the tank are considered. They must be single ring events, with a good fit to a long track muon fitter. A poor fit or extra rings suggests the presence of additional pions, gammas, or electron pairs produced by bremsstrahlung.

10.5 Michel Electrons

Michel electrons are decay electrons from stopping muons. The spectrum of electrons from muon decay is well known and should provide a good calibration source. In practice, a known electronics effect makes this more difficult.

The ATM modules which digitize hits from the photo-multiplier tubes have buffer capacity for several events. This allows the electrons from muon decay to trigger the detector separately from the initial muon. Hits from various channels are buffered and digitized in sequence. It was found that channels which have to wait longer to be digitized have a different conversion constant when they are.

The idea is that the presence of a large number of hits waiting in the buffers draws down the main voltage level, affecting the reference voltage used for the digitizing. In addition, slight leakage currents in the storage capacitors used to buffer the hits before digitization lets some of the signals charge leak out while waiting to be sampled. The combination of these two effects made calibration results different for events with an energetic muon just preceding that would fill the buffers with large numbers of hits. These ATM effects have been carefully investigated and parameterized. The effect

can now be corrected for to good accuracy.

For calibration purposes, it is better to avoid the issue entirely. Because of this, a number of special “decay-electron” calibration runs have been performed. In this mode, the ATMs are set so that for muon decays, they do not record hits from the initial muon, but rather only for the decay electron. This removes the problem of the extra hits delaying the digitization of the electron signals. Accurate calibrations have been possible with this modification.

10.6 π^0 *Rest Mass*

A clever way of checking the energy scale around 135 MeV is to look for the rare events in which a neutrino interaction results in a single π^0 essentially at rest in the tank. The π decays into two back to back gamma rays, providing a fairly distinct signature for the event. Searches can be made for events with exactly two opposing rings for which are both identified as a gamma ray in a particle identification algorithm. Figure 10.6 shows a plot of the reconstructed mass of such events made by T. Hayakawa.

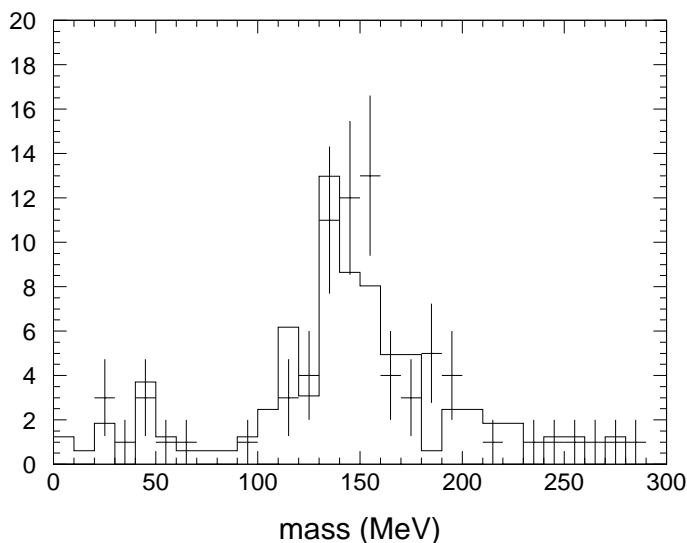


Figure 10.1: Reconstructed π^0 Mass

10.7 *Xenon Lamp*

The relative gain calibration is done using a Xe lamp. Relative gain is important to ensure that the response of the detector is uniform. This information was used in the early operation of the detector to trim the high voltage settings of the photo-multiplier tubes to make their response as similar as possible. The gain of the photo-multiplier tube, that is, the number of photoelectrons out of the dynode chain for each input photon, depends largely on the applied voltage. This voltage can only be adjusted in discrete steps within a reasonable range, however, so it is not in general possible to trim all tubes to exactly the same gain by setting the high voltage. The relative gain can change over time as well, as tubes age, dust settles, and so on.

Once the tubes have been trimmed as closely as possible to similar gains, the Xe data are then used to recalibrate the pulse heights. A table is made of the variations in the tube-to-tube gain. During regular taking, all signals in each of the 11,200 inner photo-multiplier tubes are corrected by this table. Xe calibration is carried out every few weeks to keep the detector well tuned against time-dependent effects.

The xenon lamp system is quite similar to the inner detector laser system. The Xe light goes into a fiber optic cable which is put into the tank at various positions. A diffuser ball similar to the laser ball spreads the light into the tank as isotropically as possible. The xenon ball mount includes a small vane which extends horizontally in one direction above the ball. The shadow of this vane can be seen in the data and is used to correct for any residual azimuthal asymmetries.

Xe relative gain calibration is done by flashing the lamp from various positions in the tank, usually along the center line. In this way, concentric rings on the top and bottom, and layers on the sides all receive uniform illumination. Tubes in each ring or layer are adjusted relative to each other. Data from various positions allow studies of dependence on light level, and takes out effects due to anisotropy of the diffuser ball.

Chapter 11

SIMULATION

What Super-Kamiokande actually measures are pulse shapes and times from a large array of photo-multiplier tubes. The fluxes and directions of the actual particles are deduced from this information. The detector is complicated, and moreover, the physics is complicated. Results might be skewed not only by detector inefficiencies but also by failure to account properly for some type of particle interaction. The usual thing for an experiment in this circumstance is to create a simulation.

Atmospheric neutrino events are simulated in Super-Kamiokande using two independent simulations. The two agree well. One of these, based on the “on-site” method, is used in this analysis. The purpose of the simulation is to model the interactions of atmospheric neutrinos in a simulated detector. The neutrino flux is based on models of the primary flux of cosmic rays and their interactions in the upper atmosphere. Once a neutrino interacts in the detector, Cherenkov photons are produced and tracked for those products that require them. The detector response to these incident photons is further simulated to account for effects of the data acquisition chain. The hope is to reproduce the response of the detector to the simulated neutrino flux as accurately as possible. Any variation between the data and the simulation must be due to either a flaw in the simulation (hopefully a small effect) or to an interesting physics result.

11.1 *Atmospheric Neutrino Flux*

The Super-Kamiokande simulation is based on Honda's 1995 atmospheric neutrino flux calculation[2]. That work starts with the best measured cosmic ray primary spectra and proceeds to calculate all known interactions that might ultimately produce a neutrino.

Cosmic rays colliding with oxygen and nitrogen nuclei in the atmosphere produce large numbers of π and K mesons. These decay into muons and neutrinos. The muons decay as well, ultimately leading to a ν_μ/ν_e ratio equal to 2. The production of atmospheric neutrinos is described more fully in Chapter 2.

Several factors can affect the expectations for neutrino production from cosmic rays in the atmosphere. Non-decaying muons, polarization effects, and the geomagnetic field all change the expected neutrino spectra.

Non-decaying muons

When the energy of muons exceeds about 5 GeV, relativistic effects allow a significant fraction of the particles to reach the surface of the earth before decaying. Ionization and other losses rob most of the energy so the muons decay nearly at rest or at least at a much lower energy. Electron neutrinos are produced almost solely from muon decay. This means that flux of ν_e is depleted at energies above where these muons actually decay. The flux ratio $(\nu_\mu + \overline{\nu}_\mu)/(\nu_e + \overline{\nu}_e)$ is correspondingly increased. Figure 11.1 illustrates this effect based on several atmospheric neutrino simulations. It is worthwhile noting that while the overall normalization of the cosmic ray spectrum is not known better than about 20%, the flux ratio $(\nu_\mu + \overline{\nu}_\mu)/(\nu_e + \overline{\nu}_e)$ agrees to better than 5% for various models.

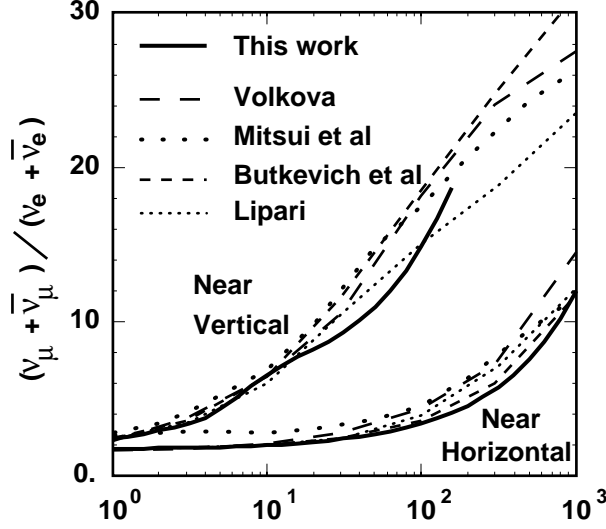


Figure 11.1: Neutrino flux ratio versus E_ν (GeV), from [2].

Polarization effects and solar activity

Polarization effects can also affect the ratio. In the pion rest frame, the decay muon is fully polarized. This is because the only other product is a neutrino(anti-neutrino) which has a fixed left(right)-handedness. In the subsequent decay of the muon, the electron neutrino is preferentially emitted in the forward direction to conserve helicity. This results in a higher energy on average for the electron neutrino than for the muon neutrino. Since the initial pions decay in flight instead of at rest, the polarization is not complete, but it is a significant effect that must be taken into account by simulations.

Low energy cosmic rays are affected by solar activity since increased solar wind tends to drive off the incident galactic cosmic rays. Models of the primary flux are done for a particular level of solar activity, usually a mid point of the solar cycle. Figure 2.1 illustrates the size of the solar modulation on the cosmic ray primary spectrum. Considering that the average 1 GeV atmospheric comes from a 20 GeV

primary parent, the solar cycle has a negligible effect on the multi-GeV neutrino sample.

Geomagnetic cutoff

The effect of the earth's magnetic field changes the spectrum of neutrinos that can be detected. The geomagnetic field tends to shield ground-based detectors from low energy cosmic rays. In order to arrive at the earth, a particle must have more than a minimum rigidity (momentum/charge). The rigidity cutoff varies as a function of the entering position on the earth and the arrival direction. Rigidity cutoff contours for the Kamioka site are shown in Figure 11.1. Units are in GV (GeV/charge) for the incident cosmic ray particle. For comparison, neutrinos of energy around 1 GeV are produced from a parent population of primary nucleons with energy about 20 GeV [51]. Only the peak in cutoff rigidity to the east has any effect on neutrino analyses above 1 GeV.

Honda [2] has examined the effect of the geomagnetic effect at the Kamioka site in detail. Figure 11.1 shows a comparison of low energy atmospheric neutrino flux simulations.¹ Above about 3 GeV the low energy calculation is spliced smoothly into a high energy calculation which neglects the geomagnetic cutoff. The difference between the dotted line and the solid line in the range between 1.3 GeV and 3 GeV gives the size of the effect. In the lower part of the range it is still significant, but is taken into account by the simulation. The geomagnetic field affects the flux of both ν_μ and ν_e in the same direction so the total effect on the ratio is still small even at 1 GeV.

The flux of atmospheric neutrinos has been calculated by a number of authors [104] [2]. These calculations agree well in shape, but have about a 20% uncertainty in

¹BGS refers to Barr, Gaisser and Stanev [104]. BN is from Bugaev and Naumov [105]. LK refers to Lee and Koh [106].

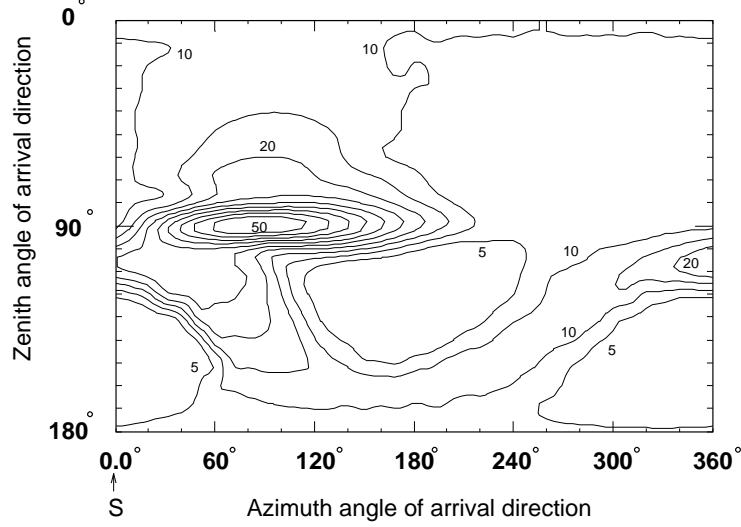


Figure 11.2: Contour map of rigidity cutoff for the ν arrival directions at Kamioka. Azimuth angles of 0° , 90° , 180° , and 270° show directions of south, east, north, and west respectively [2]

absolute flux. This comes largely from uncertainties in the primary cosmic ray flux. Typically analyses use the flux ratios $(\nu_\mu + \bar{\nu}_\mu)/(\nu_e + \bar{\nu}_e)$ in order to cancel uncertainties in the overall normalization. Such ratios are typically good to about 5% [107]. This analysis uses Honda's 1995 flux calculation which includes the geomagnetic effects for the Super-Kamiokande site and covers the energy range from 30 MeV to 1 TeV[2].

11.2 Neutrino Interactions

The atmospheric flux calculations provide the spectrum, direction, and rate of muon and electron neutrinos arriving at the Super-Kamiokande detector. Once in the detector they are allowed to interact through charged-current (CC) and neutral-current (NC) interactions with nucleons in the water tank. Neutrino-electron scattering with electrons in the water molecules is neglected. The interaction simulation is summa-

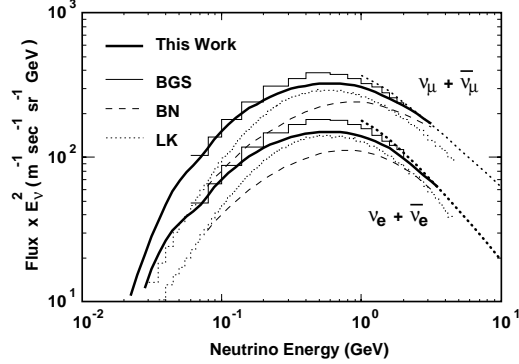


Figure 11.3: Atmospheric ν fluxes multiplied by E_ν^2 for the Kamioka site at solar mid from [2]. The dotted line is a high energy calculation without the rigidity cutoff.

rized here, details can be found in [87].

Neutrinos interact via quasi-elastic (elastic) scattering, single pion production, multiple pion production, and coherent scattering off oxygen nuclei. Each of these can occur in either a charged-current or a neutral-current mode.

Charged current quasi-elastic scattering is calculated with the standard V-A cross-section. The Fermi motion of the target nucleon is included, as is Pauli blocking for $\nu-^{16}\text{O}$ scattering. Neutral current events will only be seen if the recoil nucleon emits Cherenkov light or interacts to produce pions.

Single pion production is modeled by the Rein-Sehgal method [108] [109]. This process happens when the neutrino scattering excites a nucleon into a baryon resonance which decays with production of a pion. This process is simulated only for invariant masses under 1.4 GeV. 18 resonances under 2 GeV are simulated, $\Delta(1232)$ being the most prominent. The angular distribution from $\Delta(1232)$ production is accounted for, all other resonances are assumed to emit pions isotropically. Multiple pion production is handled by Bjorken scaling for invariant masses greater than 1.4 GeV.

The last piece involves particle interactions in ^{16}O . Neutrino scattering off the

oxygen nucleus can have a coherent interaction in which pions are produced with very little momentum transfer. This results in a sharp peak in the forward direction. The Rein-Sehgal method is again used in this simulation. Pions produced inside the oxygen nucleus can interact before they escape. Inelastic scattering, charge exchange, and absorption are taken into account.

11.3 Particle Tracking

Secondary particles are tracked through the detector using the GEANT [110] package developed at CERN. This package simulates the detector structure and manages the particles in the event. GEANT provides a convenient means of describing the structure and materials of the detector. Tracking and interactions of the particles in the different detector regions take into account the environment the particles are in. This package is very commonly used by high energy physics experiments to simulate their detectors. Hadronic interactions in the water are simulated with the CALOR package, JETSET [111] is used for high energy interactions.

Cherenkov photons are generated at each tracking step according to the formulas:

$$\cos(\theta) = 1/\beta \quad (11.1)$$

$$\frac{d^2 N}{d_x d_\nu} = \frac{2\pi\alpha}{c} \left(1 - \frac{1}{n^2\beta^2}\right) \quad (11.2)$$

Each photon is tracked until it hits a photo-multiplier tube or is absorbed. Scattering in the water is taken into account. Rayleigh scattering is dominates the light attenuation at short wavelengths. This scattering involves the interaction of photons with water molecules and has a $1/\lambda^4$ wavelength dependence. At long wavelengths, absorption becomes dominant. In addition there is scattering by particles in the water, the so-called Mie scattering, that is assumed to have no wavelength dependence. The total simulated attenuation curve agrees well with measurements made with a laser.

Photons which strike the black sheet liner of the inner detector or the reflective Tyvek liner of the outer detector are reflected or absorbed based on the measured reflectivity of the material. A tuning parameter that is often used to adjust the light tracking is an overall scaling of the Tyvek reflectivity. This can simulate a layer of dust or blocking by opaque cables.

If a photon strikes a photo-multiplier tube it generates a signal taking into account the quantum efficiency of the tube, (and of the wavelength shifter in the outer detector). The response is taken from the measured 1 p.e. distributions. For the inner detector these are taken from Ni and laser calibrations, for the outer detector they are taken from random trigger events (periodically the detector is triggered by a clock whether or not there is any activity. this is known as a NULL or Clock trigger). Random noise hits are added to improve realism.

11.4 Monte Carlo Event Summary

Ten years worth of detector live-time was simulated to determine the expected distributions of neutrino events in the Super-Kamiokande detector. Table 11.4 summarizes the number of events from various interaction types after applying the same reduction algorithms used on the data. The distributions drawn from these events are scaled by the live-time of the data to make comparison plots with the final data samples. Table 11.4 makes a similar plot for the simulated events passing the partially contained reduction criteria.

11.5 Outer Detector Monte Carlo Tuning

11.5.1 Purpose of the Simulation

The simulation of the outer detector is based on the “on-site” Monte Carlo simulation written for modeling the inner detector [112]. The important task of the outer detector simulation is to model the tracks of incoming particles. This directly affects the

Table 11.1: Fully contained multi-GeV MC sample summary

		e-like		μ -like	
$\nu_e, \bar{\nu}_e$ CC	QE	616	38.24%	2	0.10%
	non-QE	743	46.12%	9	0.45%
$\nu_\mu, \bar{\nu}_\mu$ CC	QE	15	0.93%	1093	54.14%
	non-QE	99	6.15%	907	44.92%
NC		138	8.57%	8	0.40%
Total		1611	100.0%	2019	100.00%

Table 11.2: Partially contained multi-GeV MC sample summary

		e-like		μ -like	
$\nu_e, \bar{\nu}_e$ CC	QE	-	-	7	0.28%
	non-QE	-	-	32	1.26%
$\nu_\mu, \bar{\nu}_\mu$ CC	QE	-	-	455	17.93%
	non-QE	-	-	2026	79.86%
NC		-	-	17	0.67%
Total		-	-	2537	100.00%

determination of the efficiency of the Anti Counter for rejecting these events when various fitters and reduction steps are tested on simulated data. The more closely the simulation can be made to reproduce real events in the detector, the more reliable it will be for estimating accurate efficiencies.

The author made some efforts to bring the outer detector simulation to about 10% agreement with real data. This was a necessary step to allow testing of the data reduction algorithms. The partially contained event reduction, for which the author was also partly responsible, depended the ability to simulate outer detector activity in order to estimate rejection of both background and neutrino events.

One of the main backgrounds for high energy neutrinos is incoming cosmic ray muons. The response of the outer detector was tuned by examining the hit and charge distributions for down-going vertical and horizontal through muons generated by the

simulation. These were compared to a sample of similar muons from actual data. Distributions of the total number of photoelectrons and hit tubes were checked for the top, bottom, and walls separately. Vertical muons were used for the top and bottom. For the walls, distributions for a 10 meter circle around the horizontal muon entry and exit point were examined separately.

There are several parameters built into the simulation program which allow the detector response to be tuned. Table 11.5.1 lists some common ones with their typical values.

Table 11.3: Common parameters used to tune the OD Monte Carlo Simulation

TDC Window Size	16.00 microseconds
T0 Offset	8990 nanoseconds
Dark Rate	5 kHz (parameter value)
Tyvek Reflection Ratio	0.7 (top), 0.9 (elsewhere)
PMT Collection Efficiency	22%
Wavelength Shifter Efficiency	0.7% (parameter value)
Discriminator Threshold	0.25 p.e.
PMT Dynamic Range	50 p.e.
Q Scale	3.5 nanoseconds/p.e.

11.5.2 TDC Window Size

The TDC window size parameter reflects the actual LeCroy 1877 TDC digitization window[113]. For the early data, the TDC window was set at 32 microseconds, centered on the trigger. On September 17, 1996, starting with Run 2802, this value was changed to 16 microseconds and shifted so that only 6 microseconds come after the trigger in order to solve a TDC buffer saturation problem[114]. The buffer saturation problem is described further in Section 6.2.5.

In practice the reduction algorithms use only about 500 nanoseconds around each

trigger. Simulating the entire 16 or 32 microsecond TDC window is functionally unnecessary.

11.5.3 T0 Offset

The Trigger Offset parameter determines where to place the simulated trigger in the simulated TDC window. In the real electronics the TDC window was originally adjusted so that the trigger (also called T-zero) was centered in the 32 microsecond window. After the September changes the new 16 microsecond window was adjusted so that 10 microseconds came before, and 6 microseconds came after the nominal trigger time.

For the Monte Carlo, the adjustment is made by offsetting the start of the TDC window by some fixed time. The time scale in the data has its own offset so that that the trigger actually occurs at about 1000 nanoseconds. This has to do with the generation of the trigger by the inner detector electronics. This feature is reproduced in the Monte Carlo. So, to get a total of 10 microseconds of of the Anti Counter TDC window before the trigger, it is necessary to shift the start to about -9000 nanoseconds. With the actual trigger at 1000 nanoseconds, this gives 10 microseconds before the trigger and 6 microseconds after. Again, this does not appear to correspond to the time hits arrive but rather to the TRG pulse. These numbers do correspond reasonably well to actual data.

When Monte Carlo events simulated this was were compared to data it was found that this offset was slightly off. The Monte Carlo events were consistently about 10 nanoseconds later relative to the inner detector data for both entry and exit. Figure 11.5.3 compares the time distributions near the trigger for the inner detector and the anti counter. Note that the inner detector trigger is the same, as expected. The anti-counter distribution is shifted late by about 1 bin, or 10 nanoseconds. This was corrected by changing the T0 offset by 10 nanoseconds, ending with a final value of 8990 nanoseconds.

Since the time of this tuning the trigger cabling between the inner and outer detectors was changed slightly to accommodate the new super low energy trigger. There is now a 30 nanosecond offset between the data and Monte Carlo event trigger arrival times. No adverse effect is expected from this.

11.5.4 Dark Rate

Photo-multiplier tubes at finite temperatures are not perfect two-state devices. There is always some probability that an electron can be ejected from the photo-cathode and be accelerated into the dynode structure mimicking a photon hit. Ions left on the inner surfaces from the imperfect vacuum can also find their way into the dynodes. These effects are collectively known as “dark noise”. It means that there is a uniform probability of a tube firing at any given time. The effect is well known and is combated by requiring coincidences between tubes to form triggers. It does constitute a background however and must be modeled if the expected numbers of hits are to be correct.

Y. Hayato made a short study of the Anti Counter dark noise using the NULL (Clock) triggers in the detector. These are triggers generated periodically by a clock rather than a tube hitsum. The result is that one ends up looking only at background noise rather than real events. His result was that the Monte Carlo parameter setting for dark noise should be a rate of 5 KHz per tube. This parameter does not represent the actual dark noise rate in the tubes. Instead it is used to generate hits at 5KHz which are then subjected to the discriminator threshold. Since the hits are generated with a random charge distribution based on the known response of the photo-multiplier tubes, some of the hits do not survive the threshold. About 80% do, corresponding to a real detected dark noise rate of about 3.5-4KHz per tube. This fits well with back of the envelope calculations. For many low energy events which do not enter the outer detector, there are still about 80 hits in the outer detector in a 16 microsecond window. This corresponds to about 3KHz. So the number is not

unreasonable.

For my study I looked at samples of fully contained neutrino data. “Fully contained” is a bit arbitrary as this sample could still contain events which graze the Anti Counter. To be sure I did not count those hits, I examined hits in various time windows before and well away from the trigger time. I then generated Monte Carlo events with no track in the Anti Counter, but varying dark noise rates. I compared the distributions of the numbers of hits in the various windows and found that the model with 5KHz as the Monte Carlo dark noise parameter fit the data quite well. Figure 11.5.4 shows the number of good hits counted in a 500 nanosecond and a 3 microsecond window away from the trigger. Figure 11.5.4 shows the equivalent distributions for Monte Carlo events using 5KHz for the dark noise parameter.

11.5.5 *Reflection*

A big part of any simulation of the Anti Counter has to be the treatment of light reflection from the Tyvek lining. This lining was chosen specifically for its high reflectivity in order to boost the total amount of light collected by the Anti Counter. The amount of reflection can be affected several factors. Dark cables and structure lying on the lining are not modeled separately and are treated as a reduction in the overall reflection of the Tyvek. Dirt from the diesel fumes of machinery during tank construction could not be easily cleaned. The reflectance of the Tyvek as a function of wavelength was measured by the manufacture and is listed in Table 11.4².

The Monte Carlo simulation takes this table of reflectivity versus wavelength and applies a constant scale factor to it to account for a change in the actual reflectivity. The original version allowed only one value of this scale factor for the entire detector. I changed it to allow the top, bottom and sides to be tuned separately.

One way to get a handle on the expected reflection amount is to look at the tail

²Reflectances are as listed in “tyvksg.F” in the on-site ATMPD apdetsim simulation module.

Table 11.4: Reflectance of Tyvek as a function of wavelength

300	325	350	375	400	425	450	500	550	575	600
0.691	0.710	0.839	0.879	0.888	0.895	0.899	0.897	0.894	0.893	0.892

of the time distributions for entering and exiting muons. Light collected too late to be direct, (or any light for exiting particles), must have been reflected by the Tyvek. The amount of reflection will directly affect how much light remains after successive bounces. This gives a value of the scale factor of about 0.7 for the top, and about 0.9 or more for the bottom and walls. The numbers are then adjusted further to get the total photo-electron and hit distributions more correctly aligned with data.

11.5.6 PMT Collection Efficiency

The actual collection efficiency of the photo-multiplier tube is modeled by a single number which lumps together the reflection of the glass and the quantum efficiency for a photon to eject an electron from the photo-cathode. The parameter had been set at 0.22 which roughly corresponds to about 80% transmission through the glass followed a 28% quantum efficiency averaged over wavelengths. These numbers are roughly correct. After careful study, I left the same value of 0.22.

11.5.7 Wavelength Shifter Plates

The wavelength shifter plates are sheets of acrylic doped with bis-MSB. The doping agent absorbs photons in the ultraviolet where the Cherenkov spectrum is highest and re-emits them in the green where the photo-multiplier tube sensitivity is highest. The sheet is a 60cm by 60cm square with a hole cut out of the center to accommodate the photo-multiplier tube. The effect is to increase the effective area of the tube at the cost of smearing the time resolution. Since the design of the Anti Counter relied on collection of photons over precise timing, this was an acceptable choice.

There are several different claims about what the effect of the wave-shifter plates should be. In the first Super-Kamiokande International Collaboration Meeting notes Bob Svoboda showed a simple model he was putting into an early Monte Carlo [115]. In this model he uses 100% absorption by the plate, 45% re-emission of photons inside the wave-shifter plate, and an unspecified efficiency for the interface between the plate and the photo-multiplier tube. He asserts without explanation in the notes that there is a 2.8% collection efficiency by the tube for photons incident on the wave-shifter plate. This is then multiplied by the quantum efficiency of the tube (lower near the edges of the tube) to get the overall efficiency of about 0.007. This is the value that was used in the on-site Monte Carlo and I am assuming that the choice of it came from these meeting notes.

Clark McGrew asserts a different view in his thesis [68]. In it he says that the wavelength shifter plates added 60% to the total number of photoelectrons collected by the bare tubes alone. Taking the effective areas of the photo-multiplier tube and the wavelength shifter plate into account, this suggests an overall efficiency for the plates closer to 0.023.

A third number can be found in the US Proposal for participation in the Super-Kamiokande experiment [116]. The description of the outer detector includes figures showing that the plates add 39% more photoelectrons. This would suggest an overall efficiency around 0.015.

It is clear that even given some confusion in what the number should be, the Monte Carlo is probably not modeling this effect correctly. This was not changed in this round of improvements. One reason is that the Monte Carlo already had more than enough direct photons without increasing the effectiveness of the simulated wavelength shifter plates. Doing this correctly would then mean readjusting the collection efficiency of the bare photo-multiplier tubes as well. That value was already thought to be in a reasonable range. Making all this work out really would have required a much longer time tuning and probably a much more detailed simulation

of the collection of photons in the tubes. The outer detector MC tuning is accurate enough at present that this effect is not worth pursuing.

11.5.8 Discriminator Threshold

Hits in the photo-multiplier tube are subjected to a discriminator with an adjustable threshold before being recorded in the LeCroy 1877 TDC modules. This prevents small noise fluctuations from being recorded as true hits. The same effect is modeled in the Monte Carlo. Before a hit is put into the hit list for a given event, a charge is generated for the hit based on a standard 1 photo-electron distribution. If the charge chosen is below the discriminator threshold, the hit is not recorded.

In the Super-Kamiokande Anti Counter, the discriminators are set to a threshold of 25mV in the QTC modules. What this corresponds to in terms of photoelectrons is a bit harder to extract. Most of the photo-multiplier tubes used in the Anti Counter simply do not have a one photo-electron peak. Generalizing those that do, and looking at other factors, it is expected that this threshold corresponds to about 0.5 photoelectrons. Another issue is that the gain varies quite a bit from tube to tube.

Monte Carlo samples were generated using both 0.5 p.e. and 0.25 p.e. thresholds. The higher threshold actually seemed to improve the bottom and wall distributions, but the top was best with the lower threshold. In the end I decided that the top was most important to get right since the major background comes from there. The bottom and walls are still not badly modeled with the lower threshold. In reality the higher threshold might actually be better if the issues of gain and collection efficiency were modeled more carefully. For now the choice of parameters worked as closely as it needed to and lack of further time prevented a more detailed investigation. It seems that even more careful fussing of the current parameters is probably not worthwhile anyway without doing the more careful model. The value of the threshold parameter used in the tuning was 0.25 photoelectrons.

11.5.9 PMT dynamic range

The dynamic range of the photo-multiplier tubes determines the saturation value of the tubes. At some point increasing the number of incident photoelectrons does not increase the size of the signal further. Again, this is a rough thing to model as the Anti Counter tubes are not so similar in characteristics. The Monte Carlo was using a value of 50 p.e. as the point at which the tube saturates. Examination of the maximum charge in a few tubes supported the view that this roll-off happens around 50 p.e. so the value was left as it was.

11.5.10 Q-scale

After working with the Monte Carlo for a while I discovered that the scale which relates charge to electronics counts was the same as is used in the inner detector. In the inner detector, 5.5 counts corresponds to 1 photo-electron. In the outer detector, the charge is latched into the TDC modules by the QTC modules. For those, 7 TDC counts or 3.5 nanoseconds corresponds roughly to 1 photo-electron. At the point of the data stream where this conversion takes place, the charge is reported in nanoseconds as the time over threshold. So the 3.5 ns/p.e. value should be used. It turned out that this 36% decrease in the scale was almost precisely what was needed to account for a discrepancy in the total number of photoelectrons for all parts of the detector. With the change to the correct value, both photoelectrons and hits could be made to come to much closer agreement.

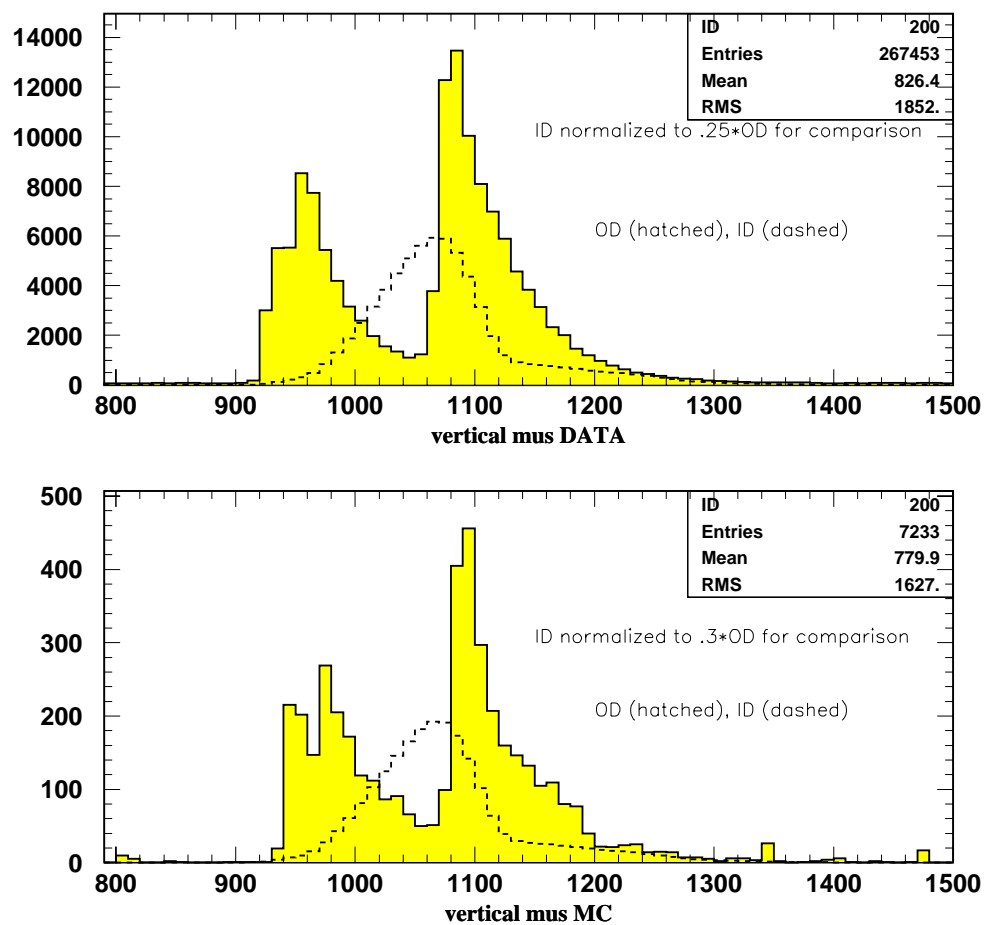


Figure 11.4: Time distributions

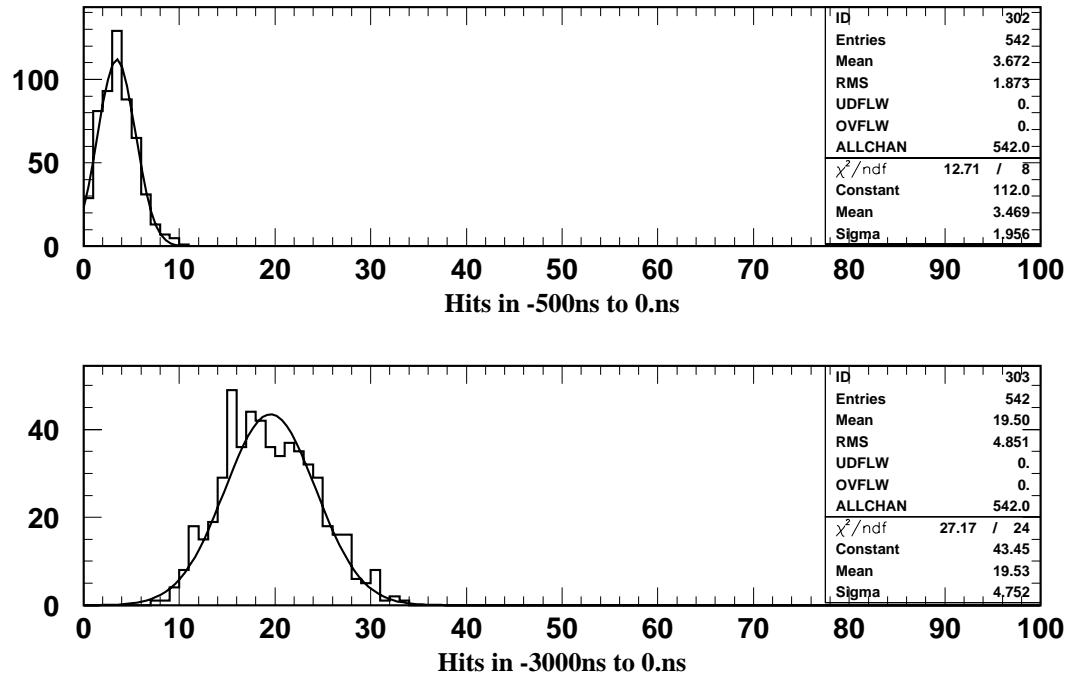


Figure 11.5: Good hit distributions for data

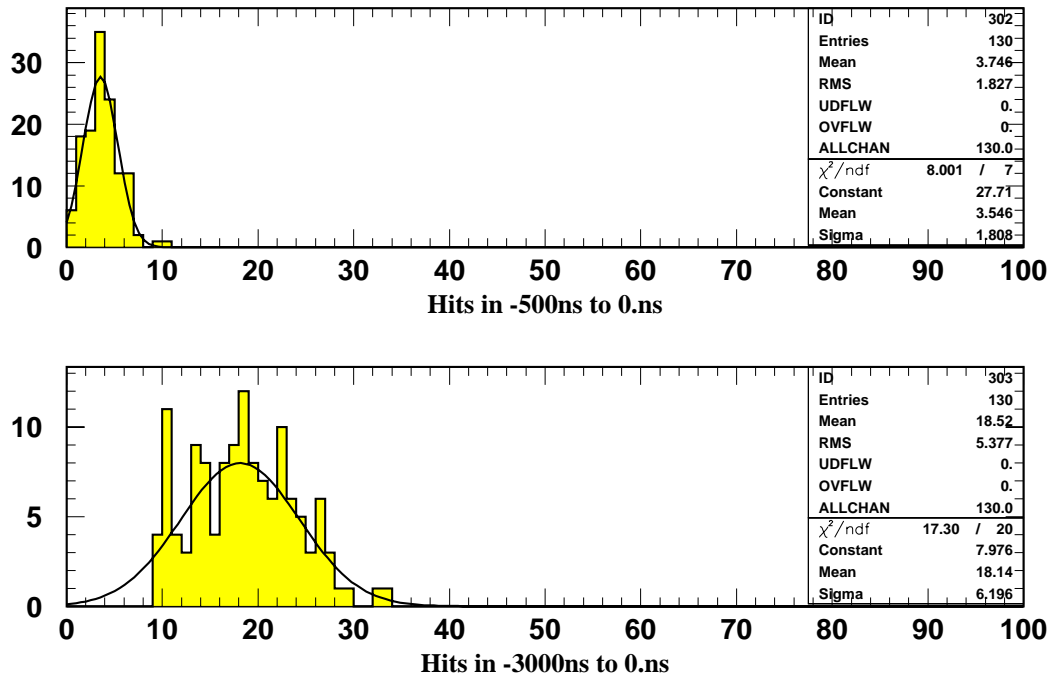


Figure 11.6: Good hit distributions for Monte Carlo and 5kHz dark noise

Chapter 12

EVENT SELECTION

The Super-Kamiokande experiment has been operating nearly continuously since it was commissioned in April 1996. A little less than 10% of the live-time on average goes to detector down time, including maintenance of electronics and detector studies and calibrations. These data never reach the analysis chains. Of the roughly 800,000 events above 5.5 MeV recorded every day, only about 14,000 are considered useful for a high energy analysis. The majority of the rejected events are low energy background events such as radon chain decays, entering gamma rays from the rock, spallation products from stopping cosmic ray muons, and a few solar neutrinos.

12.1 Initial Sample

The initial sample of high energy data are defined by first selecting only “normal” data taking runs and then removing low energy events. The sample is further refined by removing periods calibration (pedestal) events and making loose cuts on cosmic ray muon contamination. Using only “normal” runs rejects periods of detector studies or known electronics abnormalities. Occasionally the detector is run during repairs on one component to provide at least partial coverage in case of a supernova. The very low energy events are rejected by requiring more than 1000 photoelectrons in the inner detector. This corresponds to a threshold of roughly 120 MeV. Table 12.1 lists the major criteria used to further refine the initial data sample.

Table 12.1: Initial sample criteria

Remove pedestal events
Merge sub-events within 30 μ s
Remove events with no anti-counter data
Total ID charge must be > 1000 p.e. (120 MeV)
Impose 100 μ s dead-time for μ -decay rejection
OD TDC sliding window cut
OD cluster cuts, ≤ 1 OD cluster allowed

Pedestal Events

“Pedestal events” are taken every hour to provide a running calibration of the front end digitizing electronics. One by one, each online workstation (controlling one-eighth of the detector), is told to switch off the signal inputs to its digitizers and record data with open channels for 100 triggers. This records the base value of the digitizer, or the “pedestal”. The pedestal can be different for each channel due to vagaries of the board construction and layout. It must be subtracted from any measurement made by that channel in order to retrieve the true signal size. Periodic measurements are important since the pedestals can be affected by small temperature changes in the ambient environment. Super-Kamiokande’s extensive air-conditioning systems and deep location provide substantial thermal inertia so the pedestal changes are usually small and easily compensated. Pedestal events are tagged in the data record and easily filtered by the analysis streams.

Cosmic ray muons

Muon decays are a concern when attempting to distinguish electrons and muons. Stopping cosmic ray muons can decay to an electron and two neutrinos. If the muon drops below Cherenkov threshold while still in the tank it is possible that the decay

will not happen immediately after the last recorded light from the muon track. There is little directional or positional information to tie the electron to the previous muon so the decay electron could easily be taken as a separate electron neutrino interaction. To combat this problem, if an event is selected (it passes the first reduction step) then all subsequent events within 30 microseconds are recorded and merged into the original data record as “sub-events”. This time corresponds to roughly 15 muon lifetimes. Virtually all decays should occur in that time.

To further combat the chance that muon decays might skew the muon to electron ratio, a software imposed dead-time of 100 microseconds is imposed between primary triggers. This cut also conveniently makes any concern about the effect of outer detector dead-time moot as the maximum OD dead-time is less than this analysis imposed cut. The dead-time corresponds to about 45 muon lifetimes.

No outer detector data

About 5 percent of all data have no anti-counter photo-multiplier tube information. This happens because the outer detector TDC modules are dead during readout. This dead-time can range from 2 to 78 microseconds long depending on the number of hits recorded. During this time, triggers are vetoed to the OD TDC modules. The event number and trigger time are still latched by the OD central hut VME crate but there will be no data from photo-multiplier tubes to go with the event. Virtually all of the triggers arriving during this period are due to “ringing” effects and after-pulsing of the photo-multiplier tubes.

During the early stages of the detector operation the outer detector had some problems that kept it from functioning continuously. Hardware problems in the FASTBUS crates and software problems in the online data acquisition code kept some events from being matched up with data from all five electronics huts. Data which could not be completely matched were considered unreliable and thrown away. This meant that there were periods (as well as isolated events) in which there was no outer detector

data available for the events. In some cases a header was provided, in some cases there was no information whatsoever from the outer detector. Many hardware improvements and code fixes improved the situation and the detector was operating fairly smoothly by the time the water clarity stabilized in June 1996. Data without outer detector information were treated as detector dead-time.

Low energy events

By far the largest fraction of triggers in Super-Kamiokande comes from low energy events (5-100 MeV). These are largely due to radioactive decay of radon products in the water, entering gamma rays from radioactive decays in the surrounding rock, and spallation of nuclei by cosmic ray muons. Nearly all of these processes are limited in energy to a few tens of MeV. Furthermore, the effect of the geomagnetic field tends to sweep away cosmic rays lower than a few hundred MeV before they can interact in the atmosphere and produce neutrinos. For atmospheric neutrino analysis, events with less than 1000 p.e. (120 MeV) in the inner detector are rejected.

Junk events

Several types of junk noise events can be found in the raw data. Ringing and after-pulsing can produce secondary events after an especially energetic muon passes through. Another common problem comes from cross-talk in the photo-multiplier tube cables. Each photo-multiplier tube is connected to the front end electronics by a 70 meter watertight but unshielded cable. Most of the length is in water which provides plenty of shielding. At the top of the detector the cables are laid into trays and bundled together to the nearest electronics hut. At this point large pulses on one cable may induce a signal in an adjacent cable. The effect on an event display is large rectangular regions of hits with little total charge.

Through-going muons

Much of the remaining sample consists of through-going particles. A cut to reject some of these long-track events is made by histogramming the outer detector hit times for each event [117]. The beginning and end of the distribution is determined by sliding a 100 nanosecond window across the hit times and looking for more and then less than 15 hits in the window. The event is rejected if the difference between leading and trailing edges is greater than 240 nanoseconds. The light crossing time of the detector is about 210 nanoseconds on a long diagonal. A particle punching through the outer detector in two separated places might be expected to have entry and exit points widely separated in time while a fully contained particle or one penetrating the outer detector at only one point will have a shorter time distribution for outer detector hits. Stopping muons entering at only one point pass this cut as easily as exiting neutrino products.

The attack on through-going particles is refined with a fast nearest neighbor charge clustering algorithm. Clusters are defined by eliminating isolated hits and grouping remaining hits around the highest charge neighboring photo-multiplier tube. Hit tubes are required to have at least 3 hit neighbors to be part of a cluster. The completed cluster must contain at least 8 hit tubes to remain in consideration. Clusters whose charge density peaks within 8 meters of that of another cluster are removed. This cut is intended to find somewhat widely separated clusters that would indicate through-going muon events. Events with 2 or more remaining clusters after all this are rejected.

12.2 Fully Contained Neutrino Data Reduction

Fully contained events are the “golden” sample of neutrino events from the detector. These are events in which the neutrino interaction occurs within the fiducial volume of the detector and all of the interaction products also stop inside the fiducial volume. Essentially all of the neutrino energy is deposited in the inner detector. These events

tend to be lower in energy. The track length limitation places an absolute maximum of about 21m, or about 8.5 GeV, depending on the track geometry. The actual mean energy of the fully contained events is around 800 MeV. Since the neutrino energy spectrum drops steeply with energy, the fully contained sample also comprises the bulk of the neutrino events detected. In Super-Kamiokande there are about 15 fully contained events for each partially contained event. The utility of the fully contained sample lies both in its large statistical weight and in our ability to well determine the total energy of the primary particle. A disadvantage is that at these energies the initial neutrino direction is not so well known, due both to scattering considerations and the workings of the interaction.

12.2.1 FC 1st Reduction

The fully contained event first reduction contains the initial cuts to define the standard data sample by rejection of bad runs, pedestal events, and low energy events. These initial cuts are needed to reduce the total amount of raw triggers quickly to a rate which can be processed easily by the more sophisticated analysis programs.

The additional function of the first reduction is to further refine the data sample by eliminating events with activity in the anti counter. By definition, a fully contained event should have no component entering or exiting the detector. As a fast first cut on anti counter activity, events with more than 50 hits in the anti counter are also rejected. The data are reduced to about 4000 events per day.

12.2.2 FC 2nd reduction

Once the valid runs are cleanly defined by the first reduction, the second reduction makes the first cut on possible fully contained neutrino candidates.

First, the outer detector activity cut is tightened to a maximum of 25 hits. Of these, no more than 10 are allowed in a spatial cluster. The cluster is the same nearest neighbor clustering used in the initial sample definition. The cut is made loosely at

first to allow the initial sample to be used for both fully and partially contained events. Once that was done, the additional constraints for fully contained events may be applied.

Further cuts are made to remove spurious events, such as from flashing photo-multiplier tubes. One such cut is to reject events for which more than 0.5 of the total charge in the event occurs in a single tube. Such high charge concentrated in a small area is quite unusual for light from a Cherenkov cone. It is a good indicator that the event is not valid. This reduction reduces the total sample to about 500 per day.

12.2.3 FC 3rd reduction

The final stage removes remaining background and irregular events. If an event has exactly zero hits in the entire 16 μ second outer detector TDC window, the event is rejected. We cannot assume an event did not enter the detector from the outside if the outer detector information is not present. One can estimate the effect of this cut on the final neutrino sample. After all, no activity in the outer detector is the defining characteristic of a neutrino event. In practice, the outer detector photo-multiplier tubes have a dark noise rate of 5kHz. For the 1885 tubes, one expects a total hit rate of about 9.4MHz from the detector. This corresponds to one hit every 106 nanoseconds on average. On average, 160 hits are expected from dark noise in this window. Poisson statistics shows the probability of finding exactly zero hits in 16 μ seconds will be so small that there is little worry of rejecting true neutrino events with a properly working anti-counter.

$$P\left(x = 0; \mu = \frac{1600ns}{106ns}\right) = \frac{\mu^x}{x!} e^{-\mu} \approx 3 \times 10^{-7} \quad (12.1)$$

Other tests check for entering muons. There are several classifications of entering muons. The hard muon check looks for events with more than 8 sub-events (events following within 30 μ seconds. Events of this type are known to have saturated the

outer detector electronics before upgrades eliminated this possibility in October 1996. Events in the outer detector are stored in a pipelined TDC capable of latching up to 16 edges (8 hits) in a single digitization window. The length of the window was set to 32 μ seconds in early running. If an OD channel received more than 8 hits it would keep only the most recent 8. Early hits were lost from the pipeline, leaving “holes” in the hottest parts of these big events. The length of the TDC window was shortened to 16 μ seconds. This made it nearly impossible for the trigger electronics with its 800 nanosecond veto to saturate the TDC channels. A less stringent muon fitter is applied if the event has a large total charge and a saturated photo-multiplier tube at the entrance point. A stopping muon fitter searches for hot entrance points consistent with a shorter track muon in the detector.

Remaining low energy events are often difficult to distinguish from flashers. In practice neither is desirable, but they are handled separately. If the total number of inner detector hits is less than 500, a low energy event fitter is applied. If the fit succeeds and the timing is extremely short, the event is rejected as very low energy.

Several flasher cuts eliminate the various ways these events can show themselves. The simplest histogram hits in 100 nanosecond windows around the trigger. The idea is that many flashers exhibit a rather continuous time distribution so if the minimum number of hits in any window around the trigger is greater than 15 (10 if inner charge > 800 p.e.), the event is called a flasher. Other cuts remove flashers discovered in routine monitoring of hitmaps or reduction output. These flashers are identified by repeated appearances of nearly identical events and are removed by using specific features such as the charge profile and cable numbers involved. These cuts are also used in the third partially contained reduction described in section 12.3.3.

12.2.4 Final Sample Selection

The remaining sample is about 30 events per day. These events are hand scanned by two independent scanners to identify remaining background, usually flashers. Scan-

ners guide fitting algorithms and other tools to check on the data quality. A final scanner arbitrates the result and makes the actual cut to about 16 events per day.

Vertices and directions are reconstructed with an automated fitting algorithm. Once rings are identified, a particle identification program is applied to each ring and the vertex reconstruction is repeated correcting for track information.

The final step is to cut out events interacting outside the fiducial volume defined to be 2 meters from the inner detector walls. This leaves about 8.4 per day, or 3,462 events for the 414 day exposure.

12.3 Partially Contained Event Reduction

Partially contained neutrino events are those which interact inside the detector fiducial volume, but whose interaction products escape the detector. These tend to be higher energy events, but only a lower limit on the energy can be established as the products carry an unknown amount of energy away with them. As the energy increases the sample becomes almost purely muon-like. These events can be used as a rather sensitive probe of oscillations at higher energies than could ever be achieved with the fully contained events.

The size of the detector and the exponential drop of the atmospheric neutrino flux with energy conspire to give very few partially contained events. Less than 1 per day is expected. This is in stark contrast to the situation in the older Kamiokande experiment where a large fraction of events exited the detector. The large size of Super-Kamiokande means that much higher energy events will be fully contained.

The data reduction is literally a search for one event in a million. The job is done with 5 distinct data processing stages, or “reductions”, with a final check by human scanners. The partially contained reduction stream is actually designed to filter both fully and partially contained events as an extra check on both analyses. Partially contained events are separated from the sample only at the very end. The author

shared responsibility for the creation of the partially contained reduction stream with Larry Wai. Processing of PC data was done by the author.

12.3.1 1st PC Reduction

The first partially contained event reduction consists only of the initial sample cuts already described in section 12.1. Unlike the fully contained reduction, no tight cuts can be made on total outer hits since the type of event being sought is required to produce hits in the outer detector. Use of the outer detector as a veto shield must be done in a much more subtle manner. Without this additional constraint, the output of the first PC reduction is around 14,000 events per day, nearly 3.5 times as large as the corresponding fully contained reduction stage.

12.3.2 2nd PC Reduction

The second partially contained data reduction step involves a charge-gradient clustering algorithm written by Larry Wai [117]. It also brings inner detector information into play and requires correlation between inner and out hit clusters. The intention is to reject stopping muons by geometrical arguments and further reduce remaining stopping muons. Table 12.3.2 lists the criteria used to accomplish this task.

The charge-gradient technique works by binning the detector into angular bins and looking to see how much charge lands in each bin. Clusters are formed by examining the charge gradients between bins. The bin sizes are roughly 5 meters by 5 meters for the inner detector and roughly 10 meters by 10 meters in the outer detector.

Table 12.2: 2nd PC reduction criteria

Require ≤ 1 OD cluster
OD cluster must not wrap around corners
If there is an OD cluster, require a nearby ID cluster

The first criterion repeats the earlier requirement that the outer detector have a maximum of one cluster. Now the cluster finding method is much finer. Repeating this cut removes additional through-going muons whose exit clusters may have been too weak to be rejected by the earlier nearest neighbor technique. Since the charge-gradient technique may find additional clusters, the exact cut is a requirement of less than 7 hits for the outer detector cluster with the second highest charge. This ensures that there is minimal activity outside the main cluster.

Comparing the charge in a cluster that lands on the top or bottom is a way of eliminating corner clipping muons. An incoming particle can cross near enough to the edge that the outer detector entry and exit clusters can merge together. An exiting particle will leave only an exit cluster on either the top, bottom, or wall, but not more than one except for light which has leaked around the corner. Particles aimed exactly at the corner might be cut, but such a case is very rare. It has been suggested that lightproof, reflective material such as the DuPont Tyvek be placed around the top and bottom anti-regions to isolate the top, bottom, and wall sections. This would make the corner clipping cuts even more efficient. If the collaboration agreed, such a change could be made during planned maintenance upgrades in the next year or two.

The ID cluster requirement is a way of looking at the geometry of the event. If the highest charge outer detector cluster is an exit cluster, as for partially contained events, then there should be a relatively high charge inner exit cluster nearby. If the outer cluster is really an entrance, the inner entrance cluster may not be so pronounced if it exists at all. The cut is made by requiring more than 1000 p.e. in the inner detector within 200 centimeters of the highest charge OD photo-multiplier tube. If there are less than 7 hits in the OD cluster this cut is not applied so that the fully contained events can be preserved in this analysis stream.

Of the 14,000 events per day which pass the 1st reduction, about 2000 events per day survive the 2nd reduction.

12.3.3 3rd PC Reduction

After passing through the first two stages of data reduction, the data have been cut down to roughly 2000 events per day. This was considered low enough to be able to run an automatic fitting algorithm. For historical reasons a flasher algorithm was inserted here as well. Table 12.3.3 lists the criteria for this stage of processing.

Table 12.3: 3rd PC reduction criteria

Test for flasher events
No OD cluster near projected entrance

One source of spurious events is flashing photo-multiplier tubes. One failure mode is for the high voltage electrodes in the dynode chain to discharge with a spark. The light from the photo-multiplier tube exits the front of the tube, knocking electrons off of the photo-cathode and generating a real hit pulse. Escaping light can be collected in nearby tubes. Enough light can be generated to trigger the detector. With the brightest flashes the entire detector can light up. Often one can see the shadows of the dynodes in the detector hit pattern. This can happen repeatedly at high rates and the detector operation must be suspended until the offending tubes are disconnected. Flasher events can also occur at fairly low light levels, repeating only occasionally. These are the hardest to find.

Flashers do tend to have some common characteristics which are used to reject them. First, they tend to repeat. Detector hitmaps are monitored for cables that are hit unusually often. Second, flashers tend to have fairly long time distributions compared to Cherenkov light. Finally,, since the light is coming isotropically from a point source it will not fit well to a track/cone hypothesis. Point fits will find a vertex at the wall so if the flasher has not been removed by any other means it will eventually fall far outside the fiducial volume.

The flasher test is written by T. Hayakawa ¹. This routine looks at hits within a 500 nanosecond window after the trigger time (1200 to 1700 nanoseconds, the trigger is at roughly 1000 nanoseconds). The minimum number of hits in a sliding 100 nanosecond window from 1200 to 1700 nanoseconds is determined. If this minimum number is greater than 15, (or greater than 10 if the total inner charge is under 800 photoelectrons), then the event is rejected as a flasher. The idea is that flasher events tend to have rather long time distributions. Since the light crossing time of the detector is about 210 nanoseconds maximum, looking at hits beyond this is a way of separating flashers.

The main cut in the third reduction step uses a point fitter to locate a vertex and then finds a charge weighted direction for the event. The direction is then projected back into the anti-counter where an entering particle would have entered if this had been an entering event. If there are more than 10 hits within 8 meters of the projected entrance then the event is rejected. A danger comes near the walls where the fit direction can be reversed and projecting back finds the actual exit cluster. This results in low efficiency very near the walls. About 100 events per day survive the third reduction.

12.3.4 Used Run Cuts for PC Reduction

Not every run is completely perfect. Sometimes trouble starting the detector leads to short “junk runs”. Occasionally a photo-multiplier tube will “flash” sporadically. Sometimes a high voltage crate will trip off and data continue to be taken while the shift operators work to identify and get the run stopped or the problem fixed. Whatever the reason, there are some portions of some runs in which the detector is not operating at peak performance. Nearly all of these cases are known and logged. Even though the cause is determined, there is no reason to throw away an entire day’s

¹sukai:/home/atmpd/src/reduc/pat3rd/flash_test.F

data because of a known short glitch. This is why we have run or sub-run cuts. Data leaving the detector are grouped in blocks of approximately 10 minutes worth of data called “subruns”. This is the smallest block that can easily be removed from the data set due to a known detector irregularity.

The bad run cuts are made on the basis of the analysis reduction steps. After the major data reduction is complete in both the fully contained and partially contained streams, the reduction logs are examined for irregularities. Any sub-run which yields an excess of event candidates is rejected. For the partially contained stream, any sub-run yielding 10 or more candidates after the 3rd reduction is rejected. This cuts about 0.2% of the live-time. In addition, the used run cuts from the fully contained analysis are also applied. In practice the partially contained cuts are almost completely contained in the fully contained analysis cuts. Only a few events are removed on the basis of the partially contained reduction alone and these are nearly always in subruns adjacent to groups already cut.

12.3.5 4th PC Reduction

The fourth reduction is an attempt to cut those events which pass the 3rd reduction due to inefficiency in the outer detector. It uses the inner detector to refine the criteria used in the 3rd reduction. Entering events may pass the 3rd reduction even when the rough direction fit is accurate if the outer cluster is weakened. This can happen from known insensitivities due to cable bundles, support structure, low photo-multiplier tube coverage in corners, and dead photo-multiplier tubes. Some corner clipping muons also remain due to the reversal of the fit direction near the walls. The 4th reduction uses the inner detector as an additional veto counter. Table 12.3.5 summarizes the criteria that do this.

The earliest photo-multiplier tube in the inner detector is determined by sliding a window in time across the inner hits. The first tube for which the sliding window contains several hits is defined as the “early” or “entrance” tube. If the projected

Table 12.4: 4th PC reduction criteria

Early ID hits must be away from projected entrance
Apply long track muon fitter
Require the vertex to be away from the corner

entrance point based on the charge-weighted direction is close to the “entrance” tube, the event is rejected.

Now that the sample has been reduced there is time to run a long track muon fitter. This serves to reject remaining muons with weak or non-existent outer detector clusters. Some of these still have survived the above cuts because the rough direction fit is not accurate enough.

12.3.6 5th PC Reduction and Final Sample Selection

After the 4th reduction the data rate is down to 20 events per day. It is now feasible to run a precise but time consuming fitting algorithm on the data. This algorithm, developed by K. Ishihara, makes a true track fit to the inner detector hits. Vertex position, track direction, Cherenkov angle and track length are all varied to minimize the timing and charge residuals for the fit.

With the precise fit in hand, the search for a back-extrapolated entrance cluster is repeated. The new fit completely eliminates the remaining peak near the walls from poor direction reconstruction in the charge-weighted rough fit.

Only 2 events remain in the sample after the 5th reduction. A final check of the sample is made by human scanners. As in the fully contained event analysis, two independent scanners examine the events and tag background. Essentially all remaining contamination is now entering events which fit very near the walls. These must have very weak outer detector clusters to have survived this far. A final scanner arbitrates the identification of the first scanners and reduces the candidates to 0.8

per day in the full detector volume. Virtually all of the rejected events are already outside the inner fiducial volume to be used for analysis.

A final cut on the fiducial volume (2 meters from the nearest inner detector wall) reduces the finished sample to 0.6 events per day.

Chapter 13

DATA SUMMARY

The final sample of atmospheric neutrino events contains 394 fully contained and 230 partially contained events in the fiducial volume. Table 13.1 shows the breakdown of these events as electron-like or muon-like. Partially contained events are assumed to be entirely muon-like.

Table 13.1: Event summary. MC expectations are scaled to 33.0 kton-yrs.

	e-like		μ -like	
	Data	MC	Data	MC
FC	290	236	230	296
	-	-	301	372

It is important to study the sample to be certain that it is pure and free of background contamination. If background cannot be avoided, then it is at least necessary to determine where the background is coming in and in what regions of the detector it will most affect the results.

13.1 Flavor Double Ratio

The flavor double ratio $R=(\mu/e)_{DATA}/(\mu/e)_{MC}$ can be immediately read off from Table 13.1. Taking the partially contained and fully contained muons together, the result is:

$$R = 0.65 \pm 0.05(\text{stat.}) \pm 0.07(\text{syst.}) \quad (13.1)$$

The statistical errors are determined from the number of events according to:

$$\frac{\sigma_{stat.}}{R} = \sqrt{\frac{1}{N_e(Data)} + \frac{1}{N_\mu(Data)} + \frac{L_{DATA}}{L_{MC}} \left(\frac{1}{N_e(MC)} + \frac{1}{N_\mu(MC)} \right)} \quad (13.2)$$

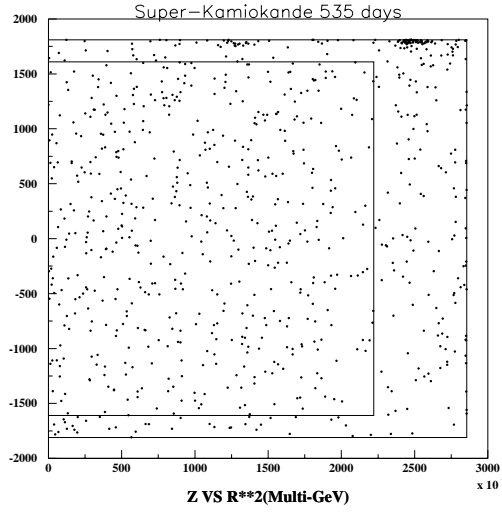
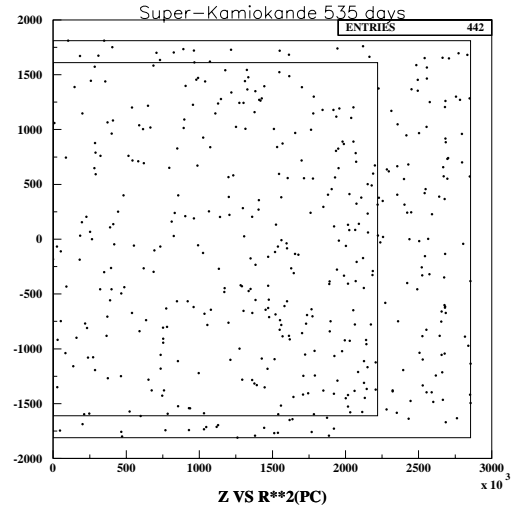
L_{DATA} and L_{MC} are the exposures of the data and Monte Carlo samples, 33.0 kton-yrs and 225.0 kton-yrs, respectively. The total systematic error is estimated in Section 13.5.

13.2 Vertex Distributions

One important check on the integrity of the data is the distribution of event vertices. Neutrinos are equally likely to interact anywhere in the tank. If there is an excess of events in one section of the detector, especially near the walls, this could be a sign of contamination from non-neutrino events. Statistical and data selection effects can cause the distributions to not be flat but the data should correspond to the simulated events which have passed through the same filtering process.

A common way to plot the event vertices is to project them onto the R-Z coordinate plane. Typically, the vertical coordinate is plotted against the square of the radial coordinate to preserve the usual sense of directions in the tank, and to keep the expected distribution uniform. Figures 13.1 and 13.2 give these distributions for the fully contained multi-GeV sample and for the partially contained events, respectively. Some remaining entering muon background excess exists near the top of the tank in the fully contained sample, but this is removed by the fiducial volume cut. The partially contained distribution does not display an obvious excess in this region.

Figures 13.3 and 13.4 show the distribution of vertices as a function of vertical height in the detector. Data for these plots are taken only from a cylindrical region with radius 14.9 meters (i.e., the wall fiducial cut), and the full height of the detector. This helps to separate the radial and vertical contributions. A simple K-S test

Figure 13.1: Z vs. R^2 (FC)Figure 13.2: Z vs. R^2 (PC)

results in a 17% (83%) probability that the FC (PC) data came from the same parent distribution as the corresponding Monte Carlo sample for events inside the fiducial volume.

The arrows show the fiducial volume cut in the vertical direction. The histogram represents 10 years of Monte Carlo simulation filtered through the same data reduction algorithms and scaled to the same live-time as the data. Figures 13.5 and 13.6 separate the fully contained sample into e-like and μ -like events. Partially contained events are assumed to be mu-like. The K-S test comparing the data to the Monte Carlo inside the fiducial volume yields a 47% probability for the electron-like events, and 38% for the muon-like events.

Figures 13.7 and 13.8 give the vertex distribution as a function of the square of the radial coordinate. The radial distribution is typically plotted this way so that the bins contain equal volume and the expected distribution should be flat. In practice, the multi-GeV sample is of high enough energy that one can see the edge effects where tracks move out of the fully contained sample into the partially contained events.

It is also interesting to look at the radial distribution of events on a linear scale. In

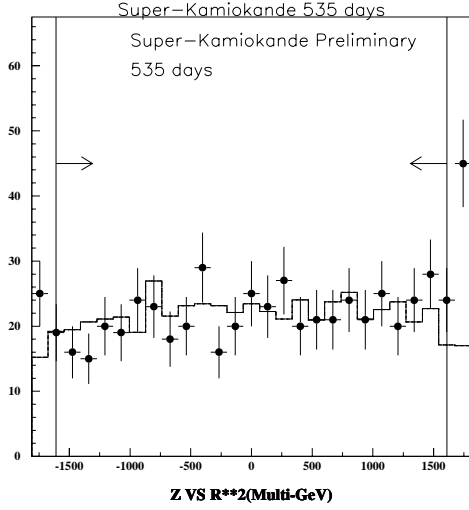


Figure 13.3: Z Distribution (FC)

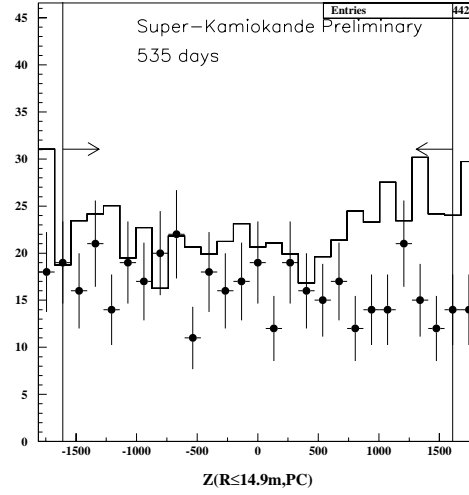


Figure 13.4: Z Distribution (PC)

this case the volume of water in each bin increases toward the outside so the expected distribution is not flat. However, if anomalies are present it is much easier to read off the location in the tank where they are happening. Figures 13.9 and 13.10 show the vertex distributions as a function of the radial coordinate for the fully contained multi-GeV sample and for the partially contained events.

The e-like and mu-like events are broken out for the fully contained sample in Figures 13.11 and 13.12. Aside from the previously noted excess of entering muons outside the fiducial volume, no particular problems are evident for either the electrons or the muons.

Figure 13.10 shows a clear excess of partially contained events near the edge of the fiducial volume. This is of some concern as it may indicate contamination from entering cosmic ray muons. Such a case would affect the overall ν_μ to ν_e ratio in this part of the detector. The efficiency of the data filtering routines would have to be improved to remove these events.

The K-S test was run for the radial distributions as well. Inside the fiducial volume, the fully contained events had a 94% probability for having the same radial

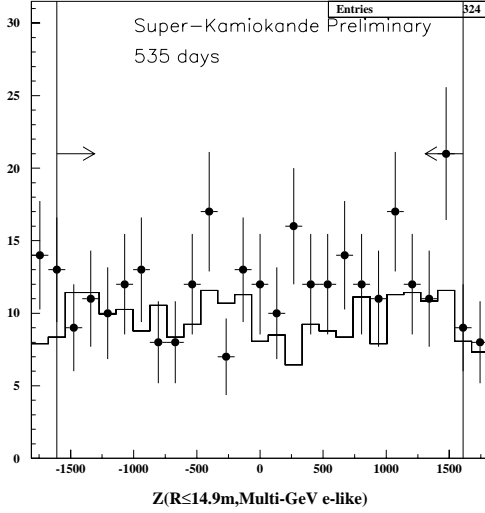


Figure 13.5: Z Distribution (FC e-like)

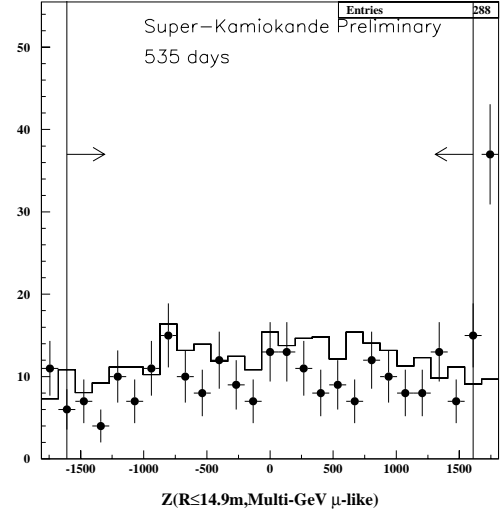


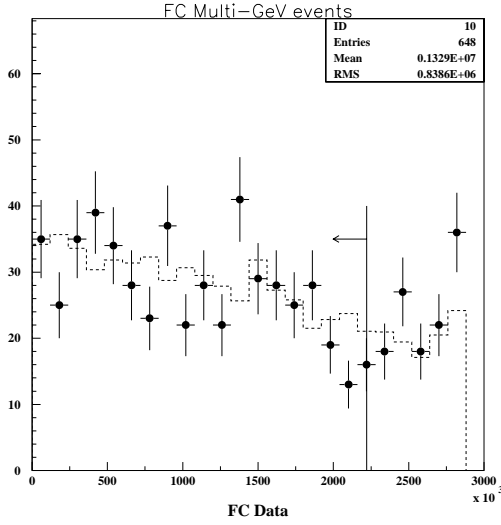
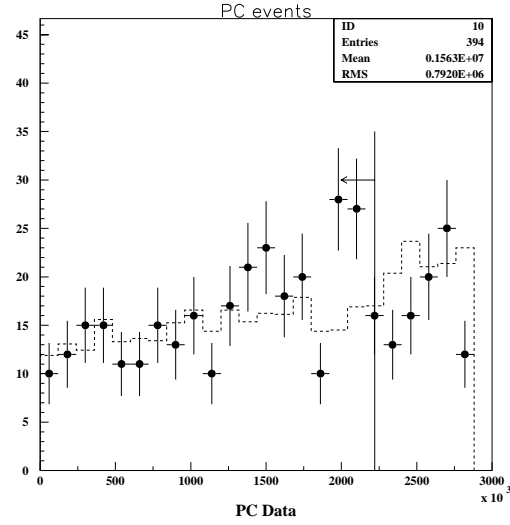
Figure 13.6: Z Distribution (FC mu-like)

distribution as the simulation. Probabilities for e-like and μ -like were also high; 88% and 79% respectively.

The radial distribution for the partially contained events does not give a good K-S probability when compared to expectations. The value is only 5%. This has a lot to do with the excess of events near the edge of the fiducial volume in the partially contained sample noted earlier. If the fiducial volume is reduced to a region 5 meters from any wall, the K-S probability for the partially contained radial distribution increases to 80%.

Figures 13.13 and 13.14 divide the data into “ingoing” and “outgoing” tracks. This division is not exact. “Outgoing” tracks are defined such that the dot product of the track direction and the position vector is positive. (The origin of position is at the center of the tank.) The excess is clearly only in the “outgoing” tracks.

As one might expect from looking at the histograms, the K-S probability for the outgoing events is only 13% while the ingoing events have a nearly 50% probability of being drawn from the same distribution as the Monte Carlo. If the fiducial volume

Figure 13.7: R^2 Distribution (FC)Figure 13.8: R^2 Distribution (PC)

cut is increased to 5 meters from the wall, these numbers jump to 90% and 86% for outgoing and ingoing distributions. This confirms that while there does appear to be some contamination problem, it is restricted to a region near the edge of the fiducial volume.

13.3 Event Properties

Number of Rings

Another useful check of the data sample is the number of rings. This helps to verify the ring finding algorithms as well as the Monte Carlo simulation of the physics. Barring inefficiencies in detecting particles, the number of rings should correspond to the number of charged particles in the interaction and hence point to the underlying physics. Figure 13.15 compares the number of rings found to the simulation for the fully-contained (FC) sample. Only data with interaction vertices inside the fiducial volume are included. The partially contained sample does not use ring counting as a selection criteria.

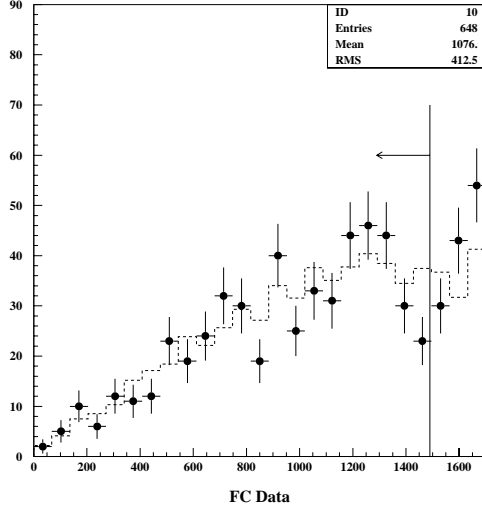


Figure 13.9: Radial Distribution (FC)

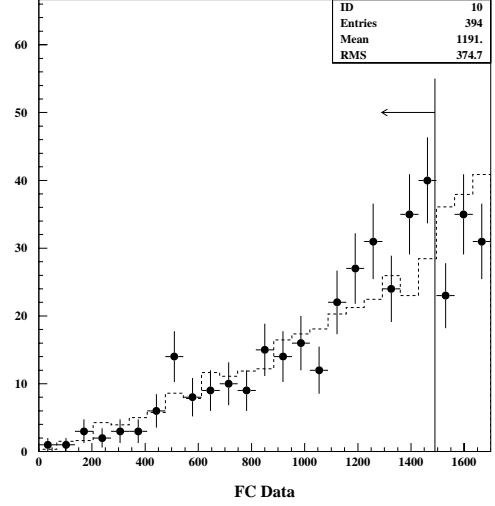


Figure 13.10: Radial Distribution (PC)

Figures 13.16 and 13.17 show the e-like and mu-like fully contained data separately. The distribution of ring numbers found in the data matches the simulation well for both electron and muon events. This lends confidence that the ring finding technique is robust and that the simulation is reproducing the necessary physics.

Visible Energy

The visible energy is an estimate of the energy of the neutrino based on the total amount of Cherenkov radiation collected in the detector. For partially-contained events this is only a lower bound on the total energy of the neutrino since the escaping particles carry some energy out of the detector. Figures 13.18 and 13.19 compare the visible energy from events in the data to the simulation.

Particle Identification

For the fully contained data, a particle identification algorithm is applied to the single ring events. Figure 13.20 shows the distribution of the likelihood parameter compared

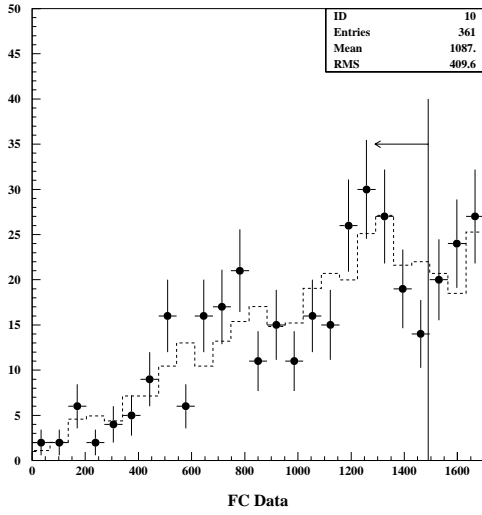


Figure 13.11: Radial Distribution (FC e-like)

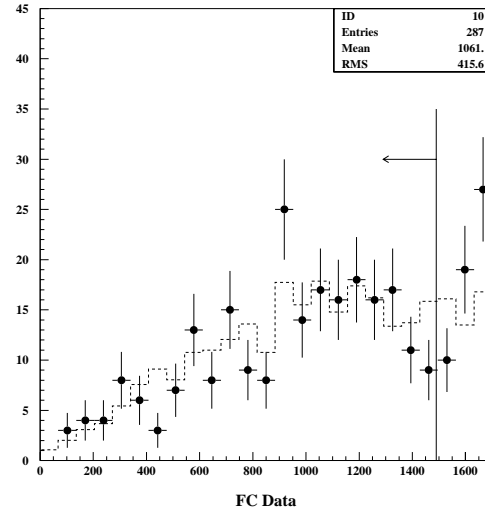


Figure 13.12: Radial Distribution (FC mu-like)

to simulation for the “Multi-GeV” sample. Partially-contained events are assumed to be all muons. Simulations of the partially-contained tracks show less than 2% of the sample are electrons (see Table 11.4).

Momentum

The momentum of the detected particles can also be calculated and can often be a better measure of the particle’s energy. This result depends on the PID algorithm to first identify the particle, then the momentum is calculated from the visible energy and cone angle, taking into account the light scattering effects. Figures 13.21 and 13.22 give the momentum distribution for e-like and μ -like multi-GeV events.

13.4 Zenith Angle Distributions

One of the most important results of the Super-Kamiokande atmospheric neutrino analysis is a study of the zenith angle dependence of the zenith angle distributions.

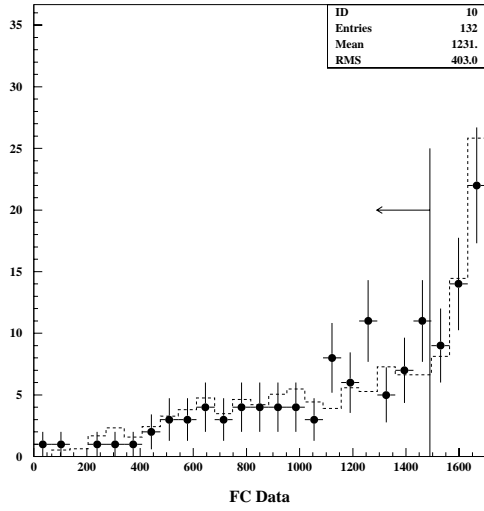


Figure 13.13: Radial Distribution (PC ingoing)

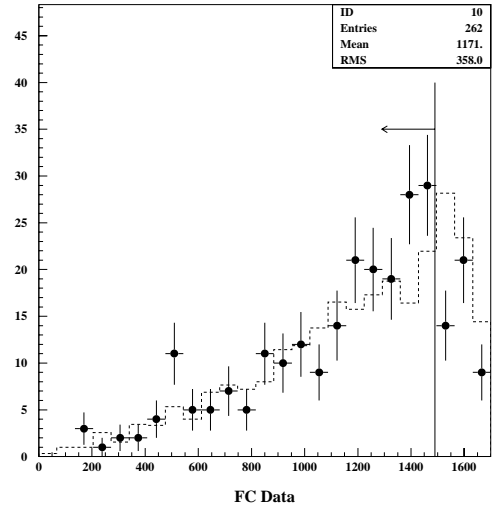


Figure 13.14: Radial Distribution (PC outgoing)

Since the source of the neutrinos is the upper atmosphere, the arrival direction corresponds to flight path. A dependence of any deficit or excess on the flight path would be very suggestive of some kind of oscillation phenomenon. Figure 13.23 gives the zenith angle dependence for single ring electron-like events in the multi-GeV regimes. Figure 13.24 shows the same for muon-like events.

With the exception of one point, the electron data correspond well to the expected zenith angle distribution. The muon data, however, exhibit a clear systematic deficit for events coming up through the earth. Figure 13.25 shows that the same effect persists in the typically higher energy partially contained data. The combined high energy muon sample (fully + partially contained) is given in Figure 13.26.

Figure 13.4 anticipates the final result by taking the ratio of the muon data and the expected Monte Carlo muon events as a function of the zenith angle. The same clear zenith angle dependence is observed. Some caution must be used with this type of plot however. The atmospheric neutrino models are only good to about 20% in absolute flux. It is only the ratio of muon to electron flux that is stable at the 5%

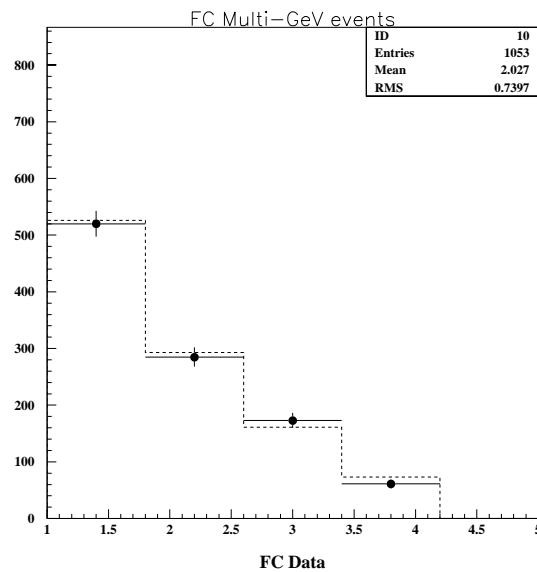


Figure 13.15: Number of rings (FC)

level due to the cancellation of similar uncertainties.

The ratio of muons to electrons is what started the atmospheric neutrino anomaly. Figure 13.28 shows the dependence of this ratio on the zenith angle. Like the earlier Kamiokande results, the Super-Kamiokande data show a clear dependence of the μ -like to e-like ratio on the zenith angle. Note that this plot contains only data and is not yet the usual “double ratio” form in which the results are usually presented.

There are a number of ways to parameterize the slope of the zenith angle distribution. The simplest is to simply fit a straight line. Given the current statistics, this is perfectly reasonable. In a neutrino oscillation hypothesis, however, one would not expect the distribution to have a constant slope. The neutrino path length changes rather slowly for angles near straight up or straight down. It changes quite rapidly near the horizon.

One convenient method of describing the slope of the zenith angle distribution is by defining an asymmetry [118]

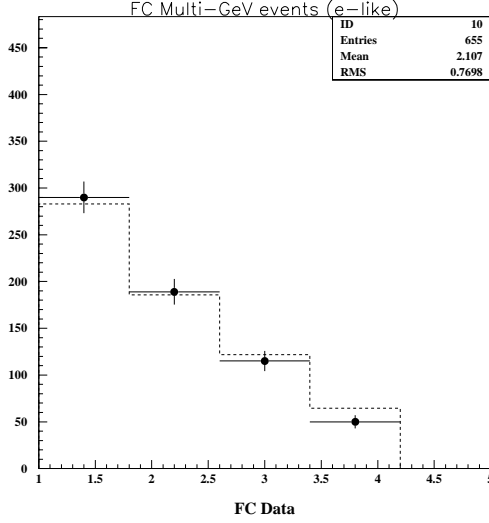


Figure 13.16: Number of rings (FC e-like)

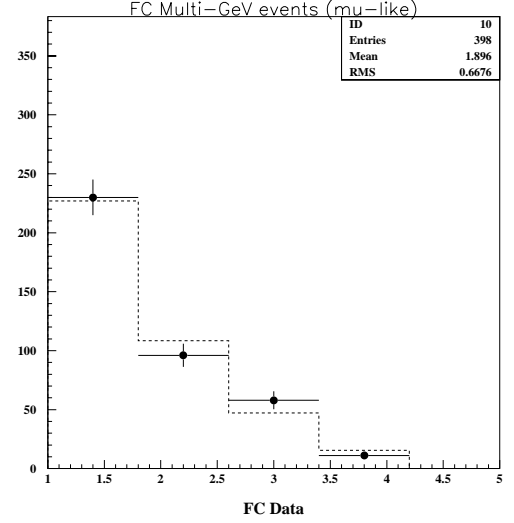


Figure 13.17: Number of rings (FC mu-like)

$$A = \frac{N_{down} - N_{up}}{N_{down} + N_{up}} \quad (13.3)$$

where N_{down} and N_{up} are the numbers of down-going or up-going particles. The asymmetry is typically defined for muons and electrons separately. In this case “up” and “down” are separated only by whether the third component of direction is positive or negative. No cut near the horizon is applied. The uncertainty in the asymmetry can be calculated by applying standard propagation of errors and assuming only statistical errors in the measurements of up and down.

$$\frac{\sigma_A^2}{A^2} = \frac{1}{N_{down} + N_{up}} \left[1 + \frac{1}{A^2} \right] \quad (13.4)$$

If there is no zenith angle dependence, the asymmetry should be equal to zero. If all events were coming from one hemisphere, A_μ would be 1. Table 13.4 gives the

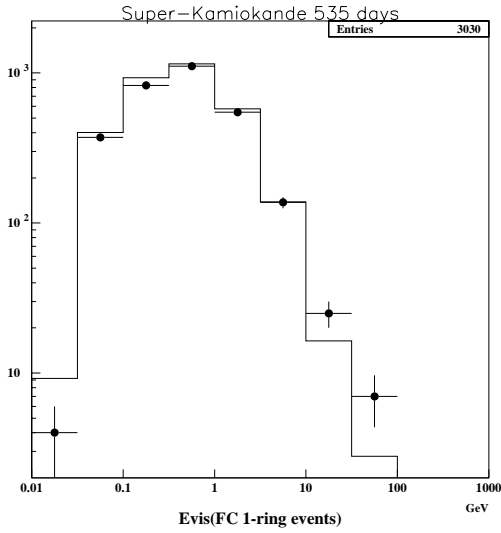


Figure 13.18: Visible energy (FC)

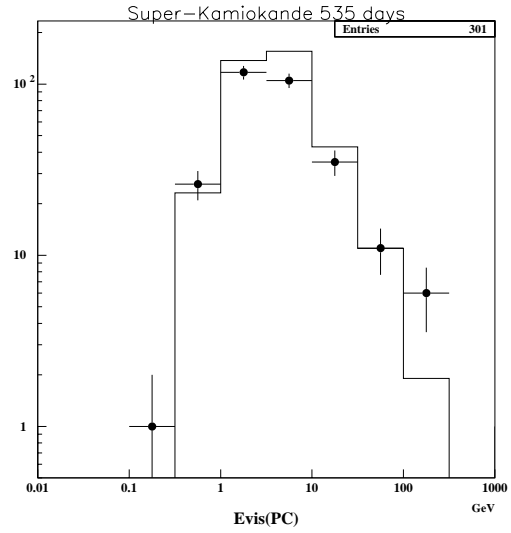


Figure 13.19: Visible energy (PC)

asymmetries for muon and electron data in the multi-GeV neutrino data sample.

Table 13.2: Up/down asymmetry

	Up	Down	Asymmetry
μ -like (FC)	86	144	0.3 ± 0.07
μ -like MC (FC)	1015	1004	-0.01 ± 0.02
μ -like (PC)	115	186	0.2 ± 0.06
μ -like MC (PC)	1283	1254	-0.01 ± 0.02
μ -like (FC+PC)	201	330	0.2 ± 0.04
μ -like MC (FC+PC)	2298	2258	-0.01 ± 0.01
e-like	144	146	-0.01 ± 0.06
e-like MC	809	802	0.0 ± 0.02

Flavor Double Ratio

It is common to calculate the flavor double ratio $R \equiv (\mu/e)_{DATA}/(\mu/e)_{MC}$. This comparison of the muon to electron ratio to the expected value allows the cancellation

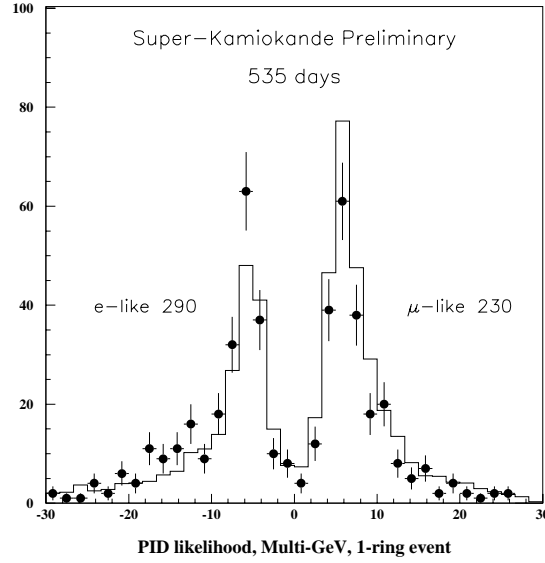


Figure 13.20: PID Likelihood for Multi-GeV 1-ring events (FC)

of the uncertainties in the absolute fluxes and can be found to greater accuracy than the fluxes themselves.

Figure 13.29 shows the dependence of the flavor double ratio on the zenith angle. Like Kamiokande, a clear zenith angle dependence can be seen. Figure 13.30 adds in the partially contained muon data. The double ratio cannot be calculated for the partially contained events alone, of course, as they consist only of muons. The partially contained events simply fill in the missing muon events from the fully contained sample at high energy.

The ratio can also be studied with respect to momentum to look for unexpected sources of the anomaly. Figure 13.31 shows that the effect is essentially independent of momentum. The highest momentum bin simply reflects the great difficulty in reconstructing the very high energy events which saturate large numbers of photomultiplier tubes.

Lastly, a check can be made to look for effects near the walls. A dependence on wall distance would suggest contamination from entering particles. Figure 13.32

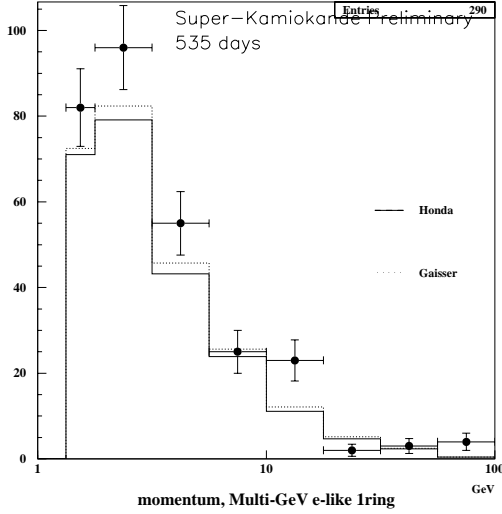


Figure 13.21: Electron-like momentum, 1-ring, multi-GeV (FC)

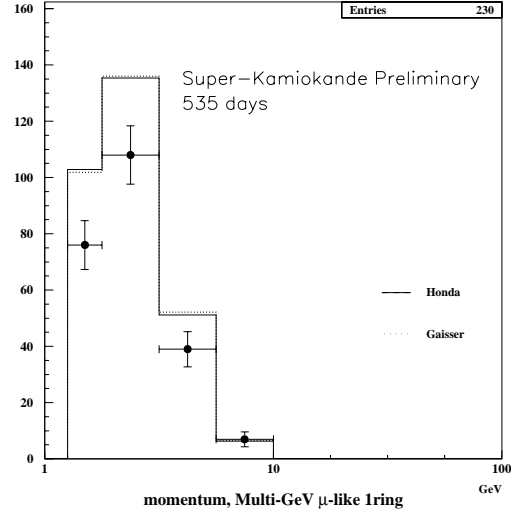


Figure 13.22: Muon-like momentum, 1-ring, multi-GeV (FC)

shows that there is essentially no such effect. There is one bin just inside the fiducial volume in the multi-GeV sample with an anomalously high R value. This corresponds to a small excess of muons in the PC sample as well as a slight deficit of electrons in the FC multi-GeV sample. The anomalous region corresponds exactly to the location of the partially contained muon excess noted earlier (see section 13.2.

13.5 Systematic Errors

A study of systematic errors is essential to a final result. Super-Kamiokande is a very large and complex detector with very involved data analysis streams. Care must be taken to be certain that the operation of the detector is well understood and that the analysis is not biasing the final result. Table 13.5 summarizes the estimated systematic error from the known sources in our detector and data analysis streams.

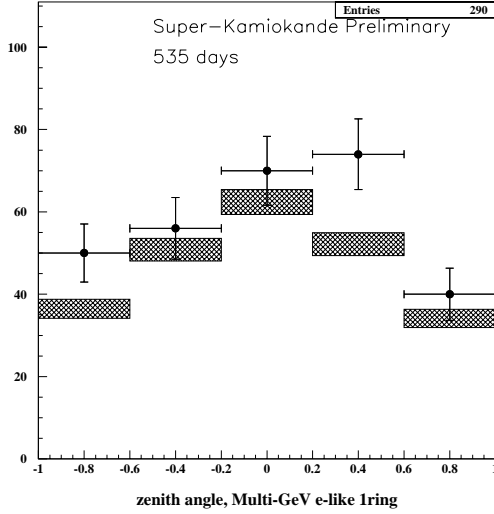


Figure 13.23: Zenith angle distribution, 1-ring e-like, multi-GeV (FC)

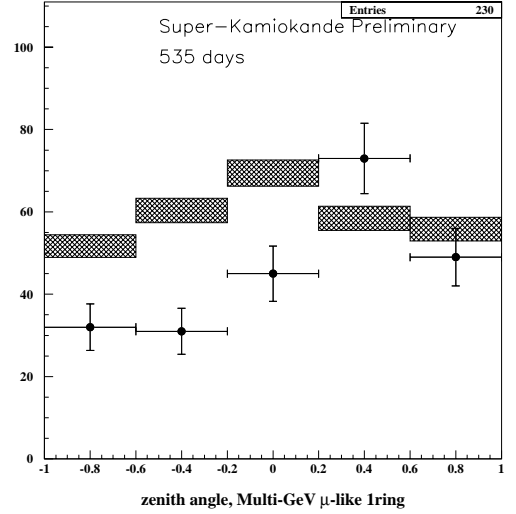


Figure 13.24: Zenith angle distribution, 1-ring μ -like, multi-GeV (FC)

13.5.1 Data reduction

One source of systematic error lies in the knowledge of the reduction efficiencies. For the fully contained data, event selection is very clean and the inner detector simulation is very precisely tuned. Systematic errors in the FC reduction are expected to be extremely small ($< 0.1\%$) [119].

For the PC reduction, the efficiency is less well known. This is partly an inherent part of using partially contained events. Since there are many more shorter tracks than longer due to the steeply falling neutrino spectrum, the requirement that the track exit the detector means many tracks begin not far inside the fiducial volume and point outward. These events are more difficult to fit. The lever arm of the track length in the inner volume may not be so long and since the cone is filled in, the inner edge of the ring is not available as an additional constraint. Furthermore, photomultiplier tubes near the exit point can often run out of dynamic range and saturate, effectively losing additional charge weighting information.

The Monte Carlo simulation is not tuned to the level of the inner detector simu-

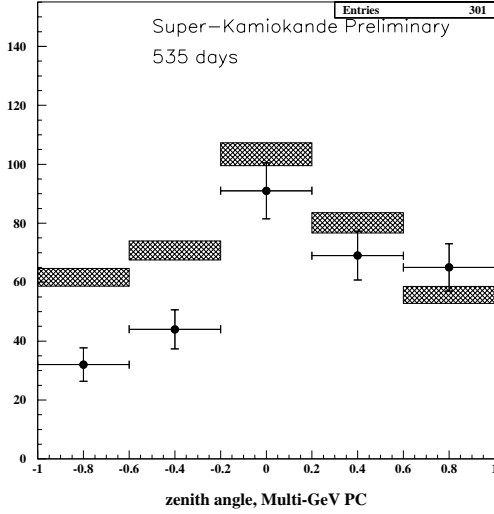


Figure 13.25: Zenith angle distribution, (PC)

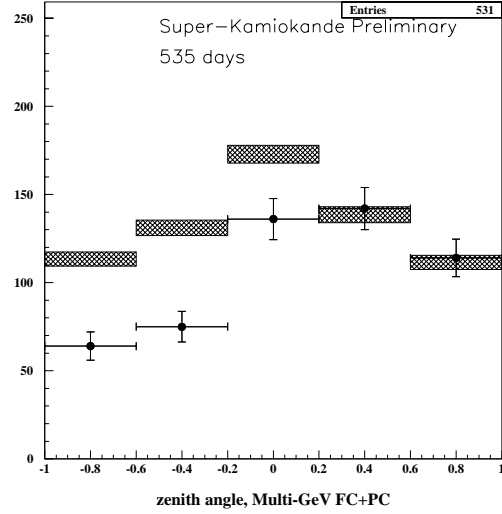


Figure 13.26: Zenith angle distribution, μ -like, multi-GeV (FC+PC)

lation either. This is not a real problem, the outer detector is not used to reconstruct tracks and does not require the level of precision needed for the inner detector. However, the outer detector Monte Carlo is used to estimate the partially contained event reduction efficiency.

Systematic uncertainty in the partially contained reduction efficiency is estimated by changing the tuning of the outer detector simulation parameters. Several parameters were adjusted to see the effect on the reduction efficiency [117].

The overall gain of the simulated photo-multiplier tubes was adjusted by $\pm 20\%$ and $\pm 40\%$. In another test, similar variations were applied randomly on a tube by tube basis to study relative gain changes. Within the statistics of the Monte Carlo ($\sim 3\%$) there was no change in the measured reduction efficiency.

A second source of systematic uncertainty in the outer detector simulation comes from the reflectivity of the Tyvek reflective liner. Dirt from construction settled on the liner which proved extremely difficult to clean. This degrades the reflectivity by an unknown amount. In the simulation, the reflectivity was adjusted by -20%

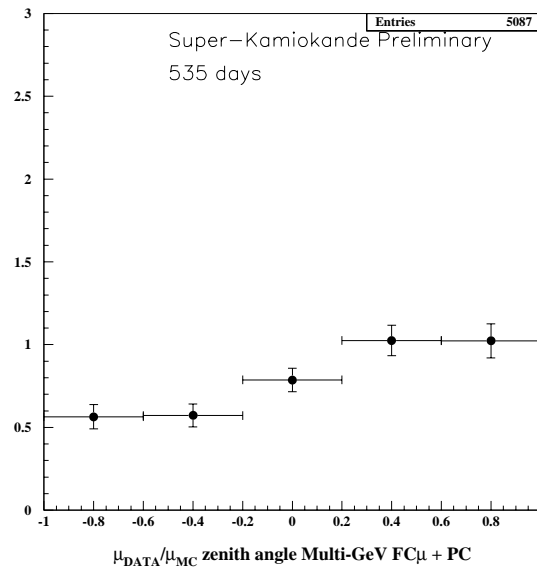


Figure 13.27: Compare μ data to MC, multi-GeV (FC+PC)

and +5%. These amounts were very generous changes based on the outer detector simulation tuning. An additional increase would have put the reflectivity over that measured by the manufacturer DuPont in clean controlled conditions. Common sense deems this unlikely and the tuning studies bear this out. With these changes, the overall reduction efficiency changed by $\leq 4\%$.

Human scanning is done at one point in the event selection. Scanning efficiency was estimated by mixing simulated events into the data. Scanners rejected less than 1% of valid neutrino events.

Adding the data reduction contributions in quadrature gives a total partially contained reduction systematic of 5%. However, partially contained muons contribute only about half of the muons in the multi-GeV sample. The other half come from the fully contained reduction stream with essentially no systematic error in reduction efficiency. Therefore the systematic reduction uncertainty in $R(\mu/e)$ is conservatively estimated to be 3%.

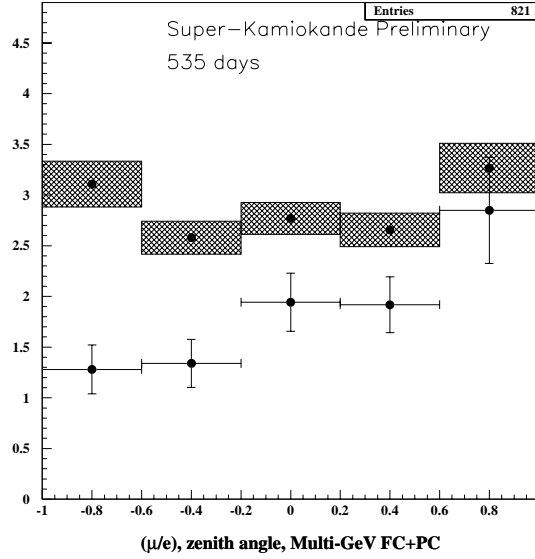


Figure 13.28: (μ/e) Ratio vs. zenith angle, 1-ring, multi-GeV (FC)

13.5.2 μ/e MC ratio

The theoretical uncertainty in the ratio $(\nu_\mu + \bar{\nu}_\mu)/(\nu_e + \bar{\nu}_e)$ has been calculated recently by several authors. In spite of the nearly 20% overall uncertainty in the absolute flux of muon or electron neutrinos, the ratio of the muon neutrino flux to the electron neutrino flux is known to within 5% [2]. This is because a major source of uncertainty in the absolute neutrino flux comes from a lack of knowledge of the absolute cosmic ray primary proton flux. This uncertainty is common to both muon and electron neutrino flux estimates and largely cancels when the ratio is taken.

13.5.3 $E^{-\gamma}$

The spectrum of primary cosmic rays is well fit to a power law $E^{-\gamma}$ with spectral index $\gamma = 2.71 \pm 0.05$. The neutrino spectrum is directly related to the primary spectrum, albeit adjusted by further energy dependent factors from the meson production cross-sections and decay probabilities. Systematic uncertainty in the primary spectrum is

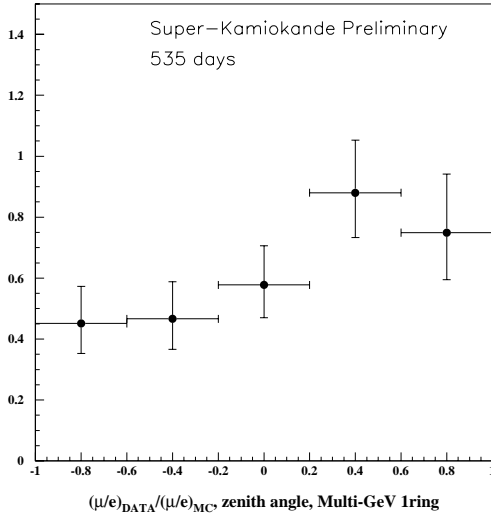


Figure 13.29: R versus zenith angle, multi-GeV (FC)

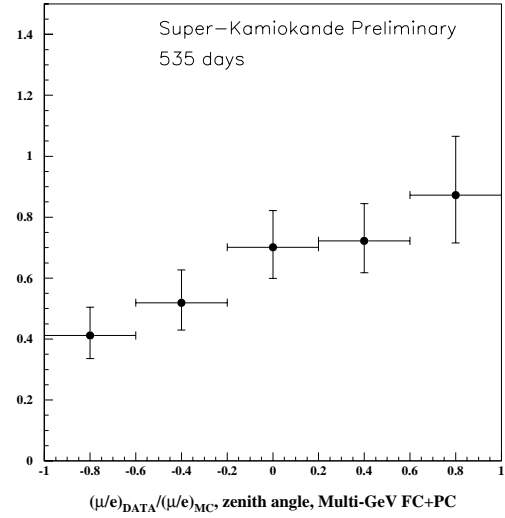


Figure 13.30: R versus zenith angle, multi-GeV (FC+PC)

also present in the neutrino spectrum.

To estimate the systematic effects of this uncertainty, the neutrino spectral index was changed by ± 0.05 . In practice this was done by weighting each Monte Carlo neutrino event that would pass appropriate cuts for the multi-GeV sample by a factor of $(E_\nu/9 \text{ GeV})^{\pm 0.05}$. The divisor of 9 GeV is included to fix the absolute flux at the mean energy of the multi-GeV muon sample. This is a somewhat arbitrary choice as the factors will cancel when the μ/e ratio is taken. Table 13.5.3 shows the effect on the expected numbers of events. Relative changes in the numbers of events are given in parentheses. The systematic uncertainty due to uncertainty in the spectral index is taken to be 1.7%.

13.5.4 Separation of μ and e

Another source of systematic error comes from the particle identification used to distinguish fully contained muons and electrons. This effect can be estimated from the charged current quasi-elastic ν_μ and ν_e lines in Table 11.4. Out of 618 total $\nu_e, \bar{\nu}_e$

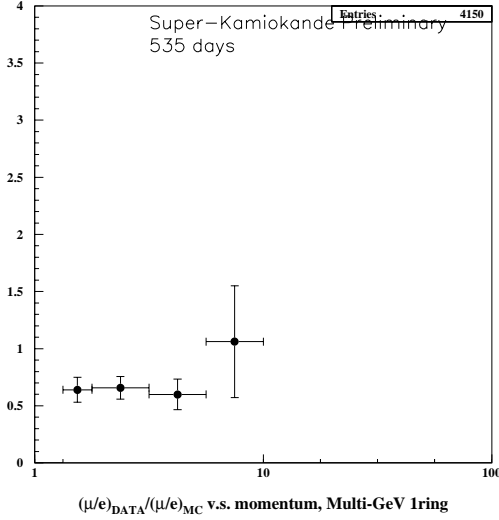


Figure 13.31: R versus momentum, multi-GeV (FC+PC)

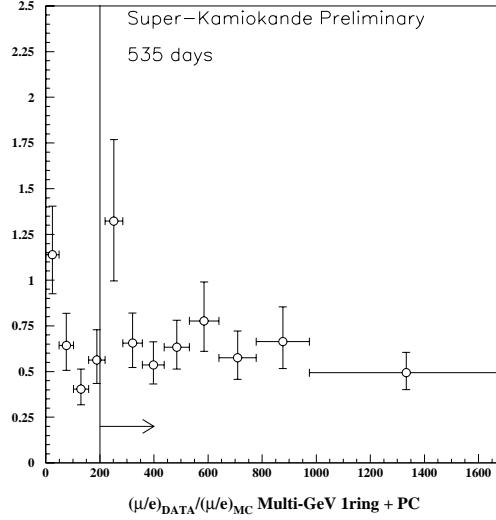


Figure 13.32: R versus wall distance, multi-GeV (FC+PC)

events, 2 (0.3%) were mis-identified as μ -like. From the 1108 $\nu_\mu, \bar{\nu}_\mu$ events, 15 (1.4%) were falsely identified as e -like.

Because of the low statistics for the mis-identified events it is more reasonable to take the 1-sigma upper limit. In this case, $2 + \sqrt{2} = 3.4$ out of 618 (0.5%) electrons are mis-identified as μ -like, and $15 + \sqrt{15} = 18.9$ out of 1108 (1.7%) muons are mis-identified as e -like.

The uncertainty in the μ/e ratio where the fully and partially contained samples have different systematics can be calculated using standard error propagation formulas. The relative error in R can be readily found to follow:

$$R = \frac{FC\mu + PC\mu}{FCe} \quad (13.5)$$

$$\frac{\sigma_R^2}{R^2} = \left(\frac{FC\mu}{FC\mu + PC\mu} \right)^2 \left(\frac{\sigma_{FC\mu}^2}{FC\mu} \right)^2 + \left(\frac{PC\mu}{FC\mu + PC\mu} \right)^2 \left(\frac{\sigma_{PC\mu}^2}{PC\mu} \right)^2 + \frac{\sigma_e^2}{FCe^2} \quad (13.6)$$

Table 13.3: Summary of systematic error

reduction	3%
$(\nu_\mu + \bar{\nu}_\mu)/(\nu_e + \bar{\nu}_e)$	<5%
$E^{-\gamma}$	1.7%
μ/e separation	3%
1/2 ring separation	5%
vertex position	2.4%
energy calibration	3.8%
non-neutrino background	
flasher	$\ll 0.5\%$
cosmic ray μ	1%
e-like background	<0.2%
CC cross-section	4.3%
NC cross-section	4%
hadron simulator	1%
PC/FC separation	0.4%
Total systematic error	11.3%
MC statistics	2.9%

There is no particle identification algorithm applied to the partially contained events. There is some electron contamination in the PC sample, but it is expected to be the same amount and in the same direction for both data and Monte Carlo. The PC separation systematic is expected to be negligible and dropped.

The fully contained errors contribute a $\sqrt{(0.44)^2 \cdot (0.017)^2 + (0.005)^2} = 0.9\%$ to the μ/e ratio. However, this is not quite correct because the number electrons increases by the same number as the muon number decreases, and vice versa. This means the actual systematic change is twice as large as expected from the variations in the individual event counts. The final uncertainty in R is taken to be 1.8%.

13.5.5 Single/Multi- ring separation

The number of rings observed in each fully contained neutrino event is determined by a ring counting algorithm as part of the automatic fitting process. Only single ring,

Table 13.4: Effect of $E^{-\gamma}$ uncertainty

	$\gamma=-2.71$	$\gamma=-2.66$	$\gamma=-2.76$
FC μ	2019	2144 (6.9%)	1902 (-5.8%)
PC μ	2537	2522 (-0.6%)	2560 (0.9%)
FC+PC μ	4556	4666 (2.4%)	4462 (-2.0%)
FC e	1611	1679 (4.2%)	1549 (-3.8%)
R(μ/e)	2.83	2.78 (-1.7%)	2.88 (+1.6%)

quasi-elastic events from the fully contained sample are included in the multi-GeV data. A systematic error can arise if the ring counting algorithm performs differently for the data as it does for the Monte Carlo simulated events.

The systematic uncertainty for the ring separation is estimated by comparing the results of human eye scanning with the automatic ring counting program. This was done for a subset of the data and Monte Carlo events in order to estimate the accuracy of the algorithm but is not done now on a regular basis due to the tremendous work load it places on the human scanners. Table 13.5.5 shows the differences between the two methods for the data and the Monte Carlo samples that were checked.

Table 13.5: Difference between eye-scan and automatic ring counting.

	Data	MC	Data/MC
FC $_{e-like}$	12/105=11.4%	27/182=14.8%	-4.4%
FC $_{\mu-like}$	15/82=18.3%	27/212=12.7%	+5.6%

The systematic uncertainty is the net shift between data and Monte Carlo and is -4.4% for e -like events and +5.6% for μ -like. Partially contained events do not have a cut on ring number and so do not contribute to this systematic. Using Equation 13.6 again, the systematic uncertainty in R for the single/multi-ring separation is taken to be 5%.

13.5.6 Vertex Position

Uncertainty in the vertex position fit can cause a systematic shift in R if the electrons are fit differently from the muons. This can cause one flavor to be preferentially pulled in or out of the fiducial volume. Only events near the edge of the fiducial volume are affected. Figure 13.32 shows that away from the edge of the fiducial volume the flavor double ratio is constant.

The systematic uncertainty due to the vertex position is estimated by calculating R for data which were fit both by hand and by the automatic fitting routine. The value of R changed by 2.4% and this was taken as the systematic error.

13.5.7 Energy Scale

Shifts in the energy calibration between electrons and muons can affect the value of R . Super-Kamiokande uses several means to calibrate the energy scale used in the analysis. Figure 13.5.7 shows a comparison of measured data to simulation for various calibration sources.

From the figure it can be seen that high energy stopping muons are shifted systematically higher by 2.1% in the data and decay electrons are shifted lower by the same amount. The systematic uncertainty in R can be estimated by shifting the electron energy scale by -2.1% and the muon energy scale by +2.1%. The effect of this is to change the number of events which pass the $E_{vis} > 1.33$ GeV cut for the fully contained events. Partially contained events do not explicitly make this cut and do not contribute to this systematic error. Table 13.5.7 shows how the number of Monte Carlo events changes when the 1.33 GeV cut is shifted. Compare these numbers to 1611 FC e -like, 2019 FC μ -like, and 4556 FC+PC μ -like for the unshifted case. The maximal systematic due to the energy scale is obtained by adding the absolute value of the relative changes and is taken to be 3.8%.

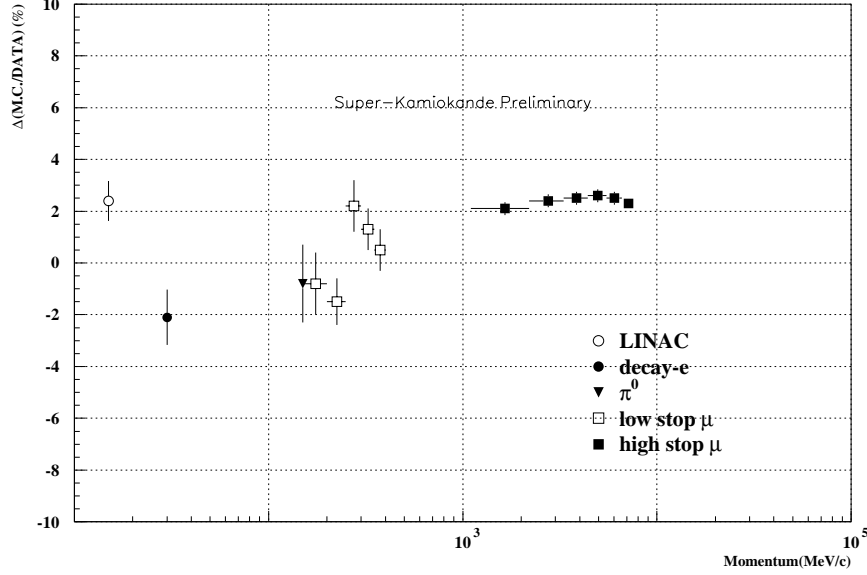


Figure 13.33: Comparison of calibration sources with Monte Carlo.

13.5.8 Non-neutrino background

The main concern with backgrounds at multi-GeV energies comes from entering cosmic ray muons. These could be left in the neutrino sample if the automatic fitting algorithms fit the interaction vertex inside the fiducial volume instead of at the wall. To check this, 500 stopping muons were selected from the raw data and the fitter was applied. Of these, only 1 event was fit inside the fiducial volume. The 90% (2σ) upper

Table 13.6: Effects of the energy scale uncertainty

FC e -like, $E_{vis} > 1.302 GeV$	1653	+2.6%
FC μ -like, $E_{vis} > 1.358 GeV$	1964	
FC μ -like+PC	4501	-1.2%
δR		3.8%

limit is estimated roughly at 2.5 events by scaling the result to 2/1000. The fraction of entering events which could be fit in the fiducial volume is $2.5/500=0.5\%$. The number of excess events outside the fiducial volume are 121 for the fully contained μ -like, and 14 for the partially contained data. Therefore a maximum of 0.6 and 0.07 entering events are expected to contaminate the multi-GeV FC and PC samples, respectively. This corresponds to a 0.4% and 0.04% change in the numbers of events. A much more conservative approach is taken and the cosmic ray systematic is simply considered to be 1%.

Flashing photo-multiplier tubes might cause some contamination, mostly likely in the electron events. In practice the timing characteristics of light from a flashing tube do not fit a cone hypothesis well and the reduction algorithms reject known flashing events with very good efficiency.

Other e -like background can come from radioactive decays in the rock or from neutron contamination leaking in from the walls. Very little contamination exists that could produce an electron at multi-GeV energies. Contamination from the walls is essentially ruled out by the distribution of e -like events in the tank. Any systematic from this effect is expected to be extremely small.

13.5.9 Cross-sections

In order to estimate systematic uncertainties in R due to the neutrino interaction cross-sections, K. Okumura changed several parameters in the interaction simulation. Table 13.5.9 shows the results of these efforts.

In the table, M_a is the axial vector mass used in the quasi-elastic cross-section calculation. P_{fermi} is the Fermi momentum. The nuclear potential $V_{nuclear}$ was not included in the quasi-elastic cross-section so it was turned on to determine its effect. The absolute charged current non quasi-elastic cross-sections were varied individually as well. The total systematic error in R due to the cross-sections is taken to be 4.3% for charged current, and 4% for neutral current.

Table 13.7: Systematics due to cross-section parameters

	FC _e	FC _μ	R(μ/e)
CC quasi-elastic			
$M_a \pm 10\%$	$\pm 3.5\%$	$\pm 3.1\%$	$\pm 3.3\%$
$P_{fermi} (250 \text{ MeV}/c \rightarrow 180 \text{ MeV}/c)$	$+2.3\%$	$+2.1\%$	-0.2%
$V_{nuclear}(\text{off} \rightarrow \text{on})$	-0.4%	-0.4%	$+0.1\%$
CC non-q.e. cross-sections			
$1-\pi \pm 30\%$, multi- $\pi \pm 20\%$	$\pm 12.5\%$	$\pm 14.7\%$	$\pm 2.2\%$
$\pm 5\%$ only in ν_e	$\pm 2.3\%$	$\pm 0.1\%$	$\pm 2.3\%$
$\pm 5\%$ only in ν_μ	$\pm 0.3\%$	$\pm 3.2\%$	$\pm 2.9\%$
CC total			4.3%
NC $\pm 50\%$	$\pm 4.3\%$	$\pm 0.3\%$	$\pm 4.0\%$

The hadron simulation program was GCALOR. This package was replaced by FLUKA as a comparison. The resulting systematic difference in R was 1%.

13.5.10 FC/PC separation

Because the fully contained and partially contained events are handled differently, a systematic error in R can result from the separation between the two samples. The definition of partially contained events required 10 or more hits in the outer detector cluster. Table 13.5.10 shows the effect on the Monte Carlo samples when the required number of outer detector cluster hits is varied by $\pm 20\%$.

Table 13.8: Effect of OD cluster cuts on FC/PC separation

	10 hits	8 hits	12 hits
FC _e	1611	1610 (-0.06%)	1613 (0.1%)
FC _μ	2019	2014 (-0.2%)	2024 (0.2%)
PC _μ	2537	2537 (0.0%)	2521 (-0.6%)

The systematic uncertainty in R due to the fully versus partially contained event separation is estimated using Equation 13.6 as before. With this, the largest systematic error is taken to be 0.4%.

Chapter 14

ANALYSIS

The atmospheric neutrino data recorded in the Super-Kamiokande detector confirm both the overall deficit of muon neutrinos and the zenith angle dependence of the effect observed by the Kamiokande collaboration. Careful estimates of the systematic errors and possible detector biases are insufficient to explain this deviation from predicted results.

One possible (and popular) explanation of the atmospheric neutrino anomaly involves neutrino flavor oscillations. This could happen if lepton number is not exactly conserved and if the neutrinos have some small but non-zero mass. There is no compelling reason why lepton number must be conserved.

There is also no compelling reason for the neutrinos to be massless. Indeed, there are some hints that the masses might be non-zero. The astrophysical dark matter problem is one, the solar and atmospheric neutrino anomalies are others. Neutrino flavor oscillations resulting from a tiny non-zero mass would be pleasing solutions to all these problems.

14.1 *Vacuum Oscillations*

How can such oscillations arise? It is easiest to begin with the simplest case, that of only two types of neutrinos propagating through a vacuum. The following discussion follows that of Perkins [120].

In the simplest case, oscillations can arise if the weak interaction (flavor) eigenstates $\{\nu_e, \nu_\mu, \nu_\tau\}$ are not mass eigenstates themselves, but rather linear combinations

of the mass eigenstates $\{\nu_1, \nu_2, \nu_3\}$. For simplicity only mixing between two types of neutrinos, ν_μ and ν_τ is described here.

The flavor eigenstates are related to the mass eigenstates through a unitary transformation:

$$\begin{pmatrix} \nu_\mu \\ \nu_\tau \end{pmatrix} = \begin{pmatrix} \cos\theta & \sin\theta \\ -\sin\theta & \cos\theta \end{pmatrix} \begin{pmatrix} \nu_1 \\ \nu_2 \end{pmatrix} \quad (14.1)$$

where θ is an arbitrary mixing angle.

The flavor wavefunctions produced in a weak interaction are actually linear combinations of the mass eigenstates

$$\nu_\mu = \nu_1 \cos\theta + \nu_2 \sin\theta \quad (14.2)$$

$$\nu_\tau = -\nu_1 \sin\theta + \nu_2 \cos\theta \quad (14.3)$$

The flavor state is determined by the interaction but the propagation through free space is determined by the mass eigenstates. The $\{\nu_1$ and $\nu_2\}$ states propagate at different rates because of the differing masses so the flavor content of the original states will change as a function of time.

$$\nu_1(t) = \nu_1(0)e^{-iE_1 t} \quad (14.4)$$

$$\nu_2(t) = \nu_2(0)e^{-iE_2 t} \quad (14.5)$$

The probability that an initial ν_μ state will be found as a ν_μ at some later time is given by:

$$P(\nu_\mu(t) | \nu_\mu(0)) = |\langle \nu_\mu(0) | \nu_\mu(t) \rangle|^2 \quad (14.6)$$

where $|\nu_\mu(t)\rangle = |\nu_1(0)\rangle e^{-iE_1 t} \cos\theta + |\nu_2(0)\rangle e^{-iE_2 t} \sin\theta$.

$$P(\nu_\mu(t) | \nu_\mu(0)) = | \cos^2\theta e^{-iE_1 t} + \sin^2\theta e^{-iE_2 t} |^2 \quad (14.7)$$

$$= \cos^4\theta + \sin^4\theta + 2\sin^2\theta \cos^2\theta \cos[(E_1 - E_2)t] \quad (14.8)$$

Using the trigonometric relations,

$$\cos 2\alpha = \cos^2\alpha - \sin^2\alpha \quad (14.9)$$

$$\sin 2\alpha = 2\sin\alpha \cos\alpha \quad (14.10)$$

$$1 = \cos^2\alpha + \sin^2\alpha \quad (14.11)$$

one can rewrite the probability as:

$$P(\nu_\mu(t) | \nu_\mu(0)) = 1 - \sin^2 2\theta \sin^2 \left[\frac{(E_1 - E_2)t}{2} \right] \quad (14.12)$$

Note that momentum conservation requires that $\vec{\mathbf{p}}_1 = \vec{\mathbf{p}}_2$. Assuming that $m_i \ll E_i$ as it is for neutrinos, one can easily find the familiar form of the oscillation formula:

$$P(\nu_\mu(t) | \nu_\mu(0)) = 1 - \sin^2 2\theta \sin^2 \left[1.27 \frac{\Delta m^2 L}{E} \right] \quad (14.13)$$

where $\Delta m^2 \equiv m_1^2 - m_2^2$ in $(eV/c^2)^2$, $L \equiv ct$ in (m), $E \equiv$ neutrino beam energy in (MeV). Clearly the probability of finding the ν_μ as a ν_μ at some later time is an oscillating function of the initial beam energy and the distance traveled.

If there is $\nu_\mu \leftrightarrow \nu_\tau$ oscillation we expect not only a disappearance of ν_μ but an appearance of ν_τ . However, the tau neutrinos will not be directly detectable in Super-Kamiokande. Because of the steeply falling neutrino spectrum, only a fraction of the muon neutrinos will have enough energy to create a real τ after oscillation. To be detectable, the τ must not only be produced but carry enough kinetic energy to get over the threshold for Cherenkov light production. This greatly suppresses the

charged current mode.

Even if a τ is produced it will decay immediately with no good way to identify that the observed products came from an intermediate τ . Neutral current interactions are possible for the ν_τ , but again this is not helpful for demonstrating the appearance of τ 's. Muon and tau neutrinos have essentially the same neutral current interactions and the total number of $\nu_\mu + \nu_\tau$ neutrinos does not change due to flavor mixing between the two.

The new data from Super-Kamiokande can be used to limit the available parameter space under the hypothesis of oscillations. The apparent deficit of muon neutrinos and zenith angle dependence strongly supports some type of muon neutrino oscillations. This is discussed further in Section 14.3. Electron neutrinos do not show any significant deficit or angular dependence. For the purpose of this analysis the electrons are assumed not to participate in oscillations at all. Only $\nu_\mu \leftrightarrow \nu_\tau$ mixing will be considered here.

In principle a sterile neutrino could take the place of the ν_τ . This would affect the ratios of neutral current events but at the present level of statistics we cannot distinguish this case. The flavor ratio and the zenith angle distribution give two essentially independent constraints on the oscillation parameters Δm^2 and $\sin^2(2\theta)$.

14.2 *Neutrino Flight Path*

Given a production altitude for an atmospheric neutrino, we often need to calculate the length of the flight path from the interaction point to the detector. This quantity is very relevant in the case of neutrino oscillations since the probability of oscillation will depend on the length of the flight path and the energy. These quantities determine the proper time seen by the neutrino during the flight. The path length calculation is a geometrical problem illustrated in Figure 14.2.

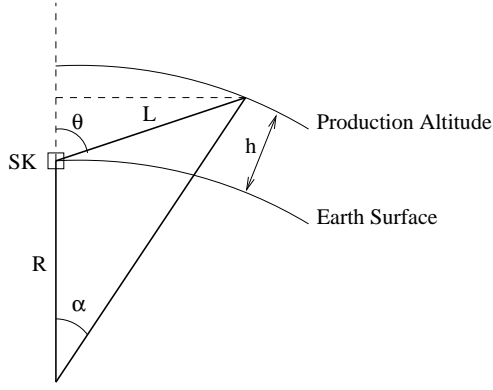
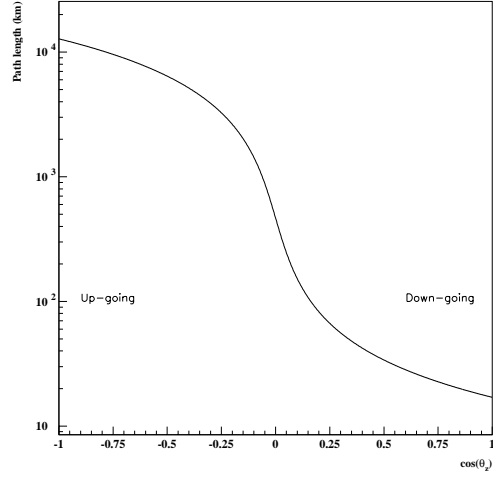


Figure 14.1: Neutrino Path Length Calculation

Figure 14.2: Neutrino flight path length vs. $\cos(\theta_z)$

The Law of Cosines gives:

$$L^2 = R^2 + (R + h)^2 - 2R(R + h)\cos\alpha \quad (14.14)$$

where $\cos\alpha = \frac{R+L\cos\theta}{R+h}$. Rearranging terms and completing the square in L gives the expression:

$$L = R[\sqrt{\cos^2\theta + (1 + h/R)^2} - \cos\theta] \quad (14.15)$$

where $\cos\theta$ is the zenith angle at Super-Kamiokande, h is the production altitude provided by Gaisser and Stanev[55], and L is the neutrino flight path length from the interaction point to the Super-Kamiokande detector. Figure 14.2 shows the variation of the neutrino flight path with the zenith arrival direction assuming an average production altitude of 17 kilometers.

The path length shows the most rapid change near the horizon. A small change in angle near vertically up or down does not change the total path very much. A

small change in angle near horizontal has a very large impact on the flight path. Figure 14.2 also illustrates the fact that the muon decay path in air is greatest for horizontal angles. At any given energy muons at shallow angles have a longer time to decay before reaching the surface of the earth than similar muons at steeper incident angles.

14.3 How Oscillations Affect the Zenith Angle Distribution

Cosmic rays interact with the atmosphere nearly isotropically. In the absence of neutrino oscillations, the neutrino flux should be nearly independent of direction. The earth is almost completely transparent to neutrinos at these energies.

If neutrinos oscillate between flavors, the probability of oscillation depends on the proper time in the frame of the neutrino. For a given mass difference and mixing angle, this translates into a dependence on L/E_ν , the length of the flight path and the energy of the neutrino.

Figure 14.3 shows the probability of detecting a muon neutrino as a muon neutrino as a function of the zenith angle arrival direction for various neutrino energies. The zenith angle corresponds directly to neutrino flight path. When the energy is fixed the flight path can be compared directly with the oscillation length.

It is clear from the figure that for all energies of interest the down-going particles travel a distance much smaller than the oscillation length. The probability that the neutrino has remained a muon type is high. As the zenith angle crosses the horizon the flight path rapidly becomes much larger than the oscillation length. The neutrinos oscillate many times before reaching the detector. The probability of seeing the particle as a ν_μ is now a rapidly varying function of the flight path or zenith angle. In a detector with perfect resolution and very high statistics one could see these rapid changes as a function of energy.

In reality we do not have a perfect detector. The finite angular and energy res-

olution mean that rapid oscillations in zenith angle tend to wash out. Averaging over energy contributes to this since the wiggles contribute to each angular bin with different phases for different energies. Figure 14.3 shows the effect of the resolution smearing for 20% angular resolution.

The general features of the expected zenith angle distribution are easy to see. For down-going neutrinos where the path length is short compared to the oscillation length for all energies under consideration, the probability of detecting all of the initial neutrinos is high. Assuming only $\nu_\mu \leftrightarrow \nu_\tau$ oscillations, the flavor double ratio $R = (\mu/e)_{DATA}/(\mu/e)_{MC}$ should remain near one.

Up-going neutrinos will go through many oscillations and the resolution and energy averaging make the probability of detecting ν_μ 's average to about 0.5 for maximal mixing. In this region R should be about 0.5 as well. Figure 13.30 shows that this is almost exactly what is seen in the real data. This is one of the prime pieces of evidence that neutrino flavor oscillations are in fact occurring.

14.4 *Chi-square Oscillation Analysis*

One traditional method of comparing the data with predictions from various oscillation parameters is to use a chi-squared analysis. This provides a statistically sound means of comparing the data results with predictions of an oscillation hypothesis with a large set of oscillation parameters. Those regions of parameter space with a good chi-squared are considered allowed regions, areas with poorer agreement are excluded.

A sample of Monte Carlo events corresponding to a 10 year live-time (225 kiloton-years) was generated and filtered through the same reduction algorithms as the data. This created a sample of events corresponding to no oscillations that is large compared to the data sample. The Monte Carlo sample was then weighted on an event by event basis to produce event distributions corresponding to different $\nu_\mu \rightarrow \nu_X$ oscillation parameters. Here ν_X is any species we do not detect, either ν_τ or a sterile species.

Each muon neutrino in the Monte Carlo sample receives a weight of $1 - P(L, E)$, where $P = \sin^2(\theta)\sin^2(1.27L/E)$ is the probability of oscillation. The neutrino path length L is determined by the Gaisser and Stanev production heights [55] and the generated vector arrival direction. The energy is also the generated vector quantity. These are used because the oscillation probability depends on the properties of the neutrino and not on the detector resolution. All muon neutrinos (in this case) are weighted regardless of their interaction mode in the detector (NC or CC) for the same reason.

The degree to which the oscillated Monte Carlo sample distribution matches the data can be described by defining a chi-squared amplitude. This can be done separately for the flavor ratio and for the zenith angle shape. Only the multi-GeV ($E < 1.33$ GeV, FC + PC) data are used in this analysis. For the zenith angle studies the data are additionally subdivided into 5 bins in zenith angle.

14.4.1 Double Ratio Constraint

The chi-squared test statistic for the ratio $R = (\mu/e)_{data}/(\mu/e)_{MC}$ is defined in Equation 14.16. The entire data set is treated together in a single bin. The model values of R for each set of oscillation parameters are not normalized to the data since the normalization is exactly what is being tested. Therefore the number of degrees of freedom is the same as the number of bins. χ_{ratio}^2 has a single degree of freedom.

$$\chi_{ratio}^2 = \frac{|R_{obs} - R_{pred}|^2}{\sigma_{pred}^2} \quad (14.16)$$

R_{obs} is the observed double ratio from the data and R_{pred} is the ratio predicted by the oscillated Monte Carlo sample for a particular set of oscillation parameters. The error here is strictly statistical and is taken to be the statistical error of the *expected*

(predicted) number of events.

$$\frac{\sigma_{pred}^2}{R^2} = \frac{1}{N_{\mu_{osc}}} + \frac{1}{N_{e_{osc}}} + \frac{L_{data}}{L_{MC}} \left(\frac{1}{N_{\mu_{MC}}} + \frac{1}{N_{e_{MC}}} \right) + \sigma_{sys}^2 \quad (14.17)$$

The first terms in $N_{\mu_{osc}}$ and $N_{e_{osc}}$ are simply the statistical error in the oscillated Monte Carlo. The terms scaled by the live-time ratio L_{data}/L_{MC} are the statistical uncertainties in the expected number of events if there are no oscillations. This is used rather than the statistical error in the data bins since if oscillations are really occurring then the numbers of data events will be reduced and not be the correct number to determine the statistical error.

Regions of the oscillation parameter space may be “excluded” at the 90% confidence level if there is less than a 10% probability that a χ^2 distribution of the specified number of degrees of freedom would exceed the calculated χ^2 using the data and Monte Carlo samples. Using a standard χ^2 table, this means that a parameter set $(\sin^2(2\theta), \Delta m^2)$ is excluded at the 90% confidence level if $\chi^2(\sin^2(2\theta), \Delta m^2) > \chi_{min}^2 + 2.7$ for one degree of freedom. Figure 14.5 shows the excluded region obtained by this method.

The region excluded at the 90% level is relatively small. The allowed region covers most of the parameter space of interest and does not have much analyzing power for selecting what the oscillation parameters should be. The reason for this is the low statistics for the multi-GeV sample. The ratio test is simply a comparison of two numbers where the overall uncertainty depends entirely on the knowledge of those two numbers. With few events in the sample, the multi-GeV data will never have the analyzing power in the ratio test that can be achieved with the lower energy sample containing roughly ten times as much data. As will be seen below, the power of the multi-GeV data comes not in the ratio, but rather in the shape test.

A useful check on these distributions can be made by taking a slice through the probability map at $\sin^2(2\theta) = 1$ to see how the χ^2 values and the probabilities depend

on Δm^2 . Figure 14.6 shows the reduced χ^2 as a function of Δm^2 at $\sin^2(2\theta) = 1$. The cut lines point out the $\Delta\chi^2 = 2.7$ contours to give an allowed range of Δm^2 .

One last useful way of estimating the allowed region for the parameter space is to plot how the expected double ratio changes as a function of Δm^2 for $\sin^2(2\theta) = 1$. Assuming maximal mixing, the allowed range of Δm^2 can be simply read off the plot by incorporating the total uncertainty in the overall ratio. Figure 14.4.1 shows how this result obtains a range of $-2.5 \leq \log_{10}(\Delta m^2) \leq -1$.

There is a particular reason for selecting $\sin^2(2\theta)$ near unity rather than something small in order to estimate the range of Δm^2 . If oscillations are occurring the discussion in Section 14.3 showed that up-going neutrinos go through many oscillations. After taking into account the angular resolution the probability (and hence R) averaged to about 0.5 with maximal mixing. If $\sin^2(2\theta)$ were much less than one, this average value would remain rather higher even for up-going events. The fact that R is very close to 0.5 for the lowest zenith angle bins in the data indicates that $\sin^2(2\theta)$ must be close to one.

14.4.2 Zenith Angle Shape Constraint

The second constraint on the possible oscillation parameters is the shape of the zenith angle distribution of events. The chi-squared test statistic for the shape constraint is defined in Equation 14.18. The multi-GeV data set is divided into five equal bins in $\cos(\theta_{zen})$. The number of events in the oscillated Monte Carlo sample are normalized to number of events in the data. This uses one degree of freedom, so from the five available data bins, χ_{shape}^2 has four remaining degrees of freedom.

$$\chi_{shape}^2 = \sum_i \frac{\left(n_{obs}^i - n_{pred}^i \frac{N_{obs}}{N_{pred}}\right)^2}{n_{pred}^i \frac{N_{obs}}{N_{pred}}} \quad (14.18)$$

Here n_{obs}^i and n_{pred}^i are the numbers of events observed in each zenith angle bin. The ratio N_{obs}/N_{pred} normalizes the overall number of events to be the same as the observed number. This takes out any effect of the overall ratio and makes the shape test a completely independent constraint.

In the same way as with the ratio test, oscillation parameter space may be excluded by drawing the 10% relative probability contour. For four degrees of freedom this corresponds to excluding regions for which the calculated $\chi^2 < \chi_{min}^2 + 7.78$. Figure 14.8 shows the excluded region obtained by this method. The point of lowest χ^2 occurs at $\sin^2(2\theta) = 0.94$, $\log_{10}(\Delta m^2) = -2.30$.

It is still useful to take a slice through the contours at large mixing angle. Figure 14.9 gives the reduced chi-square as a function of Δm^2 for $\sin^2(2\theta) = 1$. The cut lines give the range of allowed Δm^2 for the $\Delta\chi^2 = 7.78$ contour.

14.4.3 Combining Probabilities

In the Super-Kamiokande data there are two separate constraints on the possible oscillation parameters. The overall normalization of R, and its zenith angle distribution each put limits on the allowed parameters, generally with different results. One would like to combine the results of the two tests in order further improve the constraints. Eadie, et al., describe the correct procedure for combining independent tests [121].

The first question is whether the two tests are actually independent. Two tests are independent if their test statistics are independent random variables. In other words, the probability of B is irrelevant to the probability of A. Analytically, the conditional probability of A given B factorizes into the product of the probability of A and the probability of B.

$$P(A \text{ AND } B) = P(A) \cdot P(B) \quad (14.19)$$

Without writing down an analytic function, it is clear that the ratio test and the

zenith angle test of neutrino data are independent tests. The ratio test uses only a single number, the number of muon events divided by the number of electron events, without regard to energy or direction. The zenith angle test uses the additional information of direction and explicitly removes the overall normalization from consideration in the definition of the chi-squared test statistic. This being the case, the probability of an event falling into a particular zenith angle bin has no relation to the probability of obtaining a particular overall ratio.

The significance of the combination of the two tests is not simply the product of the probabilities from each test separately. That is, if $p_1 = a_1$ and $p_2 = a_2$ then the probability a that

$$p_1 p_2 < a_1 a_2 \quad (14.20)$$

is just $a = a_1 a_2$. Unfortunately, this assumption is incorrect. It assumes that both $p_1 < a_1$ and $p_2 < a_2$. Of course this is not necessary, the condition is only that the product of the probabilities be less than the $a_1 a_2$. By integrating under the curve defined in equation 14.20, the correct probability is found to be

$$a = a_1 a_2 [1 - \ln(a_1 a_2)] \quad (14.21)$$

Furthermore, for N independent tests, a variable transformation can be made as in equation 14.22. When this is done, the new variable a' is distributed as a $\chi^2(2N)$. For the Super-Kamiokande data, with two independent tests, this means that probabilities for the data matching expectations for various oscillation parameters may be calculated separately for each of the two constraints. The probabilities may be combined after the fact and treated in the standard way for a chi-squared distribution

with two degrees of freedom to determine the confidence regions.

$$a' = -2\ln \prod_{i=1}^N a_i \quad (14.22)$$

14.4.4 Combined R and Shape Constraints

The combined effect of the ratio and shape constraints is found by following the prescription of Eadie, et al, in Section 14.4.3. The combined probability $a = -2 \ln (P_{ratio} \cdot P_{shape})$ is distributed as a χ^2 with four degrees of freedom (2×2 independent tests). This means that the 90% exclusion regions can be calculated by finding the contour where $a = a_{min} + 7.78$. Figure 14.10 illustrates this region. The analysis was carried into the unphysical region of $\sin^2(2\theta) > 1$ to avoid artificial boundary effects and to be sure the preferred solution naturally chose the physical region.

A slice can be taken at $\sin^2(2\theta)$ to check the dependence on Δm^2 . Figure 14.11 and shows this as before, overlaying the previous results from the individual constraints for comparison.

The best fit point for the combined constraints is at $\sin^2(2\theta) = 1.00$ and $\log_{10}(\Delta m^2) = -2.00$. These parameters represent a particular hypothesis, that a Monte Carlo sample weighted with this type of oscillation will produce a double ratio consistent with that of the data, and a zenith angle distribution that is drawn from the same parent distribution as that of the data. Figure 14.4.4 shows the comparison of the zenith angle distribution for muon and electron events for the no-oscillation case and for the case of the best-fit oscillation parameters. The best-fit distribution agrees well with the data. Both are very clearly inconsistent with the no-oscillations case.

The dashed line corresponds to the expected distribution in the case of no oscillations. The solid histogram represents the data, and the solid crosses show the expected Monte Carlo result weighted by the best fit oscillation parameters.

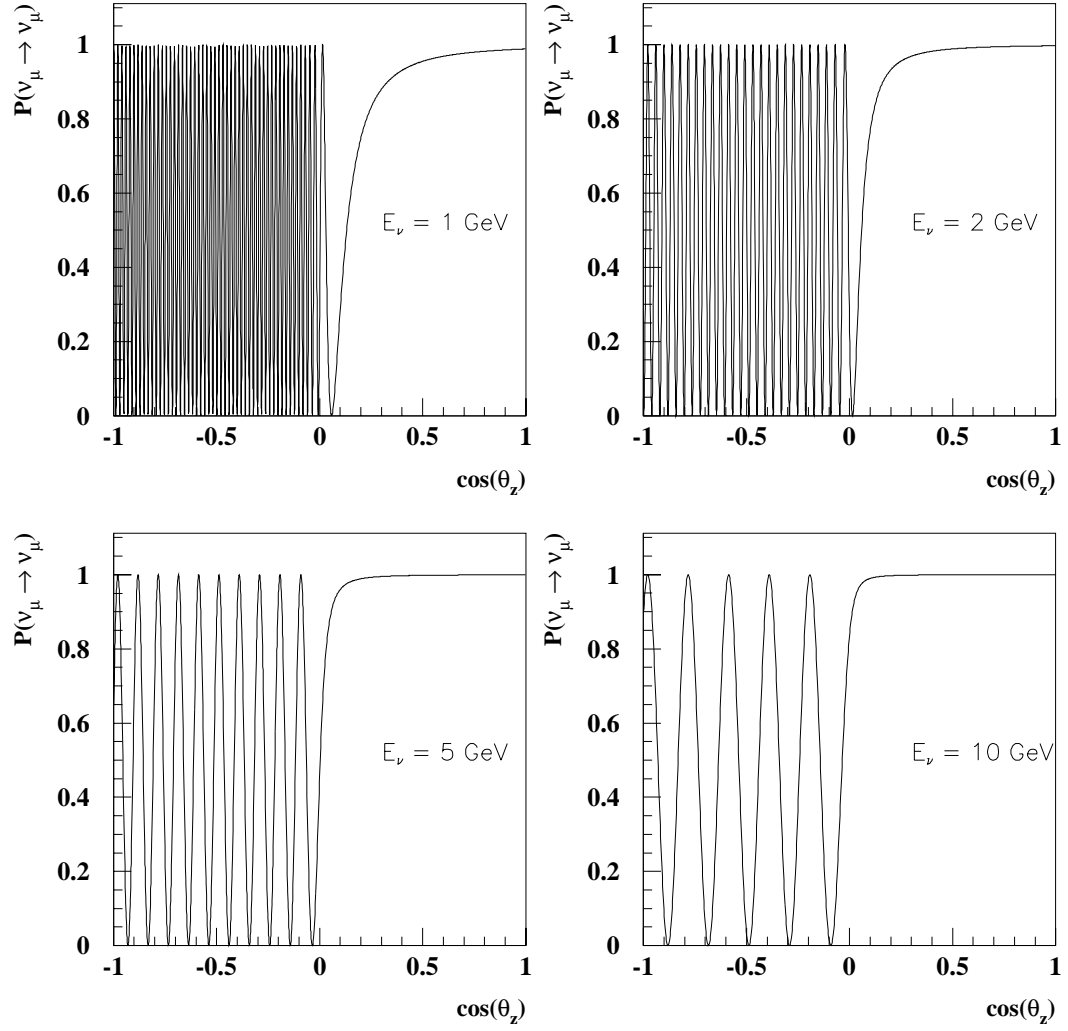


Figure 14.3: Oscillation probability as a function of zenith angle for $\sin^2(2\theta)=1$ and $\Delta m^2=10^{-2}$.

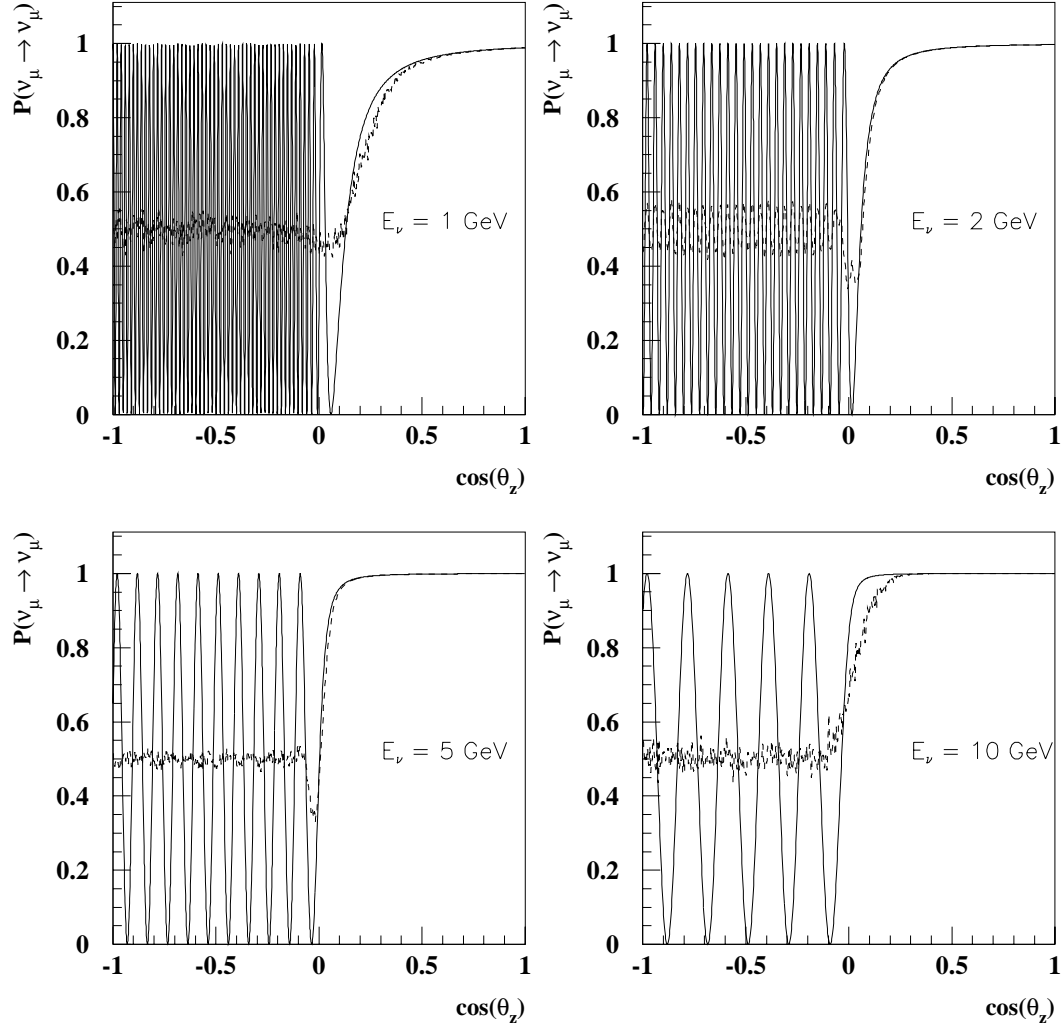
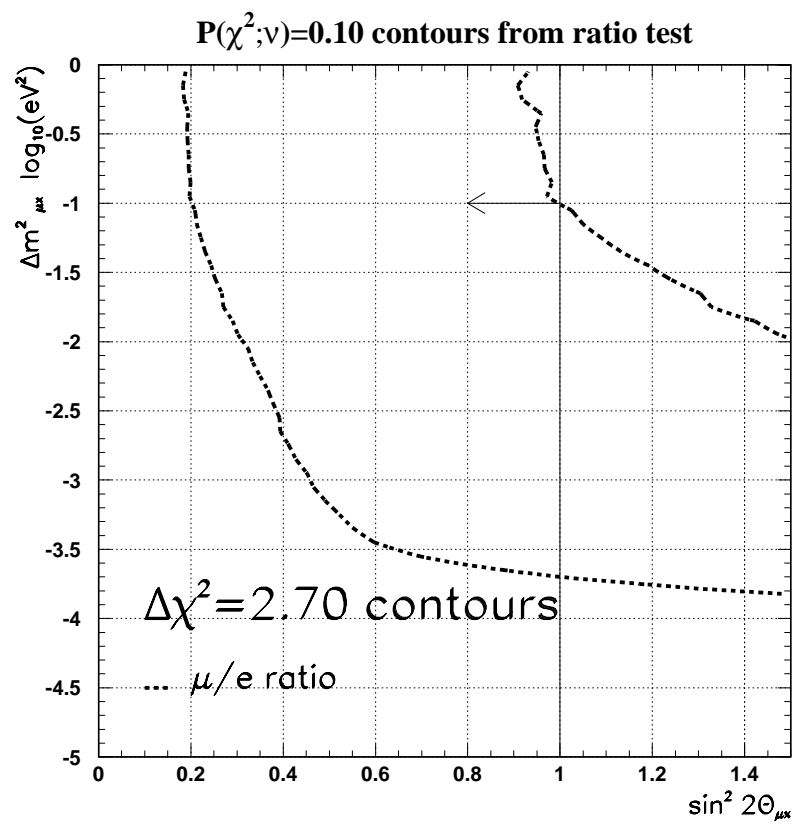


Figure 14.4: Oscillation probability as a function of zenith angle for $\sin^2(2\theta)=1$ and $\Delta m^2=10^{-2}$. The same distribution with 20% angular smearing is superimposed.

Figure 14.5: $\Delta\chi^2 = 2.7$ contours

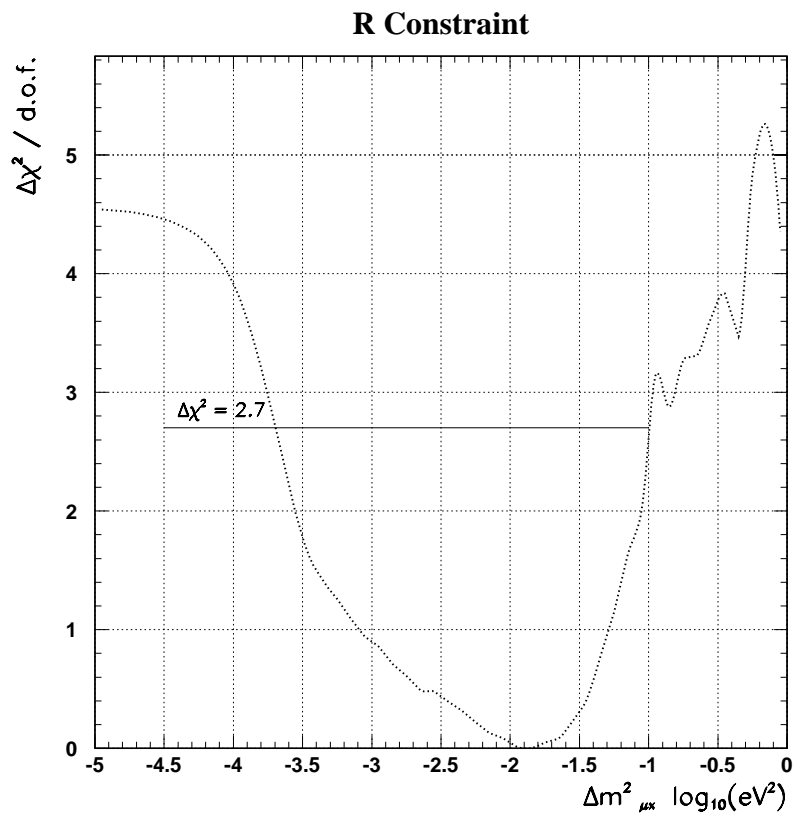


Figure 14.6: $\Delta\chi^2/\text{d.o.f}$ for $\sin^2(2\theta)=1$

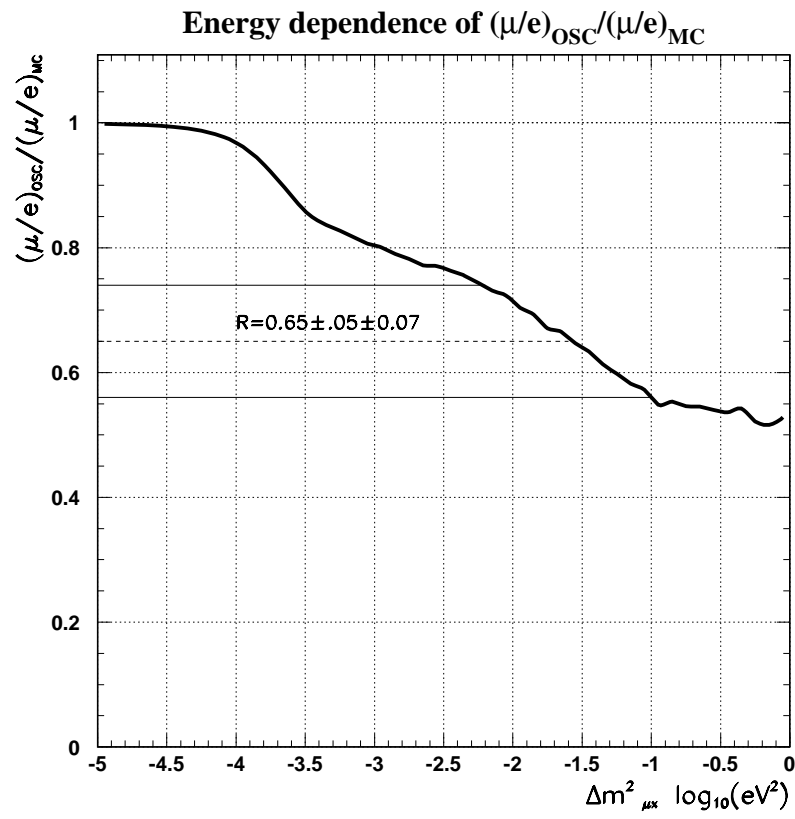
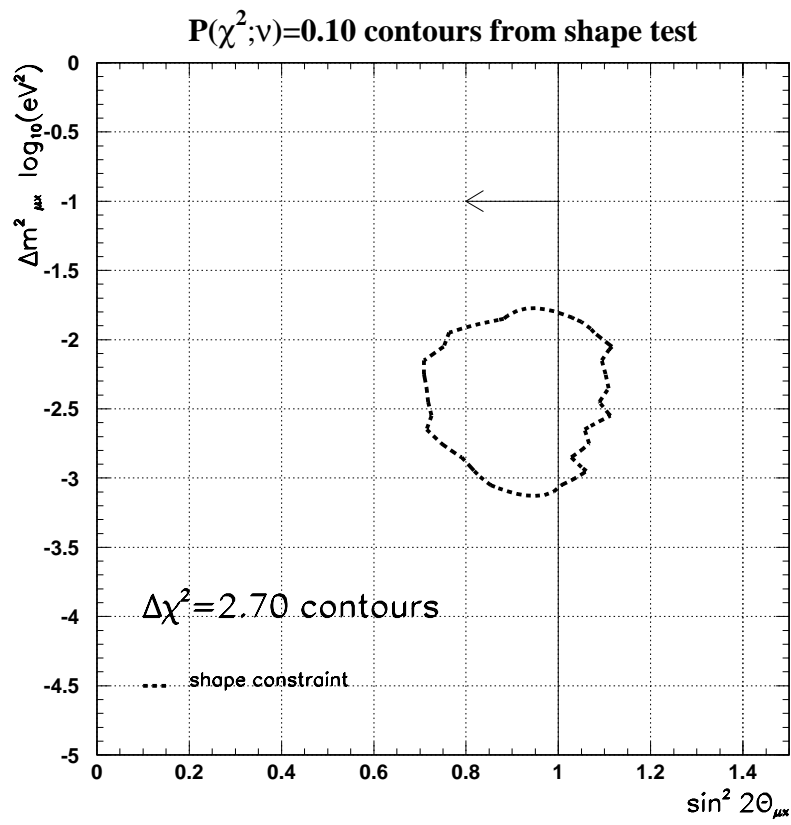


Figure 14.7: R vs Δm^2

Figure 14.8: $\Delta\chi^2 = 2.7$ contours

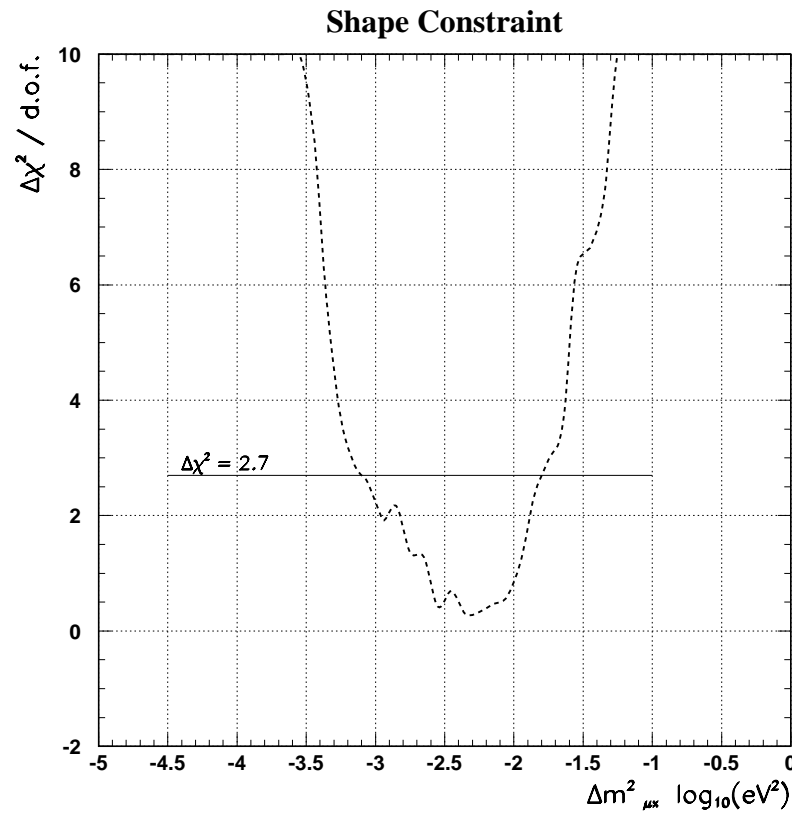


Figure 14.9: $\Delta\chi^2/\text{d.o.f}$

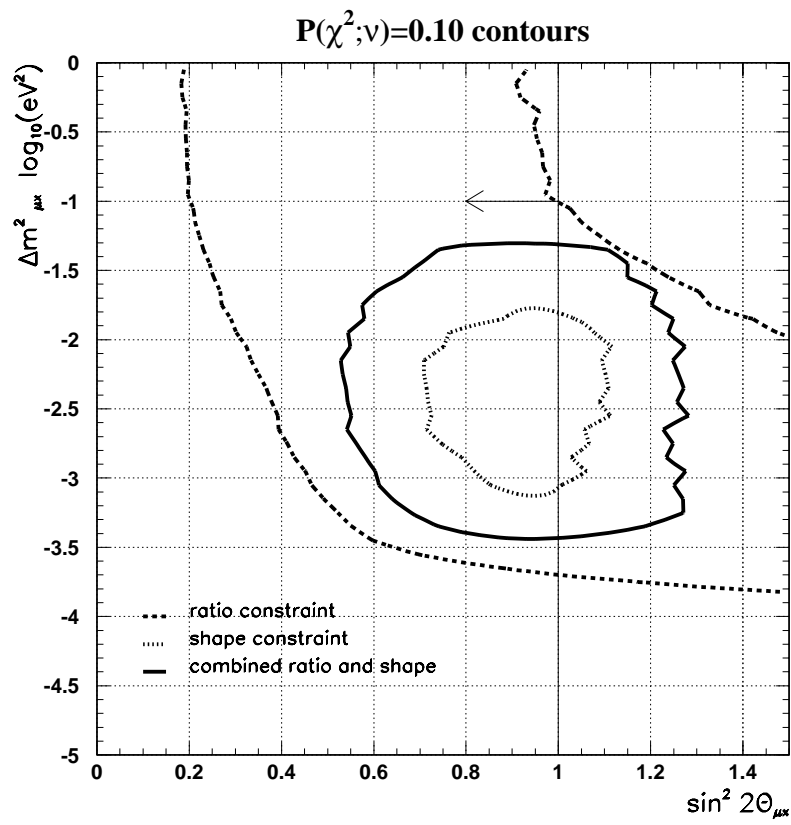


Figure 14.10: $\Delta\chi^2 = 7.78$ contours

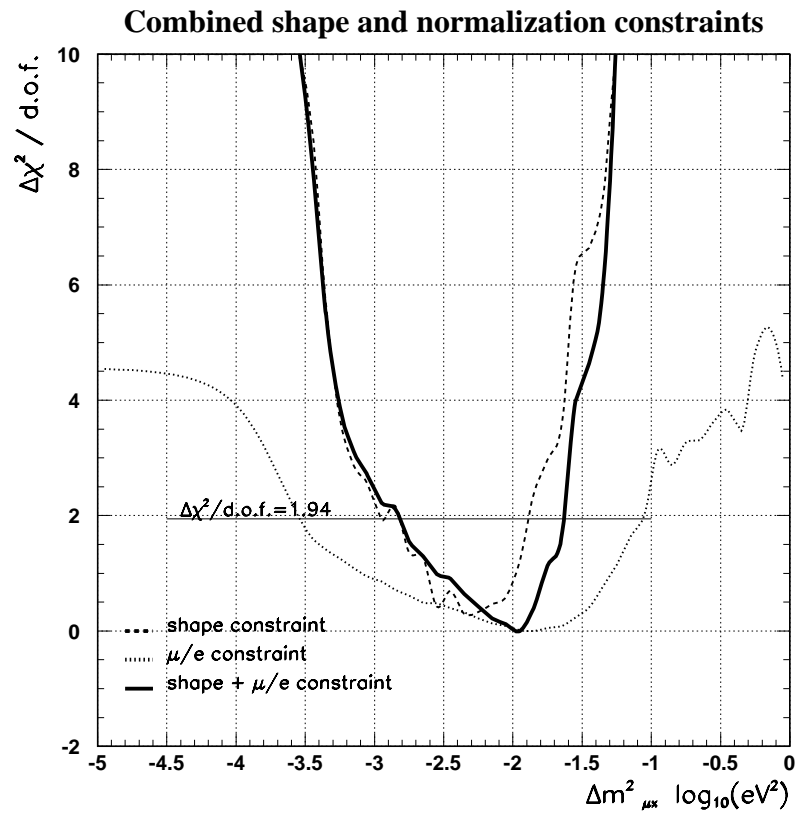


Figure 14.11: $\Delta\chi^2/\text{d.o.f}$

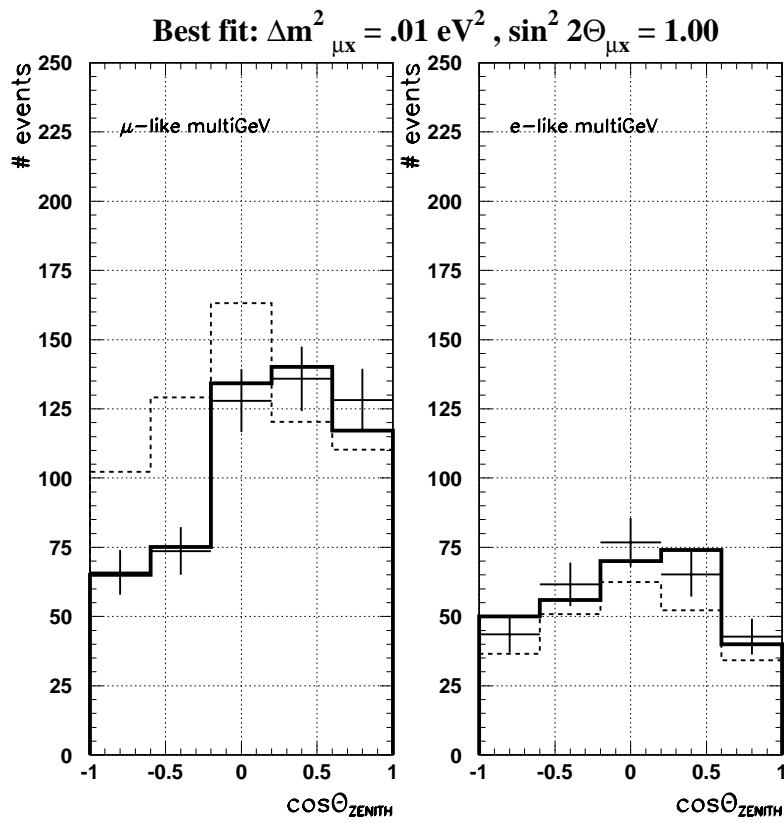


Figure 14.12: Comparison of data and Monte Carlo at best fit parameters

Chapter 15

OTHER EXPLANATIONS FOR RESULTS

The most popular (and certainly the most exciting) explanation of the Super-Kamiokande results is that neutrinos are in fact oscillating. The implications of this are important enough that it is essential to examine the alternatives before leaping to this conclusion. Some detector effect or even some ignored physics effect could be responsible.

There are several means of obtaining the atmospheric neutrino results without requiring oscillations. Background events masquerading as neutrinos, additional sources of high energy neutrinos, and detector systematics can all skew the μ/e ratio and the zenith angle distribution. Attenuation of the atmospheric neutrino by the earth might do the same.

15.1 Backgrounds

There are very few kinds of real background events that can fake atmospheric neutrinos in Super-Kamiokande. The energies involved are too high for most processes occurring locally in the tank such as spallation processes or radioactive decay. The good resolution in reconstruction also helps to eliminate fake events.

The one source of background that is a serious concern comes from misidentified cosmic ray muons. Entering muons which are not vetoed by the outer detector stand some chance of having a vertex reconstructed inside the fiducial volume of the detector. This effect is largest for the partially contained sample which has a much lower efficiency close to the walls. Indeed, there is a small excess of muon events near

the edge of the fiducial volume which may indicate a small contamination of entering cosmic ray muons.

In general, evidence for entering events comes from examining the vertex distributions in the tank. Since such events begin radiating Cherenkov light as soon as they hit the water, the vertex should reconstruct near the wall. The dominant muon flux is from above, so contamination should appear as an excess of muon-like events near the walls, and largely down-going compared to other parts of the detector. The author applied a standard one-dimensional Kolmogorov-Smirnov (K-S) statistical test to the distributions of the data and Monte Carlo event vertices in the Z and R coordinates. The K-S test is an integral test that gives a probability that two distributions came from the same parent distribution (see Section 13.2). The K-S probability is high for fully contained events, and for the Z coordinate distribution for partially contained events. The R distribution has a much lower probability, but increases as the fiducial cut is moved in.

The conclusion is that for the fully contained events there is no indication for any kind of contamination from entering particles. In the PC sample, the Z vertex distribution shows that there is no excess of events on the top of the detector as might be expected from cosmic rays. There is some indication that the radial distribution of events does not match the Monte Carlo near the edge of the fiducial boundary. This could be a sign of contamination from events entering the sides, but visual scanning of events in these radial bins showed no sign a problem with the event selection. Furthermore, entering events which survive the fiducial volume cut must have been mis-fit by the auto-fitting routines and the probability of this has been shown to be extremely small by testing on a sample of stopping muons (see Section 13.5.8).

Since there is no excess of events near the top of the detector and no sign of contamination from visual scanning, there must be another reason for the low K-S probability for partially contained events near the edge of the fiducial volume. It is believed instead that the small excess in those bins is related to small differences in

where the vertices are reconstructed. The vertex resolution for partially contained events is estimated to be 104 centimeters, compared to 23 cm for the fully contained μ -like events and 42 cm for the fully contained e -like events. This makes it more likely that effects of the fiducial cut will cause deviations farther into the volume for partially contained than for fully contained events. This is also the reason for the anomalously high value of the flavor double ratio near the edge of the fiducial volume in Figure 13.32.

Nucleon decay, if it were to happen, would be a background to the atmospheric neutrino flux. However, the rates are so low (we haven't seen one yet) that this is not an area of great concern.

Spallation and radioactive decay processes occur at much too low an energy to be of concern for the multi-GeV ($E_{vis} > 1.33$ GeV) sample. Neutron contamination from radioactive decays in the surrounding rock had been suggested as a possible explanation for the Kamiokande results. This would appear as an exponential increase of low energy electron-like events near the walls. There is essentially no evidence for this type of background even in the lower energy sample, and none at all in the multi-GeV data.

15.2 Sources of Neutrinos

If neutrinos were being produced at high energies from sources other than the atmosphere, the results would naturally be affected. Only a few possible sources exist and it is relatively easy to test for them.

Some astrophysical sources could exist in our galaxy or in other galaxies. Active galactic nuclei, black holes, and neutron stars all have environments which could conceivably be producing high energy neutrinos. Several people, J. Learned, K. Young, and R. Doyle, among others have looked for an excess of events from the galactic center or other galactic sources [122] with no clear success. A diffuse background

from many weak point sources is possible and might account for the slight overall excess of electron neutrinos compared to expectations, but at present this effect is indistinguishable from the large uncertainty in the overall flux of neutrinos from cosmic rays.

Dark matter annihilation in the sun might be a neutrino source. Tests for an excess of events in the direction of the sun by R. Doyle gave negative results at the level of the current statistics [123].

15.3 Detector Asymmetries

By far the most plausible cause of misinterpretation of the atmospheric neutrino results might be simply that they are a detector effect. If Super-Kamiokande is for some reason far more sensitive to down-going events than to up-going events then the results are meaningless. Several studies have investigated this possibility. In one, decay electrons from stopping muons were studied to examine the detector gain for checking whether the up-going events are suppressed [87]. Other studies on energy scale and efficiency systematics [124] confirm that the up/down detector asymmetry is correctly represented by the stated systematic error.

The data also go through a very complicated analysis process before becoming a final data sample. Anisotropy in the reduction criteria might also bias the sample by selecting some events with relatively higher efficiency than others. Of course, the same reduction process is applied to the simulated events. Studies of what kinds of analysis errors would have to be made in order to reproduce the atmospheric results have been made in detail [124]. They conclude that only huge errors could explain the results, and in most cases is even then inconsistent with part of what is observed.

The question of particle identification is always an issue. After the Kamiokande experiment was plagued by questions about its ability to resolve the particle type, a miniature detector was assembled at the KEK accelerator lab to test the particle

identification algorithms [125]. The Kamiokande codes were well validated in this beam test experiment and the same codes are now in use in Super-Kamiokande .

A relative shift in the energy reconstruction for muons and electrons might affect the double ratio. Calibration studies of the energy resolution rules out a large enough shift to explain the results (see Section 13.5.7. Furthermore, such a shift affects only the double ratio, but cannot explain the zenith angle result.

Another possible distortion of the data could come from azimuthal effects such as the geomagnetic cutoff. As with many other effects, the geomagnetic effect is small for the multi-GeV data. The flux of individual species is still affected but the μ/e ratio is not changed very much even at 1 GeV. These effects are taken into account in the atmospheric neutrino simulation and are described in more detail in Section 11.1.

The Kamioka site has a prominent peak in the geomagnetic rigidity cutoff contour map toward the southeast (see Figure 11.1). This produces an asymmetry in the expected azimuthal neutrino distribution. As the primary cosmic ray energy (and hence neutrino energy) increases, it is more likely to be above the rigidity cutoff in all directions. Figure 15.3 shows the azimuthal arrival directions for simulated Monte Carlo events with energies below and above 1.3 GeV. The multi-GeV data are included with statistical error bars for each azimuthal bin. The lower energy Monte Carlo events clearly show the east-west effect matching the shielding from the rigidity cutoff. Actual data from the lower energy sample match the simulation very well. The fact that an east-west effect exists and can be predicted at lower energies is a powerful argument that the source of these neutrinos is in fact in the atmosphere [126]. At the higher energies relevant to this analysis no significant effect remains.

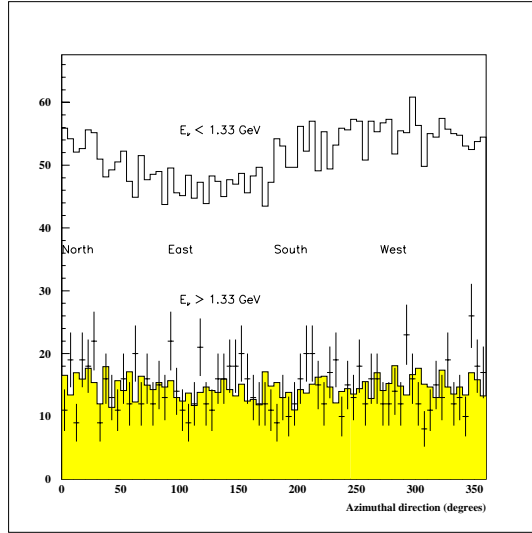


Figure 15.1: Azimuthal arrival directions for simulated events at Super-Kamiokande

15.4 Physics Effects

One ordinary physics effect that is generally not taken into account is absorption of neutrinos in the earth. The neutrino cross-section is small, but there are a lot of protons in the earth. Such an effect at least has the right properties to mimic the zenith angle distribution. A rough estimate is enough to convince one that at Super-Kamiokande energies the absorption is not strong enough to account for the results. Taking the diameter of the earth to be 13×10^8 cm and the mean rock density to be 4.5 g/cm^3 , there are about 3×10^{33} protons/cm² along the flight path of an upcoming neutrino. The cross-section for neutrino-proton interactions at a few GeV is about 10^{-38} cm^2 . This gives only 10^{-5} interactions for every up-going neutrino, not nearly enough to explain the factor of two difference in the Super-Kamiokande atmospheric neutrino results.

15.5 Summary

Collaborators in Super-Kamiokande have looked for biases in the detector, the analysis, and the physics to explain the atmospheric neutrino results. No evidence for background contamination, outside neutrino sources, detector systematics, or ordinary physics effects has been found that could produce the measured double ratio and zenith angle distribution. With no plausible ordinary explanation available, we are forced to consider something new to explain what is seen.

Chapter 16

CONCLUSIONS

16.1 *Summary of Results*

The flux of atmospheric neutrinos has been measured during a 25.5 kiloton-year exposure in the Super-Kamiokande detector. A total of 218 electron-like and 176 muon-like fully contained single ring events with visible energy $E_{vis} > 1.33$ GeV were recorded in the 22.5 kiloton fiducial volume. In addition, 230 partially contained events were recorded. These are assumed to be muon-like.

The data are compared with a detailed Monte Carlo simulation based on a model of the atmospheric neutrino flux [2]. This gives a value of the flavor double ratio of:

$$R = \frac{(\mu/e)_{DATA}}{(\mu/e)_{MC}} = 0.65 \pm 0.05(\text{stat.}) \pm 0.07(\text{syst.}) \quad (16.1)$$

This result confirms previous measurements in the Kamiokande, IMB, and Soudan-2 experiments. It is consistent with results from those detectors.

The Super-Kamiokande data also confirm a zenith angle dependence of the double ratio. The value of R is significantly lower for events coming up through the earth than for events coming down from above. The degree to which R depends on the zenith angle can be parameterized by the asymmetry

$$A = \frac{N_{down} - N_{up}}{N_{down} + N_{up}} \quad (16.2)$$

For the combined fully and partially contained multi-GeV sample, $A_\mu = 0.20 \pm 0.04$ and $A_e = 0.01 \pm 0.01$ assuming statistical errors only. The muon asymmetry is

inconsistent with zero by 5 standard deviations. The electron data are consistent with having no zenith angle dependence.

The anomalously small value of R combined with the observed zenith angle dependence is suggestive of neutrino flavor oscillations. A chi-squared fit to a two flavor mixing hypothesis was done in which $\nu_\mu \rightarrow \nu_X$ where X is either a τ neutrino or some new sterile species. After combining the independent constraints of R and the shape of the zenith angle distribution, the allowed region of parameter space lies in the range $4 \times 10^{-4} \text{ eV}^2 \leq \Delta m^2 \leq 5 \times 10^{-2} \text{ eV}^2$ with $\sin^2(2\theta) \geq 0.55$ at the 90% confidence level. The best fit point is at $\Delta m^2 = 10^{-2} \text{ eV}^2$ and $\sin^2(2\theta) = 1$.

16.2 Comparison with Other Analyses

The results presented in this thesis are one analysis of Super-Kamiokande multi-GeV data. The Super-Kamiokande collaboration has presented an analysis incorporating both sub-GeV and multi-GeV data which finds a best fit point at $\sin^2(2\theta) = 1.0$ and $\Delta m^2 = 2.2 \times 10^{-3} \text{ eV}^2$ [127]. This mass difference is somewhat lower than that found by the present analysis. A few comments are needed to explain why this occurs.

The difference between the present analysis and the “official” Super-Kamiokande results for all energies lies largely in the method used to combine the independent ratio and zenith angle distribution (“shape”) constraints. The ratio test favors somewhat higher values of Δm^2 than the shape test (see Figure 14.11). These two constraints are used together in some way to achieve a complete result.

In the present analysis, the ratio and shape results are combined on an equal footing. The method for doing this is described in Section 14.4.3. This gives substantial weight to the ratio constraint which favors a larger mass difference. The combined result is pulled toward higher Δm^2 .

The Super-Kamiokande results presented by the collaboration for all energies use a different approach toward combining the two constraints. In this method, a single

χ^2 is defined with 70 bins (5 zenith angle bins, 7 momentum bins, 2 lepton flavors). A single overall parameter determines the normalization of the data relative to the Monte Carlo, effectively a ratio test. In this method the ratio test receives a much smaller weight compared to the zenith angle constraint than in the “equal footing” method. The combined result is then pulled much less strongly to higher Δm^2 , the best fit falls to a smaller mass difference.

If one looks only at the shape constraint in the present analysis, the best fit point is at $\Delta m^2 = 5 \times 10^{-3} \text{ eV}^2$. This is quite close to the collaboration result. It is a good indication of how strongly that result depends on the zenith angle shape compared to the overall (μ/e) ratio. The present analysis uses the ratio much more heavily, even though it is known that the low statistics make it a much less powerful constraint. The zenith angle distribution has a very good analyzing power in the multi-GeV region because the charged leptons more accurately reflect the neutrino direction. The combination of the two gives a much larger allowed region of parameter space than could be obtained by using only the zenith angle information.

16.3 *The Future*

The Super-Kamiokande detector is continuing to take data with very high efficiency. Normal operation is expected to continue until the summer of 1999, when the water tank will be drained and some maintenance work will occur. By that time the data set will have grown to nearly double the number of events used in this analysis. It is hoped that the systematic error can be brought down, however two of the largest sources of uncertainty have to do with knowledge of the expected atmospheric neutrino flux and the charged current neutrino cross-sections. New data from different experiments, and possibly new theoretical calculations will be required to improve the accuracy of these numbers.

Following the maintenance shutdown, Super-Kamiokande is expected to continue

to take data for many years. A long baseline neutrino oscillation experiment known as K2K (KEK E362) will send a muon neutrino beam from the KEK accelerator laboratory to the Super-Kamiokande detector. The pathlength is about 250 km and can be measured precisely. The energy of the beam can be adjusted to sweep out a region in L/E space to look for a characteristic oscillation signal.

This work is only one contribution to the growing body of experimental evidence supporting the idea of neutrino flavor oscillation. The implications of this on neutrino masses are profound. If, as the data would indicate, neutrinos do have mass, it will impact our understanding from the very deepest levels of fundamental interactions to the farthest flung reaches of observational astrophysics. It is an exciting time for neutrino physics!

BIBLIOGRAPHY

- [1] M. Honda et al. Atmospheric neutrinos. *Prog. Theor. Phys. Suppl.*, 123:483–490, 1996. Proceedings of YKIS '95, From the Standard Model to Grand Unified Theories. (hep-ph/9511223).
- [2] M. Honda and T. Kajita. Calculation of the flux of atmospheric neutrinos. *Phys. Rev. D*, 52(9):4985–5005, 1995.
- [3] P. Grieder. DUMAND-II: String 1 deployment, initial operation, results and system retrieval. *Nucl. Phys. B (Proc. Suppl.)*, 43:145–148, 1995.
- [4] H. Berns et al. Acoustical locating system for DUMAND-II. In *Proceedings of the 23rd International Cosmic Ray Conference*, pages 542–545, 1993.
- [5] J. Learned and R. J. Wilkes. Acoustical detection of cascades in DUMAND. In *Proceedings of the 23rd International Cosmic Ray Conference*, volume 4, pages 538–541, 1993.
- [6] J. George. Estimated flux limits for high energy particle cascades using acoustical detection techniques. In *Proceedings of the 24th International Cosmic Ray Conference*, volume 1, page 812, 1995.
- [7] R. J. Wilkes et al. Super-Kamiokande outer DAQ system. In *Proceedings of the 24th International Cosmic Ray Conference*, volume 1, pages 1019–1022, 1995.
- [8] J. George. OD event builder data format (preliminary). Technical report, University of Washington, 1995. UW internal note: UWA-SUPERK 95-05.
- [9] J. George. Coordinating UTC and local time in SuperK. Technical report, University of Washington, 1995. UW internal note: UWA-SUPERK 95-07.
- [10] J. George, J. Wilkes, and H. Berns. The Super-Kamiokande UTC clock system. Technical report, University of Washington, 1998. UW internal note: UWA-SUPERK 98-01.
- [11] H. Becquerel. On the invisible radiation emitted by phosphorescent substances. *Compt. Rend.*, 122:501, 1896.

- [12] L. Brown. The idea of the neutrino. *Physics Today*, 31(9):23–28, September 1978.
- [13] R. Kronig and V.F. Weisskopf, editors. *Collected Scientific Papers by Wolfgang Pauli*, volume II. Wiley-Interscience, 1964.
- [14] F. Perrin. Natural particles of intrinsic mass 0. *Compt. Rend.*, 197:1625–1627, 1933.
- [15] E. Fermi. An attempt of a theory of beta radiation. *Z. Phys.*, 88:161–177, Jan 1934. Translated in *The Development of Weak Interaction Theory* (P.K.Kabir, ed.), Gordon & Breach, New York, 1963.
- [16] E. Commins. *Weak Interactions*, chapter 1. McGraw-Hill, 1973.
- [17] G. Gamow and E. Teller. Selection rules for the β -disintegration. *Phys. Rev.*, 49:895, 1936.
- [18] H. A. Bethe and R. Peierls. *Nature*, 133:532, 1934.
- [19] F. Reines. 40 years of neutrino physics. *Prog. Part. Nucl. Phys.*, 32:1–12, 1994.
- [20] F. Reines. The early days of experimental neutrino physics. *Science*, 203(4375):11–16, 1979.
- [21] F. Reines and C. Cowan, Jr. A proposed experiment to detect the free neutrino. *Phys. Rev.*, 90:492–3, 1953.
- [22] F. Reines and C. Cowan, Jr. Detection of the free neutrino. *Phys. Rev.*, 92:830–1, 1953.
- [23] C. Cowan, Jr. et al. Detection of the free neutrino: a confirmation. *Science*, 124(3212):103–4, 1956.
- [24] T. Lee and C. Yang. Parity nonconservation and a two-component theory of the neutrino. *Phys. Rev.*, 105:1671–1675, 1957.
- [25] G. Danby et al. Observation of high-energy neutrino reactions and the existence of two kinds of neutrinos. *Phys. Rev. Lett.*, 9:36–44, 1962.
- [26] S. Glashow et al. Weak interactions with lepton-hadron symmetry. *Phys. Rev. D*, 2:1285–1292, 1970.

- [27] S. Glashow and S. Weinberg. Breaking chiral symmetry. *Phys. Rev. Lett.*, 20:224–227, 1968.
- [28] A. Salam. On symmetries of weak interactions. *Nucl. Phys.*, 5:447–454, 1958.
- [29] F. Hasert et al. Observation of neutrino-like interactions without muon or electron in the Gargamelle neutrino experiment. *Phys. Lett.*, 46B:138, 1973.
- [30] A. Benvenuti et al. Observation of muonless neutrino induced inelastic neutrino interactions. *Phys. Rev. Lett.*, 32:800, 1974.
- [31] S. W. Herb et al. Observation of a dimuon resonance at 9.5 GeV in 400 GeV proton - nucleus collisions. *Phys. Rev. Lett.*, 39:252, 1977.
- [32] M. Perl et al. Evidence for anomalous lepton production in e^+e^- annihilation. *Phys. Rev. Lett.*, 35:1489, 1975.
- [33] D. Karlen. The number of light neutrino types from collider experiments. *Phys. Rev. D*, 54:286, 1996.
- [34] J. Christenson et al. Evidence for the 2 pion decay of the K_L meson. *Phys. Rev. Lett.*, 13:138, 1964.
- [35] E. Kolb, D. Schramm, and M. Turner. Astrophysical and cosmological constraints to neutrino production. In K. Winter, editor, *Neutrino Physics*. Cambridge University Press, 1991.
- [36] W. Haxton and G. Stephenson, Jr. Double beta decay. *Prog. Part. Nucl. Phys.*, 12:409–479, 1984.
- [37] B. Cleveland et al. Update on the measurement of the solar neutrino flux with the Homestake chlorine detector. *Nucl. Phys. B (Proc. Suppl.)*, 38:47–53, 1995.
- [38] W. Hampel et al. GALLEX solar neutrino observations: Results for GALLEX III. *Phys. Lett. B*, 388:384–396, 1996.
- [39] J. Abdurashitov et al. The Russian-American Gallium Experiment (SAGE) Cr neutrino source measurement. *Phys. Rev. Lett.*, 77:4708–4711, 1996.
- [40] A. Cummings and W. Haxton. ^3He transport in the sun and the solar neutrino problem. *Phys. Rev. Lett.*, 77:4286, 1996.

- [41] R. Barnett et al. Lepton particle listings. *Phys. Rev. D*, 54:275–302, 1996. Review of Particle Properties.
- [42] Y. Fukuda et al. Solar neutrino data covering solar cycle 22. *Phys. Rev. Lett.*, 77:1683, 1996.
- [43] Y. Fukuda et al. Atmospheric ν_μ/ν_e ratio in the multi-GeV energy range. *Phys. Lett. B*, 335:237–245, 1994.
- [44] M. Apollonio et al. Initial results from the CHOOZ long baseline reactor neutrino oscillation experiment. *Phys. Lett. B*, 420:397–404, 1998.
- [45] C. Athanassopoulos et al. Candidate events in a search for $\overline{\nu}_\mu \rightarrow \overline{\nu}_e$ oscillations. *Phys. Rev. Lett.*, 75:2650–2653, 1995.
- [46] J. Hill. An alternative analysis of the LSND neutrino oscillation search data on $\overline{\nu}_\mu \rightarrow \overline{\nu}_e$. *Phys. Rev. Lett.*, 75:2654–2657, 1995.
- [47] C. Athanassopoulos et al. Evidence for $\overline{\nu}_\mu \rightarrow \overline{\nu}_e$ oscillations from the LSND experiment at the Los Alamos Meson Physics Facility. *Phys. Rev. Lett.*, 77:3082–3085, 1996.
- [48] K. Assamagan et al. Measurement of the muon momentum in pion decay at rest using a surface muon beam. *Phys. Lett. B*, 335:231–236, 1994.
- [49] D. Buskulic et al. An upper limit for the τ neutrino mass from $\tau \rightarrow 5\pi^\pm(\pi^0)\nu_\tau$ decays. *Phys. Lett. B*, 349:585–596, 1995.
- [50] D. Cinabro et al. Limit on the tau neutrino mass. *Phys. Rev. Lett.*, 70:3700–3704, 1993.
- [51] T. Gaisser. *Cosmic Rays and Particle Physics*. Cambridge University Press, 1990.
- [52] W. Webber and J. Lezniak. *Astrophys. Space Sci.*, 30:361, 1974.
- [53] P. Capiluppi et al. Charged particle production in proton-proton inclusive reactions at very high energies. *Nucl. Phys. B*, 79:189–258, 1974.
- [54] R. Barnett et al. Review of particle properties. *Phys. Rev. D*, 54(1), 1996.
- [55] T. Gaisser and T. Stanev. Pathlength distributions of atmospheric neutrinos. *Phys. Rev. D*, 57:1977–1982, 1998.

- [56] K. Nakamura et al. Kamiokande. In M. Fukugita and A. Suzuki, editors, *Physics and Astrophysics of Neutrinos*. Springer-Verlag, 1994.
- [57] H. Kume et al. 20 inch diameter photo-multiplier tube. *NIM*, pages 443–449, 1983.
- [58] A. Suzuki. Kamiokande: A historical account. In M. Fukugita and A. Suzuki, editors, *Physics and Astrophysics of Neutrinos*. Springer-Verlag, 1994.
- [59] K. Hirata et al. Results from one thousand days of real-time, directional solar-neutrino data. *Phys. Rev. Lett.*, 65:1297, 1990.
- [60] K. Hirata et al. Real-time, directional measurement of ^8B solar neutrinos in the Kamiokande II detector. *Phys. Rev. D*, 44:2241, 1991.
- [61] K. Hirata et al. Observation of a neutrino burst from the supernova SN1987A. *Phys. Rev. Lett.*, 58:1490–1493, 1987.
- [62] K. Hirata et al. Experimental study of the atmospheric neutrino flux. *Phys. Lett. B*, 205:416, 1988.
- [63] K. Hirata et al. Observation of a small atmospheric ν_μ/ν_e ratio in Kamiokande. *Phys. Lett. B*, 280:146–152, 1992.
- [64] E. Beier et al. Survey of atmospheric neutrino data and implications for neutrino mass and mixing. *Phys. Lett. B*, 283:446–453, 1992.
- [65] H. Georgi and S. Glashow. Unity of all elementary-particle forces. *Phys. Rev. Lett.*, 32:438, 1974.
- [66] R. Becker-Szendy et al. IMB-3: a large water Cherenkov detector for nucleon decay and neutrino interactions. *NIM*, A324:363–382, 1993.
- [67] J. Van Der Velde et al. Neutrinos from SN1987A in the IMB detector. *NIM*, A264:28–31, 1988.
- [68] C. McGrew. *A Search for Baryon Non-Conservation using the IMB-3 Detector*. PhD thesis, University of California at Irvine, 1994.
- [69] R. Becker-Szendy et al. Electron- and muon-neutrino content of the atmospheric flux. *Phys. Rev. D*, 46:3720, 1992.

- [70] R. Clark et al. The atmospheric muon neutrino fraction above 1 GeV. *Phys. Rev. Lett.*, 79:345, 1997.
- [71] S. Ahlen et al. First supermodule of the MACRO detector at Gran Sasso. *NIM*, A324:337–362, 1993.
- [72] S. Ahlen et al. Atmospheric neutrino flux measurement using upgoing muons. *Phys. Lett. B*, 357:481–486, 1995.
- [73] C. Berger et al. The Fréjus nucleon decay detector. *NIM*, A262:463–495, 1987.
- [74] C. Berger et al. Study of atmospheric neutrino interactions with the Fréjus detector. *Phys. Lett. B*, 227:489–494, 1989.
- [75] C. Berger et al. A study of atmospheric neutrino oscillations in the Fréjus experiment. *Phys. Lett. B*, 245:305–310, 1990.
- [76] W. Allison et al. The Soudan 2 detector: The design and construction of the tracking calorimeter modules. *NIM*, A376:36–48, 1996.
- [77] W. Allison et al. Measurement of the atmospheric neutrino flavor composition in Soudan 2. *Phys. Lett. B*, 391:491–500, 1997.
- [78] O. Ryazhskaya. Is there an excess of electron neutrinos in the flux in the atmosphere? *JETP Lett.*, 60:617, 1994.
- [79] G. Battistoni et al. The NUSEX detector. *NIM*, A245:277–290, 1986.
- [80] M. Aglietta et al. Experimental study of atmospheric neutrino flux in the NUSEX experiment. *Europhys. Lett.*, 8(7):611–614, 1989.
- [81] M. Aglietta et al. Experimental study of upward stopping muons in NUSEX. *Europhys. Lett.*, 15(5):559–564, 1991.
- [82] E. Alekseyev et al. Baksan underground scintillation telescope. In *Proceedings of the 16th International Cosmic Ray Conference*, volume 10, pages 276–281, 1979.
- [83] M. Boliev et al. Measurements of the upward-going muon flux with the Baksan underground telescope. In *Proceedings of the 24th International Cosmic Ray Conference*, volume 1, pages 686–689, 1995.

- [84] M. Boliev et al. Search for astrophysical sources of neutrinos and neutrino oscillations using the Baksan data. In *Proceedings of the 24th International Cosmic Ray Conference*, volume 1, pages 722–725, 1995.
- [85] J. Jackson. *Classical Electrodynamics*. John Wiley & Sons, second edition, 1975.
- [86] A. Suzuki et al. Improvement of 20 in. diameter photomultiplier tubes. *NIM*, A329:299, 1993.
- [87] S. Kasuga. *Observation of a Small ν_μ/ν_e Ratio of Atmospheric Neutrinos in Super-Kamiokande by the Method of Particle Identification*. PhD thesis, University of Tokyo, 1998.
- [88] Bit 3 Computer Corporation, 8120 Penn Avenue South, Minneapolis, MN 55431-1393. *Model 467-1 Adaptor Hardware Manual*, revision 1.0 edition, March 1995.
- [89] LeCroy 1877 Multihit Time-to-Digital Converter. Technical report, LeCroy Corp., 700 Chestnut Ridge Road, Chestnut Ridge, New York, 10977-6499, 1996.
- [90] H. Berns. private communication.
- [91] M. Kirsch. Struck STR137-ECL Multi-Event Input Latch. Technical report, Struck Corp., 1996.
- [92] Fermi National Accelerator Laboratory. *FASTBUS Smart Crate Controller (FSCC) Hardware Manual*, PC4b edition, November 1995.
- [93] Access Dynamics, Inc. *DM-115 RS-485 Input Module User Manual*. M2115B.
- [94] Access Dynamics, Inc. *DC-2 VSB Input Controller*. M2002B.
- [95] Bit 3 Computer Corporation, 8120 Penn Avenue South, Minneapolis, MN 55431-1393. *Model 944 Software Support Manual*, revision 2.0 edition, January 1995.
- [96] C.A.E.N., Costruzioni Apparecchiature Elettroniche Nucleari S.p.A., Via Vetraria, 11-55049 VIAREGGIO, Italy. *Technical Information Manual, Model V533*, Jan 1994.
- [97] TrueTime, 2835 Duke Ct., Santa Rosa, CA 95407. *TrueTime Model XL-DC Time and Frequency Receiver Manual*, N/C edition, June 1995.

- [98] TrueTime, 2835 Duke Ct., Santa Rosa, CA 95407. *TrueTime Model VME-SG Timing Card Manual*, NC edition, May 1993.
- [99] W. Peterson. *The VMEbus Handbook*. VFEA International Trade Association, 10229 N. Scottsdale Rd, Suite B, Scottsdale, AZ 85253, 3rd edition, 1993.
- [100] M. Nomachi and Y. Takeuchi. NOVA buffer manager for SDC portable DAQ – users manual. Technical report, National Laboratory for High Energy Physics [KEK] (Nomachi), Tokyo Institute of Technology (Takeuchi).
- [101] L. Wai and H. Berns. Super-Kamiokande anti-detector event building. Technical report, University of Washington, 1997.
- [102] Z. Conner. *A Study of Solar Neutrinos Using the Super-Kamiokande Detector*. PhD thesis, University of Maryland, 1997.
- [103] M. Nakahata et al. Calibration of Super-Kamiokande using an electron LINAC. Submitted to NIM, 7/98.
- [104] G. Barr, T. Gaisser, and T. Stanev. Flux of atmospheric neutrinos. *Phys. Rev. D (Rapid Comm.)*, 39(3):3532–3534, 1989.
- [105] E. Bugaev and V. Naumov. On the interpretation of the Kamiokande experiment. *Phys. Lett. B*, 232:391, 1989.
- [106] H. Lee and Y. Koh. A new calculation of atmospheric neutrino flux. *Nuovo Cimento B*, 105:884, 1990.
- [107] T. Gaisser et al. Comparison of atmospheric neutrino flux calculations at low energies. *Phys. Rev. D*, 54:5578–5584, 1996.
- [108] D. Rein. Angular distribution in neutrino-induced single pion production processes. *Z. Phys.*, C35:43, 1987.
- [109] D. Rein and L. Sehgal. Neutrino-excitation of baryon resonances and single pion production. *Ann. of Phys.*, 133:79, 1981.
- [110] *GEANT Detector Description and Simulation Tool*, 1993. CERN Program Library W5013.
- [111] *PYTHIA and JETSET - Physics and Manual*. CERN Program Library W5035/W5044.

- [112] M. Nakahata. Monte Carlo status. In Nakamura and Takita [128], pages 333–353.
- [113] LeCroy Corp., 700 Chestnut Ridge Road, Chestnut Ridge, New York, 10977-6499. *Model 1877 96 Channel FASTBUS TDC*, March 1995.
- [114] L. Wai. Three major DAQ improvements by U. Wash. In 10/96 [131].
- [115] R. Svoboda. Outer detector Monte Carlo. In Nakamura and Takita [128], pages 107–130.
- [116] Proposal to participate in the Super-Kamiokande project, December 1992.
- [117] L. Wai. Partially contained atmospheric neutrino data reduction and analysis. Technical report, University of Washington, 1997. Super-Kamiokande Internal Note 97-02.
- [118] J. Flanagan et al. Up-down asymmetry: A diagnostic for neutrino oscillations. *Phys.Rev. D*, 57:2649–2652, 1998.
- [119] Y. Fukuda et al. Measurement of the atmospheric neutrino flux ratio ν_μ/ν_e in the multi-GeV energy range. Accepted by Phys. Lett. B, 7/98.
- [120] D. Perkins. *Introduction to High Energy Physics*. Addison-Wesley Publishing Company, 3rd edition, 1987.
- [121] W. Eadie et al. *Statistical Methods in Experimental Physics*, chapter 11. North Holland Publishing Company, 1971.
- [122] J. Learned, K. Young, and R. Doyle. private communication, 1988.
- [123] R. Doyle. private communication, 1998.
- [124] C. McGrew. Systematic error in shape and reduction. In 11/97 [133].
- [125] S. Kasuga et al. A study on the e/μ identification capability of a water Cerenkov detector and the atmospheric neutrino problem. *Phys. Lett. B*, 374:238–242, 1996.
- [126] T. Futagami et al. Observation of the east-west effect in the atmospheric neutrinos. Manuscript in preparation for publication, July 1998.

- [127] Y. Fukuda et al. Evidence for oscillation of atmospheric neutrinos. Submitted to Phys. Rev. Lett, 7/98.
- [128] K. Nakamura and M. Takita, editors. *First Super-Kamiokande International Collaboration Meeting*, KEK, Japan, February 1994.
- [129] *Super-Kamiokande Collaboration Meeting Minutes*, Osawano, Japan, April 1996.
- [130] *Super-Kamiokande Collaboration Meeting Minutes*, Kamioka, Japan, July 1996.
- [131] *Super-Kamiokande U.S. Collaboration Meeting Plenary Sessions*, Los Alamos, New Mexico, USA, October 1996.
- [132] *Super-Kamiokande Collaboration Meeting Minutes*, Kamioka, Japan, November 1995.
- [133] *Super-Kamiokande Collaboration Meeting Minutes*, Kamioka, Japan, November 1997.
- [134] S. Kim. *Real Time, Directional Measurement of ^8B Solar Neutrinos in the Kamiokande-II Detector and Search for Short-Time Variation*. PhD thesis, University of Pennsylvania, 1989.
- [135] Y. Takeuchi. *Measurement of Solar Neutrinos from One Thousand Days of Data at Kamiokande-III*. PhD thesis, Tokyo Institute of Technology, January 1995.
- [136] S. Ohara. Background study on ^8B solar neutrinos. Master's thesis, University of Tokyo, 1989.
- [137] K. Kihara. *An Experimental Study on the ^8B Solar Neutrino Flux in the Kamiokande-II Detector*. PhD thesis, University of Tokyo, 1992.
- [138] M. Nakahata. *Search for ^8B Solar Neutrinos at Kamiokande-II*. PhD thesis, University of Tokyo, 1988.
- [139] K. Hirata. *Search for Supernova Neutrinos at Kamiokande-II*. PhD thesis, University of Tokyo, 1991.
- [140] P. Langacker. Neutrino physics. In J. Gunion et al., editors, *Beyond the Standard Model IV*. World Scientific, 1995.

- [141] M. Wolfke. *Acad. Polonaise Sci. et Lettres, Bull.*, 3-4A:107–109, March-April 1935.
- [142] A combination of preliminary electroweak measurements and constraints on the standard model. CERN-PPE/96-183, Dec. 1996.
- [143] C. De Marzo et al. MACRO: A large area detector at the Gran Sasso Laboratory. *Nuovo Cimento 9C*, 9C:281–292, 1986.
- [144] M. Calicchio et al. The MACRO detector at the Gran Sasso Laboratory. *NIM*, A264:18–23, 1988.
- [145] R. Bellotti et al. Simultaneous observation of extensive air showers and deep-underground muons at the Gran Sasso Laboratory. *Phys. Rev. D*, 42:1396–1403, 1990.
- [146] S. Ahlen et al. Study of penetrating cosmic ray muons and search for large scale anisotropies at the Gran Sasso Laboratory. *Phys. Lett. B*, 249:149–156, 1990.
- [147] S. Ahlen et al. Arrival time distributions of very high energy cosmic ray muons in MACRO. *Nucl. Phys. B*, 370:432–444, 1992.
- [148] S. Ahlen et al. Study of the ultrahigh energy cosmic ray composition with the MACRO experiment. *Phys. Rev. D*, 46:895–902, 1992.
- [149] S. Ahlen et al. Measurement of the decoherence function with the MACRO detector at Gran Sasso. *Phys. Rev. D*, 46:4836–4845, 1992.
- [150] S. Ahlen et al. Search for neutrino bursts from collapsing stars with the MACRO detector. *Astroparticle Phys.*, 1:11–25, 1992.
- [151] S. Ahlen et al. Search for nuclearites using the MACRO detector. *Phys. Rev. Lett.*, 69:1860–1863, 1992.
- [152] S. Ahlen et al. Muon astronomy with the MACRO detector. *Astrophysical Journal*, 412:301, 1993.
- [153] S. Ahlen et al. Search for slowly moving monopoles with the MACRO detector. *Phys. Rev. Lett.*, 72:608–612, 1994.
- [154] M. Ambrosio et al. Coincident observation of air Cerenkov light by a surface array and muon bundles by a deep underground detector. *Phys. Rev. D*, 50:3046–3058, 1994.

- [155] M. Aglietta et al. Study of the primary cosmic ray composition around the knee of the energy spectrum. *Phys. Lett. B*, 337:376–382, 1994.

Appendix A

CALCULATING LIVE-TIME

One of the most important questions to get right is also one of the simplest. How long was the detector on? All of the measured and expected rates are pinned to the exact length of exposure that the detector has. Getting this quantity right turns out to be a complicated process.

Live-time in this analysis is calculated on an event by event basis, one sub-run at a time. Each sub-run contains approximately 10 minutes of data for easier handling. From the outset only runs identified as normal data taking runs are considered.

For each sub-run, the total run time is simply the time between the first and last good events as measured by the central 48 bit 50 MHz clock counter. This would be the live-time if all events were recorded perfectly with full detector sensitivity at all times. In reality, several effects such as regular pedestal calibration, ATM module dead time, outer detector dead time, etc., all conspire to reduce the detector sensitivity for a small fraction of the actual run time. The reported live-time must take this reduced sensitivity into account.

A.1 Event by Event Corrections

Table A.1 lists the six categories of event by event corrections to the total live-time. The time an event takes is defined as the time between that event and the one just previous. This is an arbitrary and convenient definition which allows us to remove problem events in a systematic way. Each of the cuts is taken in order and are exclusive. For example, pedestal dead time is not double counted as inner workstation

Table A.1: Event by event corrections to live-time

pedestal	used to calibrate signal inputs
trigger veto	flags dead time of digitizing modules
ID WS dead	inner DAQ workstation is down or off
OD WS dead	outer DAQ workstation is down or off
Tdiff	analysis imposed minimum dead time
no ODTDC	outer detector has no data

dead time.

A.1.1 Pedestal Events

Pedestal events occur when one inner detector workstation turns off the inputs to the ATM modules under its control. Each inner detector workstation controls one eighth of the detector. The inputs are left off for one hundred events at a time. Each of the workstations takes a turn operating in this mode once each hour. Since an eighth of the detector is not taking data during this time these events are simply rejected for purposes of analysis. By digitizing the signal inputs with no signal present we can measure the base value, or “pedestal value” of each channel. The actual signal size during normal operation must have this base value subtracted off. The size of the pedestal can be affected by mean temperature variations and so is closely monitored.

A.1.2 Trigger Veto

Trigger veto events reflect the slight dead time of the inner detector data acquisition electronics. The ATM modules contain two channels to provide dead time-free operation in theory. In practice the modules are more limited. The ATM modules have only an 8-bit internal event counter. If more than 256 events are recorded in a short time there would be ambiguity about which events the hits belonged to. To avoid

this possibility the LIME modules puts a veto on the trigger signal if the rate goes too high.

In addition to this dead time, events in which both outer and inner detectors had a workstation turned off are considered in this category. Events with only one inner workstation dead, or only the outer workstation dead are counted separately.

In a few cases a data acquisition workstation can crash or simply be turned off. This might be due to a hardware fault or simply by choice. During some types of calibration runs for instance the outer detector workstation is switched off. The outer detector data are not needed and takes up disk and tape storage space unnecessarily. An inner workstation might be switched off momentarily to correct a high voltage problem or flashing tube. In many of these cases the run is allowed to continue so that at least some coverage is provided in case of a supernova. A missing workstation is simply tagged in the data and these events are removed during analysis.

A.1.3 Tdiff Requirement

One of the big concerns in doing atmospheric neutrino analysis is that one might somehow skew the ratio of muon-like to electron-like events. The ratio of these is one of the primary results. The number of electron events can be affected by muon decay. A stopping muon can decay in the tank and produce an electron. If the muon decays well above threshold then the electron is detected in the tail of the muon light. If the muon drops under the Cherenkov threshold, however, it can slow enough to remain in the tank for several lifetimes before decaying. In this case the electron would be detected as a new separate event with its own trigger. It would look exactly like the product of an electron neutrino interaction but it actually came from cosmic ray muon decay. We cannot afford to have this kind of ambiguity.

The solution to this problem is to require that events be many muon lifetimes apart. This imposes a minimum dead time for each event on the detector and shortens the overall time the detector is available to detect neutrinos should one choose

to interact. The requirement for this analysis is that events be more than 100 microseconds apart. This corresponds to forty-five average muon lifetimes. This should make it virtually impossible for a muon decay product to be misinterpreted as an electron neutrino. The Tdiff correction is calculated by counting 100 microseconds for every event which is greater than 100 microseconds from the previous event. If an event is closer than this to the previous event, only the time to the previous event is counted. This makes the counts come out right for handling several events happening in a very short time. It ensures that only events which have no previous event within 100 microseconds are included in the live-time.

The “Tdiff” self-imposed veto of 100 microseconds also sidesteps a second issue which has confused previous attempts to calculate the correct live-time. The outer detector data acquisition has its own dead time due to FASTBUS TDC digitizing. This dead time is measured and stored in the event header that the outer detector provides to the event builder along with the outer detector data. The problem is that this value is unreliable over the course of the detector operation. For most of the first year the value was “mostly” right, but with occasional wild results. When the problems were finally identified and solved, a broken lead [??] kept the value from being recorded at all. Furthermore, the exact value is irrelevant for this analysis. The TDC dead time has a known maximum of 78 microseconds. It will always be shorter than our imposed veto of 100 microseconds to avoid muon decay products. We can simply ignore the outer detector TDC dead time.

A.1.4 No OD TDC Data

The last category deals with outer detector problems. Throughout the first year of running, but primarily at the beginning, there have been short periods where the outer detector failed to provide TDC information. Without this information there is effectively no anti-counter. The risk of contaminating our result with cosmic ray muons or their products is too high to allow analysis of data without this anti-counter

Table A.2: Reasons to cut a sub-run

Failed FC reduction	Could not complete FC reduction
Failed PC reduction	Could not complete PC reduction
High “muon” rate	Measures detector performance
Mismatches	OD data matched with wrong ID event
Cut by hand	Cuts based on FC and PC reduction histograms

in operation. Any event with zero outer detector hits is rejected. Since commencement of “split-trigger” operation the outer detector does not receive a trigger for all events. This condition was modified to require non-zero hits in the outer detector for any event that has one of two trigger bits set meaning that the outer detector should have recorded something.

A.2 Sub-run Corrections

When the event by event checks are completed for each sub-run, the totals for each category are recorded. The sub-run is then subject to further review based on the outcome of the reduction steps. The idea is to watch for any possible change in the performance of the detector and eliminate data from affected times. Table A.2 lists some reasons that a sub-run might be cut from the analysis.

Occasionally the automated reduction processes will fail. Where possible these are restarted and the data are recovered. In a few cases this cannot be done and the affected subruns must simply be dropped. This can happen because of disk or tape writing errors, computer crashes, or other similar problems. The Super-Kamiokande experiment has provided such a flood of data that it is simply not worth the effort for our already thin-spread work force to try to save every last second of live-time. When data cannot be recovered without tremendous effort we will simply throw it out. This is a very happy and unusual circumstance.

At the time of this writing the FC and PC failed reduction cuts are taken separately. This is expected to change in a few days. Runs which do not pass both reductions will be removed from both samples to keep the data sets as alike as possible. At present the partially contained reduction analysis is about 20 days behind the fully contained analysis. Around 17 days of this are runs that were simply not processed by the partially contained reduction and these are being made up now. The remaining three days correspond to runs for which the PC reduction steps failed, largely due to disk copy problems. We will attempt to recover as much of these as possible. The remaining live-time discrepancy between the analyses will probably be simply dropped from the fully contained sample.

For most runs the automated reduction works just fine. We still would like to characterize the performance of the detector. We cannot risk a detector glitch allowing background events to fake neutrino events. While calculating live-time for each sub-run we also keep running checks on two other quantities to ensure that the data we keep for analysis is from a perfectly operating detector. These quantities are the average muon rate and a measure of inner and outer detector mismatch events.

A.2.1 *Muon Rate*

The cosmic ray muon rate serves an ever present control for our data. The average rate is essentially constant for our purposes. Any significant variations in the detected rate then are a prime signal that something has changed with the detector operation. Failure to detect the expected number is a sign that part of the detector is inoperative or has reduced efficiency. A large increase in rate is a sign of extra background, possibly a flashing tube, high voltage or other gain changes, or some type of electronics noise.

At this stage of the analysis one is not of course fitting the events as muon candidates. This would take far too long for the kind of quick characterization that we are after. In each sub-run the number of events are counted such that inner charge

exceeds 500 photoelectrons and the number of outer hits exceeds 100. Any event with a pedestal, trigger veto, or ID/OD workstation off tag is not included. This number is divided by the net live-time for the sub-run to obtain the “muon rate”. Any sub-run with less than 1.8 Hz for this rate is rejected. Subruns with a substantially higher rate are checked for a reason as part of the usual reduction process. Some of these might be rejected by hand once the reason is known. Figure A.1 shows how the cut is determined.

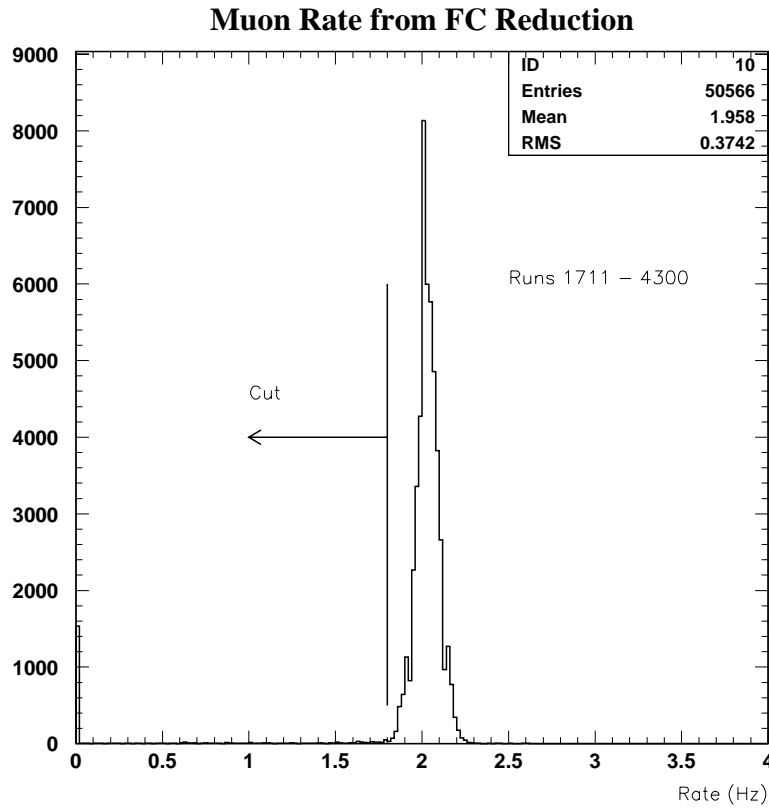


Figure A.1: Muon rate distribution

This definition is sensitive to flashing photo-multiplier tubes and electronics noise. Inner tubes are not light-proofed in back and can pump quite a lot of light into the dead region of the photo-multiplier tube support structure. The light-proof barrier

on this structure is “leaky”, especially when the light is produced in the middle. High signals in the cables can also be picked up by nearby cables in the trays leading to the quadrant huts. It is really not hard for many outer hits to be generated by high charge signals in the inner detector. Also, since Super-Kamiokande’s location, albeit a mile inside a mountain, is above the horizon, most of the detector gets exposure to cosmic ray muons. A drop in performance almost anywhere in the detector will be seen as a drop in the expected muon flux.

A.2.2 OD/ID Mismatch Events

Another worry for our analysis is the performance of the outer detector as a veto counter. At the beginning of detector operation it was known that the outer detector data would sometimes become shifted and matched to the wrong event number. The event builder would then assemble events which do not have the correct outer detector information. If a through going muon in the inner detector is matched with a low energy event in the outer detector this would be disastrous. The event could be interpreted as a neutrino since the veto counter is quiet. Special measures were taken to identify and reject these events early on, as well as making sure that the outer detector got “back on track”. Hardware and software problems causing this were identified and solved within a few months. In the meantime we had to identify such events and even now we are on guard against this kind of error. Figure A.2 shows the decline of mismatch events over time.

Mismatch events are detected by searching for events that trigger the outer detector yet do not have sufficient hits to justify the trigger. The exact requirement is that a “mismatch” event must have both outer detector and high energy trigger flags set, but have less than fifty outer hits. The number of outer hits must be non-zero to avoid counting a simply dead outer detector. If any sub-run has more than five of these events the sub-run is rejected.

Mismatch events were somewhat common in the first days of operation. The

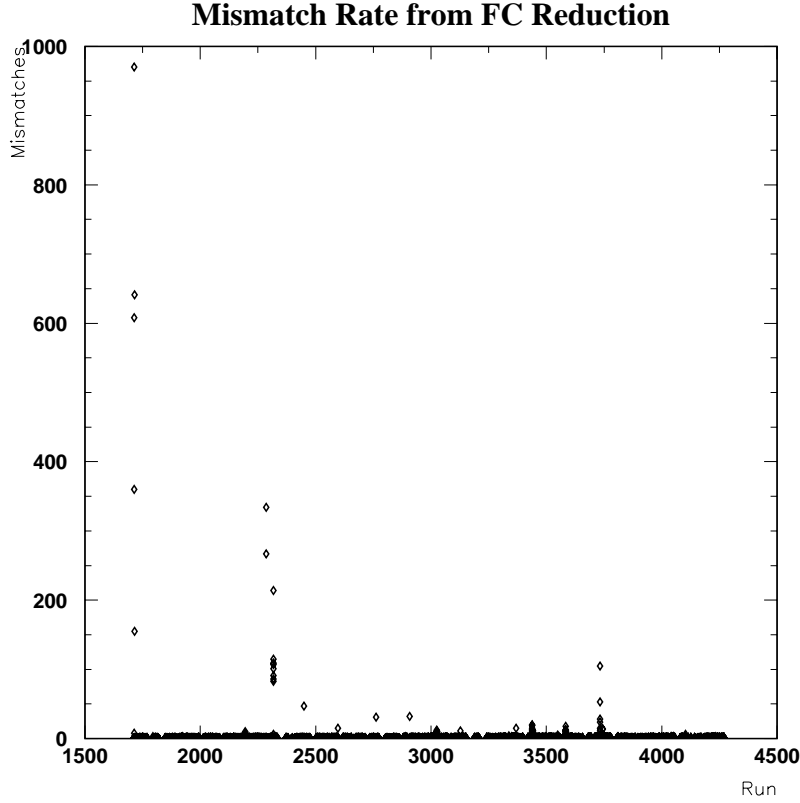


Figure A.2: Mismatched events vs. run

problems had been largely fixed at the point that serious data analysis began. Only brief intermittent occurrences showed up after that and now this problem is completely solved. The only recent cases of mismatched events happened during known problem (“junk”) runs which would not have been analyzed in any case.

A.2.3 Hand Sub-run Cuts

Most subruns rejected from data analysis fall into one of the above categories. A few remaining subruns are simply cut by hand. The reduction processes are monitored very closely. Each member of the analysis group is expected to take rotating week-long “reduction shifts”. The sole duty of the reduction shift person is to monitor

and log all available information about each and every run. This includes log book information, shift worker comments, numerous reduction and data quality histograms, and any other known activity around the detector. Any variation from “standard” operating conditions or detector performance is carefully checked.

The simplest indicator of detector problems is the rate of candidate events from each of the reduction stages. Flashing photo-multiplier tubes will cause high numbers of fully contained neutrino candidates. These can be quickly detected by scanning the candidate files. The rate can also tell us which subruns are affected. This lets us keep as much valid data as we can. While we are not wasteful of data we are in the enviable position of being able to sacrifice live-time for data purity. The rejected data comprises such a small fraction of the total sample that we are happy to drop a few subruns in favor of a more reliable result.

The hand cuts are largely taken on the basis of the fully contained reduction steps. The partially contained reduction is also monitored. A few additional cuts are made based on the output rate of the partially contained result. This is particularly useful because a high rate of partially contained candidates can mean that the outer detector is not functioning as well as a veto counter. If many of those are nearly contained it could be an indicator of concern for the fully contained sample as well. Any sub-run with 10 or more partially contained candidates after the PC 3rd reduction is rejected. This cuts only about 0.7% of the live-time, nearly all of which corresponds to runs already excluded by the fully contained reduction cuts. Figure A.3 shows how this cut is made.

A.3 Net Live-time

All of this calculating generates a list of subruns with the total live-time and totals for the sub-run of the pedestal time, trigger veto, dead workstation, muon and mismatch rates, etc. Subruns that fail one of the sub-run cuts including the hand cut list are

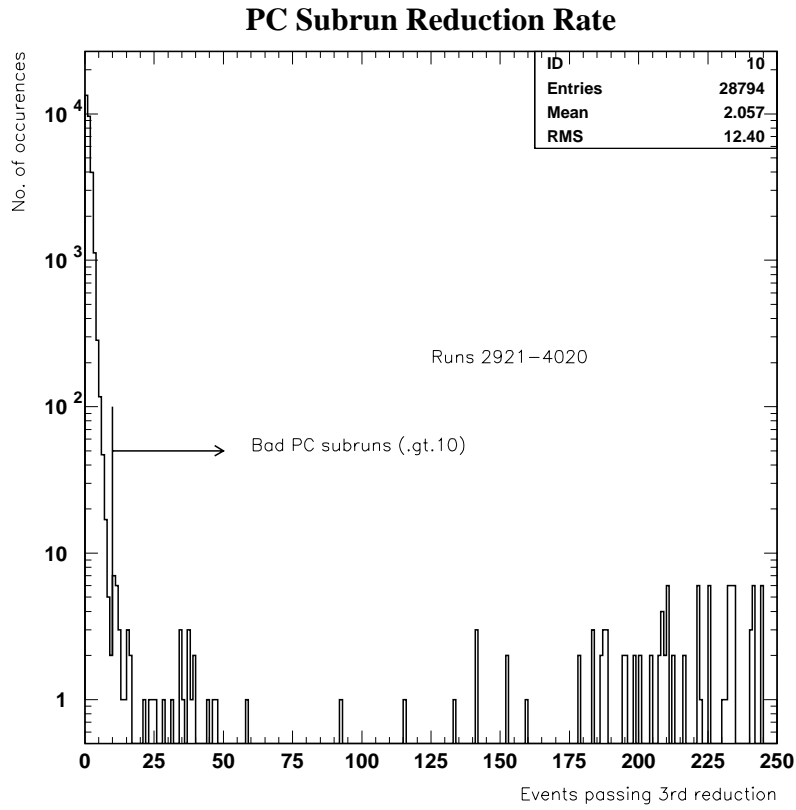


Figure A.3: PC bad subruns cut by hand

removed. What remains is only good subruns. The net live-time for each of these subruns is then calculated by Equation A.1. The sum of the net livetimes for each sub-run is the total net live-time for a group of runs.

$$\begin{aligned}
\textit{Net Livetime} = \textit{Total Livetime} \\
& - \textit{Pedestal} \\
& - \textit{Veto} \\
& - \textit{ID Workstation dead} \\
& - \textit{OD Workstation dead} \\
& - \textit{Tdiff} \\
& - \textit{No OD TDC Data}
\end{aligned}
\tag{A.1}$$

VITA

Jeffrey S. George

Personal Data

3022 NE 87th St.
Seattle, WA 98115
(206) 527-0846 (Home)
(206) 543-9584 (Office)
(206) 685-9242 (FAX)

Box 351560
Department of Physics
University of Washington
Seattle, WA 98195-1560
georgej@phys.washington.edu

Education

June 1994	Ph.D. Candidate in Physics, Advisor, Dr. R. Jeffrey Wilkes, University of Washington.
June 1992	M.S. in Physics, University of Washington.
June 1990	B.S. in Physics, summa cum laude, Seattle Pacific University.

Professional Experience

August 1995 - present

Super-Kamiokande Solar Neutrino Experiment
Department of Physics, University of Washington
Research Assistant

October 1997 - December 1997

Department of Physics, University of Washington
Teaching Assistant – Phy 110

April 1992 - August 1995

The DUMAND Astrophysical Neutrino Telescope
 Department of Physics, University of Washington
Research Assistant

October 1990 - September 1992

Department of Physics, University of Washington
Teaching Assistant – Phy 131

Responsibilities**Super-Kamiokande**

Had primary responsibility for online data acquisition software for the Super-Kamiokande detector Veto Counter. I also contributed to software to reformat online data for delivery to the main host computer via Ethernet and FDDI fiber optic network. Software was written in C on Sun SPARCstation 20 UNIX workstations.

Designed data analysis and data reduction strategies. I have primary responsibility for organizing the data reduction and reporting final results for the Multi-GeV partially contained atmospheric neutrino event sample. I wrote data analysis software in C and FORTRAN using the CERN physics packages.

Wrote hardware interface software for fast data acquisition electronics. Modules included FASTBUS time-to-digital converters, VME-based dual-port memories, pipelined latches, and a GPS satellite receiver. Software also used a hardware interface between a Sun SPARCstation 20 SBus card and the VME crate controller.

Participated in the design and construction of custom front end electronics for the data acquisition system. Also participated in the final phase of detector construction leading to the on-schedule commissioning of the fully operational detector in April 1996.

System administrator for the working group. I directly manage 3 Sun SPARCstations and 3 PCs. Operating systems include SunOS, Solaris, Windows 3.11, Windows 95, and Linux.

DUMAND

Worked on all phases of the design and construction of the environmental sensors and acoustic positioning subsystems of the DUMAND Deep Undersea Muon and Neutrino Detector.

Designed and constructed the power distribution system for underwater environmental sensor packages.

Coordinated the integration of all environmental electronics and sensors in preparation for deployment at ocean bottom.

Participated in deployment of detector on ocean bottom and laying of fiber optic/power cable to a shore laboratory.

Participated in data analysis of system test data as well as sound and video recordings from ocean bottom.

Worked on feasibility of acoustic detection of high energy particles in ocean water.

Phy 110

Responsible for four twice-a-week tutorial sessions for a liberal arts undergraduate physics course. I chose and prepared demonstrations and activities, provided help with assigned problems, and graded midterm exams. I also supervised an undergraduate assistant.

Phy 131

Responsible for teaching of physics concepts in freshman physics laboratory courses. I was entirely responsible for all grading for these laboratory sections. The three hour sessions began with an explanation of physics concepts followed by assisting and encouraging students as they completed the laboratory exercise.

Journal Publications

- “Measurement of the Atmospheric Neutrino Flux Ratio ν_μ/ν_e ,” Y. Fukuda, et al. **Accepted by Phys. Lett. B, 4/98.**

- “Measurement of the Atmospheric Neutrino Flux Ratio ν_μ/ν_e in the Multi-GeV Energy Range,” Y. Fukuda, et al. **Accepted by Phys. Lett. B, 5/98.**
- “Evidence for oscillation of atmospheric neutrinos,” Y. Fukuda, et al. **Submitted to Phys. Rev. Lett., 7/98.**
- “Measurements of the Solar Neutrino Flux from Super-Kamiokande’s First 300 days,” Y. Fukuda, et al. **Accepted by Phys. Rev. Lett., 6/98.**
- “Search for proton decay via $p \rightarrow e^+ \pi^0$ in a large water Cherenkov detector,” M. Shiozawa, et al. **Submitted to Phys. Rev. Lett., 5/98.**
- “Calibration of Super-Kamiokande using an electron LINAC,” M. Nakahata, et al. **Submitted to NIM A, 7/98.**

Conference Presentations

- “Estimated Flux Limits for High Energy Particle Cascades Using Acoustical Detection Techniques.” J. George, for the DUMAND Collaboration. *Proc. 24th International Cosmic Ray Conference*. Rome, 1995. 1:812.
- “High Precision Underwater Positioning System for the DUMAND-II Astrophysical Neutrino Detector.” J. George, for the DUMAND Collaboration. Presented at the General Meeting of the American Physical Society. Seattle, 1993.

Conference Proceedings

- “Solar Neutrino Results from Super-Kamiokande ,” Z. Conner, for the Super-Kamiokande Collaboration. *Proc. 25th International Cosmic Ray Conference*. Durban, 1997. 7:69.
- “Underground Muons in Super-Kamiokande ,” J. G. Learned, for the Super-Kamiokande Collaboration. *Proc. 25th International Cosmic Ray Conference*. Durban, 1997. 7:73.
- “Mapping the Earth’s Interior with Astrophysical Neutrinos,” H. J. Crawford, *et. al.*, for the DUMAND Collaboration. *Proc. 24th International Cosmic Ray Conference*. Rome, 1995. 1:804-807.

- “Monte Carlo Study of DUMAND Three-String Array,” A. Okada, for the DUMAND Collaboration. *Proc. 24th International Cosmic Ray Conference*. Rome, 1995. **1**:766-769.
- “Update on the Status of DUMAND-II,” C. M. Alexander, *et. al.*, for the DUMAND Collaboration. *Proc. 23rd International Cosmic Ray Conference*. Calgary, 1993. **4**:515-518.
- “Estimate of Down-going Atmospheric Muon Background Events in DUMAND-II,” A. Okada and K. Mauritz O’Brien, for the DUMAND Collaboration. *Proc. 23rd International Cosmic Ray Conference*. Calgary, 1993. **4**:523-526.
- “Capabilities of the DUMAND-II Phase I 3-String Array,” V. Stenger, for the DUMAND Collaboration. *Proc. 23rd International Cosmic Ray Conference*. Calgary, 1993. **4**:527-530.
- “Trigger Strategies and Processing for DUMAND,” U. Camerini, *et. al.*, for the DUMAND Collaboration. *Proc. 23rd International Cosmic Ray Conference*. Calgary, 1993. **4**:530-533.
- “An Optical Sensor for DUMAND-II – European Version,” P. C. Bosetti, for the DUMAND Collaboration. *Proc. 23rd International Cosmic Ray Conference*. Calgary, 1993. **4**:534-537.
- “Acoustical Detection of Cascades in DUMAND,” J. Learned and R. J. Wilkes, for the DUMAND Collaboration. *Proc. 23rd International Cosmic Ray Conference*. Calgary, 1993. **4**:538-541.
- “Acoustical Locating System for DUMAND-II,” H. G. Berns, *et. al.*, for the DUMAND Collaboration. *Proc. 23rd International Cosmic Ray Conference*. Calgary, 1993. **4**:542-545.
- “The DUMAND-II Digitizer,” , E. Hazen, for the DUMAND Collaboration. *Proc. 23rd International Cosmic Ray Conference*. Calgary, 1993. **4**:768-771.
- “On the Detection of UHE Cascade Showers with DUMAND-II,” A. Okada and J. Hauptman, for the DUMAND Collaboration. *Proc. 23rd International Cosmic Ray Conference*. Calgary, 1993. **4**:772-775.

Seminar Presentations

- “Experimental Study of the Atmospheric ν_μ/ν_e Ratio in the Multi-GeV Energy Range.” *Ph.D. Final Examination*. University of Washington. July 1998.
- “Atmospheric Neutrinos in Super-Kamiokande,” *Particle Astrophysics Seminar*. University of Washington. May 1998.
- “Super-Kamiokande Results and Analysis.” *Space Radiation Laboratory Seminar*. California Institute of Technology. May 1998.
- “Super-Kamiokande Results and Analysis.” TRIUMF Accelerator Facility, Vancouver B.C. April 1998.
- “Super-Kamiokande Results and Analysis.” New York University. March 1998
- “Calibration of Super-Kamiokande,” *Particle Astrophysics Seminar*. University of Washington. February 1998.
- “Atmospheric Neutrinos in Super-Kamiokande,” *Guest Lecture for Nuclear and Particle Physics students*. Seattle Pacific University. May 1997.
- “Summary of 24th Intl. Cosmic Ray Conference,” *Cosmic Ray Seminar*. University of Washington. October 1995.
- “Acoustic Detection of High Energy Cascades in DUMAND,” *Cosmic Ray Seminar*. University of Washington. April 1995.
- “DUMAND Test Cruise Preparations,” *Cosmic Ray Seminar*. University of Washington. August 1994.
- “Correlation of Acoustic and Optical Signals from Neutrino-Induced HE Cascades in DUMAND,” *General Exam*. University of Washington. April 1994.
- “Acoustic Data from DUMAND,” *Cosmic Ray Seminar*. University of Washington. March 1994.

References

- | | |
|--|---|
| <ul style="list-style-type: none"> • Dr. R. Jeffrey Wilkes
Box 351560
Department of Physics
University of Washington
Seattle, WA 98195-1560
(206) 543-4232
(206) 685-9242 FAX
wilkes@phys.washington.edu • Dr. Kenneth Young
Box 351560
Department of Physics
University of Washington
Seattle, WA 98195-1560
(206) 543-4186
(206) 685-9242 FAX
young@phys.washington.edu • Dr. Henry Sobel
Physics Department
University of California at Irvine
Irvine, CA 92717
(714) 824-6431
(714) 824-7478 FAX
sobel@master.ps.uci.edu • Dr. Jordan Goodman
University of Maryland
College Park, MD 20742
(301) 405-6033
(301) 699-9195 FAX
goodcos@umdhep.umd.edu | <ul style="list-style-type: none"> • Dr. Takaaki Kajita
Kamioka Observatory
Inst. for Cosmic Ray Research
Higashi-mozumi, Kamioka-cho
Yoshiki-gun, Gifu 506-12, JAPAN
kajita@suketto.icrr.u-tokyo.ac.jp • Dr. Yoichiro Suzuki
Kamioka Observatory
Inst. for Cosmic Ray Research
Higashi-mozumi, Kamioka-cho
Yoshiki-gun, Gifu 506-12, JAPAN
suzuki@icrkm4.icrr.u-tokyo.ac.jp • Dr. Y. Totsuka
Kamioka Observatory
Inst. for Cosmic Ray Research
Higashi-mozumi, Kamioka-cho
Yoshiki-gun, Gifu 506-12, JAPAN
totsuka@icrkm4.icrr.u-tokyo.ac.jp • Dr. James Crichton
Department of Physics
Seattle Pacific University
3307 3rd Avenue West
Seattle, WA 98119
(206) 281-2149
(205) 281-2882 FAX
crichton@spu.edu |
|--|---|